

DESIGN AND DEVELOPMENT OF FUNCTIONAL BIOPOLYMERIC MATERIALS FOR ENVIRONMENTAL APPLICATIONS

Doctoral Thesis

by

Anoop Singh
(2019cyz0006)



DEPARTMENT OF CHEMISTRY
INDIAN INSTITUTE OF TECHNOLOGY
ROPAR

July, 2024

DESIGN AND DEVELOPMENT OF FUNCTIONAL BIOPOLYMERIC MATERIALS FOR ENVIRONMENTAL APPLICATIONS

A Thesis Submitted
In Partial Fulfillment of the Requirements
for the Degree of

Doctor of Philosophy

by

Anoop Singh

2019CYZ0006



DEPARTMENT OF CHEMISTRY
INDIAN INSTITUTE OF TECHNOLOGY
ROPAR

July, 2024

Anoop Singh: “Design and Development of Functional Biopolymeric Materials
for Environmental Applications”

Copyright©2024, Indian Institute of Technology Ropar

All Rights Reserved

Dedicated to My Parents and Family



Indian Institute of Technology Ropar
Department of Chemistry

DECLARATION BY THE CANDIDATE

I, Mr. Anoop Singh, hereby declare that the work presented in the thesis entitled “*Design and Development of Functional Biopolymeric Materials for Environmental Applications*”, submitted for the degree of **Doctor of Philosophy** in Chemistry to the Indian Institute of Technology Ropar, Rupnagar, India has been carried out by me under the supervision of **Prof. Narinder Singh** in the Department of Chemistry, Indian Institute of Technology Ropar, Rupnagar, India. The work is original, based on experimental findings, and has not been submitted in part or full by me elsewhere for a degree. In keeping parity with the general practice of reporting scientific observations, due acknowledgment has been made wherever the work described is based on the findings of other investigators.

Ropar

3-July, 2024

Anoop Singh

(Ph.D. Student)

This is to certify that the above statement made by the candidate is correct to the best of my knowledge.

Prof. Narinder Singh

(Research Supervisor)

Department of Chemistry

Indian Institute of Technology Ropar

Rupnagar, Punjab 140001



Indian Institute of Technology Ropar
Department of Chemistry

CERTIFICATE

This is to certify that the work incorporated in the thesis entitled “*Design and Development of Functional Biopolymeric Materials for Environmental Applications*” was carried out by the candidate, Mr. Anoop Singh under my supervision in the Department of Chemistry, Indian Institute of Technology Ropar, Rupnagar, India. I am forwarding the above-mentioned thesis of his being submitted for the degree of **Doctor of Philosophy in Chemistry** of this Institute. To the best of my knowledge, the present work or any part thereof has not been submitted elsewhere for a degree.

Ropar
3-July, 2024

Prof. Narinder Singh
(Research Supervisor)
Department of Chemistry
Indian Institute of Technology Ropar
Rupnagar, Punjab 140001

Acknowledgment

Firstly, I would like to express my sincere gratitude to my research supervisor Prof. Narinder Singh for giving me an opportunity to carry out my doctoral study in his research group, and for his continuous support, guidance, and invaluable advice during my PhD. I appreciate his immense knowledge, patience, and motivation that encouraged me in all the time of my academic research. He has been the paragon of hard work, sincerity, and his mentorship was paramount in providing a well-rounded experience that helped me to grow as an experimentalist, chemist, and an independent thinker.

I would like to thank my DC members: Dr. T.J Dhillip Kumar (Department of Chemistry, IIT Ropar), Dr. Yashveer Singh (Department of Chemistry, IIT Ropar), Dr. CM Nagaraja (Department of Chemistry, IIT Ropar) and Dr. KC Jena (Department of Physics, IIT Ropar) for continuously monitoring the progress of the work and providing valuable suggestions along with the much required continuous encouragement and support. I am also profoundly grateful to Prof. Navneet Kaur, Department of Chemistry, Panjab University Chandigarh for her expert advice and continuous encouragement. I am also profoundly grateful to our international collaborator Prof. Doo Ok Jang, Department of Chemistry, Yonsei University, South Korea for his advice and continuous encouragement.

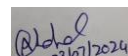
Also, I would like to extend my gratitude and thanks to Director IIT Ropar for providing access to different facilities and equipment for conducting experiments. I would like to thank those individuals for their scientific contributions to the work presented in this thesis: Mr. Manish Kumar (for recording NMR), Mr. Amit Kumar (for recording SEM and EDS), Ms. Hanspreet Kaur (for recording mass data), and Harsimran (AFM analysis) who were always so helpful and provided me with their assistance throughout my dissertation. I am also very grateful to all those at the Department office, especially Mr. Nagendra, Ms. Poonam Kataria, Ms. Samita Saini, and others who were always helpful and provided me with their assistance during this period. I would like to thank Dr. Dinesh Siddaiah, Head librarian for his continuous help in providing reference material.

I gratefully acknowledge the funding received for my PhD from the IIT Ropar. This PhD study would not have been possible without the cooperation, support, and encouragement of my seniors Dr. Gagandeep Singh, Dr. Amanpreet Singh, Dr. Pushap Sharma, Dr. Mayank, Dr. Jagpreet Singh Sidhu, Dr. Deepak Bains, Dr. Monika, Dr. Harupjit Singh, Dr. Sanjeev Saini. I would like to thank my friends and lab mates, Manish Kumar, Kamalpreet Kaur, Arun Sharma, Ranbir, Bulle Shah, Renu Devi, Sarabjit Singh, Shubham, Umang, Naveen Kumar, and Sneha Maithil for a cherished time spent together in the lab and their support all through my studies. Especially, I would like to thanks Dr. Shilpa Sharma, Dr. Richa, and Dr. Beant Kaur Billing for their suggestions and words of encouragement.

I specially thanks to my friends and Ph.D. batchmates Mr. Sandeep, Mr. Priyank, Mr. Rakesh, Mr. Gulshan, Mr. Ganesh, Mr. Vishal, Ms. Ritika, Ms. Akansha, Mr. Man Singh, Mr. Vatan, Mr. Sambhu, Mr. Shain, Ms. Sweta, Mr. Saurav, Mr. Arijit for all kind of support and spend quality time together.

I would like to thank my friend Vikas Kumar Jangra for all kind of support and spend quality time together

I am forever indebted to my beloved parents and my family members Sh. Suresh Pal Chahal, Smt. Angrejo Devi, Mr. Nitesh Chahal, and Ms. Seema Devi. for their generous support, encouragement, unconditional love, invaluable blessings, and untold sacrifices for my better and bright career. They were always there when I needed them and without their encouragement and understanding, it would have been impossible for me to finish this work. I would like to express my special thanks of gratitude to my wife Ritu for always being there for me and also supporting the family. Thanks to my cute & loving niece and nephew Aashvi Chahal and Aarvik Chahal who made my life filled with joy.



Anoop Singh

CHAPTER-1

Classifications of biopolymers and synthesis of biopolymeric materials for environmental applications

1.1 Introduction	2-3
1.2 Classifications of Biopolymers.....	3
1.2.1 Polysaccharide.....	3-4
1.2.2 Polypeptides.....	4
1.2.3 Polynucleotides.....	4
1.3 Common Examples of biopolymer.....	4
1.3.1 Cellulose.....	5-6
1.3.2 Chitin.....	7
1.3.3 Gelatin.....	8
1.3.4 Sodium Alginate.....	8-9
1.4 Applications of biopolymeric materials for environmental applications.....	9-10
1.4.1 Water Purification	10-13
1.4.2 Catalysis	13-16
1.4.3 Biopolymer for Antibacterial activity.....	16-18
1.4.4 Biopolymers in sensing.....	18-20
1.5 References.....	20-30

CHAPTER-2

Chitosan–poly(vinyl alcohol)–ionic liquid-grafted hydrogel for treating wastewater

2.1 Aim and Objective.....	32
2.2 Introduction.....	32-34
2.3 Experimental.....	34
2.3.1 Materials.....	34
2.3.2. Characterization method.....	34
2.3.3 Synthesis of ionic liquid.....	35

2.3.4 Synthesis of CS–PVA–IL gel.....	35
2.3.5 Dye adsorption.....	35-36
2.4 Result and Discussion.....	36
2.4.1 Preparation of CS–PVA–IL gel.....	36-37
2.4.2 Optimization of the CS–PVA–IL gel.....	37-39
2.4.3 FTIR spectroscopy.....	40-41
2.4.4 XPS analysis.....	41-42
2.4.5 PXRD analysis.....	42-43
2.4.6 Surface morphology analysis.....	43-45
2.4.7 Rheological studies and Zeta potential.....	45-46
2.4.8 Thermal stability.....	46-47
2.4.9 Dye adsorption.....	47-52
2.4.10 Nitrite-removal studies.....	53
2.4.11 Lead adsorption.....	53-54
2.4.12 Oil recovery.....	55
2.5 Conclusion.....	55
2.6 References.....	56-61

CHAPTER-3a

Cellulose-reinforced polymer (PEVA) supported silver nanoparticles (AgNPs) with excellent catalytic properties: the synthesis thioamides via Willgerodt-Kindler Reaction

3a.1 Aim and Objectives.....	64
3a.2 Introduction.....	64-65
3a.3 Experimental Section.....	66
3a.3.1 General information.....	66
3a.3.2 Cellulose isolation from rice straw.....	66-67
3a.3.3 Preparation of the AgNPs@cellulose–PEVA hybrid.....	67
3a.3.3.1 Preparation of cellulose-PEVA.....	67
3a.3.3.2 Preparation of AgNPs.....	67

3a.3.4 Catalytic activity of the AgNPs@cellulose–PEVA hybrids for the Willgerodt–Kindler reaction.....	68-73
3a.4 Results and Discussion.....	73
3a.4.1 FTIR spectroscopic analysis.....	73-74
3a.4.2 PXRD Analysis.....	74-75
3a.4.3 SEM and EDX analyses.....	75-76
3a.4.4 RGB analysis.....	76-77
3a.4.5 Mechanical Testing.....	77-78
3a.4.6 Catalytic activity of the AgNPs@cellulose-PEVA nanohybrid for the Willgerodt–Kindler reaction.....	78-82
3a.4.7 Reusability of the AgNPs@cellulose–PEVA hybrid catalyst.....	82-83
3a.4.8 Proposed mechanism.....	83-84
3a.5 Conclusion.....	84
3a.6 References.....	85-90

CHAPTER-3b

Ionic liquid functionalized Fe₃O₄ core–shell nanoparticles: A magnetically separable Brønsted acid catalyst for the synthesis of polythioamides

3b.1 Aim and Objectives.....	92
3b.2 Introduction.....	92-94
3b.3 Experimental Section.....	94
3b.3.1 General information.....	94
3b.3.2 Synthetic procedures.....	95
3b.3.3 Synthesis of ionic liquids.....	95-99
3b.4 Results and Discussion.....	99
3b.4.1 Crystal structure and crystallinity.....	99-100
3b.4.2 Surface morphology analysis.....	100-102
3b.4.3 Atomic force microscopy (AFM).....	102-103
3b.4.4 X-ray photoelectron spectroscopy (XPS).....	104
3b.4.5 Photophysical properties of catalyst.....	104-105

3b.4.6 Adsorption isotherm and acidic strength of catalyst.....	105
3b.4.7 Thermal stability of catalyst.....	106
3b.5 Experimental Section.....	106
3b.5.1 Multicomponent Tandem polymerization via Willgerodt Kindler Reaction.....	106-107
3b.5.2 Catalytic activity of magnetite IL1-2@Fe ₃ O ₄ nanohybrids.....	107-108
3b.5.3 Synthesis of polythioamides in the presence of catalyst.....	109-110
3b.5.4 Polymerization Reaction in presence of new catalyst.....	110-111
3b.5.5 Fluorescence behavior of synthesized poly-thioamides (P1-P9)...	112
3b.5.6 Reusability of Catalyst.....	112-113
3b.6 Conclusion.....	113-114
3b.7 References.....	113-118

CHAPTER-4

Biomass-derived Ionic liquid functionalized Cellulose embedded with AuNPs as Solid Support Catalyst: An efficient Catalyst for the Synthesis of Iodixanol and Iohexol

4.1 Aim and Objectives.....	120
4.2 Introduction.....	120-122
4.3 Experimental Section.....	122
4.3.1 Materials.....	122-123
4.3.2 Preparation of Benzimidazole based ionic liquid (ASC-1).....	123-125
4.3.3 Preparation of Cellulose-Ionic liquid hybrid.....	125
4.3.4 Preparation of Au@CIL hybrid.....	125-126
4.3.5 Characterization method.....	126
4.3.6 Catalytic activity of Au@CIL hybrid for selective Nitro-Reduction.	127
4.4 Result and Discussion.....	127
4.4.1 Characterizations.....	127
4.4.1.1 Fourier Transform Infrared-Spectroscopy (FTIR).....	127-128
4.4.1.2 Crystal structure and crystallinity-X-Ray diffraction.....	128-129
4.4.1.3 Surface Morphology Analysis.....	129-131

4.4.1.4 Zeta potential.....	131-132
4.4.2 Catalytic activity of Au@CIL for selective nitro reduction.....	132-139
4.4.3 Mechanistic insight.....	132-139
4.4.4 Synthesis of iodixanol.....	139-140
4.4.5 Synthesis of iohexol.....	140
4.5 Conclusion.....	140
4.6 References.....	141-147

CHAPTER-5a

Development and characterization of Ionogel Polymeric Film with Antibacterial and Antioxidant properties for food packaging

5a.1 Aim and objective.....	150
5a.2 Introduction.....	150-152
5a.3 Materials and method.....	152
5a.3.1 Materials.....	152
5a.3.2 Synthesis of ionic liquid (IL).....	152-155
5a.3.3 Film preparation.....	156
5a.3.4 Antibacterial Activity Test against <i>E. coli</i> and <i>S. aureus</i> bacterial strain.....	157
5a.3.5 Sample preparation of bacterial strain for AFM and SEM analysis..	157
5a.3.6 Characterization.....	157-158
5a.4 Result and discussion.....	158-159
5a.4.1 FTIR & PXRD investigation.....	159-160
5a.4.2 Morphological and elemental composition of polymeric films.....	160
5a.4.3 Mechanical properties.....	161-162
5a.4.4 Thermal degradation analysis.....	162-163
5a.4.5 Rheology study.....	163-164
5a.4.6 Optical (light transmission) properties.....	164-165
5a.4.7 Antibacterial Activity.....	165-167
5a.4.8 Bacterial sample preparation for SEM and AFM analysis.....	168-169
5a.4.9 Antioxidant properties.....	168

5a.4.9.1 Radical scavenging method.....	168-169
5a.4.9.2 Developed polymeric film for food packaging.....	169-170
5a.5 Conclusions.....	170
5a.6 References.....	170-174.

CHAPTER-5b

Biodegradable Sodium alginate/COF Based Polymeric Film That Monitor Food Spoilage and Extend Shelf Life

5b.1 Aim and objective.....	176
5b.2 Introduction.....	176-178
5b.3 Materials and method.....	179
5b.3.1 Materials.....	179
5b.3.2 Material Characterization.....	179-180
5b.3.3 Synthesis of COF.....	180
5b.3.4 Smart polymeric strips for monitoring food spoilage.....	180-181
5b.3.5 Antibacterial Activity Test.....	181
5b.3.6 Active packaging for preservation of peanuts.....	181-182
5b.3.7 Synthesis of smart sensing strips for food monitoring.....	182-183
5b.4 Result and Discussion.....	183
5b.4.1 PXRD and FTIR Spectra of COF.....	183-184
5b.4.2 Scanning Electron Microscopy (SEM) Observations.....	184-185
5b.4.3 Brunauer-Emmett teller (BET) Isotherm.....	185-186
5b.4.4 X-ray Photoelectron Spectroscopy (XPS).....	186-187
5b.4.5 Mechanical properties of SA and SA/COF film.....	187-188
5b.4.6 Electrochemical performance of COF.....	188-191
5b.4.7 Smart labeling for packaging of food items.....	191-192
5b.4.8 COF/SA for food packaging.....	192-194
5b.5 Conclusion.....	194
5b.6 References.....	194-200

CHAPTER-6

6.1 Conclusion.....	201-204
----------------------------	----------------

Appendix	205-234
-----------------------	----------------

List of Figures

Figure 1.1.	Sources of biopolymer.	1-3
Figure 1.2.	Classification of biopolymers based on their origin.	1-4
Figure 1.3.	Chemical structure of biopolymers.	1-6
Figure 1.4.	Arrangement and orientation of chitin microfibrils in α -, β -, and γ -chitin.	1-7
Figure 1.5.	Applications of biopolymers.	1-10
Figure 1.6.	Biopolymer derived materials for wastewater treatment.	1-11
Figure 1.7.	Porous materials for Catalysis.	1-14
Figure 1.8.	Biopolymers and organic compounds derived polymeric film for smart sensing and active packaging of food.	1-18
Figure 1.9.	Biopolymers and COF based materials for food smart sensing and active food packaging.	1-19
Figure 2.1.	Schematic of the synthesis of the CS–PVA–IL gel.	2-37
Figure 2.2.	Swelling optimization of the CS–PVA–IL gel by varying different parameters: A) IL content, B) time, C) temperature, D) initiator content, E) water content, and F) pH.	2-39
Figure 2.3.	FTIR spectra of A) CS, B) PVA, C) CS + PVA, and D) CS–PVA–IL gel.	2-41
Figure 2.4.	XPS peaks of A) all atoms present in the CS–PVA–IL gel, and the B) C1s, C) N1s, and D) O1s spectra.	2-42
Figure 2.5.	A) PXRD patterns of i) CS, ii) PVA, iii) CS–PVA mixture, and iv) CS–PVA–IL gel. B) PXRD patterns of CS–PVA–IL gel and CS–PVA–IL gel–dye.	2-43

Figure 2.6.	A) SEM image of CS-PVA-IL gel, B) EDS spectrum of CS-PVA-IL gel and individual elemental dot mapping of C) carbon, D) nitrogen, E) oxygen, and F) bromine.	2-44
Figure 2.7.	BET adsorption isotherm for CS-PVA-IL gel.	2-45
Figure 2.8.	A) Dynamic mechanical analysis of G' and G'' , and B) viscosity analysis of the CS-PVA-IL gel.	2-46
Figure 2.9.	Zeta potential of CS-PVA-IL gel at different pH.	2-46
Figure 2.10.	TGA curve of the CS-PVA-IL gel.	2-47
Figure 2.11.	A) UV-vis spectra of the adsorption of murexide and B) percentage removal of murexide as a function of time using the CS-PVA-IL gel.	2-48
Figure 2.12.	A) UV-vis spectra for the adsorption of murexide and B) percentage removal of murexide as a function of the CS-PVA-IL gel dose.	2-48
Figure 2.13.	UV-vis spectra for the adsorption of murexide at different pH A) pH 3, B) Ph 5, C) pH 9, and D) pH 11. E) Percentage removal of murexide as a function of pH.	2-50
Figure 2.14.	A) and B) RSM plot for optimization of dye adsorption. C) Freundlich-adsorption-isotherm-fitted dye adsorption and D) pseudo-second-order kinetic fit for murexide.	2-52
Figure 2.15.	Plots showing the reusability of the CS-PVA-IL gel.	2-52

Figure 2.16.	A) Ion-chromatography area under the curve for removing nitrite anions with CS–PVA–IL gel and B) decreasing concentration of nitrite anion as a function of time.	2-53
Figure 2.17.	A) and B) Freundlich-adsorption-isotherm model for adsorption of Pb^{2+} , C) plausible mechanism for the adsorption of Pb^{2+} on the CS–PVA–IL gel surface, and D) decreasing Pb^{2+} concentrations at different intervals.	2-54
Figure 2.18.	Images of A) biphasic oil–water (before treatment) and B) water treated using the CS–PVA–IL gel.	2-55
Figure 3a.1.	^1H NMR (CDCl_3) of 1 .	3a-69
Figure 3a.2.	^{13}C NMR (CDCl_3) of 1 .	3a-69
Figure 3a.3.	HRMS of 1 .	3a-70
Figure 3a.4.	Fourier-transform infrared spectra of (A) poly(ethylene-co-vinyl acetate) (PEVA), (B) cellulose, (C) cellulose–PEVA composite, and (D) AgNPs@cellulose–PEVA hybrid.	3a-74
Figure 3a.5.	Powder X-ray diffraction patterns of (A) raw cellulose, (B) cellulose, (C) poly(ethylene-co-vinyl acetate) (PEVA), (D) the cellulose–PEVA composite, and (E) AgNPs@cellulose–PEVA hybrid.	3a-75
Figure 3a.6.	Scanning electron microscopy images of the (A) cellulose–poly(ethylene-co-vinyl acetate) (PEVA) composite and (C) AgNPs@cellulose–PEVA hybrid. Energy-dispersive X-ray mappings of the (B) cellulose–PEVA composite and (D) AgNPs@cellulose–PEVA hybrid.	3a-76

Figure 3a.7.	(A) Square regions of the digital images selected for RGB analysis of the (i) rice straw (RS), (ii) poly(ethylene-co-vinyl acetate) (PEVA), (iii) the cellulose–PEVA composite and (iv) the AgNPs@cellulose–PEVA hybrid. (B) Bar graph of the RGB intensities of RS, PEVA, the cellulose–PEVA composite and the AgNPs@cellulose–PEVA hybrid.	3a-77
Figure 3a.8.	(A) Stress–strain and (B) force–position curves of poly(ethylene-co-vinyl acetate). (C) Stress–strain and (D) force–position curves of the cellulose–poly(ethylene-co-vinyl acetate) composite.	3a-78
Figure 3a.9.	(A) Reusability of the AgNPs@cellulose–PEVA catalyst. (B) Reaction yields with or without the AgNPs@cellulose–PEVA catalyst.	3a-83
Figure 3b.1.	^1H -NMR Spectra of IL1.	3b-96
Figure 3b.2.	^{13}C -NMR Spectra of IL1.	3b-96
Figure 3b.3.	Mass spectroscopy of IL1.	3b-97
Figure 3b.4.	IR spectroscopy of IL1.	3b-97
Figure 3b.5.	Chemical Structure of prepared ionic liquids (A) IL1 and (B) IL2.	3b-99
Figure 3b.6.	(A) PXRD spectra of (i) Fe_2O_3 , (ii) IL1@ Fe_3O_4 , and (iii) IL2@ Fe_3O_4 . Dynamic light scattering (DLS) of (B) Fe_2O_3 , (C) IL1@ Fe_3O_4 , and (D) IL2@ Fe_3O_4 .	3b-100
Figure 3b.7.	SEM Image of (A) Fe_2O_3 , (C) IL1@ Fe_2O_3 , and EDS spectra of (B) Fe_2O_3 , (D) IL1@ Fe_2O_3 . Elemental dot mapping of IL1, individual mapping of (E) C (9.16 %), (F) O	3b-101

	(11.40 %), (G) N (2.36 %), and (H) Fe (45.16%).	
Figure 3b.8.	SEM Image of (A) IL1@Fe ₂ O ₃ , EDS spectra of (B) IL2@Fe ₂ O ₃ , and (C) HRTEM Image of Core-shell IL1@Fe ₂ O ₃ nanoparticles.	3b-102
Figure 3b.9.	Atomic force microscopy (AFM) images in (A) 2-dimensional and (B) 3-dimensional of IL1@Fe ₂ O ₃ .	3b-103
Figure 3b.10.	Magnetically separation of A) Fe ₃ O ₄ , B) IL1@Fe ₃ O ₄ , and C) IL2@Fe ₃ O ₄ .	3b-103
Figure 3b.11.	XPS spectra of A) IL1@Fe ₃ O ₄ core peak of C1s, N1s, O1s, and Fe2p, B) 1s core peaks of C, O, N, and C) 2p core peaks of Fe.	3b-104
Figure 3b.12.	N ₂ adsorption-desorption spectra (BET) of Fe ₂ O ₃ , IL1@Fe ₂ O ₃ , and IL2@Fe ₂ O ₃ .	3b-105
Figure 3b.13.	TGA of A) IL2@Fe ₃ O ₄ and B) IL1@Fe ₃ O ₄ .	3b-106
Figure 3b.14.	Molecular structure of synthesized poly-thioamides (P1-P9).	3b-108
Figure 3b.15.	Gel Permeation Chromatography for synthesis of polythioamides.	3b-111
Figure 3b.16.	(A) Image of polymer (P1) under UV chamber and (B) Emission profile of the synthesized poly-thioamides (P1-P9) in methanol (10 Mm) excited at a wavelength of 340 nm.	3b-112
Figure 3b.17.	A) SEM image of IL1@Fe ₂ O ₃ after 7 th cycle and B) DLS image of IL1@Fe ₂ O ₃ after 7 th cycle.	3b-113
Figure 3b.18.	Reusability of the IL1-2@Fe ₃ O ₄ catalyst.	3b-113
Figure 4.1.	HRMS data of ASC-1	4-124
Figure 4.2.	¹ H-NMR of ASC-1	4-124
Figure 4.3.	¹³ C-NMR of ASC-1	4-125

Figure 4.4.	A) FTIR Spectra of (I) Cellulose, (II) Cellulose-lactic acid, (III) Cellulose-ionic liquid and B) (I) Cellulose-ionic liquid, (II) Au@CIL.	4-128
Figure 4.5.	A) PXRD Spectra of (I) Cellulose, (II) Cellulose-lactic acid, (III) Cellulose-ionic liquid and B) (I) Cellulose-ionic liquid, (II) Au@CIL.	4-129
Figure 4.6.	SEM images of A) Cellulose-ionic liquid and B) Au@CIL, EDX of C) Cellulose-ionic liquid, and D) Au@CIL.	4-130
Figure 4.7.	HRTEM of A) Au@CIL, B) trigonal and hexagonal shape of AuNPs embedded on CIL Surface, and C) pentagonal shape of AuNPs embedded on CIL Surface. Elemental dot mapping of Au@CIL shows uniformly distribution of all atoms D) Carbon (yellow), E) Oxygen (orange), F) Nitrogen (green), and G) Gold (violet). AFM images of Au@CIL in H) 2D and I) 3D.	4-130
Figure 4.8.	Zeta potential A) Comparison of CNC with CIL and B) Comparison of CIL with Au@CIL as a function of pH values.	4-132
Figure 4.9.	Time dependent UV-visible spectra of 4-nitrophenol reduction by Au@CIL.	4-135
Figure 4.10.	A) Time dependent UV-visible spectra of 2-nitrobenzaldehyde reduction by Au@CIL and B) time dependent reduction of 2-nitrobenzaldehyde.	4-136
Figure 4.11.	A) UV Absorption titration curve of 3-nitroaniline and B) 2-nitrobenzoic acid.	4-137

Figure 4.12.	Comparative LCMS titration during reduction of 1e with A) PdO and B) Au@CIL.	4-138
Figure 5a.1.	Mass of ASC-1	5a-153
Figure 5a.2.	¹ H NMR of ASC-1	5a-154
Figure 5a.3.	¹³ C NMR of ASC-1	5a-154
Figure 5a.4.	¹ H NMR of IL	5a-155
Figure 5a.5.	¹³ C NMR of IL	5a-155
Figure 5a.6.	Schematic diagram for synthesis of antibacterial and antioxidant polymeric film.	5a-156
Figure 5a.7.	Synthesis diagram of CMC-gelatin and ionic liquid (IL) polymeric film.	5a-156
Figure 5a.8.	Digital images of prepared polymeric films with different proportions of ionic liquid A) IL0%, B) IL5%, and C) IL20%.	5a-159
Figure 5a.9.	(A) IR spectra of a polymeric matrix with different compositions of ionic liquid I) IL0%, II) IL5%, and III) IL20%. (B) PXRD spectra of a polymeric matrix with different compositions of ionic liquid I) IL0%, II) IL5%, and III) IL20%.	5a-160
Figure 5a.10.	Schematic diagram to show the crosslinking between the gelatin and CMC through hydrogen bonding of IL (crosslinker).	5a-161
Figure 5a.11.	(A) SEM image and (B) electron diffraction spectroscopy (EDS) graph of PF@IL20%.	5a-161
Figure 5a.12.	Three-dimensional AFM images for the morphology of prepared polymeric films with inclusion of ionic liquid (A) IL0%, (B) IL5%, and (C) IL20%.	5a-162
Figure 5a.13.	Mechanical study of polymeric films with different percentages of ionic liquid (A)	5a-162

	tensile strength, (B) modulus, and (C) break distance.	
Figure 5a.14.	(A) Thermogravimetric analysis (TGA) of all prepared matrices and (B) rheology study of PF@IL20%.	5a-164
Figure 5a.15.	(A) Transmittance of prepared polymeric films with different compositions of ionic liquid and (B) Sun protection factor of prepared polymeric films with different compositions of ionic.	5a-165
Figure 5a.16.	Films against bacteria (A) <i>E. coli</i> and (B) <i>S. aureus</i> treated with polymeric films with inclusion of IL0%, IL5%, and IL20%. Percentage bacterial viability of polymeric films against bacteria (C) <i>E. coli</i> and (D) <i>S. aureus</i> .	5a-165
Figure 5a.17.	Time course of persisting growth curve of (A) <i>E. coli</i> and (B) <i>S. aureus</i> .	5a-166
Figure 5a.18.	SEM images (A) untreated <i>E. coli</i> bacteria, treated <i>E. coli</i> bacteria with PF@IL20% (B) after h and (C) after 4 h. (D-F) AFM images of <i>S. aureus</i> after being treated with PF@IL in three different modes.	5a-168
Figure 5a.19.	Radical scavenging activity (RSA) of prepared polymeric films with different compositions of ionic.	5a-169
Figure 5a.20.	Food preservation test for a piece of red apple using PF@IL20%, (A) control piece of red apple after 150 min and (B) piece of apple with a coating of PF@IL20% with different time intervals upto 7 h.	5a-170

Figure 5b.1.	Schematic diagram for synthesis of SA/COF sensing strip.	5b-181
Figure 5b.2.	Active packaging of (A) chicken, (B) peanuts using SA/COF polymeric film, and (C) total mold growth on peanuts with and without active packaging.	5b-182
Figure 5b.3.	(A) Response of COF strips in different pH environments, (B) equilibria of COF in acidic and basic medium, (C) color of SA/COF strips prepared at pH of 4, 7 and 11, (D) degradation of SA/COF film in soil at normal environmental conditions, and (E) response time of SA/COF strips compared with literature.	5b-183
Figure 5b.4.	(A) FTIR, (B) PXRD spectra of COF, and (C) simulated structure of COF.	5b-184
Figure 5b.5.	(A) FESEM and (B) EDS spectra of COF, (C) FESEM and (D) EDS spectra of SA/COF, (E-H) elemental mapping of COF.	5b-185
Figure 5b.6.	AFM images of COF in 2-dimensional and 3-dimensional.	5b-185
Figure 5b.7.	(A) N ₂ adsorption and desorption curve of COF, and (B) mean pore diameter spectra of COF using BJH plot.	5b-186
Figure 5b.8.	XPS (A) elemental survey, (B) C1s, (C) N1s, and (D) O1s spectra of COF.	5b-187
Figure 5b.9.	Stress/strain curve of pure sodium alginate (SA) and SA/COF.	5b-188
Figure 5b.10.	a) Comparative cyclic voltammetry graphs of bare GCE, COF/GCE, COF@Spermine/GCE, b) Cyclic voltammetry response at COF/GCE with	5b-190

gradual addition of varying concentration of BA's (0.0125 to 240 μM) at a scan rate of 100 mV/s, c) CV profiles of COF/GCE at varying scan rate (20-220 mV/s) in PBS buffer (pH 7.4) consisting 240 μM of BA's, and d) EIS plot and cyclic voltammetry profiles of bare GCE, COF/GCE at frequency 50 to 3×10^6 Hz

Figure 5b.11.	a) Linear calibration plot showing relationship between anodic and cathodic current peak vs square root of scan rate, (b) Comparison of active surface area of differently modified electrodes, (c) Cyclic voltammetry profile of bare GCE, COF/GCE in mixture of 0.1 M KCl consisting $\text{K}_3[\text{Fe}(\text{CN})_6]$ and $\text{K}_4[\text{Fe}(\text{CN})_6]$, (d) Cyclic voltammetry response of COF/GCE with varying scan rates from 20 to 220 mV/s in a mixture of 0.1 M KCl consisting $\text{K}_3[\text{Fe}(\text{CN})_6]$ and $\text{K}_4[\text{Fe}(\text{CN})_6]$ and (e) Linear calibration plot of the anodic peak current versus square root of scan rate.	5b-191
Figure 5b.12.	ZOI of pure sodium alginate (SA) and SA/COF in, (A) E. coli and (B) S. aureus, FESEM of E. coli (C) Live, and (D) dead.	5b-193
Figure 5b.13.	Photographs of raw peanuts packaged with active SA/COF film and cling film.	5b-194

List of Table

Table 1.1	Properties of cellulose-based polymer.	1-5
Table 2.1	Optimized amounts of materials used for the hydrogel synthesis.	2-39
Table 2.2	Crystalline sizes of materials are calculated using the Shears equation.	2-43
Table 2.3	The percentage removal of dye as a function of time.	2-48
Table 2.4	The percentage removal of dye as a function of the applied hydrogel.	2-49
Table 3a.1	Optimization of the reaction conditions for the synthesis of thioamides using the Willgerodt–Kindler reaction.	3a-79
Table 3a.2	Synthesis of various substituted thioamides using the Willgerodt–Kindler reaction and AgNPs@cellulose–PEVA as the catalyst.	3a-80
Table 3b.1	Acidic strength calculation of Fe ₃ O ₄ , IL1@Fe ₃ O ₄ and IL2@Fe ₃ O ₄ .	3b-105
Table 3b.2	Effect of solvent on the synthesis of poly-thioamides.	3b-110
Table 3b.3	Screening of catalyst for polymerization.	3b-110
Table-3b.4	GPC data and solubility of all synthesized polymers (P1-P9)	3b-111
Table-4.1	Reductions of various aromatic nitro derivatives into corresponding amines using Au@CIL as a heterogeneous catalyst.	4-134

List of Abbreviations

AgNPs	Ag nanoparticles
AIBN	Azobisisobutyronitrile
APD	Average pore diameter
AFM	Atomic force microscopy
ACN	Acetonitrile
BET	Brunauer Emmett teller
BJH	Barrett Joyner Halenda
CS	Chitosan
CIL	Cellulose-ionic liquid hybrid
CMC	Carboxy methyl cellulose
CF	Correction factor
CV	Cyclic voltammetry
COF	Covalent organic frameworks
DMF	Dimethylformamide
DMSO	Dimethyl sulfoxide
DLS	Dynamic light scattering
DP	Degree of polymerization
EDX	Energy-dispersive X-ray spectrometry
EPA	Environmental protection agency
<i>E. coli</i>	<i>Escherichia coli</i>
EWG	Electron withdrawing group
EDG	Electron donating group
EIS	Electrochemical impedance spectroscopy
FESEM	Field emission scanning electron microscopy
FTIR	Fourier-transform infrared
FWHM	Full width at half-maximum
GC	Gas chromatography
GPC	Gel permeation chromatography
GRAS	Generally recognized as safe
GL	Gelatin
GCE	Glassy carbon electrode
HPLC	High-performance liquid chromatography

HRMS	High-resolution mass spectroscopy
HRTEM	High-resolution transmission electron microscopy
IC	Ion chromatography
ICI	Iodine monochloride
IL	Ionic liquid
KDa	Kilodalton
MCR	Multicomponent reaction
MB	Methylene blue
MO	Methylene orange
MIC	Minimum inhibitory concentration
MOF	Metal-organic framework
NMR	Nuclear magnetic resonance
OD	Optical density
PEVA	Poly(ethylene-co-vinyl acetate)
PDI	Poly-dispersive index
PV	Pore volume
PEVA	Poly(ethylene-co-vinyl acetate)
PXRD	Powder X-ray diffraction
PVA	Polyvinyl alcohol
PBS	Phosphate buffer saline
RSA	Radical scavenging activity
SA	Surface area
SERS	Surface-enhanced Raman spectroscopy
<i>S. aureus</i>	<i>Staphylococcus aureus</i>
SPF	Sun protection factor values
SSA	Specific surface area
SA	Sodium alginate
TLC	Thin layer chromatography
TGA	Thermogravimetric analysis
TFP	Triformylphloroglucinol
VA	Vinyl acetate
WHO	World Health Organization

ZOI

Zone of inhibition

Introduction

The naturally derived polymers have attracted extensive research interest for large abundance, biodegradability, high mechanical properties, and good biocompatibility. Biopolymers are the class of biodegradable polymers, produced by living organisms. In addition to this, some polymers can also be extracted from biological sources such as sugars, proteins, amino acids, and oils, which can also be described as biopolymers. Compared to synthetic polymers, biopolymers have more defined and precise three-dimensional structures. Chitosan, cellulose, sodium alginate, and gelatin are some of the biopolymers, which can be derived from biomass sources such as animal residue, industrial residue, agriculture residue, sewage, etc (Figure 1). A large number of functional groups and reactive sites are present over the biopolymer, which can be chemically modified accordingly for desired applications.

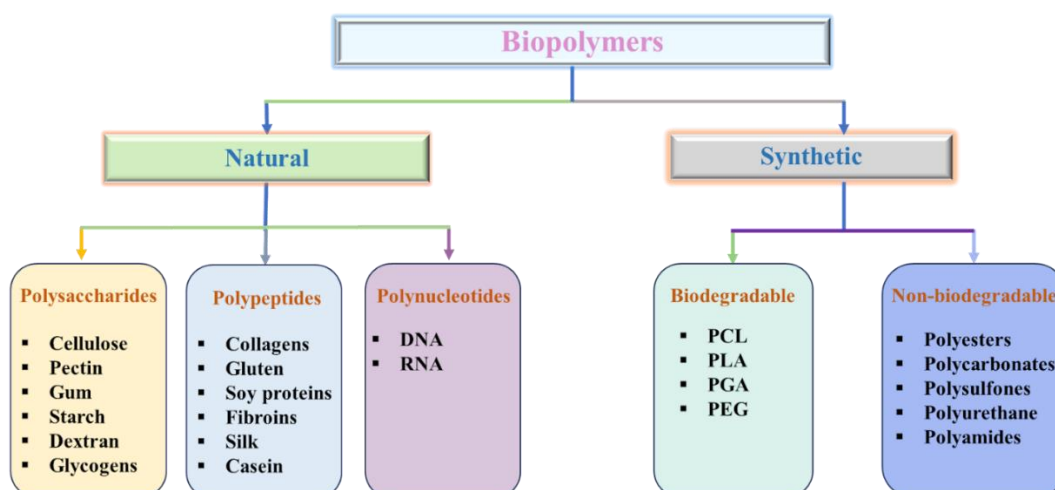


Figure-1. Classification of Biopolymers.

Chapter-1

Biopolymers are a kind of material that can be used to adjust, control, or participate in the various parts of the living system, to facilitate the operation and function of the living system. They can be used individually or as a part of a complex system. In this whole thesis work, biopolymeric materials were used with the inclusion of metal NPS, ionic liquids, and covalent organic framework for various environmental applications

including catalysis, sensing, active food packaging, antimicrobial membranes, and water purifications (Figure 2).

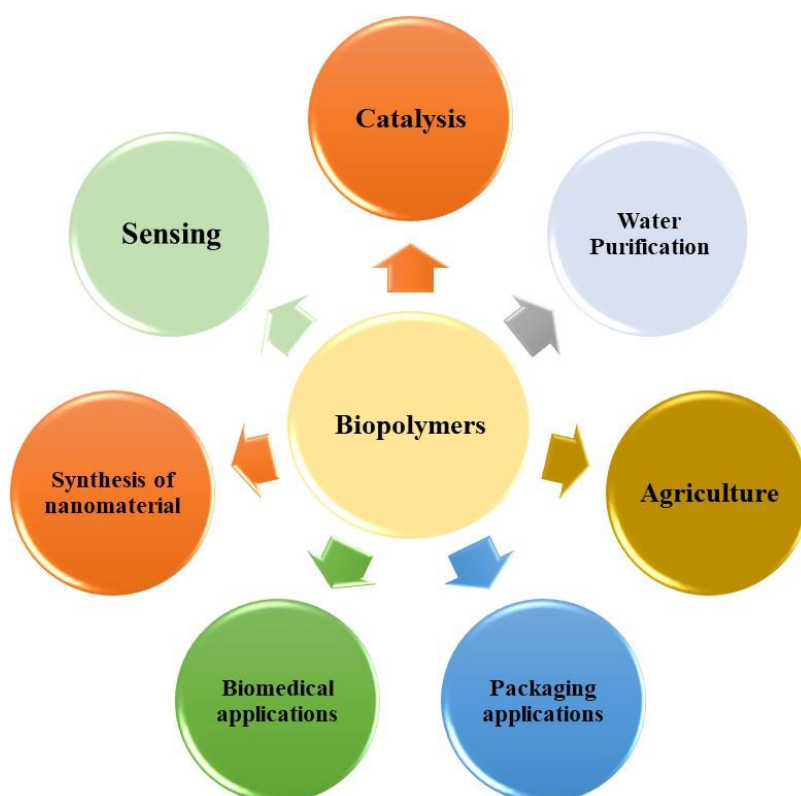


Figure-2. Applications of Biopolymers.

Chapter-2

Herein, a cationic hydrogel was designed and synthesized using a simple and facile method yielding excellent adsorption capacity, thereby enabling the rapid removal of organic dyes, nitrite anions, and Pb^{2+} from polluted water, as well as oil–water separation. The backbone of the hydrogel was composed of CS and poly(vinyl alcohol) (PVA) with glutaraldehyde as the crosslinker. An ionic liquid (IL) was grafted onto the backbone *via* a radical reaction. The synthesized hydrogel was optimized by varying the amounts of crosslinker, monomer, temperature, reaction time, initiator, and solvent to obtain maximum adsorption affinity. The interstitial voids and cationic charge on the hydrogel increased its binding affinity for organic dyes and anions (Figure 3). The positively charged hydrogel electrostatically interacted with the dyes and nitrite (NO_2^-), facilitating their removal from wastewater.

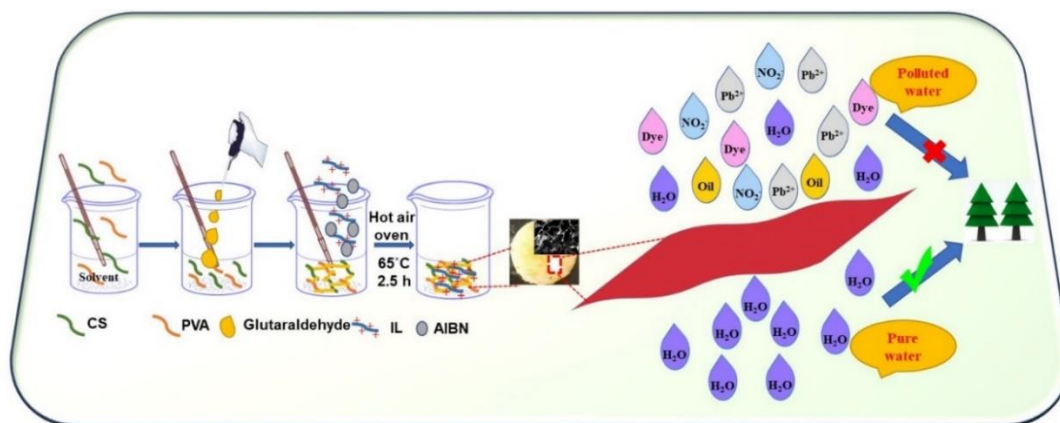


Figure-3. CS/PVA hydrogel grafted with IL for wastewater treatment.

Chapter-3

Chapter-3A: In this study, cellulose was extracted from rice straw, and a highly active solid-supported catalytic model (ASC-1) was developed. Cellulose conjugated with poly(ethylene-co-vinyl acetate) (PEVA) followed by insertion of AgNPs. The process involved the reduction of silver nanoparticles in the presence of sodium-borohydride. The synthesized catalytic hybrid was successfully applied to Willgerodt Kindler's reaction of aromatic aldehydes, amines, and sulfur for the formation of thioamides in excellent yields (Figure 3).

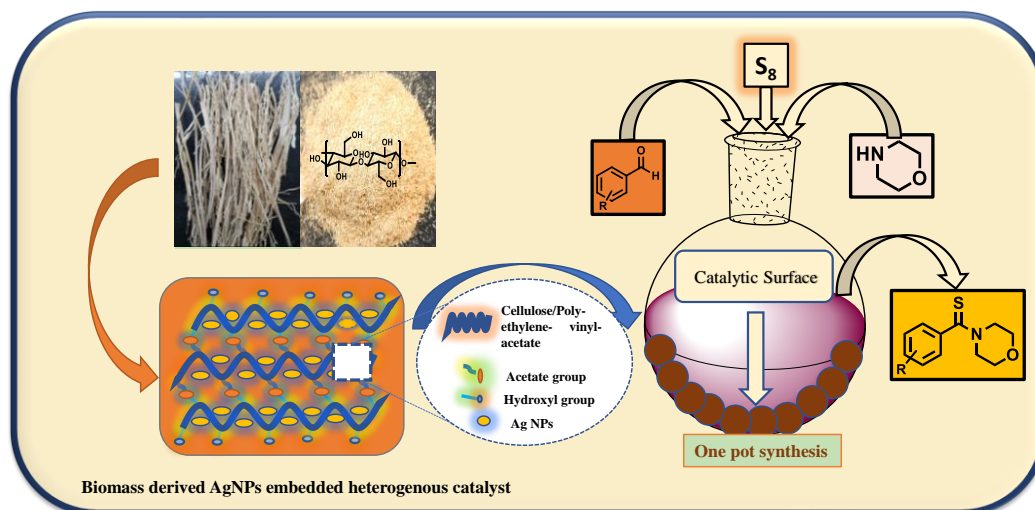


Figure-3. Syntheses of thioamides using biopolymers-based catalyst.

Chapter-3B: Herein magnetically removal of IL1-2@Fe₃O₄ heterogeneous catalysts was developed, which were further used for the synthesis of polymers via willgerodt kindler reaction with a simple and facile method (Figure 4). Fe₃O₄ NPs have high affinity towards the functional groups, present in ionic liquid and we found that IL1-

Magnetically Removal

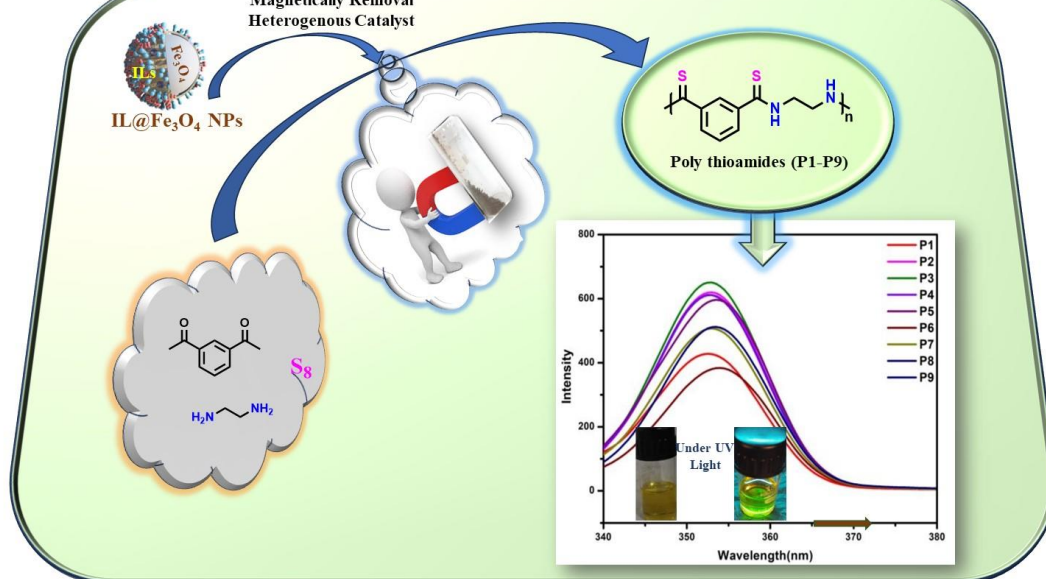


Figure-4. Ionic liquid-based magnetically removal heterogeneous catalyst for synthesis of polythioamides.

Chapter-4

This chapter deals with the synthesis of Au NPs embedded solid support catalyst (Au@CIL) for selective reduction of Nitro compounds, with a simple and facile method. Abundant hydroxyl groups present on the surface of ionic liquid functionalized cellulose help in the adsorption of Au NPs. Ionic liquid stabilized the solid support system by a combination of electrostatic protection layers. Because of variation the size of Au NPs makes them are used as heterogeneous catalysts in wide applications. We found that Au@CIL performed excellent catalytic properties for selective reduction of NO₂ group and recycling with minimum loss of catalytic activity (Figure 5).

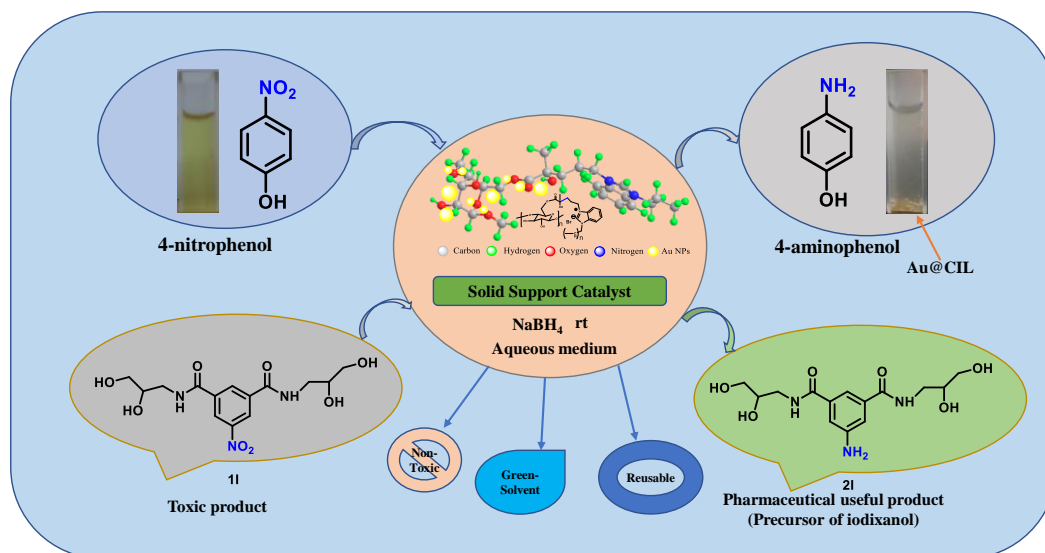


Figure-5. Au NPs embedded over the cellulose surface for selective nitro reduction.

Chapter-5

Chapter-5A: In present work, we developed a polymeric matrix from biopolymers with inclusion of ionic liquid which have potential to increase shelf life of food. In this regard, an ionic liquid was synthesized from 1-methyl imidazole and salicylate anion, where anionic moiety showed excellent antioxidant properties and cationic moiety has potential towards antibacterial action (Figure 6). Furthermore, ionic liquid also works as a cross-linker between the gelatin and CMC to strengthen the polymeric matrix.

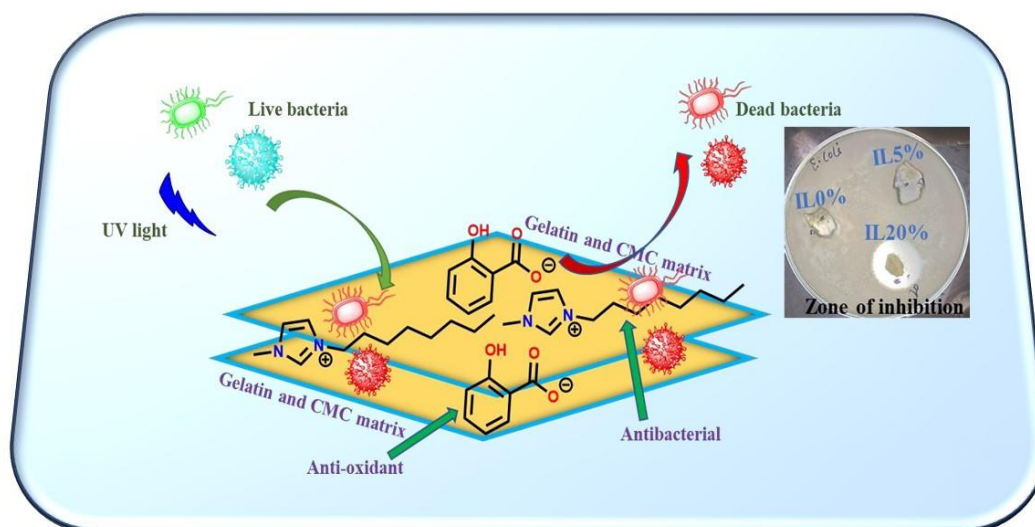


Figure-6. Gelatin/CMC polymeric film embedded with ionic liquid for increasing the shelf life of food.

Chapter-5B: In this chapter smart sensing strips and antimicrobial active food packaging films were synthesized to monitor the food quality. For smart sensing of food spoilage, 2D covalent organic frameworks (COFs) were synthesized from 2,4,6-triformylphloroglucinol (TFP) and p-phenylenediamine. Thereafter, COF was incorporated into sodium alginate polymeric material to obtain sensing strips with highly colorimetric response and augmented mechanical properties (Figure 7). The smart sensing strips were demonstrated on packaged poultry meat. Sensing strips are highly pH-responsive and their color changes according to pH of the surroundings.

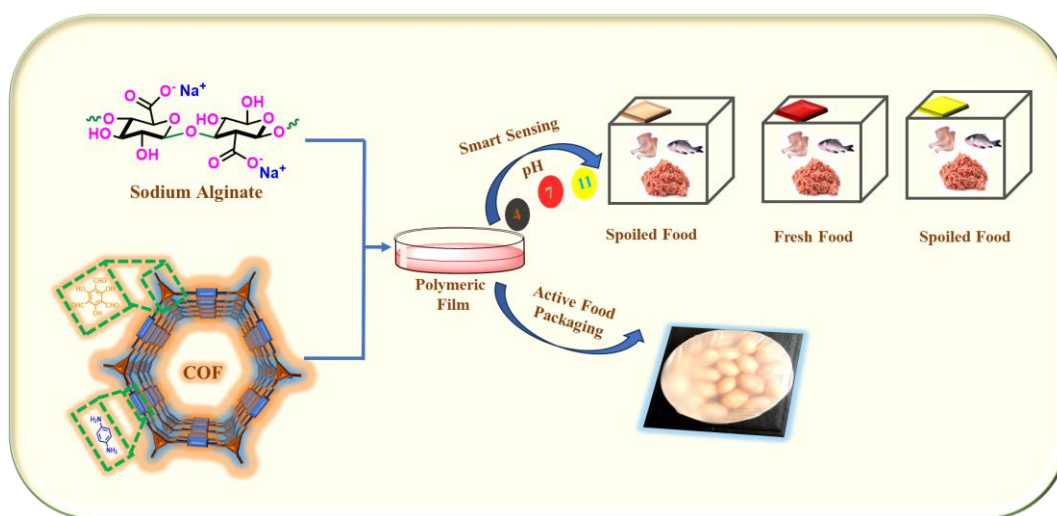


Figure-7. Sodium Alginate and COF-based polymeric film for smart sensing and active food packaging.

Chapter-6

Includes the overall summary of thesis work, where various functions of biopolymers with inclusion of metal nanoparticles, ionic liquids, and covalent organic framework have been developed. Synthesized materials have potential for environmental remediation applications including catalysis, removal of dyes, toxic metal ions, oil, toxic anions from wastewater, smart sensing, and active packaging of food.

Chapter -1

Introduction and Literature Review

1.1 Introduction

Repeating units of monomer or small molecule are usually combined via polymerization techniques, either solution, bulk, emulsion, or suspension polymerization, to form a large molecule known as a polymer [1]. Based on type of repeating unit and monomer, polymers are classified as homopolymers and copolymers [2]. Biopolymers have various advantages over synthetic polymers [3]. Naturally derived polymers have attracted extensive research interest because of their large abundance, biodegradability, reusability, high mechanical properties, and good biocompatibility [4]. Biopolymers are the class of biodegradable polymers, which are produced by living organisms and have been on the earth for millions of years as compared to chemically derived synthetic polymers [5]. As biopolymers are arranged in a well-defined structure and break down easily into smaller chains by actions of enzymes, heat, moisture, and other natural factors [6]. Biopolymers are found in all types of living matter, also called the building blocks of nature [6]. In addition to this some polymers extracted from biological sources such as sugars, proteins, amino acids, and oils can also be described as biopolymers [7]. Many biopolymers have an electrical charge due to of very sequences and chemical composition and therefore can be isolated by ion exchange technique [7]. Biopolymers as compared to synthetic polymers have a more defined and precise three-dimensional structure and follow the principle of reduce, reuse, and recycle [8]. Biopolymers include chitosan, cellulose, sodium alginate, and gelatin, which can be derived from biomass sources such as animal residue, industrial residue, agriculture residue, sewage, etc (Figure 1.1) [9-10]. A large number of functional groups and reactive sites are present over the biopolymer, which can be chemically modified accordingly for desired applications [11]. In addition to all these properties, water is an excellent solvent for biomass processing, due to its large abundance, green solvent and feasible under hydrothermal conditions [12]. Moreover, biomass-derived products contain abundant oxygen species, which leads to their solubility in water at ambient conditions [13]. Although biopolymers have renewable and abundant sources [13]. However, the very low solubility of biopolymers in conventional solvents due to strong hydrogen bonding between the molecules, makes it difficult to prepare materials [14]. Among all biopolymers, only certain polysaccharides exhibit solubility in some polar solvents such as dimethyl formamide (DMF), water, dimethyl sulfoxide (DMSO), and pyridine [15]. Biopolymers derived from living organisms are classified into three categories including

polysaccharides, polypeptides, and polynucleotides [16]. Polysaccharides include chitosan, cellulose, starch, and chitin, which are the long hydrocarbon chain of carbohydrates composed of repeated monosaccharides that bind through glycosidic linkage [17]. This highly ordered crosslinking makes it difficult to dissolve in most of the conventional solvents [14]. Based on their response to, heat biopolymers can also be classified as thermoset and thermoplastic [15].

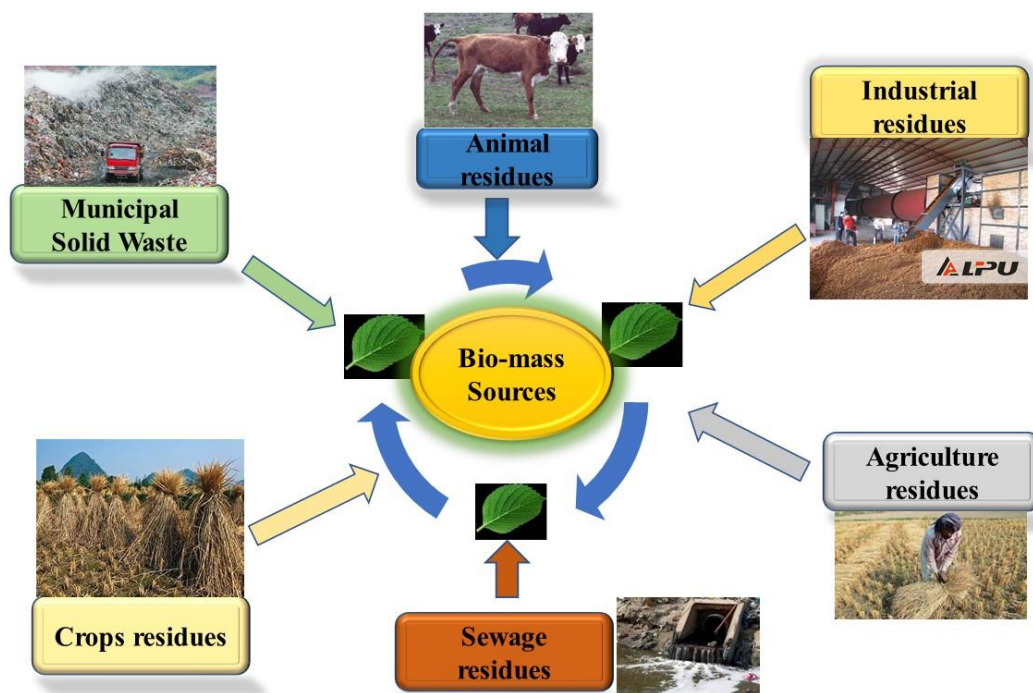


Figure-1.1: Sources of biopolymer.

1.2 Classification of biopolymers

The synthesis and creation of so-called biodegradable polymers, which could be degraded under sustainable environmental conditions of temperature, moisture, and oxygen, have received a lot of attention from researchers over the last few years [6]. Depending upon the natural origin and based on their structural arrangement, biopolymers are classified (Figure 1.2) into three main categories [16]:

1.2.1 Polysaccharides: This is the most abundant class of biopolymers and organic material present on earth. According to the literature, starch, α and β -glucose, and cellulose are the most abundant polysaccharides by volume [16]. The analogs of polysaccharides differ only through the position of anomeric carbon and glycosidic linkage between the monosaccharides determine its properties and diversity [15-16]. Polysaccharides are mainly extracted from plant and animal sources [16]. The physical and chemical properties of polysaccharides depend upon their degree of polymerization

(DP) and their water solubility decreases with increasing DP [15]. It has a wide range of applications such as food industries, packaging material, pharma industries, drug delivery, etc [18].

1.2.2 Polypeptides: These are the repeating amino acid unit joint through peptide bonds between the carboxylic end (-COOH) of one amino acid and amine (-NH₂) end of another amino group [19]. Based on the type of bonding and interactions between the amino groups, polypeptides are categorized as primary, secondary, and tertiary structures [19]. As of unique structure, it has various functions in the nervous, immune, muscular, cardiovascular, and endocrine systems [19].

1.2.3 Polynucleotides: These are the type of polymers where nucleotide monomers are connected through covalent bonding [16]. Generally, 14 or more nucleotide monomers are connected to each other in a single polynucleotide molecule, for example, RNA (ribonucleic acid) and DNA (deoxyribonucleic acid) [20]. Based on maintaining life it has a very specific role and it is produced in very low quantities as compared to polysaccharides [20].

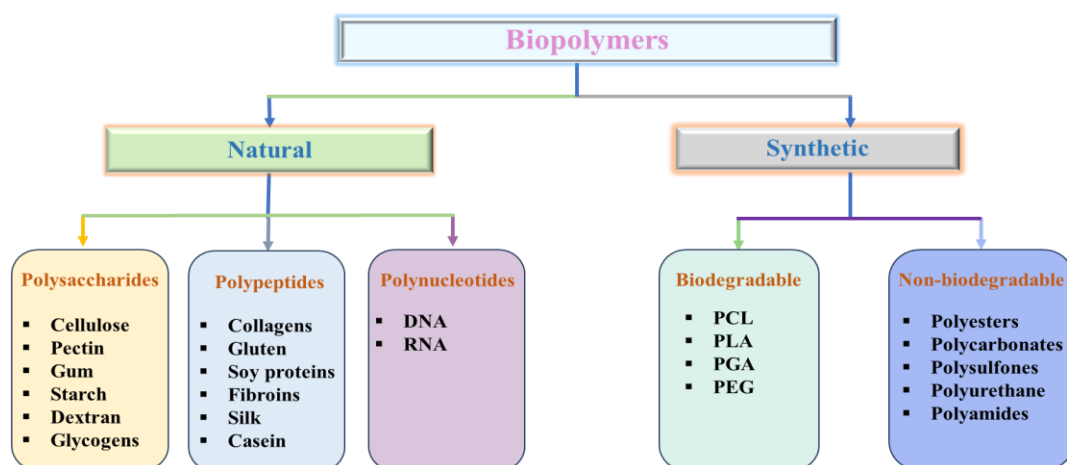


Figure-1.2: Classification of biopolymers based on their origin.

1.3 Common Examples of biopolymer

A huge number of biopolymers are available in our environment, based on the structure and type of functional groups present over the natural origin polymers. Some common examples of biopolymers are listed below.

1.3.1 Cellulose

Cellulose is the most abundant renewable natural biopolymer with a general formula $(C_6H_{10}O_5)_x$ available on the Earth in the form of micro and nanocrystalline cellulose with a high surface area [21]. Naturally occurring cellulose is found in the form of microfibrils in association with other materials including proteins, hemicellulose, and lignin [21]. Cellulose is a linear polysaccharide with β -(1,4)-glycosidic linkage and the most abundant natural biopolymer material (Figure 1.3) [21]. The straight shape of cellulose through collagen bond, allows the molecule to pack closely [22]. Hydrogen bonding and β -(1,4)-glycosidic linkage provide strength and it's very difficult to break cellulose [22]. Since cellulose has a tremendous hydrogen bonding network and high crystallinity, results in decreases in the solubility of cellulose directly in most of the solvents, which hampers the processability of native cellulose into functional format [22].

The primary source of cellulose is agriculture and forest land [22]. Cellulose could be processed into nanocellulose with different structures such as cellulose nanofibril, cellulose nanocrystals, and bacterial cellulose [23]. Almost all biopolymers can be extracted from the biowaste with varied compositions [23]. Cellulose is one of the most common polymers found in biowaste in the range of 40-50%, which depends upon the concentration of hemicellulose and lignin [23]. With the functionalization of cellulose, many different biopolymers such as carboxymethyl cellulose (CMC), sodium alginate, etc. can be derived which have excellent physical and chemical stability, properties of some cellulose-derived materials are given in table-1.1 [23].

Table 1.1 Properties of cellulose-based polymer.

Cellulose-based polymers	Elastic modulus (GPa)	Tensile strength (GPa)
Wood	10-40	1
Jute	26-25	0.39-0.77
Ramie	60-128	0.40-0.94
Cotton	5-13	0.28-0.60
Flax	27-100	0.34-1.03

Basically, CMC is synthesized through the reaction of chloroacetic acid with cellulose and used as the sodium salt of carboxymethyl cellulose [8]. This most popular

linear, negatively charged, and low-toxic biomaterial is used for three-dimensional (3D) printing [22]. Cellulose nanofibers (CNFs) could be prepared from amorphous cellulose through hydrolysis, and also have the potential for a wide range of applications because of their unique morphology, nanoscale dimension, low density, high surface area, mechanical strength, and low cost [23]. Cellulose nanorods, nanowhiskers, microfibrillated, and nanofibers are some stable forms of CNFs, which can also be used as stabilizing agents [24]. Three different types of cellulose such as cellulose acetate (CA), cellulose esters, and cellulose nitrate could be generated upon chemical treatment of natural cellulose to explore more applications towards environmental remediations [24]. Some of the reported cellulose esters include hydroxyethyl cellulose, ethyl hydroxyethyl cellulose, hydroxypropyl methyl cellulose, carboxymethyl cellulose, methyl hydroxyethyl cellulose, methyl cellulose, and hydroxypropyl cellulose [25].

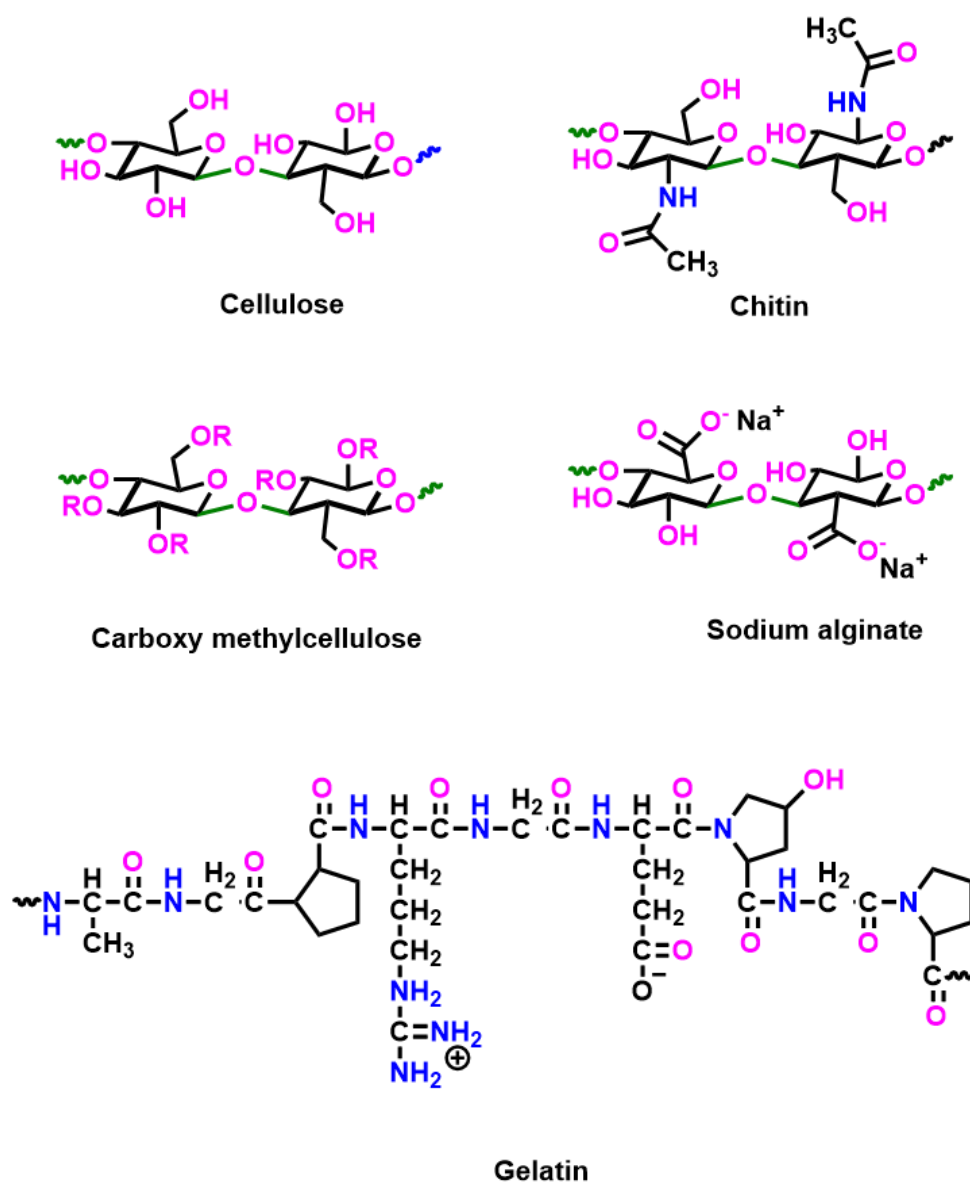


Figure-1.3: Chemical structure of some common biopolymers.

1.3.2 Chitin

Chitin a linear polymer of N-acetyl-d-glucosamine, is the second most abundant biopolymer after cellulose, spread on the Earth [26]. Chitin is mainly extracted from insects, crustacea, and fungi [27]. It has a structure similar to cellulose with a difference in acetamido group at C2 position of glucose unit and which is not soluble in water and most of organic solvents, therefore it is difficult to use [28]. In nature, chitin is found in three different crystalline forms such as α -, β -, and γ chitin (Figure 1.4) [29]. With strong intermolecular and intramolecular bonds, α -chitin is the most common form with antiparallel orientation of its chain, γ -chitin is commonly found in the cocoon fibers and stomach of *Loligo* [29]. Biodegradability, biocompatibility, non-toxicity, haemostaticity, bio-adhesiveness, and immunostimulant activity are some useful properties of chitin and chitosan that make them biopolymers of economic interest [29]. Chitin and Chitosan find applications in the agriculture, food industry, sanitary, tissue engineering, wastewater treatment, biomedical, biotechnological, textile cosmetic sectors, and paper industries [30]. Chitin is the best material in the agriculture sector due to its slow fertilizer-release properties, which help in the growth of plants and control diseases [31]. Chitosan is a linear and heteropolysaccharide obtained via chemical or enzymatic deacetylation of chitin, consisting of the elimination of acetyl group from chitin and leaving the reactive amino group [31]. In addition to these properties, chitosan also has drawbacks due to its poor stability in water [31]. Besides all these limitations, applications of chitosan may be improved after their chemical modifications to form chitosan derivatives mainly include carboxymethyl chitosan, quaternary ammonium chitosan, phosphorylated chitosan, and sulfonated chitosan [32].

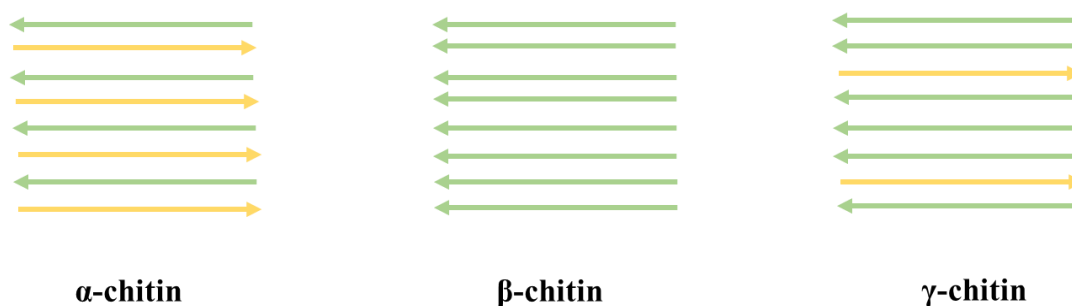


Figure-1.4: Arrangement and orientation of chitin microfibrils in α -, β -, and γ -chitin.

1.3.3 Gelatin

Gelatin is a type of fibrous protein composed of 19 amino acids, produced from the denaturation of type-1 collagen consisting of cysteine [33]. Owing to its unique physical and chemical nature, it has a large number of applications such as food packaging, cosmetic industries, pharmaceutical industries, drug carrier agents, water binding ability, film formation, good biocompatibility, foam forming ability, and photography due to its gel formation ability [34]. Depending upon the method of synthesis, gelatin is of two types namely type-A and type-B, synthesized via acid hydrolysis and alkaline hydrolysis respectively, among them, type-A is more edible [35]. Gelatin is found with large chemical properties and a wide range of blooms; selection can be made depending upon the need of applications [36]. For example, gelatin (type A, bloom 300) may be utilized to increase self-life and avoid the spoilage of food [35]. It also helps for separation of water from cottage cheese and sour ice cream, which is called syneresis [35]. Formulations of gelatin are used as an aqueous polyhydric solvent for the preparations of desserts, marshmallows, and candy [36]. In addition to these, gelatin can also have the potential to be used in frozen foods such as pies and dairy products including ice creams, which prevents the crystallization of sugar and ice [36].

Gelatin itself has poor mechanical properties, and is highly hygroscopic, which limits its application for food packaging [35]. The mechanical property of gelatin would be improved through the formation of a composite with another biopolymer and thus gelatin composite is applied for food packaging [36]. Chemically modified gelatin also has the potential to be used for wide pharmaceutical applications such as drug carriers [36]. Gelatin nanoparticles can also be prepared using techniques including water in oil (W/O) emulsion, coacervation, and desolvation, which are further used for detecting cancer cells, and multimodality imaging agents for the detection of amyloid beta fibril [37].

1.3.4 Alginate

A water-soluble, non-toxic, and biodegradable polysaccharide that can be extracted from cell walls of marine algae with molecular weight varies from 50 to 100,000 KDa [38]. Gelatin itself is not much stable to use directly for various applications, so its chemical modifications are required to make it more stable [39]. Alginate is mainly available in two forms sodium alginate and calcium alginate [40]. It is an anionic and linear copolymer of $\beta(1-4)$ d-mannuronic acid (M) and $\alpha(1-4)$ l-guluronic acid (G) unit

arranged in an irregular pattern, which provides the strength and flexibility to alginate [41]. Alginate has freely hydroxyl and carboxylic groups on the structural backbone and thus can be modified accordingly [41]. It shows excellent hydrogel formation ability, due to tremendous affinity towards di and trivalent metal ions, high viscosity, high stability, and high gelling properties [42]. Hydrogel derived from alginate has many biomedical applications such as stabilizing agents, drug delivery, and environmental remediation [42]. Besides these alginates have been widely used in the form of nanoparticle drug delivery systems [42]. Due to its immunogenicity, biocompatibility, easy handling, and low toxicity, alginate is applied for the synthesis of polymeric beads, hydrogel, and nanoparticles, for various applications such as water treatment, antimicrobial films, cell encapsulation, drug delivery, and wound healing [43].

1.4 Applications of biopolymeric materials for environmental applications

Utilization of biopolymers or biodegradable polymers towards catalysis, water purification, smart sensing, active food packaging, and other environmental remediation applications is a prominent alternative over synthetic polymers [42]. These polymers process unique properties including sustainability, renewability, and reusability [43]. The use of biopolymers in the power sources of portable electronic devices such as power banks, laptops, and mobile phones has been increasing over the past few years. Degradation of biopolymers occurs easily in the presence of appropriate conditions such as temperature, oxygen, and moisture without releasing any toxic materials [43]. Considering all the aforementioned information about the positive feedback of biopolymers and limitations of synthetic non-biodegradable polymers, biopolymers find their applications in many places (Figure 1.5).

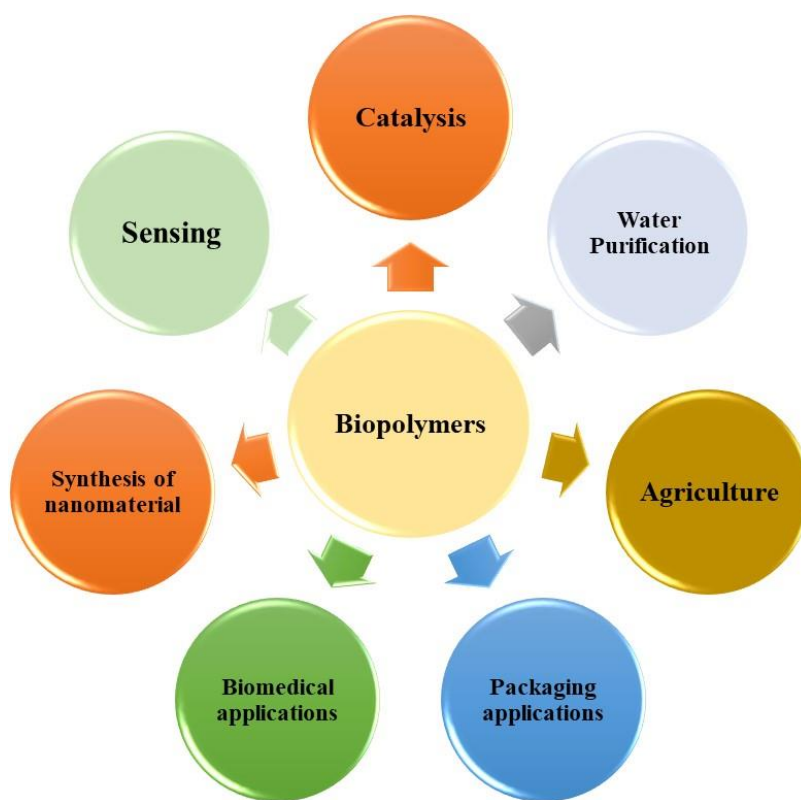


Figure-1.5: Applications of biopolymers-based materials.

1.4.1 Water Purification

Maintaining and cleaning our planet Earth is the most urgent economic, scientific, ethical, and social challenge of the present day. In the last few decades, humans have already crossed the boundary of safe operating systems on Earth such as the nitrogen cycle, climate change, and biodiversity loss [44]. According to the present scenario, water can be polluted by various hazardous effluents, including dyes, cosmetics, toxic heavy metals, pharmaceuticals, pesticides, and inorganic anions [44]. Toxic metal ions including Hg^{2+} , Pb^{2+} , Co^{2+} , Cd^{2+} , Ni^{2+} , Cr^{6+} , Cu^{2+} , As^{3+} , etc are responsible for a large number of fatal diseases beyond their optimum consumption limit [43]. In addition, these anions also cause a lot of fatal diseases beyond their permissible limit [45]. According to a report many countries including India, Afghanistan, China, Pakistan, Africa, Mexico, western USA, and Argentina are affected due to high concentrations of fluoride in water [46]. Industries such as glass manufacturing and semiconductor manufacturing are responsible for high concentrations of fluoride across the world [45-46]. The continuously growing population imposes significant demands on the production of leather, textiles, and cosmetics, which require a large amount of water for dyeing; used dyes are then discharged into natural water sources [45]. Besides all these

water pollutants, oil water pollution is also a serious problem in this industrialization era [45]. The discharge of oil in water increases very rapidly from industries such as food processing, petroleum industries, human processing, and machinery manufacturing [46]. Leakage of oil during the transportation is one of the major water pollutions [46]. Oil-water pollution has a very dangerous effect on aquatic life and human life survival [47].

Direct consumption of polluted water can cause a lot of serious health issues such as diarrhea, cholera, typhoid, malaria, hepatitis, etc. [45]. Sometimes, even very low concentrations of toxic heavy metals in contaminated water and food can accumulate significant side effects over time [45]. Above the permissible limits of metals and anions can harm the digestive, nervous, cardiovascular, and hematopoietic systems [43]. As the human population is increasing day by day, which increases the demand for drinking water [44]. In this regard, it is essential to develop materials and techniques for removing toxic pollutants from polluted waters to resolve industrial and biological issues [44]. The developed method (Figure 1.6) should be eco-friendly, easy to handle, less energy consumption, green synthesis, reusability, and high efficiency [47].

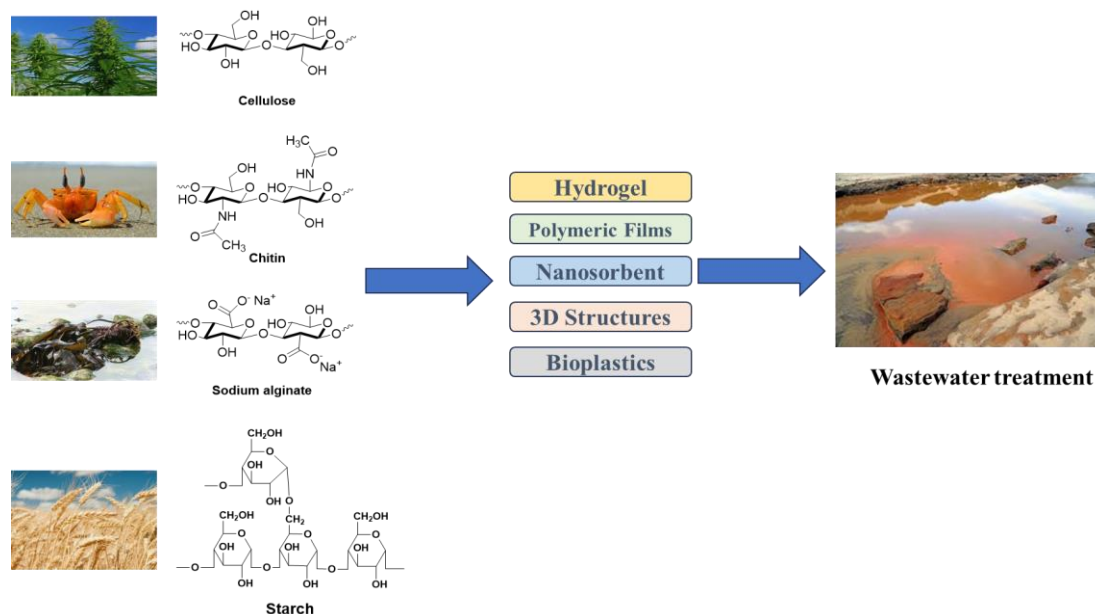


Figure-1.6: Biopolymer-derived materials for wastewater treatment.

Over the last few days, considerable efforts have been made to ensure high-quality fresh water for consumption of animals and human beings. Many techniques for water treatment have been developed by the researchers such as precipitation, coagulation, ion exchange, adsorption, photothermal-assisted technology, electrodialysis, sedimentation, membrane-based technology, and chemical precipitation [48]. Adsorption of pollutants

from wastewater using biopolymer-derived hydrogel is one of the noticeable methods in the present day [48]. Due to the excellent physical and chemical properties of biopolymer, it is an excellent raw material, used to fabricate economical and environmentally friendly membranes [48]. Therefore, biopolymer can be utilized for the synthesis of hydrogel, which is further applied for water purification [49]. Basically, hydrogels are a chemical or physically derived three-dimensional crosslinked polymeric network, that has an excellent tendency to adsorb large amounts of water [49]. Hydrogels are divided into two categories: natural or biopolymer-based and synthetic hydrogel [49]. Based on biodegradability, handling, biocompatibility, and tissue-mimicking consistency, hydrogel derived from biopolymers acquired increasing attention in the last few years [46-49]. Various biopolymers including cellulose, chitosan, gelatin, dextrin, sodium alginate, and carboxymethyl cellulose, have been used for the synthesis of hydrogel [47]. As hydrogel tends to adsorb large amounts of water and biological fluids, it shows excellent potential for a wide range of applications such as feminine care products, drug delivery, disposable diapers, adsorption of pollutants (pesticides, toxic heavy metals, and organic dyes), wound dressing, etc [48]. Based on the type of interactions, hydrogels are of two types: physically crosslinked hydrogel and chemically crosslinked hydrogel [50]. In case of physical crosslinked hydrogels, there are physical interactions such as hydrogen bonding, hydrophobic interactions, van der Waals forces, and electronic associations [50]. Whereas, covalent bonding is present in chemical crosslinked hydrogel [50].

Several hydrogels synthesized from biopolymers were reported which have great potential for adsorption of pollutants from wastewater. For example, Gokhale et al. reported porous hydrogel microparticles from poly (ethylene glycol) diacrylate (PEGDA) with incorporation of micelles and used for adsorption of hydrophobic micropollutants from water [51]. In another report, agarose and chitosan hybrid backbone with the incorporation of Fe-Al nanocomposite were utilized by Mruthyunjayappa et al. for the synthesis of hydrogel [52]. In this report, the author was able to remove dyes, fluoride, and arsenate pollutants from water even at high concentrations with excellent adsorption capacity [52]. To treat wastewater, material was synthesized by Zhao et al. using cellulose doped with $\text{Fe}(\text{OH})_3$ nanoparticles for the removal of Congo red with a maximum adsorption capacity of 689.65 mg/g [52]. In another study, a polymeric material was derived by Sharma et al. from dextrin and

polyvinyl alcohol backbone with a maximum percentage of swelling was 295 % [53]. This research work involved detection and removal of Cu^{2+} and Pb^{2+} from real water samples [53]. The synthesized material was able to remove up to 97 % of Cu^{2+} and 94 % Pb^{2+} from metal-containing samples [53]. In addition to all these works, Singh et al. Developed a hydrogel from chitosan with the incorporation of iron oxide nanoparticles and graphene oxide for adsorption of cationic dye, methylene blue (MO) [54]. This nanocomposite exhibits fastest dye removal performance with a rate constant of $0.06 \text{ g mg}^{-1} \text{ min}^{-1}$ and can be used for up to four cycles without significant loss in adsorption capacity [54]. Over the last few years, contamination of water with the discharge of oil has been a worldwide problem. In lieu of this Zhang et al. synthesized a three-dimensional interlinked macrostructure superhydrophobic ($\theta_{\text{oil}} \sim 162^\circ$) hydrogel from chitosan via a simple freezing drying process with a density that varies from 10.19 to 36.05 mg/cm^3 [55]. Hydrogel in the aerogel state has an excellent porous structure, which provides huge storage space and incredible potential for the separation of oil from oil-contaminated water [55].

In the field of water purification systems, Qian et al. also developed a method for adsorption and photocatalytic degradation of organic dyes such as methylene blue, malachite green, and crystal violet from polluted water using hydrogel [56]. Here, the author used the sodium alginate and polyacrylamide polymeric backbone with immobilization of $\text{La}(\text{OH})_3$ nanoparticles for the synthesis of a hydrogel [56]. Thereafter, hydrogel was applied for the removal of malachite green, methyl orange, and crystal violet from water samples [56]. From the obtained data it was observed that the material shows excellent adsorption capacity of 3000.08, 993.29, and 1610.34 mg/g for malachite green, crystal violet, and methylene blue respectively [56].

1.4.2 Catalysis

Mesoporous materials such as carbon nanotubes (CNTs), covalent organic frameworks (COFs), molecular organic frameworks (MOFs), zeolites, biopolymers, and silica with high surface area, are widely employed for catalysis (Figure 1.7) [57]. MOFs are porous crystalline materials and because of their excellent host-guest interactions, have the potential for a large number of applications such as CO_2 reduction, catalysis, hydrogen reduction, etc [57]. Similarly, COFs are also porous materials, which are synthesized through reversible condensation reactions [57]. In addition to these, functionalized CNTs also have different binding groups that can anchor metals to carry out organic reactions [57]. Among all these types of catalytic support materials, biopolymer is an

excellent solid support material because of its large abundance, biodegradability, reusability, easy handling, high mechanical strength, and excellent catalytic efficacy [50].

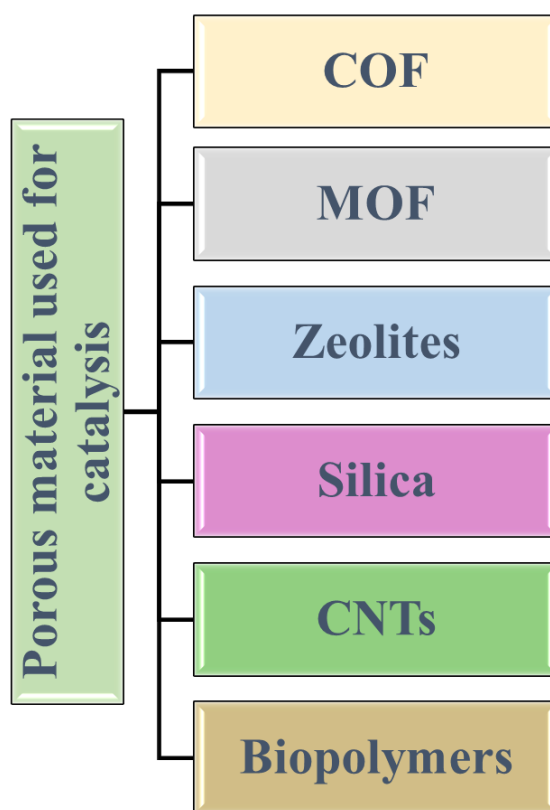


Figure-1.7: Porous materials for Catalysis.

Almost all biopolymers contain large numbers of hydroxyl, carboxylic, and amino groups, which can interact with metal ions, leading to changes in physical and chemical properties at the interface [50]. The modified biopolymers are considered the ideal support in the catalytic system due to their nontoxic, earth-abundant, renewable, and biodegradable nature [55]. All these functional groups present over the biopolymer help in the binding of metal ions via electrostatic interaction or hydrogen bonding [55]. Metal nanoparticles play an excellent role in various organic syntheses [57]. However, the direct use of metal nanoparticles causes severe issues for human health and the environment [58]. Thus, heterogeneous metal nanoparticles that are attached to solid supports are required for recovery and reusability [57]. Biopolymers including starch, gelatin, cellulose, chitosan, and sodium alginate provide solid support in heterogeneous catalysis, showing extraordinary ability in organic synthesis [58]. Cellulose is mostly found in plants, but also in some animals and bacteria, which can be functionalized for the synthesis of different derivatives [21]. Because of spherical and porous beads of

cellulose, its catalytic efficacy can be increased to a greater extent by the insertion of metal ions and nanoparticles [57]. Moreover, the application of cellulose becomes more widened in chemically modified hydrophobic states [59]. The cross-linking properties and large cavity size of the biopolymers help in insertion of metal with strong binding energy [59]. Major drawbacks like solubility in water can be enhanced by chemical modifications [59].

In the last few years, organic synthesis has drawn attention in the field of medicinal chemistry owing to its broad range of biological activities [60]. These organic derivatives are an integral part of many biologically important entities exhibiting interesting properties such as antioxidant, antimicrobial, anticonvulsant, antithyroid, and anticancer activities [60]. Moreover, their unique characteristic features of varying bond lengths and bond rotation make them superior candidates over amides in peptidomimetics [59-60]. For the use of biopolymer-based materials for the synthesis of medicinally important organic compounds, various methods have been made to synthesize catalysts with high purity and active sites over the surface [57]. In this area, a catalyst was designed and used for the synthesis of cycloaddition reaction, where the author proposed a new way for the utilization of lignin [57]. A biomass-based catalyst was derived by Guo et al. from lignin and was further used for the reaction of carbon dioxide and epoxides through a green chemistry approach [60]. Similarly, Sun et al. developed a catalyst from chitosan and ionic liquid, which has excellent properties such as biodegradability, non-toxic, high adsorption capacity, and bio-compatibility [61]. The designed catalyst was further applied for the catalytic synthesis of cyclic carbonate [61]. Guan et al. reported the catalytic action of biopolymer-derived material for selective hydrogenation of acetylene [62]. In this work author synthesized the catalyst from palladium doped over the surface of chitosan and 90 % selectivity with 100 % conversion of acetylene hydrogenation was achieved at 90 °C [62]. The material derived from chitosan exhibits great potential for a wide range of applications at mild temperature and solvent-free conditions [62]. Pettignano et al. performed the Passerine three-component reaction using biopolymer derived catalyst [63]. Here, carboxymethyl cellulose (CMC) a derivative of cellulose was chemically modified according to the designed catalyst for Passerine reaction via multicomponent approach [63]. The presence of a carboxylic group over the surface of the CMC backbone paves the way for further chemical modification [63]. Passerine reaction can be carried out in both water and organic solvent [63]. Based on a biopolymer catalyst Tang et al. also reported

a work for the hydrolysis of p-nitrophenyl palmitate in a biphasic system [64]. Here, an oil-water biphasic solution was stabilized using lignin/chitosan nanoparticles, which are alkali-resistant [64]. Lignin/chitosan nanoparticles provide large and stable oil-water reaction interface areas [64]. Thereafter, progress of the reaction was monitored, and a 100 % reaction conversion rate within 30 min was observed [64]. A new green magnetically removal nanocatalyst was derived by Ghasemi et al. from the AgNPs/Fe₃O₄@Chitosan/PVA backbone, which was used for the synthesis of multicomponent reaction (MCR) of piperidine, phenylacetylene, and benzaldehyde [65]. Here, the author used a magnetic nanocatalyst for the synthesis of propargylamine and triazole derivatives under low cost, excellent yield, and an environmentally friendly approach [65]. In addition to this nanocatalysts exhibit excellent reusability up to six cycles without any significant loss in activity [65]. Another, MCR of aldehyde, alkyl acetoacetate, and ammonium acetate was carried out by Safaiee et al. using cellulose and oxo-vanadium-based catalyst [66]. Here, the author is able to synthesize the dihydropyridine and triaryl pyridines via multicomponent reaction using a reusable vanadium-based catalyst with excellent yield [66]. Likewise, many more similar examples are available in the literature, revealing the use of biopolymer-based catalysts for multicomponent reactions.

1.4.3 Biopolymer for Antibacterial Activity

Nearly, 30 % of the food undertakes spoilage during the harvest and postharvest transportation, which leads to wastage of food globally [67]. So, it is necessary to reduce the spoilage of food from mechanical damage, pathogenic microorganisms, and ultraviolet radiation [67]. Among various packaging materials available, biopolymer-based materials are predominantly due to their excellent chemical and physical stability, lightweight, reusability, accretive demand for sustainable material, biodegradable, and excellent mechanical strength [67]. As biopolymers contain a large number of functional groups that enhance their antimicrobial activity, such as chitosan contains hydroxyl and amino groups helps for its excellent application in the biomedical field [68]. In this field synthesis of biopolymer-derived material using an eco-friendly method with antibacterial and antioxidant properties has fuelled great interest of scientists (Figure 1.8) [68]. Because of all these properties biopolymer-based materials can be applied in antifungal, anti-inflammatory, antibiofilm, and drug delivery [67-68]. In the field of biomedical application Hasanzadeh et al. derived a material from cellulose

nanocomposite with immobilization of ionic liquid and silver nanoparticles over the surface and thereafter, prepared material was applied in vitro antibacterial activity for *Pseudomonas aeruginosa* and *Staphylococcus aureus* [69]. This material helps to inhibit the growth of bacteria on equipment and surfaces, to reduce nosocomial infections in intensive care units (ICU) and surgery rooms in hospitals [69]. Verma et al. extracted the cellulose nanocrystals (CNC) from sugarcane bagasse and thereafter used them for antibacterial packaging applications [70]. Herein, the author derived a polymeric film that exhibits excellent visual color-sensing properties for *Escherichia coli* bacteria [70]. Also, Ali et al. derived material from chitosan with the inclusion of silver nanoparticles, and was tested against *Sclerotium rolfsii*, *Escherichia coli*, *Fusarium oxysporum*, and *Staphylococcus aureus* bacteria [71]. The material showed tremendous antifungal activity with 76.67 % and 100 % growth inhibition against *F. oxysporum* and *S. rolfsii* respectively [71]. In addition to these Liu et al. proposed an antibacterial material from soybean polysaccharides with the incorporation of silver nanoparticles embedded over the surface of biopolymer [72]. Furthermore, the prepared material exhibits excellent antibacterial properties against both *Staphylococcus aureus* and *Escherichia coli* bacterial strains and has great potential for pharmaceutical packaging applications [72]. In this field, Shen et al. published a research work, where he synthesized hydrogel from a biopolymer alginate dialdehyde [73]. Thereafter, synthesized hydrogel was demonstrated for biomedical applications [73]. In the area of food packaging application Zare et al. prepared a material from chitosan, that offers excellent antimicrobial activity against bacterial strains [73]. Obtained hybrid polymeric films offer a replacement for traditional petrochemical-based polymers used for increasing the shelf life of food and packaging of poultry items [74].

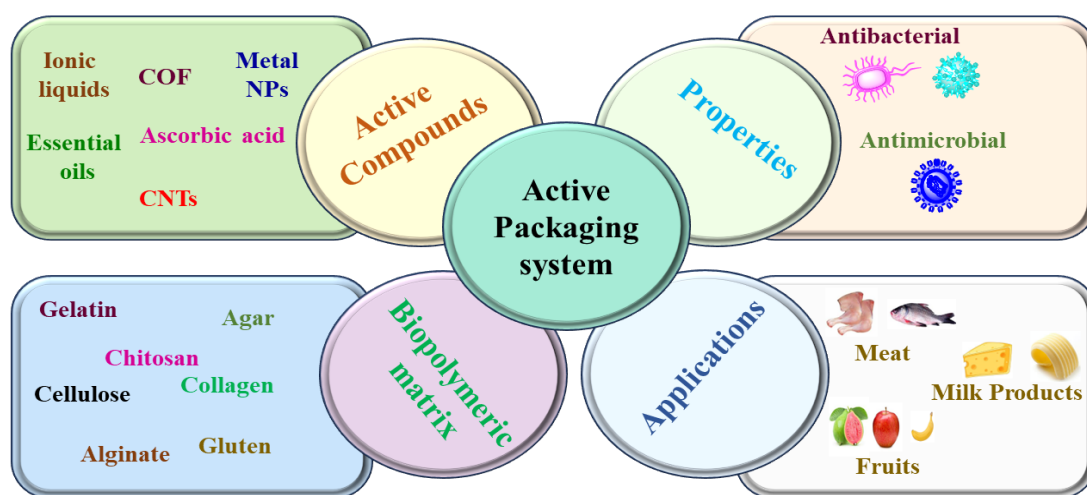


Figure-1.8: Biopolymers and organic compounds derived polymeric film for smart sensing and active packaging of food.

Traditionally, synthetic antioxidants such as butylated hydroxytoluene (BHT), tertiary butylated hydroxy quinone (TBHQ), propyl gallate (PG), and butylated hydroxy anisole (BHA) have been used in food from the past few years [75]. But all these synthetic antioxidants have several health-related issues and have aroused interest in natural antioxidants, such as gelatin, which is an inexpensive, biodegradable, and easily derived from plants that have received significant attention due to its excellent antioxidant and antibacterial properties [76-77]. According to the Food and Drug Administration, pectin, chitosan, gelatin, xanthan gum, sodium alginate, starch, and cellulose are some classified as generally recognized as safe (GRAS), which means that all these biopolymers can be directly added to food items to increase their life [78].

Over last few years, the use of ionic liquids has been found to be highly beneficial for the synthesis of antibacterial and antioxidant polymeric matrix, because of its excellent plasticizing and solvating properties [79]. There are a few examples reported by some researchers, where they developed materials from bio-polymer and ionic liquid which exhibit properties of both antibacterial and antioxidant [79]. Few methods were reported from biopolymers-based material doped with ionic liquids which exhibit antimicrobial properties and were further investigated by the observation of inhibition zones against bacterial strain [80]. Aboomeirah et al. synthesized a material from gelatin and alginate utilized for wound healing properties and further, used for biomimicking skin substitutes [81]. The antioxidant properties of the matrix used for prevention of fruits were calculated via the DPPH free radical scavenging method [82].

1.4.4 Biopolymers in sensing

Biopolymers also play a pivotal role in increasing the shelf life of food, and smart monitoring the quality of packaged food [83]. So, it is also necessary to design smart packaging material from biopolymers with the incorporation of appropriate ligands [83]. There is a visual color change in smart labeling on material when it comes into contact with the surrounding of spoilage food [83]. According to the European Food Safety Authority (EFSA), smart materials are those, which monitor the spoilage and surrounding environments such as temperature, pH, moisture level, and gaseous composition of packaged food [84]. Smart chips or labels derived from biopolymers help to identify spoilage or changes in packaged food quality [84]. Smart food

packaging also contributes to improving the Quality Analysis and Critical Control Points (QACCP) and Hazard Analysis and Critical Control Points (HACCP) systems [84]. Thus, biopolymer-derived smart material helps to detect the food quality changes on-site in real-time, ensuring food safety, and maintaining food quality [85]. Besides, all the above benefits smart labeling also plays a tremendous role in reducing food wastage [85]. Some organic and inorganic ligands including ionic liquids, molecular organic frameworks, organic molecules, and covalent organic frameworks play a pivotal role in smart sensing [85]. Smart material is basically pH dependent and relatively working on a simple principle i.e., metabolites produced during the spoilage of food react with material resulting in color changes and spoilage of food determined visually [84].

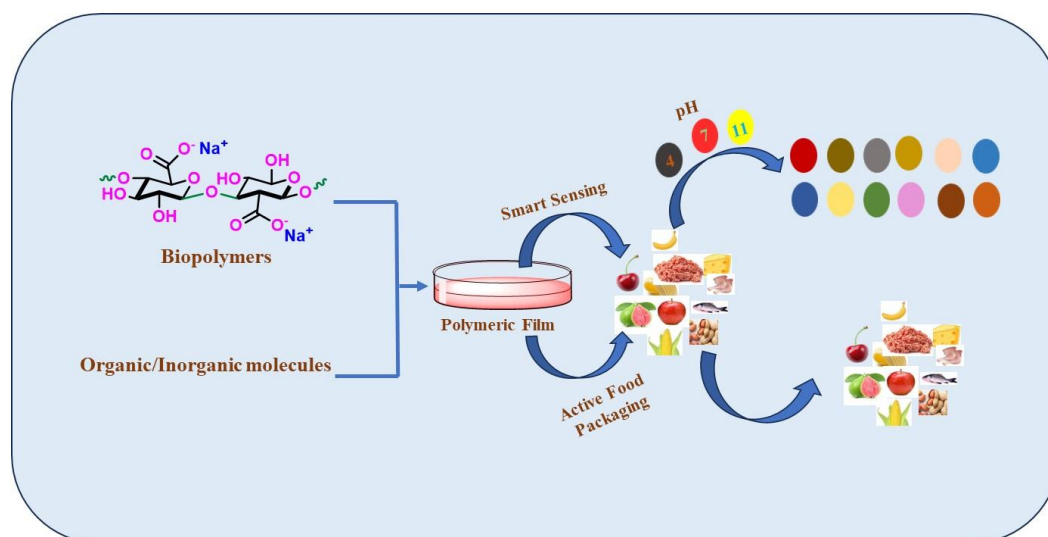


Figure-1.9: Biopolymers and COF-based materials for smart sensing of food and active food packaging.

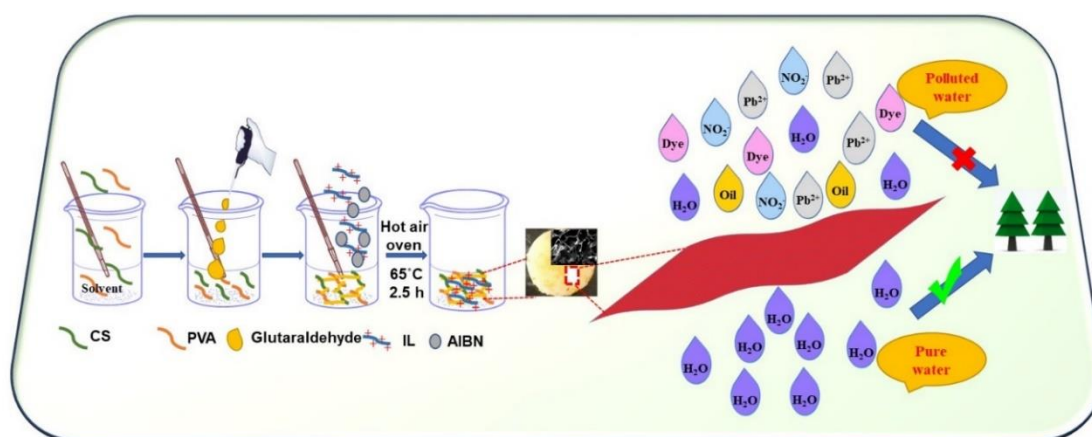
This technique replaces the sophisticated tools that pass data to computer systems used for monitoring the spoilage and quality of food [85]. In this area, Yuan et al. used the petunia flowers as a biomass source to extract the petunia dye and developed a colorimetric sulfur dioxide (SO_2) gas sensor to monitor the quality of packaged food [85]. As the concentration of SO_2 increases, the color of petunia dye-based film starts changing which can be visually by the naked eye [85]. Si et al. also reported a fluorescent probe for the detection of biogenic amines in food materials [86]. In this work cellulose nanofibers were extracted from biowaste and doped with ortho-phenylenediamine to generate fluorescent probes [86]. Thus, the cellulose carbon dots film helps to monitor the visual food freshness [86]. Thereafter, priyadarshi et al. reported a work for active food packaging, where the author derived a packaging film from gelatin/agar

biopolymers doped with sulfur quantum dots [23]. The insertion of sulfur dots increases the UV barrier properties of gelatin/agar film and shows excellent antimicrobial properties for active food packaging [23].

Chitosan film decorated with silver nanoparticles was reported by Zhang et al. for monitoring the spoilage and quality of food samples [87]. The prepared material showed excellent stability and high sensitivity at room temperature for up to five weeks and was applied for the detection of pesticides on the samples of lettuce, cabbage, onion, and apples [87]. Plant *Lithospermum erythrorhizon* was used for the extraction of shikonin and incorporated between the biopolymers [87]. Shikonin increases the water vapor permeability, UV-light barrier of polymeric film, and was applied for monitoring the freshness of shrimps [88]. Similarly monitoring the freshness of shrimps and fish was also reported by Koshy et al. where the author synthesized a polymeric sensing film using arrowroot as a polymer source [87]. Color indication of polymeric strips attached inside the box containing fresh shrimps changed according to inside pH of the box [87-88]. The pH of the box changed according to the evolution of total volatile basic nitrogen [87]. Furthermore, Amaregouda and Kamanna prepared a film from chitosan and polyvinyl alcohol with inclusion of anthocyanins extracted from *Stachytarpheta jamaicensis* [89]. The prepared film changed from pink to dark yellow at room temperature when pH of food samples varied from 1 to 13 [89].

Chapter-2

Chitosan–poly(vinyl alcohol)–ionic liquid-grafted hydrogel for treating wastewater



Singh, A.; Singh, N.; Kaur, N.; Jang, D. O. *New Journal of Chemistry*, 2023, **47**, 11196–11209.

2.1 Aim and Objectives

The demand for fresh water increasing with the growth of industrialization and inworld population. As industrialization increases rapidly to fulfill the population's demand for textiles, fertilizers, food, etc. All these types of industries pollute water by discarding their wastes such as organic dyes, pesticides, toxic heavy metals, and toxic anions directly into natural water sources and the percentage of fresh drinking water on earth is decreasing day by day. Direct consumption of all these pollutants causes a lot of serious diseases such as dysentery, cholera, hepatitis, polio, typhoid, and diarrhea. So, it is necessary to develop and design materials for wastewater treatment from naturally abundant biopolymers with the incorporation of monomers. This chapter deals with the synthesis of reusable hydrogel from chitosan–poly(vinyl alcohol) with grafting of ionic liquid for removal of murexide, Pb^{2+} , nitrite, and oil from wastewater.

2.2 Introduction

Water can be polluted by various hazardous effluents, including toxic heavy metals, inorganic anions, dyes, pesticides, cosmetics, and pharmaceuticals [1-4]. Industrial chemicals destroy the environment and affect the health of humans and marine animals [5-6]. The continuously growing population imposes significant demands on the production of leather, textiles, and cosmetics, which require a large amount of water for dyeing; used dyes are then discharged into natural water sources [7-8]. Worldwide, $>7 \times 10^5$ tons of industrial waste dyes from different sources are released into natural waters, which are detectable even at low concentrations. Another contaminant, Pb^{2+} , is designated as a harmful heavy metal by the Environmental Protection Agency (EPA) and is frequently found in alloys, batteries, catalysts, fuel cells, and therapeutic devices. Even trace concentrations of heavy metals can accumulate to significant amounts over time, contaminating water and food. Pb^{2+} concentrations above the permissible limit can harm the digestive, nervous, cardiovascular, and hematopoietic systems [9]. In this regard, efficiently removing dyes and Pb^{2+} from polluted waters is essential for resolving industrial and biological issues [10-11].

To remove dyes and Pb^{2+} from wastewater, various methods, including ion exchange, physical adsorption, activated carbon removal, chemical precipitation, and biodegradation, have been reported for industrial wastewater treatment [12-15]. Among these techniques, adsorption is preferred owing to its facile implementation, low energy

consumption, economic feasibility, and high efficiency [16]. Li et al. developed a hydrogel using epichlorohydrin and ethylenediamine to remove toxic dyes through hydrophobic interactions [17]. Qian et al. reported an alginate-based hydrogel for pollutant adsorption via electrostatic interactions and hydrogen bonding from wastewater [18] and Yang et al. prepared a polysaccharide hydrogel via electrically induced covalent crosslinking for dye adsorption [19]. Also, Mondal et al. synthesized a peptide-based hydrogel, and strong electrostatic interactions between the gelator molecules and cationic dyes resulted in the adsorption of organic dyes from industrial wastewater [20]. Du et al. prepared an acrylic-acid-grafted xanthan gum hydrogel for the adsorption of rhodamine B with strong electrostatic interactions between -COO^- and $\text{-N}^+(\text{C}_2\text{H}_5)_2$ with high efficacy [21]. Singh et al. developed a method for methylene blue removal through electrostatic interactions by embedding iron oxide nanoparticles in chitosan (CS)–graphene oxide-derived hydrogel [22]. However, all these materials have low adsorption capacity and require more time for the removal of pollutants from wastewater.

In addition, anions, including nitrite, nitrate, fluoride, chloride, bromide, perchlorate, phosphate, and sulfate can be harmful when their levels exceed respective concentration limits [23]. These harmful anions can cause many severe human health issues and ecological degradation [24]. Nitrites, which play a vital role in food and drink preservation, are carcinogenic owing to their ability to form *N*-nitroso derivatives *in vivo*. Excessive nitrite use can cause a fatal disease called "blue baby syndrome" [25–26]. The World Health Organization (WHO) has expressed concerns regarding the high consumption of nitrite-processed meat, recommending a maximum nitrite level of 65 mM [27]. Many analytical approaches are used for the determination of nitrites, including gas chromatography (GC), high-performance liquid chromatography (HPLC), fluorometry, and surface-enhanced Raman spectroscopy (SERS) [28]. However, these analytical techniques require long operation times and a well-trained operator.

The discharge of oil from factories and oil-spill accidents have caused severe ecological damage and water contamination, necessitating the urgent development of oil–water separation technologies [29]. Many methods have been reported, including adsorption, centrifugation, gravity, ultrasonication, and filtration [30]. In particular, adsorption has received attention owing to its relatively low cost, high efficiency, and facile implementation, and the use of porous materials with hydrophobic surfaces has attracted significant interest in oil-water separation [31–32].

Herein, a cationic hydrogel was designed and synthesized using a simple and facile method yielding excellent adsorption capacity, thereby enabling the rapid removal of organic dyes, nitrite anions, and Pb^{2+} from polluted water, as well as oil–water separation. The backbone of the hydrogel was composed of CS and poly(vinyl alcohol) (PVA) with glutaraldehyde as the crosslinker. An ionic liquid (IL) was grafted onto the backbone *via* a radical reaction. The synthesized hydrogel was optimized by varying the amounts of crosslinker, monomer, temperature, reaction time, initiator, and solvent to obtain maximum adsorption affinity. The interstitial voids and cationic charge on the hydrogel increased its binding affinity for organic dyes and anions. The positively charged hydrogel electrostatically interacted with the dyes and nitrite (NO_2^-), facilitating their removal from wastewater.

Moreover, the hydrophobic tails on the IL promoted oil–water separation through hydrophobic–hydrophobic interactions and enabled the reuse of the separated oil. The maximum hydrogel swelling was approximately 330 %, and the exhibited excellent reusability after being washed with methanol. Owing to the high adsorption capacity, the hydrogel removed up to 97 % and 96 % of the organic dyes and Pb^{2+} contaminants, respectively, without significant losses of adsorption efficiency.

2.3 Experimental

2.3.1 Materials

CS, PVA, glutaraldehyde, and azobisisobutyronitrile (AIBN) were purchased from Sigma Aldrich. Benzimidazole, allyl bromide, and 1-bromopropane were purchased from TCI Chemicals. All chemicals were of analytical grade and were used as-received without further purification. The deionized water used to synthesize the hydrogel was purified using a water BIO-AGE (Dura-Q-Classic-5) purification system.

2.3.2 Characterization method

IL synthesis was confirmed using a JEOL nuclear magnetic resonance (NMR) spectrometer operated at 400 and 100 MHz to obtain the ^1H and ^{13}C NMR spectra, respectively. Deuterated solvent was used as an internal standard to reference the chemical shifts. Furthermore, monomer synthesis was confirmed via high-resolution mass spectroscopy (HRMS) using an XEVO G2-XS QTOF mass spectrometer. Fourier-transform infrared (FTIR) spectroscopy was performed using a Hyperion 2000 FTIR system (Bruker Optics). The surface morphologies of the synthesized materials were examined by performing scanning electron microscopy (SEM), energy-dispersive X-ray

spectroscopy (EDS), and elemental dot mapping using a JEOL JSM-6610-LV microscope. Surface chemical characterizations were carried out by X-ray photoelectron spectroscopy (XPS) (Thermo, Model ESCALAB 250). The thermostability of the samples was obtained using a Pyris-1 thermogravimetric analysis (TGA) system (PerkinElmer, USA) in the range 40–800 °C at a heating rate of 10 °C min⁻¹ under a nitrogen atmosphere. Zeta potential experiment was performed using a Nanotrac Wave II zeta potential analyzer at 25 °C. A Miniflex (Rigaku) diffractometer was used to acquire powder X-ray diffraction (PXRD) patterns to determine the crystallinity and material planes. An ultraviolet (UV)–visible (vis) absorption spectrophotometer (Shimadzu UV-2400) was used to determine the dye adsorbed by the synthesized hydrogel. The cuvette used for UV–vis experiments was composed of quartz and had a path length of 1.0 cm. The treatment of nitrite-polluted water was monitored using ion chromatography (930 Compact IC Flex Metrohm). The residual concentration of Pb²⁺ was monitored using micro-plasmonic atomic-emission spectrometry (MP-AES; Agilent Technology 4200) at frequencies of 217 nm and 406 nm. The swollen and shrunken hydrogel samples were placed on a measuring plate of a rheometer (MCR301; Anton Paar, Graz, Austria) with a 25 mm diameter parallel plate fixture (25 mm diameter). The diameter and thickness of the samples in the as-prepared state were 40.0 mm and 1.5 mm, respectively.

2.3.3 Synthesis of ionic liquid

Benzimidazole (118 mg, 1 mmol) and NaOH (8 mg, 0.2 mmol) were dissolved in CH₃CN (5 mL) at 80 °C, and 1-bromooctane (193 mg, 1 mmol) was added to the mixture and stirred at 80 °C overnight. Allyl bromide (130 mg, 1.5 mmol) was added, and the mixture was stirred again overnight at 80 °C. After evaporation, IL was fully characterized with HRMS, ¹H-NMR, and ¹³C-NMR (Figure A1-A3). ¹H NMR (400 MHz, DMSO-*d*₆) δ 7.57 (d, *J* = 2.9 Hz, 2H), 7.18 (dd, *J* = 6.1, 3.1 Hz, 2H), 6.06–5.93 (m, 1H), 5.33 (dd, *J* = 16.8, 1.3 Hz, 2H), 5.11 (dd, *J* = 9.9, 1.5 Hz, 2H), 4.08 (d, *J* = 7.3 Hz, 2H), 1.74 (t, *J* = 6.9 Hz, 2H), 1.34–1.20 (m, 10H), 0.81 (t, *J* = 6.8 Hz, 3H). ¹³C NMR (100 MHz, DMSO-*d*₆) δ 144.0, 144.8, 135.1, 134.6, 124.5, 123.6, 120.0, 115.4, 111.8, 47.5, 35.8, 34.7, 32.8, 29.1, 28.6, 28.1, 22.6, 14.5. MS: calculated *m/z* 271.65; found *m/z* 271.69.

2.3.4 Synthesis of CS–PVA–IL gel

CS (0.5 g) and PVA (0.5 g) were mixed in a 30 mL solution comprising 27 mL deionized water and 3 mL acetic acid. The solution was mixed to make it homogenous through continuous stirring for 10 min at room temperature. Thereafter, the IL (0.5 g),

glutaraldehyde (0.4 mL), and AIBN (0.10 g) were subsequently added to the mixture, which was placed in a hot-air oven at 65 °C for 2.5 h. The mold was dried at 50 °C in the oven and washed with deionized water to remove unreacted compounds [9].

2.3.5 Dye adsorption

Murexide (3 mg) was dissolved in water (100 mL), and the **CS–PVA–IL** gel (30 mg) was added to the aqueous solution at room temperature. During adsorption, the aqueous solution pH was adjusted to 7. After 18 min, the aqueous murexide solution was passed through Whatman filter paper, and the concentration was calculated at each time interval using UV–vis spectroscopy at 522 nm. The dye-removal efficiency of the **CS–PVA–IL** gel was calculated using the following equation [34].

$$\text{Dye removal (\%)} = \frac{C_o - C_t}{C_o} \times 100 \quad (2.1)$$

where C_o and C_t are the concentration of murexide at the beginning of the process and at time t , respectively. The adsorption capacities, q_t , and q_e , were calculated according to Equations (2.2) and (2.3):

$$q_t = \frac{(C_o - C_t)V}{m} \quad (2.2)$$

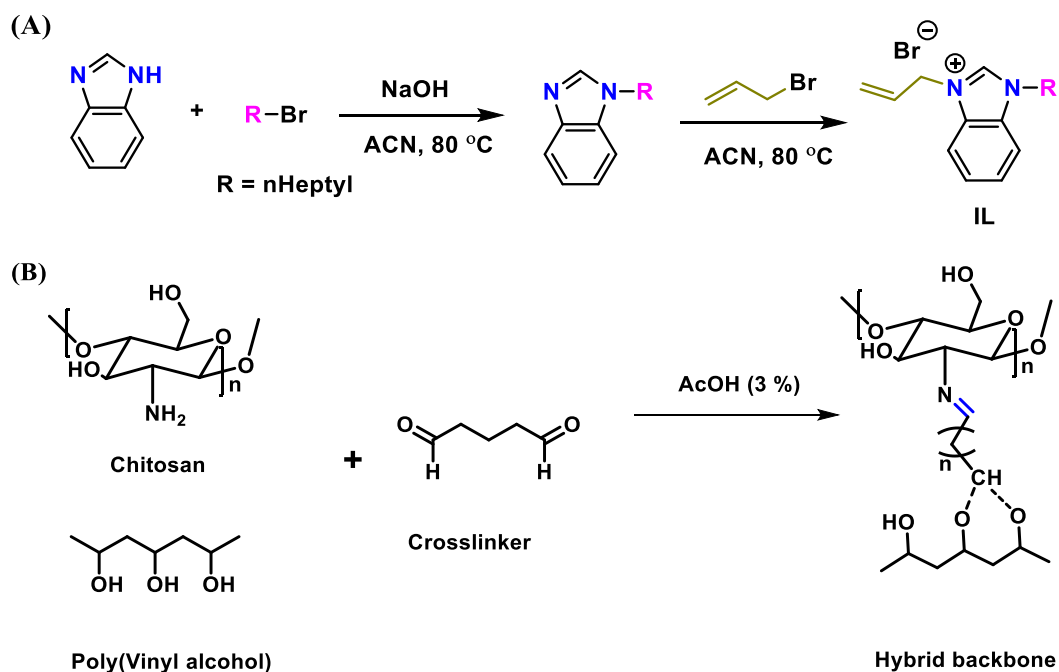
$$q_e = \frac{(C_o - C_e)V}{m} \quad (2.3)$$

where C_e represents the murexide concentration at equilibrium, m is the mass of **CS–PVA–IL** gel, and V is the dye solution volume.

2.4 Result and Discussion

2.4.1 Preparation of CS–PVA–IL gel

A schematic of the synthesis of the **CS–PVA–IL** gel is presented in Figure 2.1. The IL was prepared *via* the reaction of benzimidazole with 1-bromooctane and allyl bromide (Scheme 2.1a), which was initially prepared by reacting CS, PVA, glutaraldehyde, and IL in the presence of AIBN in a hot-air oven at 65 °C for 2.5 h (Figures 2.1 and scheme 2.1b). The hydrogel formed as a mold (**CS–PVA–IL** gel) was washed with deionized water and dried at 50 °C in a hot-air oven. The graft ratio of graft polymer was found around 1:0.27. The solid material obtained after drying is referred to as a xerogel. The above parameters were selected via optimization experiments and used to determine the percentage swelling of the hydrogel.



Scheme 2.1. Synthesis of A) IL and B) hybrid backbone.

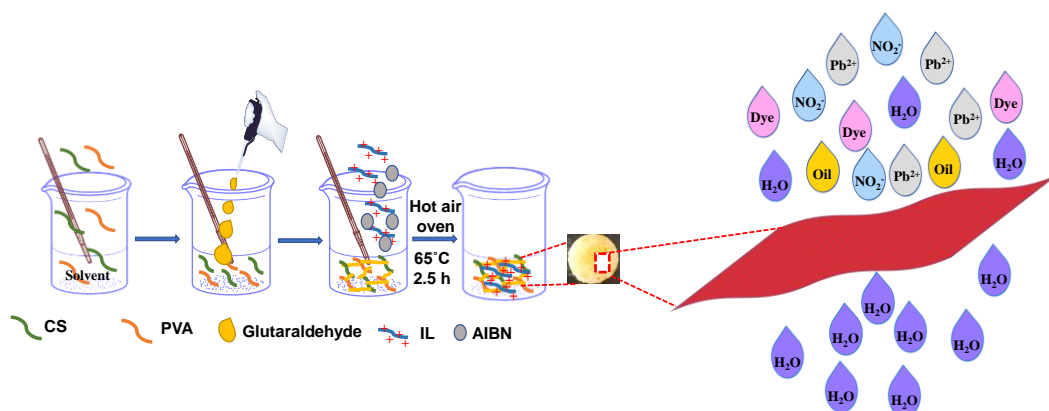
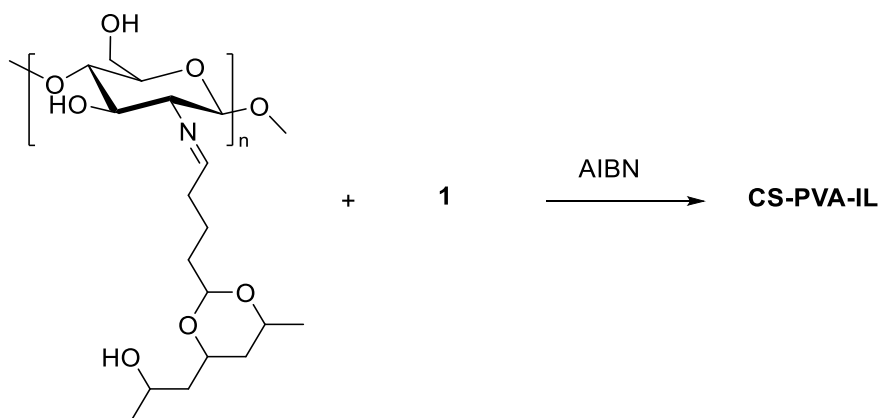


Figure 2.1. Schematic of the synthesis of the CS-PVA-IL gel.



Scheme 2.2. Tentative model for the synthesis of the CS-PVA-IL gel.

2.4.2 Optimization of the CS-PVA-IL gel

To maximize the swelling percentage, the hydrogel was optimized under controlled conditions by varying different parameters, including time, pH, temperature, water content, IL content, and initiator concentration (Figure 2.2), one at a time and keeping the other parameters constant [Table-2.1]. The hydrogel was kept in contact with distilled water to examine its swelling properties. The swelling percentage was calculated using Equation (2.4), where W_d and W_s denote the weight of the dried hydrogel (xerogel) and swollen hydrogel, respectively [9].

$$\text{swelling (\%)} = \frac{W_s - W_d}{W_d} \times 100 \quad (2.4)$$

A maximum swelling percentage of 325 % was obtained using 0.5 g of the IL (Figure 2.2a), where the swelling rate increased with increasing IL concentration. However, after the optimum value was reached, swelling decreased with a further increase in the IL concentration, which was attributed to the compact network between the monomeric units. The maximum swelling percentage of 311 % was obtained using the hydrogel prepared in 2.5 h (Figure 2.2b). After a certain time, all free radicals were consumed, which tended to decrease the swelling percentage. The percentage of swelling increased to 320 % at 65 °C (Figure 2.2c), but above this temperature, the crosslinks between the backbones started to break. The subsequent decrease in swelling percentage was possibly due to the decrease in hydrophilic interactions and increased molecular kinetic energy.

The amount of radical initiator influenced the percentage swelling of the hydrogel, with a maximum swelling uptake of 330 % using 0.1 g AIBN (Figure 2.2d). At low AIBN concentrations, free radicals were generated during the reaction, whereas higher concentrations resulted in chain termination, which affected the crosslinker density. The hydrogel formed using 30 mL of water exhibited optimal swelling, achieving a swelling percentage of 320 % (Figure 2.2e). Increasing the amount of water promoted the formation of –OH groups, which facilitated radical formation. Above the optimum concentration of water, the chain is terminated. The pH is another parameter that significantly affects the swelling properties of the hydrogels. A maximum swelling percentage of 311 % was obtained at pH 7 (Figure 2.2f). After optimizing all parameters, a maximum swelling of 330 % was achieved.

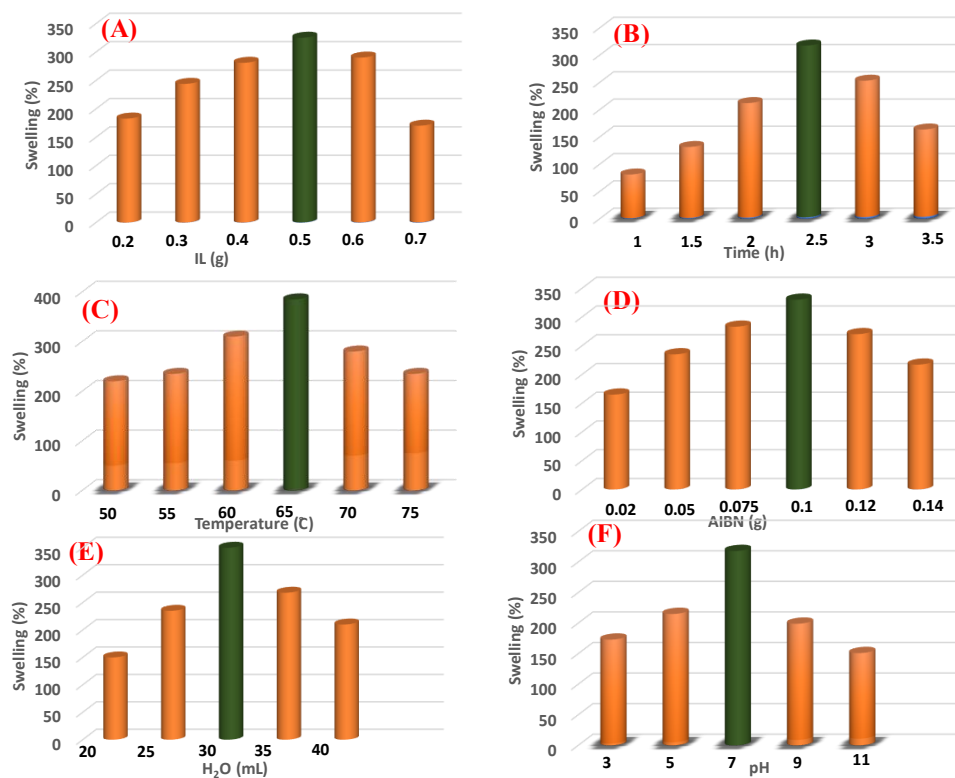


Figure 2.2. Swelling optimization of the CS-PVA-IL gel by varying different parameters: A) IL content, B) time, C) temperature, D) initiator content, E) water content, and F) pH.

Table 2.1. Optimized amounts of materials used for the hydrogel synthesis.

Entry	Reactant	Amount
1	CS	0.5 g
2	PVA	0.5 g
3	Glutaraldehyde	0.5 mL
4	Monomer	0.5 g
5	Initiator	0.1 g
6	Solvent	30 mL

7	Temperature	65 °C
8	pH	7
9	Time	2.5 h

2.4.3 FTIR spectroscopy

The FTIR spectral data of the prepared hydrogel backbone confirmed the presence of C–H, O–H, and N–H stretching at 3375, 3277, and 2884 cm^{-1} , respectively (Figure 2.3a). The characteristic C–O band in CS was observed at 1066 cm^{-1} , and PVA gave rise to C–H and O–H IR stretching bands at 3339 and 2939 cm^{-1} , respectively (Figure 2.3b). The characteristic C–O band in PVA appeared at 1020 cm^{-1} , and the backbone—a mixture of CS and PVA—produced bands at 3283 and 1023 cm^{-1} , corresponding to the stretching vibrations of O–H and C–O groups, respectively (Figure 2.3c). The primary O–H and N–H bands in the **CS–PVA–IL** gel were observed at 3380 and 3283 cm^{-1} , respectively (Figure 2.3d). The presence of the hydroxyl group confirms the free-radical polymerization of the IL grafted onto the backbone. The intense bands centered at 1646 and 1550 cm^{-1} corresponded to the NCN bond of the IL, confirming grafting onto the backbone. An additional band at 1690 cm^{-1} arose owing to imine bond formation between the backbone and glutaraldehyde. The intense band at 1019 cm^{-1} indicated acetal group formation between PVA and glutaraldehyde.

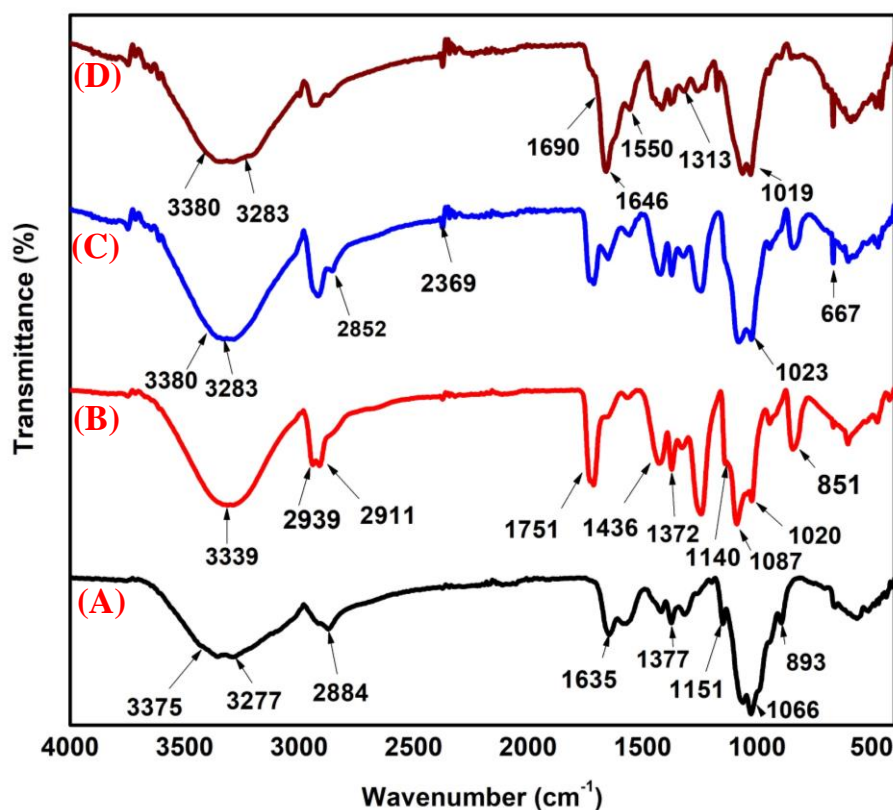


Figure 2.3. FTIR spectra of A) CS, B) PVA, C) CS + PVA, and D) CS-PVA-IL gel.

2.4.4 XPS analysis

The XPS data confirmed the existence of carbon (C 1s), oxygen (O 1s), nitrogen (N 1s), and bromine (Br 3d) in the **CS-PVA-IL** gel. The multiple peaks in the spectrum indicated the formation of numerous bonds with carbon, oxygen, and nitrogen (Figure 2.4a), where a sharp peak implied the inclusion of a single type of bond, and a broad peak indicated the same type of bonding at multiple locations in the polymeric network. For the C 1s spectrum, three peaks appeared at 285.4, 285.6, and 286.2 eV, corresponding to C-C, C-O, and C-N bonding, respectively (Figure 2.4b). Similarly, the N 1s spectrum exhibited peaks at 398.3 and 399.9 eV, indicating the presence of sp^2 -ized (R-N=) and sp^3 -ized (R-N-R) nitrogen, respectively, in the **CS-PVA-IL** gel (Figure 2.4c). Oxygen bonding (O 1s) at binding energies of 531.6 and 539.1 eV confirmed the presence of O-C and C-O-C bonds, respectively (Figure 2.4d).

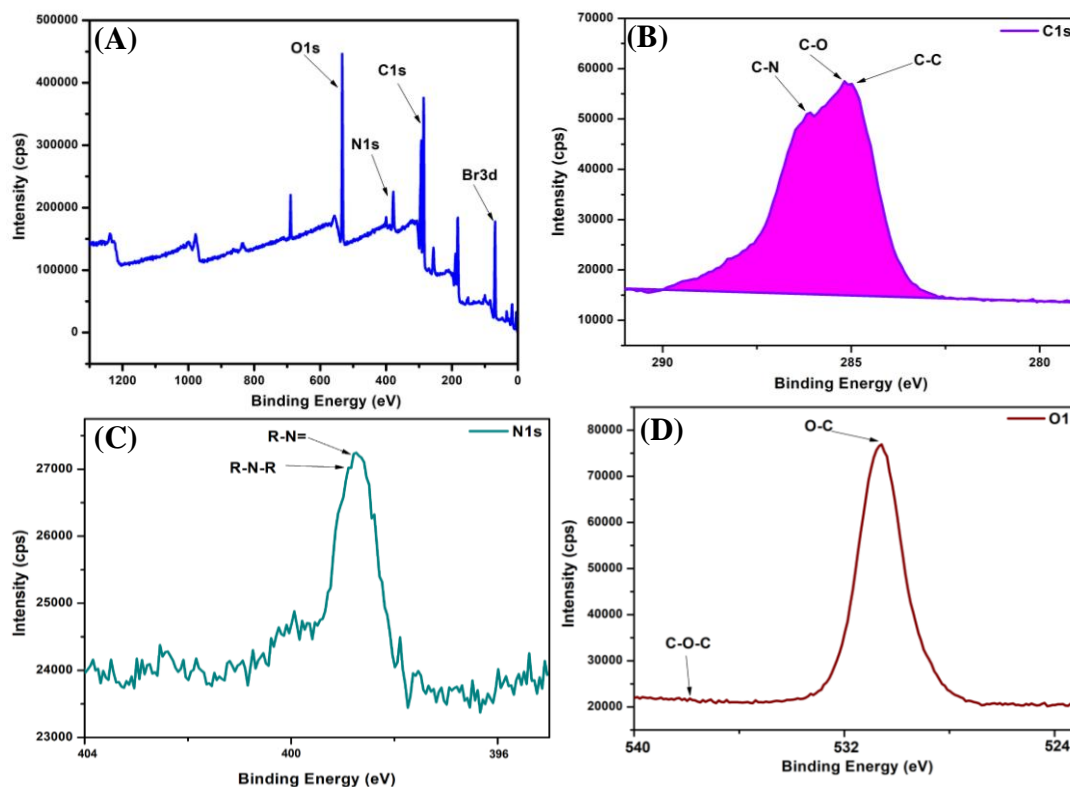


Figure 2.4. XPS peaks of A) all atoms present in the **CS-PVA-IL** gel, and the B) C 1s, C) N 1s, and D) O 1s spectra.

2.4.5 PXRD analysis

PXRD revealed variations in the crystal structure and planes of the materials. The PXRD data also reveal the crystalline size and percentage of crystallinity of the materials, with intense peaks at different 2θ values. The crystal size was calculated using the Scherrer equation (Equation (2.5)) [35].

$$D_p = \frac{k\lambda}{\beta \cos\theta} \quad (2.5)$$

where D_p is the average crystal size, β is the line-broadening in radians (full width at half-maximum (FWHM)), k is the Scherrer constant (0.9), λ is the X-ray wavelength, and θ is the Bragg angle. The crystalline sizes of CS, PVA, CS-PVA mixture, **CS-PVA-IL** gel, and **CS-PVA-IL** gel after dye adsorption (**CS-PVA-IL** gel-dye) were 3.91, 2.77, 1.86, 3.15, and 4.93 nm, respectively (Figure 2.5). The larger crystalline size of the **CS-PVA-IL** gel was attributed to the consistently oriented crosslinking patterns [Table-2.2]. After dye adsorption, the crystalline size increased and produced additional peaks, exhibiting a trend similar to that of murexide.

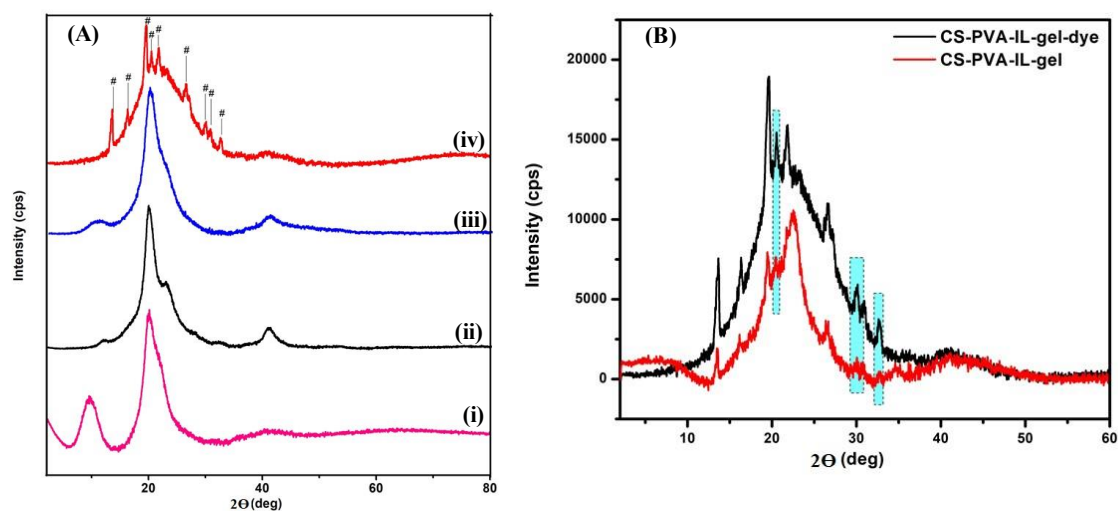


Figure 2.5. A) PXRD patterns of i) CS, ii) PVA, iii) CS–PVA mixture, and iv) CS–PVA–IL gel. B) PXRD patterns of CS–PVA–IL gel and CS–PVA–IL gel–dye.

Table 2.2. Crystalline sizes of materials are calculated using the Shears equation.

Entry	Material	2 θ	FWHM	Crystalline size (nm)
1	CS	9.67	2.13	3.91
2	PVA	19.81	3.04	2.77
3	CS + PVA	41.47	4.77	1.86
4	Hydrogel	19.41	2.68	3.15
5	Used hydrogel	19.51	1.71	4.93

2.4.6 Surface morphology analysis

The SEM analysis of the **CS–PVA–IL** gel revealed that the hydrogel possessed a crosslinked three-dimensional (3D) network (Figures 2.6a and Figure A4), in which the pore size varied from submicrometers to several micrometers depending on the IL and glutaraldehyde concentrations. The cavity on the hydrogel surface led to strong electrostatic interactions between the cationic moiety and anionic dyes, which facilitated their adsorption from polluted water. EDS and elemental dot mapping results indicated

the homogeneous presence of C, O, N, and Br in the **CS–PVA–IL** gel, demonstrating their uniform distribution over the surface (Figures 2.6b-f). The EDS data showed that the hydrogel contained carbon (57.98 %), oxygen (31.38 %), nitrogen (10.49 %), and bromine (0.15 %), with the bromine content originating from the IL. The specific surface area of **CS–PVA–IL** gel by Brunauer-Emmett-Teller (BET) was investigated by varying the relative pressure from 0 to 1.0 (Figures 2.7). The surface area of **CS–PVA–IL** gel was 230.636 m²/g with a correlation coefficient of >0.99. **CS–PVA–IL** gel has a maximum nitrogen adsorption capacity of 487 cm³/g at an outgas temperature of 110 °C (Figure A5).

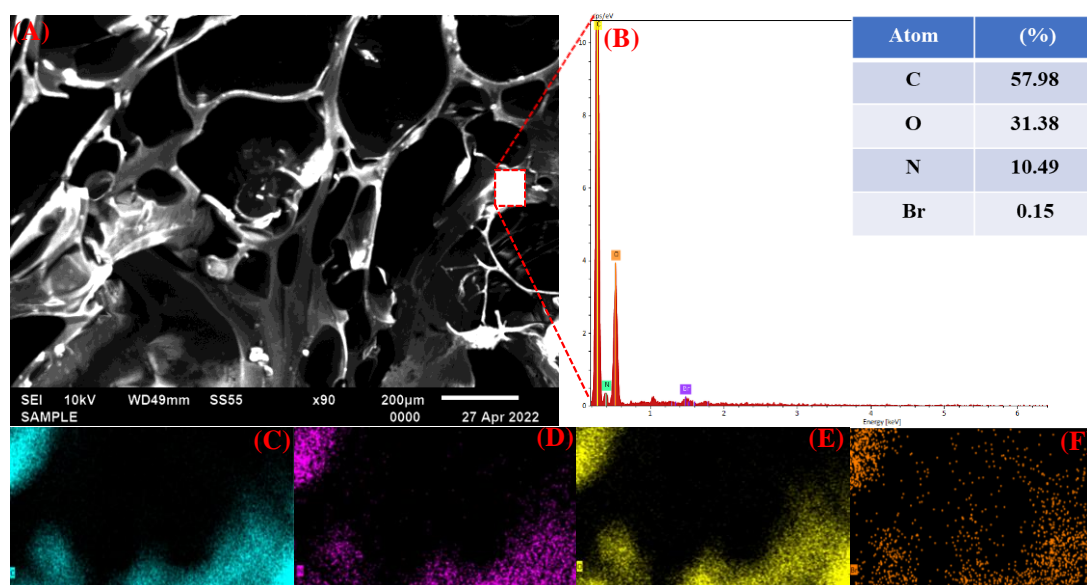


Figure 2.6. A) SEM image of **CS–PVA–IL** gel, B) EDS spectrum of **CS–PVA–IL** gel and individual elemental dot mapping of C) carbon, D) nitrogen, E) oxygen, and F) bromine.

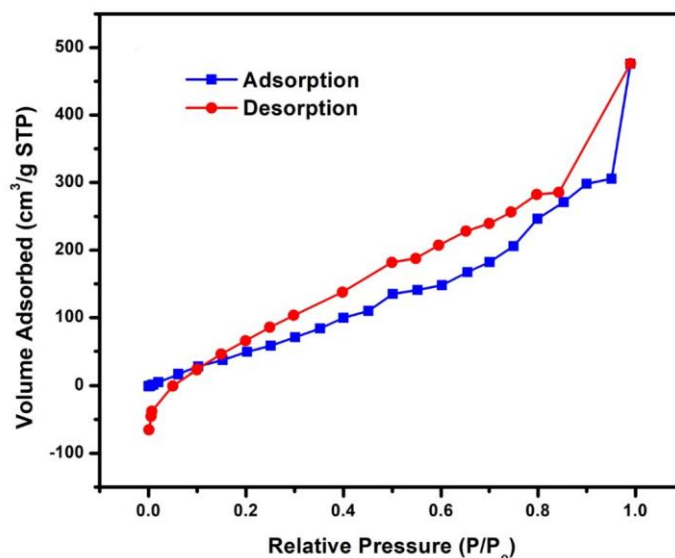


Figure 2.7. BET adsorption isotherm for **CS-PVA-IL** gel.

2.4.7 Rheological studies and Zeta potential

Rheological experiments on the **CS-PVA-IL** gel were performed in an aqueous medium (pH 7), and the results are shown in Figure 2.8. All frequency-sweep experiments were performed under identical conditions. The rheological experiments revealed that the storage modulus (G') was independent of the angular frequency (rad/s), and the loss modulus (G'') was less than G' , which is characteristic of a gel-phase material (Figure 2.8a). Comparing the loss modulus with the storage modulus at the same angular frequency of 17.8 rad/s, G' was 4454 Pa. At the same angular frequency, G'' was 682 Pa, which is lower than the storage modulus. A high G' value indicates that a material is in a gel state. The complex viscosity of the **CS-PVA-IL** gel was measured with respect to angular frequency, and the complex viscosity was found to decrease with increasing angular frequency (Figure 2.8b). A zeta potential experiment was performed using a Nanotracer Wave II zeta potential analyzer at 25 °C (Figure 2.9). It was observed that the zeta potential decreases with an increase in the pH of the solution. The protonation of the hydroxy group in the polymeric membrane in an acidic medium increases the zeta potential value while the deprotonation in a basic medium decreases the zeta potential value. Therefore, the adsorption performance of hydrogel in an acidic medium improves while that in a basic medium reduces.

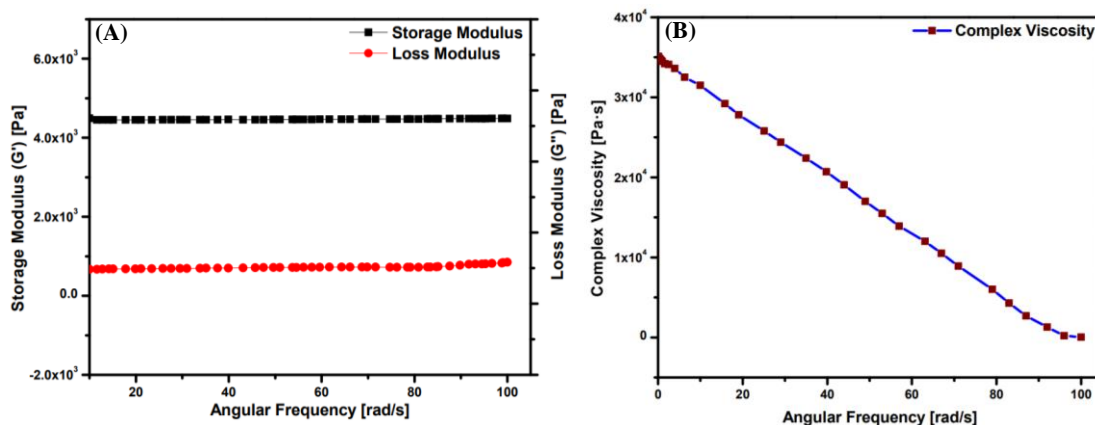


Figure 2.8. A) Dynamic mechanical analysis of G' and G'' , and B) viscosity analysis of the CS-PVA-IL gel.

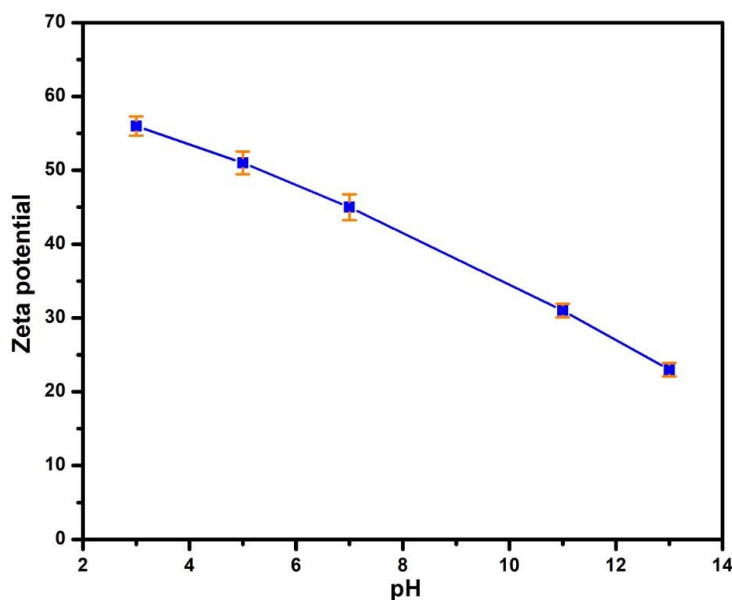


Figure 2.9. Zeta potential of CS-PVA-IL gel at different pH.

2.4.8 Thermal stability

The thermogravimetric analysis (TGA) of the experimental results shows that the thermal decomposition of CS-PVA-IL gel can be divided into three stages occurring in the temperature ranges of 70–170 °C, 340–400 °C, and >420 °C (Figure 2.10). The first stage involved moisture evaporation; subsequently, the formation of volatile components began during the second stage of thermal decomposition. Furthermore, the hydrogel decomposed into carbon and hydrocarbons at temperatures exceeding 420 °C. During the initial phase of thermal decomposition, 16 % weight loss was observed, whereas during the formation of volatile components, the weight loss was approximately 58 %.

At $>420\text{ }^{\circ}\text{C}$, the entire hydrogel decomposed into carbon and hydrocarbons, with a weight loss of 70 %.

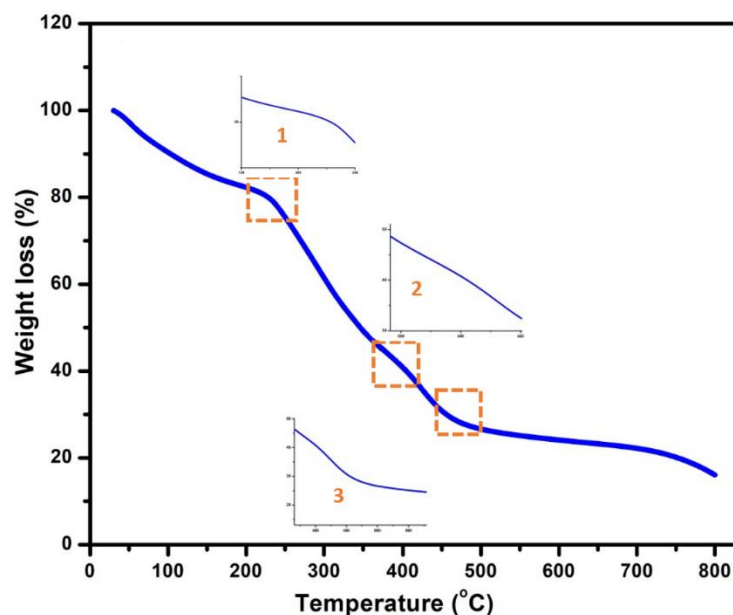


Figure 2.10. TGA curve of the **CS-PVA-IL** gel.

2.4.9 Dye adsorption

The removal of hazardous and toxic dyes from industrial wastewater is a persistent issue, as these dyes pollute water and affect human and aquatic biota [36]. Therefore, it is imperative to develop an environmentally friendly, economical, and efficient handling method to remove hazardous dyes from wastewater. In this regard, porous gels are potentially valuable reusable materials for this purpose, and a time-dependent approach was used for their removal [Table 2.3]. Herein, the **CS-PVA-IL** gel was used to adsorb toxic anionic dyes that pollute industrial water (Figure A6). The adsorption performance of the xerogel was also analyzed to account for the effects of dye diffusion from the solution to the trapped water in the **CS-PVA-IL** gel [Table 2.4]. The adsorption of the anionic dye murexide onto the cationic **CS-PVA-IL** gel occurred rapidly; 97 % of the anionic dye in wastewater was adsorbed in 18 min (Figure 2.11). The amount of applied **CS-PVA-IL** gel was optimized using UV-vis spectroscopy, with the optimal amount determined as 0.3 g (Figure 2.12).

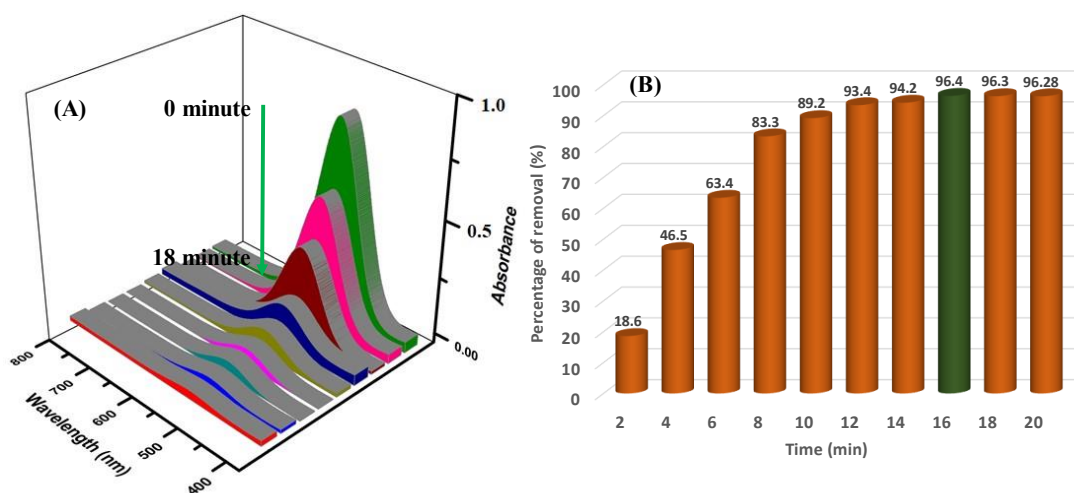


Figure 2.11. A) UV–vis spectra of the adsorption of murexide and B) percentage removal of murexide as a function of time using the **CS–PVA–IL** gel.

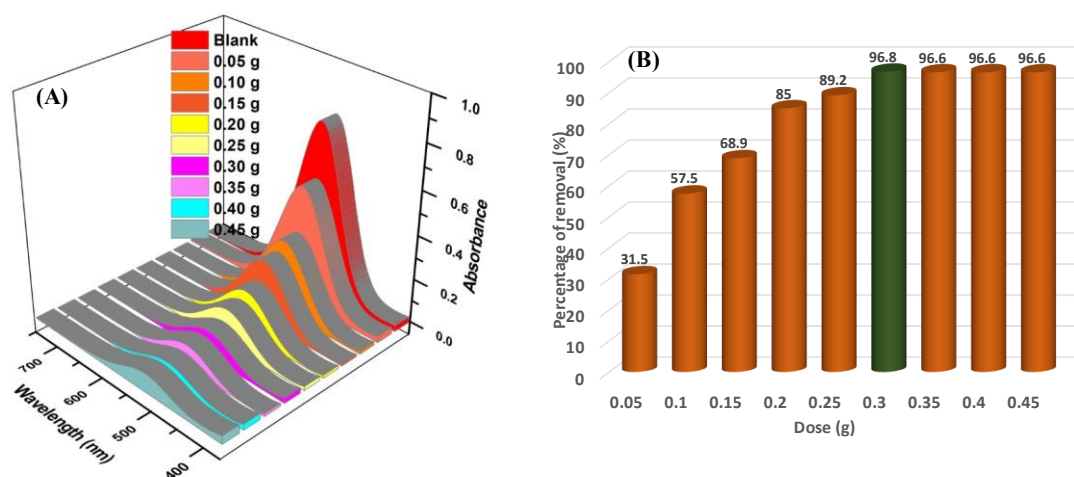


Figure 2.12. A) UV–vis spectra for the adsorption of murexide and B) percentage removal of murexide as a function of the **CS–PVA–IL** gel dose.

Table 2.3. The percentage removal of dye as a function of time.

Entry	Initial concentration (C_0 , ppm)	Final concentration (C_t , ppm)	Percentage of removal (%)
1	30	24.43	18.6
2	30	16.06	46.5
3	30	10.96	63.4

4	30	5.09	83.3
5	30	3.23	89.2
6	30	1.99	93.4
7	30	1.75	94.2
8	30	1.36	95.5
9	30	1.12	96.3

Table 2.4. The percentage removal of dye as a function of the applied hydrogel.

Entry	Initial concentration (C₀, ppm)	Final concentration (C_t, ppm)	Percentage of removal (%)
1	30	20.55	31.5
2	30	12.75	57.5
3	30	9.32	68.9
4	30	4.51	85.0
5	30	3.23	89.2
6	30	0.96	96.8
7	30	1.01	96.6
8	30	1.01	96.6
9	30	1.02	96.6

The pH effect on the adsorption performance of hydrogel was investigated using a murexide dye solution at different pH, as shown in Figure 2.13. It was observed that pH also influences the adsorption rate. The percentage of dye removal capacity of hydrogel decreased with increasing the pH of a solution. The Hydroxy group on the hydrogel surface is deprotonated in a basic medium, affording more negative charge on the hydrogel. This fact leads to a decrease in the electrostatic interaction between the anionic dye and the hydrogel, resulting in lower dye adsorption over the hydrogel surface. In contrast, the hydroxy group in an acidic medium is protonated, affording a more positive charge, which increases the electrostatic interaction between the hydrogel and the dye. This fact leads to an increase in adsorption capacity in an acidic medium.

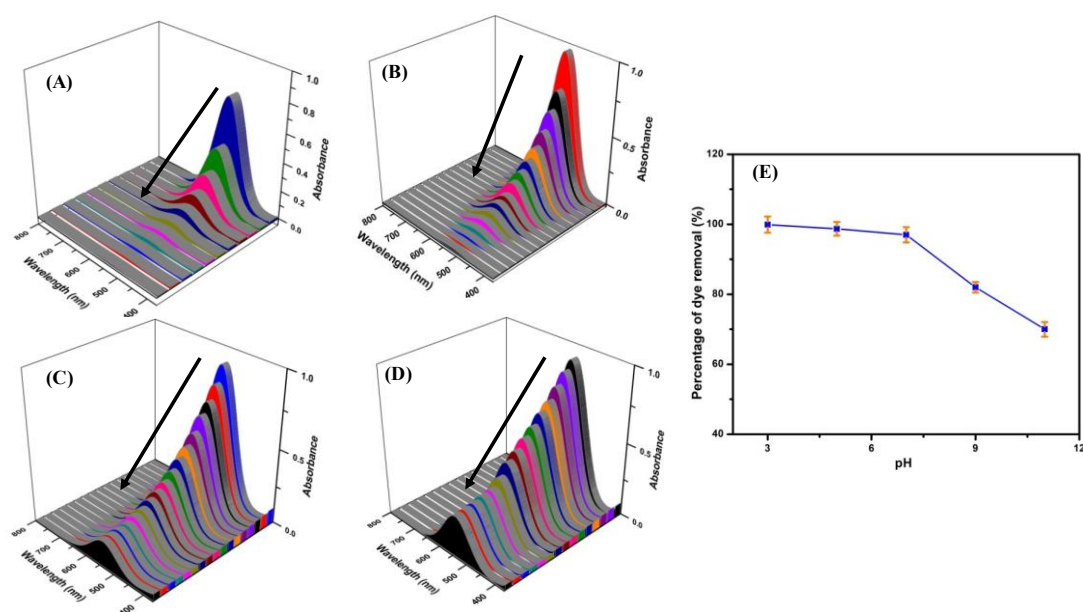


Figure 2.13. UV–vis spectra for the adsorption of murexide at different pH A) pH 3, B) Ph 5, C) pH 9, and D) pH 11. E) Percentage removal of murexide as a function of pH.

The response surface methodology (RSM) method was used to optimize the adsorption capacity and percentage of dye removal (Figures 2.14a and 2.14b). In the RSM method, three parameters were used at a time: the ionic strength of coexisting ions, the pore size of **CS–PVA–IL** gel, and the available adsorption site [37].

Different dye solutions were prepared and charged on the dried gels at various concentrations. The adsorption study results were fitted using the Freundlich adsorption isotherm model, which supports the multilayer adsorption mechanism (Figure 2.14c). The Freundlich adsorption isotherm is expressed as follows:

$$\log q_e = \log K_f + \frac{1}{n} \log C_e \quad (2.6)$$

where q_e represents the equilibrium adsorption capacity of the dye adsorbed on the dried gel surface, and C_e is the equilibrium concentration of the adsorbate (mg/L) [38]. K_f and n are the Freundlich isotherm constant and the heterogeneity factor, respectively. The kinetic study on murexide adsorption was performed at room temperature at different intervals. The obtained kinetic data were fitted to a pseudo-second-order reaction using Equation 2.7 (Figure 2.14d):

$$\frac{t}{q_t} = \frac{1}{K_2 q_e^2} + \frac{t}{q_e} \quad (2.7)$$

where q_e and q_t are the amounts of adsorbed dye at equilibrium and at time t (min), respectively. K_2 (min^{-1}) is the pseudo-second-order rate constant. The coefficient of determination (R^2) for the pseudo-second-order kinetics is high ($R^2 = 0.9919$), indicating that anionic dye adsorption is a pseudo-second-order reaction. The adsorption capacity of **CS-PVA-IL** gel was calculated to be 1062 mg/L for murexide.

Subsequently, a reusability experiment was conducted to examine the large-scale utility of the prepared gel. The xerogel was recovered using methanol, where the dye remained, and no physical changes were observed on the hydrogel during murexide adsorption. The **CS-PVA-IL** gel exhibited excellent reusability for up to eight cycles without substantial efficiency losses, indicating its potential application in real-life wastewater treatment (Figure 2.15).

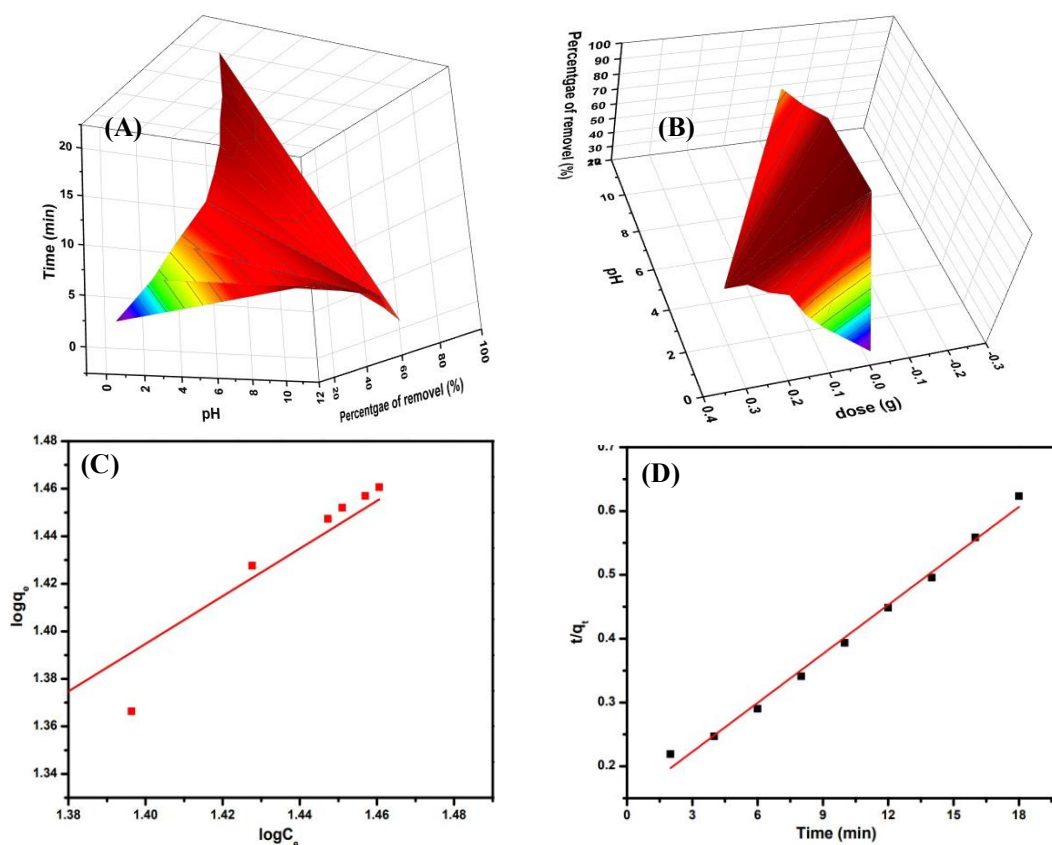


Figure 2.14. A) and B) RSM plot for optimization of dye adsorption. C) Freundlich-adsorption-isotherm-fitted dye adsorption and D) pseudo-second-order kinetic fit for murexide.

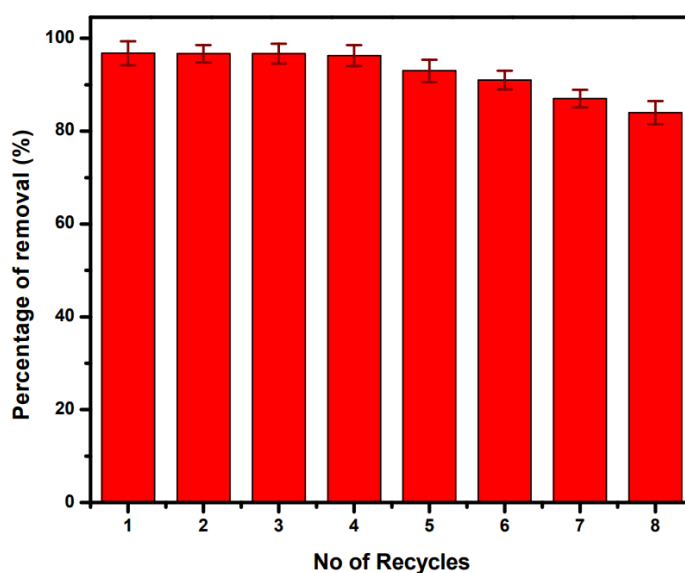


Figure 2.15. Plots showing the reusability of the CS-PVA-IL gel.

2.4.10 Nitrite-removal studies

Toxic anions found in industrial wastewater, including nitrite, are dangerous to the environment and have harmful effects on human health. When present beyond its safe concentration limits, nitrite can cause severe diseases, including stomach cancer; decrease blood-oxygen carrying capacity; and lead to other fatal diseases [39]. Therefore, it is crucial to remove nitrite from contaminated water. A nitrite adsorption study was performed using ion chromatography at different intervals (Figures 2.16a). Initially, the area under the curve for nitrite was 59.39 (μscm^{-1}) min. After 2 min, the area under the curve decreased to 44.43 (μscm^{-1}) min, indicating the adsorption of nitrite on the **CS–PVA–IL** gel. After 18 min, the area of the **CS–PVA–IL** gel decreased to 7.98 (μscm^{-1}) min.

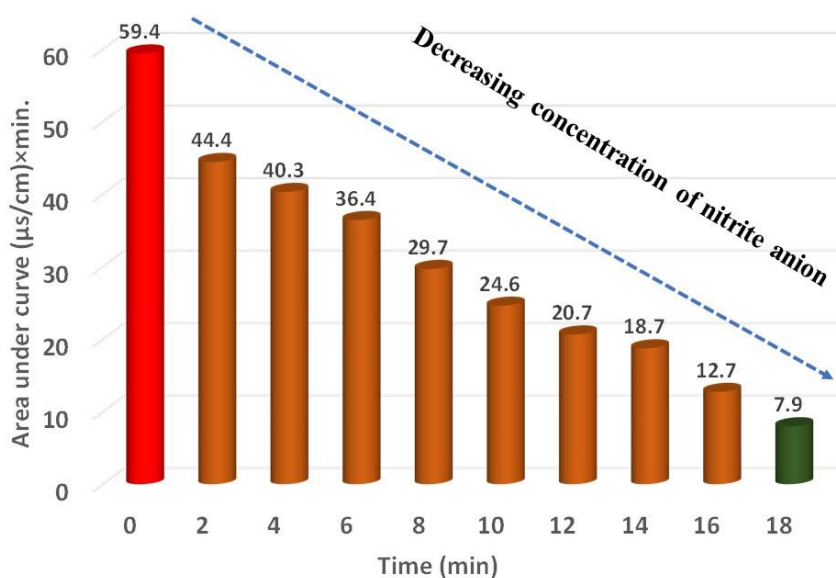


Figure 2.16. a) Ion-chromatography area under the curve for removing nitrite anions with **CS–PVA–IL** gel.

2.4.11 Lead adsorption

The adsorption of heavy metals from wastewater was studied using a batch method employing various metal-ion solutions (5 ppm: Pb^{2+} , Cu^{2+} , Co^{2+} , Fe^{2+} , Ni^{2+} , and Mg^{2+} nitrate salts). The most prominent result was Pb^{2+} adsorption using the **CS–PVA–IL** gel as an adsorbent. The residual concentration of Pb^{2+} was monitored using MP-AES at 217 and 406 nm. The calibration curve was plotted at 217 and 406 nm using four standard solutions with concentrations of 5, 15, 20, and 25 ppm. The correlation coefficients of 0.9999 and 0.9999 at frequencies of 217 and 406 nm, respectively, were high, indicating the optimum-fit calibration curve (Figure A7). The adsorption capacity (Q_t) at a specific

time was calculated according to Equation (2.8), showing that the adsorption capacity of the material was $\approx 346 \text{ mg g}^{-1}$.

$$Q_t = \frac{(C_o - C_t)V}{m} \quad (2.8)$$

Similarly, the distribution coefficient (K_d) was calculated using Equation (2.9): [40]

$$K_d = \frac{(C_o - C_f)V}{mc_f} \quad (2.9)$$

where C_o , C_t , and C_f are the Pb^{2+} concentrations at the initial, time t , and final stages, respectively; V is the volume of the solution; and m is the amount of **CS-PVA-IL** gel used for adsorption. The high performance of the **CS-PVA-IL** gel for Pb^{2+} adsorption is reflected by its high K_d value ($0.7 \times 10^4 \text{ mL/g}$), which also indicates the strong interaction of metal ions with the hydroxyl groups of the **CS-PVA-IL** gel. Moreover, a material with a distribution coefficient of 10^3 – 10^5 mL/g is considered an ideal adsorbent. Therefore, the **CS-PVA-IL** gel shows significant potential for Pb^{2+} removal, as the material can remove up to 88 % of Pb^{2+} from the water sample within 40 min (Figure 2.17d and Figure A8). The adsorption isotherm of Pb^{2+} follows pseudo-second-order kinetic (Figures 2.17a and 2.17b). A plausible mechanism for Pb^{2+} adsorption on the surface of the **CS-PVA-IL** gel is shown in Figure 15C. From the optimization data, it can be concluded that IL plays a pivotal role for excellent swelling of **CS-PVA-IL** gel. More is the swelling higher will be the adsorption of Pb^{2+} . Experimentally, it was also observed that percentage of Pb^{2+} adsorption decreased without inclusion of IL onto the **CS-PVA-IL** gel, and percentage of Pb^{2+} decreased to 68 %.

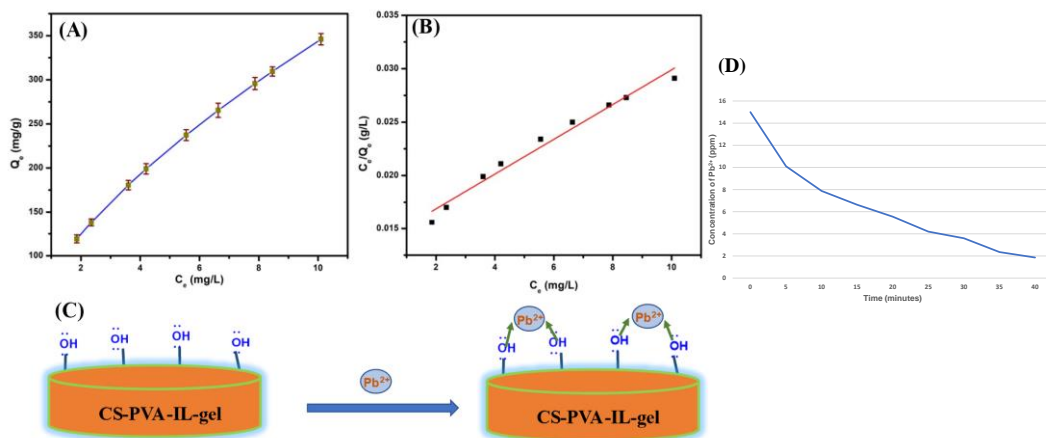


Figure 2.17. A and B) Freundlich-adsorption-isotherm model for adsorption of Pb^{2+} , C) plausible mechanism for the adsorption of Pb^{2+} on the **CS-PVA-IL** gel surface, and D) decreasing Pb^{2+} concentrations at different intervals.

2.4.12 Oil recovery

The conventional process for the separation of oil from an oil–water mixture involves multiple steps and complex procedures. Herein, the **CS–PVA–IL** gel was applied to recover oil from a biphasic solution of mustard oil and water. The oil–water mixture was poured into a tube filled with hydrogel. Quickly water permeated through the gel and dropped into the beaker below and meanwhile oil remained onto the surface of CS–PVA–IL hydrogel. After oil separation (Figure 2.18), the adsorbed oil was collected via mechanical squeezing. This method has several advantages over previously reported methods, including non-toxicity, economic stability, biodegradability, excellent oil-separation efficiency, recyclability, and facile handling.

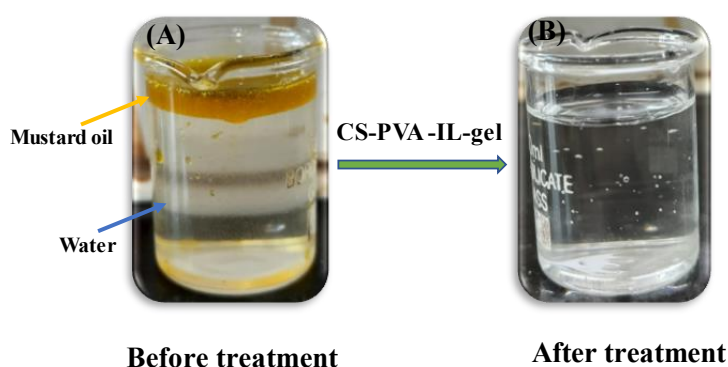


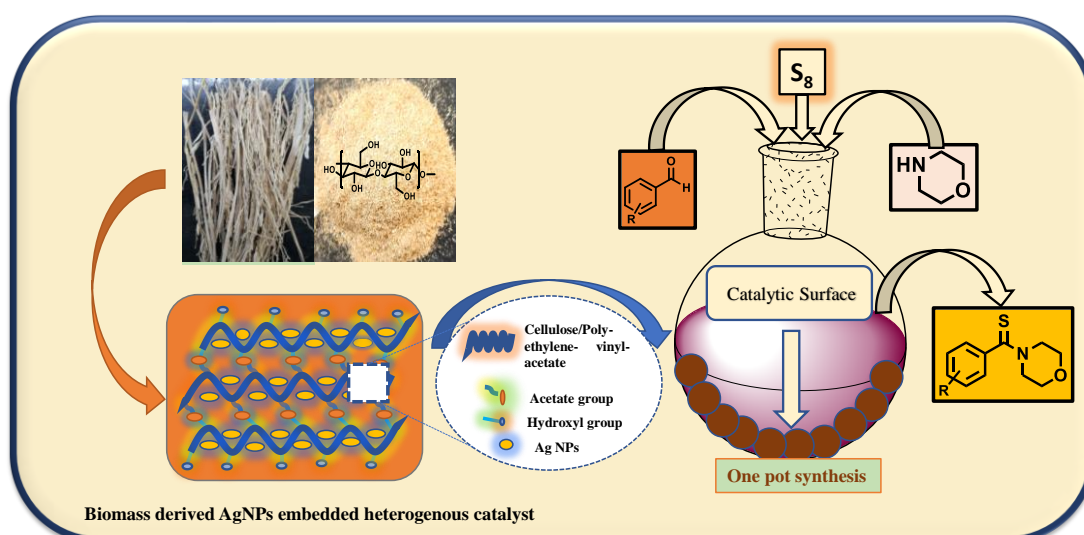
Figure 2.18. Images of a) biphasic oil–water (before treatment) and b) water treated using the **CS–PVA–IL** gel.

2.5 Conclusion

A **CS–PVA–IL** gel was prepared from CS, PVA, and an IL. The swelling properties of the hydrogels were optimized by varying the solvent, pH, time, and temperature, and the maximum swelling of the optimized hydrogel was 330 %. The hydrogel was applied in the removal of toxic organic dyes, toxic anions, Pb^{2+} , nitrite, and oil from contaminated water. The hydrogel effectively removed up to 97 % of the dye and 88 % Pb^{2+} and could be reused for 8 cycles after methanol washing without significant activity losses. The adsorption capacity (mg/g) for removing dye and Pb^{2+} are 1062 mg/g and 346 mg/g, respectively. The adsorbed oil was easily collected via mechanical squeezing. This material is biodegradable, affording an eco-friendly approach for environmental remediation.

Chapter 3A

Cellulose-reinforced polymer (PEVA) supported silver nanoparticles (AgNPs) with excellent catalytic properties: the synthesis of thioamides via Willgerodt-Kindler Reaction



Singh, A.; Saini, S.; Singh, N.; Kaur, N.; Jang, D. O. *RSC Adv* 2022, *12*, 6659–6667.

3a.1 Aim and Objectives

Heterogeneous catalysts play a critical role in organic synthesis and environmental remediation and are mainly synthesized with the inclusion of metal and metal oxide nanoparticles. In lieu of the importance of heterogeneous catalysts, this study focuses on the synthesis of green and cost-effective catalysts from biopolymers and is further applied to carry out Willgerodt–Kindler reaction for synthesis of thioamides. In this context, cellulose was extracted from rice straw, and a highly active solid-supported catalytic model was developed. First, cellulose was conjugated with poly(ethylene-co-vinyl acetate) (PEVA), and then Ag nanoparticles (AgNPs) were inserted into the cellulose–PEVA composite. The process involved the reduction of AgNPs in the presence of sodium borohydride. Thereafter, the obtained hybrid was used as a catalyst for the Willgerodt–Kindler reaction of aromatic aldehydes, amines, and elemental sulfur to synthesize thioamides with excellent yields. The developed catalytic system exhibited high stability and recyclability.

3a.2 Introduction

Recently, thioamides have garnered increasing attention in the field of medicinal chemistry owing to their broad biological activity range. Thioamide derivatives, which are critical components of many biologically important entities, exhibit remarkable antioxidant, antimicrobial, anticonvulsant, antithyroid, and anticarcinogenic properties [1-4]. Moreover, owing to their unique characteristics, namely their varying bond lengths and bond rotation ability, thioamides are better candidates than amides for peptidomimetics [5-8]. Several thioamide synthesis methods have been developed. Among them, the Willgerodt–Kindler reaction, which involves the reaction of an aryl ketone/aldehyde with an amine in the presence of elemental S, is an economical method for thioamide fabrication [9-12]. However, the Willgerodt–Kindler reaction presents several disadvantages, including low product yields and long reaction times; moreover, purification of the desired product from the reaction mixture is difficult. Several approaches have been used to overcome these limitations [13-15]. The Willgerodt–Kindler reaction has been modified using additives, such as $K_2S_2O_8$, $C_{12}H_{25}SH$, K_3PO_4 , $TsOH$, $Na_2S \cdot 9H_2O$, K_2CO_3 , and β -CD, to improve reaction efficiency [16-22]. Furthermore, environmentally benign reaction conditions have been developed, such as

solvent-less and catalyst-free conditions; in addition, water or glycerol was used as the solvent [23-24]. However, these modifications decreased the reaction yield and prolonged the reaction time. In terms of green and sustainable chemistry, the development of a sustainable catalyst that can be recovered and subsequently reused is a priority for Willgerodt–Kindler reaction researchers.

Heterogeneous catalysts are more easily recovered from reaction systems than homogeneous catalysts [25]. Moreover, metal nanoparticles (NPs) play important roles in various organic synthesis reactions [26]. However, the direct use of metal NPs can cause significant human health and environmental problems [27]. Therefore, heterogeneous metal NPs that are attached to solid supports are required for catalysts with facile recovery and good reusability [28]. Biopolymers, including starch, gelatin, cellulose, chitosan, and sodium alginate, serve as solid supports for heterogeneous catalysts and exhibit remarkable catalytic ability during organic synthesis [29]. Cellulose is primarily found in plants and also in some animals and bacteria [30]. Because of the spherical and porous beads of cellulose, its catalytic efficacy can be significantly increased via the insertion of metal ions and NPs into its matrix [31]. Moreover, chemically modified hydrophobic cellulose has been increasingly used [32]. The cross-linking properties and large cavity sizes of biopolymers promote the insertion of metals with high binding energies [33]. In addition, the primary drawbacks of biopolymers, such as their low water solubility, can be overcome via chemical modification [34].

Cellulose has been used to enforce polymer composites because of its high mechanical strength, low density, high surface area, and non-covalent interactions [35-40]. In this study, to achieve remarkable thermal stability and high surface area, cellulose was grafted with the PEVA copolymer. The vinyl acetate (VA) content of PEVA ranged between 3 % and 40 % (w/w), and the mechanical and chemical properties of PEVA depended on its VA content. Thereafter, Ag nanoparticles (AgNPs) were anchored to the cellulose-reinforced PEVA to obtain AgNPs@cellulose–PEVA, which was used as an efficient and sustainable heterogeneous catalyst for the synthesis of thioamides using the Willgerodt–Kindler reaction. The developed catalyst presented high thermal stability and remarkable mechanical strength and was recycled for more than eight cycles without catalytic activity loss.

3a.3 Experimental Section

3a.3.1 General information

All the chemicals were purchased from Sigma-Aldrich Co and were used as received without further purification. A PEVA copolymer with a VA content of 12 wt.% was used as the composite matrix. Melting points were measured using an SMP30 (BIBBY) melting point meter. Fourier-transform infrared (FTIR) spectra were recorded using a Hyperion 2000 (Bruker Optics) FTIR system. A JEOL instrument operated at 400 and 100 MHz was used to obtain ^1H nuclear magnetic resonance (NMR) and ^{13}C NMR spectra. The chemical shifts were measured in parts per million using a deuterated solvent as the internal reference. High-resolution mass spectroscopy (HRMS) was performed using a Xevo G2-XS QTOF (WATERS) mass spectrometer. Scanning electron microscopy (SEM) was performed using a LEO Supra 55 VP (Zeiss) instrument. Powder X-ray diffraction (PXRD) measurements were performed using a Miniflex (Rigaku) diffractometer. Energy-dispersive X-ray spectrometry (EDX) analysis was performed using a JSM-6610-LV (JEOL) instrument. Digital images of the components of the hybrid catalyst were obtained using a smartphone and were utilized for RGB analysis employing the Image J software. Tensile tests were performed using a UTM (INSTRON) tensile tester without an extensometer at 25 °C. The samples used for the tensile tests were 3.20 mm wide and 7.20 mm thick, and their calculated surface area was 23 mm².

3a.3.2 Cellulose isolation from rice straw

Rice straw was cut into small pieces and passed through a 0.5 mm sieve. The obtained mixture was added to distilled water and stirred for 2 d at 50 °C. The obtained solid fraction was washed three times with distilled water, followed by drying. Cellulose was extracted using a literature-reported method, as follows [44]: the lignin and hemicellulose fractions of rice straw were removed, followed by alkaline treatment. A 150 mL aqueous solution comprising sodium chlorite (NaClO_2 ; 1.50 g) and acetic acid (CH_3COOH ; 0.3 mL) was added to the dried rice straw sample (4 g) in a 250 mL round-bottom flask. The mixture was heated at 75 °C for 2 h, and delignification was repeated three times by adding 1.50 g of NaClO_2 and 0.3 mL of CH_3COOH every hour. The solid residue was extracted and washed with distilled water to a neutral pH. Lastly, the dried

solid residue was heated to 80–85 °C in 200 mL of a 4.5 wt.% potassium hydroxide solution for 2 h, followed by washing four times with distilled water.

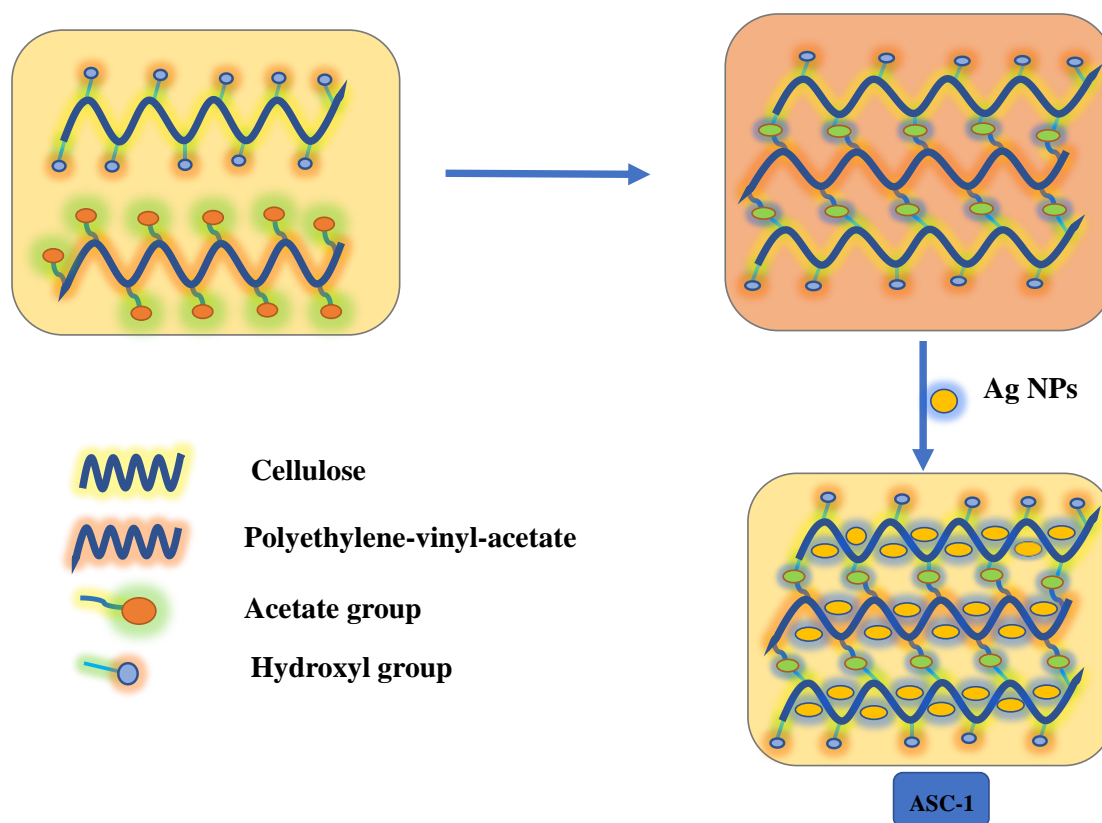
3a.3.3 Preparation of the AgNPs@cellulose–PEVA hybrid

3a.3.3.1 Preparation of cellulose-PEVA

PEVA (1 g) was dissolved in CHCl_3 (10 mL) at 55 °C. Thereafter, cellulose (0.2 g) was added to the solution in the presence of the catalytic amount of sulfuric acid. The mixture was stirred for 3 h to homogeneity, followed by transfer to a Petri dish and air-drying.

3a.3.3.2 Preparation of AgNPs

A 50 μM citric acid solution (1 mL) was added to a 0.64 mM AgNO_3 solution (39 mL), and the mixture was stirred for 30 min to homogeneity. Next, a 25 mM NaBH_4 solution (10 mL) was added dropwise to the solution until it turned gray, indicating the formation of AgNPs. Lastly, to prepare the AgNPs@cellulose–PEVA hybrids, the cellulose–PEVA mixture was added to the AgNP dispersion, and the blend was allowed to react for 12 h to ensure the adsorption of AgNPs on the surface of the cellulose–PEVA composite. The positively charged silver nanoparticles were embedded over the cellulose-PEVA backbone through physical and electrostatic interactions. Thereafter, AgNPs@cellulose–PEVA was separated via centrifugation (Scheme-3a.1). Spectroscopy testing confirmed that the AgNPs were dispersed on the surface of the cellulose–PEVA composite.



Scheme 3a.1. - Schematic representation of synthesis of a catalytic system (ASC-1).

3a.3.3. Catalytic activity of the AgNPs@cellulose–PEVA hybrids for the Willgerodt–Kindler reaction

A mixture of aldehyde (1 mmol), morpholine (1.2 mmol), and elemental S (1.2 mmol) reactants and AgNPs@cellulose–PEVA catalyst (5 mg) in dimethylformamide (DMF; 10 mL) was stirred at 80 °C for 2.5 h. After reaction completion, which was confirmed using thin-layer chromatography, the residue was separated by concentrating the organic layer over an evaporator. Lastly, the residue was purified via column chromatography to isolate the final product and characterized through NMR and HRMS spectroscopy (Figure 3a.1-3a.3).

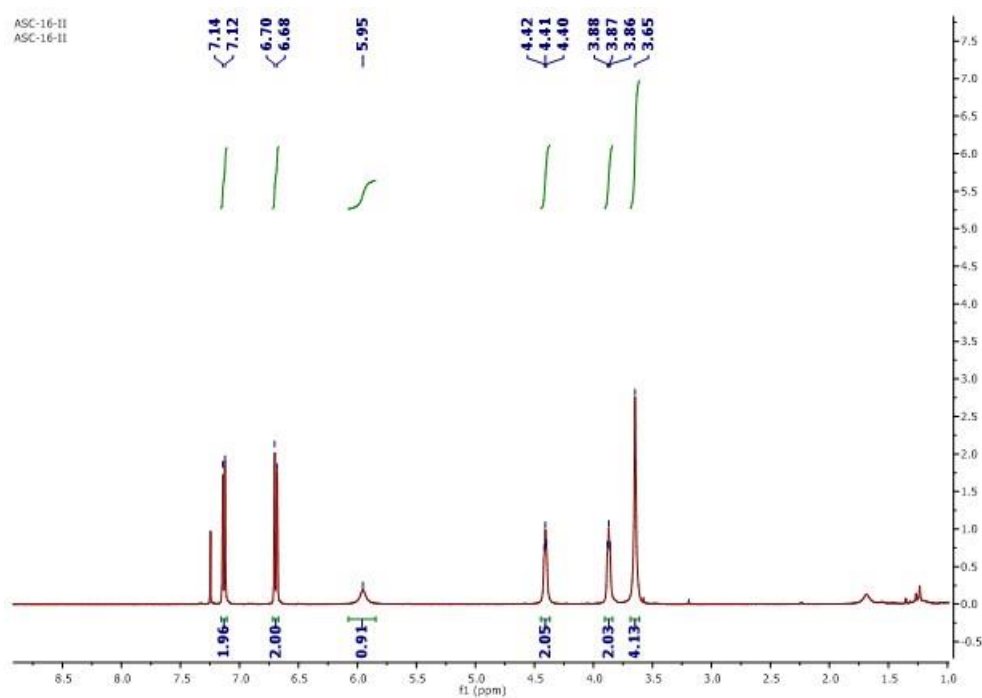


Figure 3a.1. ^1H NMR (CDCl_3) of 1.

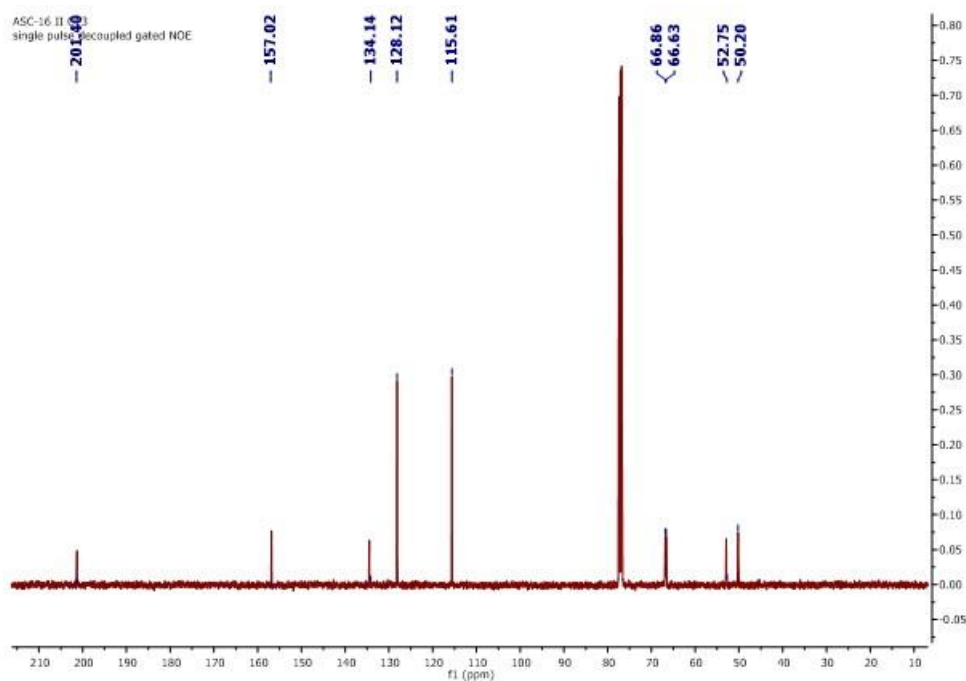


Figure 3a.2. ^{13}C NMR (CDCl_3) of 1.

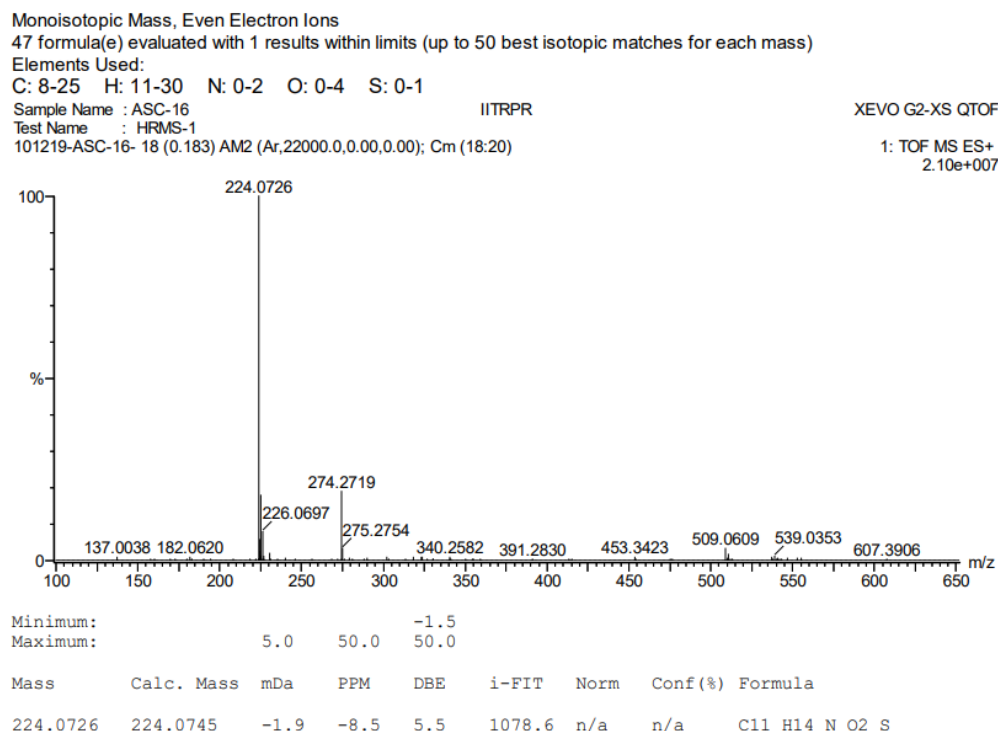


Figure 3a.3. HRMS of **1**.

4-Hydroxyphenyl-morpholine-methanethione (**1**) [45] ^1H NMR (400 MHz, CDCl_3) δ 7.16–7.1(d, J = 8.3 Hz, 2H Ar–H), 6.71–6.68 (d, J = 8.1 Hz, 2H, Ar–H), 6.01–5.59 (s, 1H –OH), 4.47–4.38 (t, J = 3.8 Hz, 2H –CH₂), 3.91–3.84 (t, J = 3.65 Hz, 2H, –CH₂), 3.69–3.61 (s, 4H, 2xCH₂). ^{13}C NMR (100 MHz, CDCl_3), δ 201.4, 157.0, 134.2, 128.1, 115.6, 66.9, 66.6, 52.75, 50.2. HRMS: [M+H]: calculated: 224.0726, found: 224.0746.

2-Hydroxyphenyl-morpholine-methanethione (**2**) [45] ^1H NMR (400 MHz, CDCl_3) δ 6.85–6.80 (d, J = 8.5 Hz, 1H Ar–H), 6.49–6.45 (d, J = 1.9, Hz 1H, Ar–H), 6.38–6.35 (d, J = 2.1, Hz 1H, Ar–H), 6.34–6.32 (d, J = 1.8 Hz, 1H, Ar–H) 4.06–4.01 (s, 1H –OH), 3.87–3.70 (m, 6H, –CH₂), 3.51–3.43 (dd, J = 14.3 Hz, 1H, –CH₂), 2.98–2.86 (d, J = 19.7 Hz, 1H, –CH₂). ^{13}C NMR (100 MHz, CDCl_3), δ 207.4, 154.4, 131.3, 126.5, 125.9, 66.8, 31.05. HRMS: [M+H]: calculated: 224.0745, found: 224.0746.

3-Hydroxyphenyl-morpholine-methanethione (**3**) [46] ^1H NMR (400 MHz, CDCl_3) δ 7.21–7.13 (t, J = 7.7 Hz, 1H–Ar–H), 6.73 (d, J = 7.0 Hz, 2H, Ar–H), 6.04–6.74 (s, 1H, –OH), 4.45–4.37 (t, J = 7.7 Hz, 2H, –CH₂), 3.91–3.84 (t, J = 6.71 Hz, 2H, –CH₂), 3.605 (m, 4H, 2x–CH₂). ^{13}C NMR (100 MHz, CDCl_3), δ 200.5, 155.8, 143.2, 130.1, 117.2, 115.9, 112.9, 66.9, 66.6, 52.5, 49.5. HRMS: [M+H]: calculated: 224.0738, found: 224.0745.

2,4-Dimethoxyphenyl-morpholine-methanethione (**4**) ^1H NMR (400 MHz, CDCl_3) δ 7.27–7.24 (d, $J = 4.5$ Hz, 1H Ar–H), 6.51–6.48 (d, $J = 10.5$ Hz, 1H, Ar–H), 6.39–6.38 (s, 1H, Ar–H), 4.46–4.41 (dd, $J = 9.0$ Hz, $J = 4.7$ Hz, 2H, $-\text{CH}_2$), 3.79 (s, 6H, $-\text{CH}_3$), 3.70–3.65 (dd, $J = 9.0$ Hz, $J = 4.9$ Hz, 1H, $-\text{CH}_2$), 3.60–3.54 (dd, $J = 8.0$ Hz, $J = 5.4$ Hz, 1H, $-\text{CH}_2$), 3.53–3.49 (dd, $J = 6.5$ Hz, $J = 3.0$ Hz, 1H, $-\text{CH}_2$), 3.48–3.39 (m, 2H $-\text{CH}_2$). ^{13}C NMR (100 MHz, CDCl_3), δ 199.1, 161.7, 153.8, 130.2, 124.6, 105.3, 98.4, 66.6, 55.7, 51.9, 49.5. HRMS: $[\text{M}+\text{H}]$: calculated: 261.1001, found: 261.1007.

4-Hydroxy-3-methoxyphenyl-(morpholinomethanethione) (**5**) [47] ^1H NMR (400 MHz, CDCl_3) δ 6.95–6.92 (d, $J = 2.0$ Hz, 1H Ar–H), 6.85–6.82 (s, 1H, Ar–H), 6.76–6.72 (d, $J = 2.0$ Hz 1H, Ar–H), 5.85–5.76 (s, 1H, $-\text{OH}$), 4.44–4.37 (s, 2H, $-\text{CH}_2$), 4.0–3.88 (s, 3H $-\text{CH}_3$), 3.88–3.84 (t, $J = 3.9$ Hz 2H, $-\text{CH}_2$), 3.71–3.61 (d, $J = 2.9$ Hz, 4H, $-\text{CH}_2$). ^{13}C NMR (100 MHz, CDCl_3), δ 201.2, 146.7, 146.5, 134.5, 119.1, 114.0, 110.4, 66.9, 66.6, 56.1, 53.0, 50.2. HRMS: $[\text{M}+\text{H}]$: calculated: 254.0851, found: 254.0832.

4-Dimethylaminophenyl-morpholine-methanethione (**6**) [46] ^1H NMR (400 MHz, CDCl_3) δ 7.30–7.25 (d, $J = 8.4$ Hz, 2H Ar–H), 7.63–7.58 (d, $J = 8.6$ Hz, 2H, Ar–H), 4.54–4.27 (dd, $J = 7.3$ Hz, 2H, $-\text{CH}_2$), 3.91–3.60 (d, $J = 18.6$ Hz, 6H, $-\text{CH}_2$), 2.98–2.96 (s, 6H $-\text{CH}_3$). ^{13}C NMR (100 MHz, CDCl_3), δ 202.28, 151.31, 129.78, 128.80, 111.15, 66.85, 53.15, 50.13, 40.35. HRMS: $[\text{M}+\text{H}]$: calculated: 251.1218, found: 251.1203.

Morpholino(phenyl)-methanethione (**7**) [48] ^1H NMR (400 MHz, CDCl_3) δ 7.37–7.35 (t, $J = 7.66$ Hz, 1H Ar–H), 7.35–7.31 (d, $J = 5.21$ Hz, 2H, Ar–H), 7.29–7.26 (t, $J = 7.45$ Hz, 1H, Ar–H), 7.26–7.25 (t, $J = 7.39$ Hz, 1H, Ar–H), 4.47–4.37 (t, $J = 4.1$ Hz, 2H, $-\text{CH}_2$), 3.92–3.82 (t, $J = 4.05$ Hz, 2H, $-\text{CH}_2$), 3.68–3.61 (t, $J = 4.0$ Hz, 2H $-\text{CH}_2$), 3.61–3.54 (t, $J = 4.0$ Hz, 2H $-\text{CH}_2$). ^{13}C NMR (100 MHz, CDCl_3), δ 201.1, 142.5, 129.0, 128.7, 126.0, 66.8, 66.6, 52.6, 49.6. HRMS: $[\text{M}+\text{H}]$: calculated: 208.0796, found: 208.0797.

4-Fluoro-morpholine-methanethione (**8**) [49] ^1H NMR (400 MHz, CDCl_3) δ 8.13–8.12 (d, $J = 3.2$ Hz, 1H Ar–H), 7.30–7.28 (d, $J = 5.3$ Hz, 1H, Ar–H), 7.15–7.13 (d, $J = 8.6$ Hz, 1H, Ar–H), 7.07–7.03 (d, $J = 8.5$ Hz, 1H, Ar–H), 4.43–4.40 (t, $J = 4.9$ Hz, 1H, $-\text{CH}_2$), 3.92–3.83 (d, $J = 4.8$ Hz, 2H, $-\text{CH}_2$), 3.67–3.61 (t, $J = 4.4$ Hz, 2H $-\text{CH}_2$), 3.61–3.56 (t, $J = 8.8$ Hz, 2H, $-\text{CH}_2$), 3.19–3.15 (t, $J = 7.7$ Hz, 1H, $-\text{CH}_2$). ^{13}C NMR (100 MHz, CDCl_3), δ 200.11, 170.8, 167.7, 132.9, 128.3, 125.6, 115.7, 66.8, 52.7, 49.8, 44.3. HRMS: $[\text{M}+\text{H}]$: calculated: 226.0702, found: 226.0699.

1,3-Phenylenebis(morpholinomethanethione) (**9**) [50] ^1H NMR (400 MHz, CDCl_3) δ 7.38–7.32 (t, $J = 7.0$ Hz, 1H, Ar–H), 7.28–7.23 (d, $J = 2.9$ Hz, 2H, Ar–H), 7.22–7.19 (s,

1H, Ar-H), 4.45–4.34 (t, $J = 4.3$ Hz, 4H, $-\text{CH}_2$), 3.89–3.82 (t, $J = 4.8$ Hz, 4H, $-\text{CH}_2$), 3.67–3.56 (d, $J = 15.1$ Hz, 8H, $-\text{CH}_2$). ^{13}C NMR (100 MHz, CDCl_3), δ 199.4, 142.6, 129.0, 128.9, 126.4, 123.9, 66.8, 66.6, 52.7, 49.7. HRMS: $[\text{M}+\text{H}]$: calculated: 337.1044, found: 337.1019.

2-Hydroxy-5-nitro-phenyl-(morpholinomethanethione) (**10**) ^1H NMR (400 MHz, CDCl_3) δ 11.55 (s, 1H, $-\text{OH}$), 8.09–8.04 (d, $J = 11.9$ Hz, 1H, Ar-H), 8.0–7.98 (s, 1H, Ar-H), 6.99–6.95 (d, $J = 9.1$ Hz, 1H, Ar-H), 4.37–4.30 (dd, $J = 16.5$ Hz, $J = 4.5$ Hz, 1H, $-\text{CH}_2$), 4.21–4.14 (dd, $J = 16.7$ Hz, $J = 4.8$ Hz, 1H, $-\text{CH}_2$), 3.74–3.69 (t, $J = 4.9$ Hz, 2H, $-\text{CH}_2$), 3.58–3.52 (dd, $J = 10.3$ Hz, $J = 5.2$ Hz, 2H, $-\text{CH}_2$), 3.45–3.39 (t, $J = 4.4$ Hz, 2H, $-\text{CH}_2$). ^{13}C NMR (100 MHz, CDCl_3), δ 192.9, 157.5, 140.0, 130.7, 126.2, 126.3, 66.5, 66.1, 52.3, 49.3. HRMS: $[\text{M}+\text{H}]$: calculated: 269.0596, found: 269.05967.

3-Nitrophenyl-morpholine-methanethione (**11**) [46] ^1H NMR (400 MHz, CDCl_3) δ 8.20–8.18 (s, 1H, Ar-H), 8.15–8.10 (d, $J = 9.0$ Hz, 1H, Ar-H), 7.63–7.59 (d, $J = 7.6$ Hz, 1H, Ar-H), 7.58–7.53 (t, $J = 7.8$ Hz, 1H, Ar-H), 4.44–4.41 (t, $J = 4.7$ Hz, 2H, $-\text{CH}_2$), 3.91–3.89 (t, $J = 4.8$ Hz, 2H, $-\text{CH}_2$), 3.68–3.65 (t, $J = 4.6$ Hz, 2H, $-\text{CH}_2$), 3.59–3.57 (t, $J = 4.3$ Hz, 2H, $-\text{CH}_2$). ^{13}C NMR (100 MHz, CDCl_3), δ 197.3, 148.3, 143.8, 131.8, 130.0, 123.6, 121.1, 66.7, 66.53, 52.8, 49.6. HRMS: $[\text{M}+\text{H}]$: calculated: 253.0634, found: 253.0647.

(1H-imidazole-4-yl) (morpholino)methanethione (**12**) ^1H NMR (400 MHz, $\text{DMSO}-\text{D}_6$) δ 12.48 (s, 1H), 7.67 (s, 1H), 4.17 (t, $J = 17.8$ Hz, 2H), 3.59 (t, $J = 15.6$ Hz, 6H). ^{13}C NMR (100 MHz, $\text{DMSO}-\text{D}_6$), 189.9, 142.3, 135.1, 125.1, 67.1, 66.6, 53.0, 51.0. HRMS: $[\text{M}+\text{H}]$: calculated: 198.0701, found: 198.0689.

2-Hydroxy-N-phenylbenzothioamide (**13**) ^1H NMR (400 MHz, $\text{DMSO}-\text{D}_6$) δ 12.11 (s, 1H), 9.89 (s, 1H), 8.35 (t, $J = 3.0$ Hz, 1H), 8.25 (d, $J = 3.1$ Hz, 1H), 8.05 (d, $J = 7.3$ Hz, 1H), 7.46 (t, $J = 1.3$ Hz, 2H), 7.30 (t, $J = 7.0$ Hz, 1H), 7.22 (d, $J = 1.1$ Hz, 1H), 7.19 (dd, $J = 3.2, 1.6$ Hz, 1H), 7.15 (d, $J = 1.3$ Hz, 1H). ^{13}C NMR (100 MHz, $\text{DMSO}-\text{D}_6$), 185.5, 139.1, 137.6, 134.1, 126.8, 124.6, 124.0, 122.7, 121.3, 118.7, 113.0. D-Mass $[\text{M}+\text{H}]$: calculated: 230.2552, found 230.2561.

2-hydroxy-N-(4-nitrophenyl)benzothioamide (**14**) ^1H NMR (400 MHz, CDCl_3) δ 8.64 (s, 1H), 8.64 (s, 1H), 8.27 (d, $J = 2.6$ Hz, 1H), 8.24 (d, $J = 2.6$ Hz, 1H), 8.03 (d, $J = 8.2$ Hz, 1H), 7.96 (d, $J = 7.6$ Hz, 1H), 7.56 (t, $J = 7.7$ Hz, 1H), 7.49 (t, $J = 7.1$ Hz, 1H), 7.20 (d, $J = 5.1$ Hz, 1H), 7.18 (d, $J = 5.6$ Hz, 1H). ^{13}C NMR (100 MHz, $\text{DMSO}-\text{D}_6$), 172.5,

161.7, 150.4, 136.2, 132.6, 132.2, 131.7, 130.8, 119.7, 117.6, 116.7, 115.6, 113.4. D-Mass [M+H]: calculated: 275.2318, found 275.2350.

3a.4 Result and Discussion

3a.4.1 FTIR spectroscopic analysis

In the FTIR spectrum of PEVA, the characteristic bands of VA emerged at 1736, 1236, and 1017 cm^{-1} , whereas the bands of the ethylene group were observed at 2918, 2848, 1469, 1373, and 720 cm^{-1} (Figure 3a.4a). The primary bands at 3308, 1632, and 1027 cm^{-1} in the FTIR spectrum of cellulose were ascribed to the stretching and bending of the O–H bonds and the stretching of the skeletal C–O–C pyranose ring, respectively (Figure 3a.4b). The VA bands shifted from 1737, 1236, and 1017 cm^{-1} in the FTIR spectrum of PEVA to 1735, 1230, and 1015 cm^{-1} , respectively, in the FTIR spectrum of the cellulose–PEVA composite (Figure 3a.4c). Moreover, the width and intensity of the band at 3600–3000 cm^{-1} , which was attributed to the O–H vibration, increased, indicating that the –OH groups on the cellulose surface and the polar VA groups of PEVA interacted. Upon the addition of AgNPs to the cellulose–PEVA composites, the intensity of the band at 3264 cm^{-1} , which corresponded to the O–H vibration, decreased significantly. Moreover, the bands at 2915 and 2845 cm^{-1} , which were ascribed to the methylene groups, and the band at 1735 cm^{-1} , which was attributed to the vibration of the carbonyl bonds of the acetate groups, shifted to 2920, 2855, and 1720 cm^{-1} , respectively (Figure 3a.4d). These results indicated that the AgNPs interacted with the cellulose–PEVA composites, and in particular, the –OH groups of cellulose played a critical role in immobilizing the AgNPs and preventing their aggregation via hydrogen bonding [41].

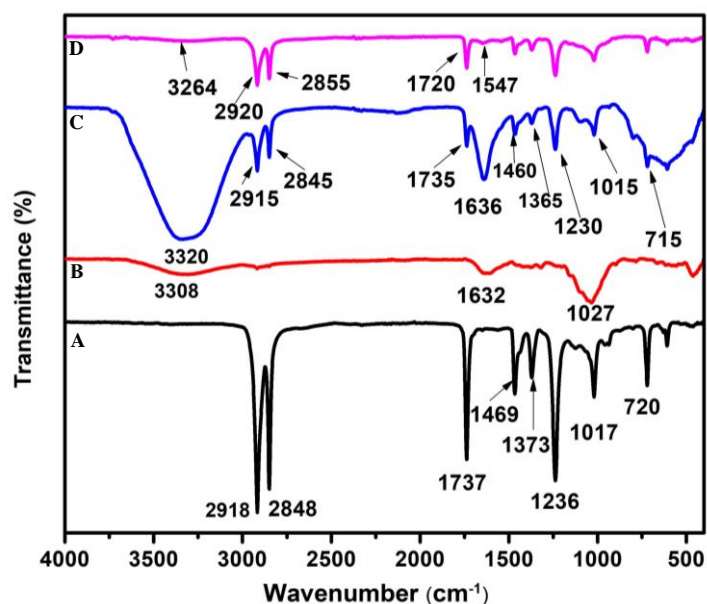


Figure 3a.4. Fourier-transform infrared spectra of (A) poly(ethylene-co-vinyl acetate) (PEVA), (B) cellulose, (C) cellulose–PEVA composite, and (D) AgNPs@cellulose–PEVA hybrid.

3a.4.2 PXRD Analysis

The characteristic peaks at 16.04° , 22.46° , and 34.38° , which corresponded to the (110), (200), and (004) lattice planes of cellulose, respectively, were observed in the PXRD patterns of raw and treated cellulose (Figure 3a.5a and 3a.5b, respectively). The primary crystalline peak in the PXRD pattern of PEVA, which was observed at 22.46° and presented an intensity of 100 %, confirmed the crystallinity of the polymer. The PXRD patterns of PEVA and the PEVA–cellulose composite are illustrated in Figure 3a.5c and 3a.5d, respectively. The characteristic peaks of PEVA at 21.44° and 23.4° were observed in the PXRD pattern of the cellulose–PEVA composite, indicating that cellulose was grafted with PEVA. These peaks were also observed in the PXRD patterns of the AgNPs@cellulose–PEVA hybrid, indicating that the cellulose–PEVA composite served as the support for the hybrid (Figure 3a.5e). Furthermore, the presence of the peaks at 15.61° , 24.35° , 26.84° , 35.90° , 40.82° , 43.20° , and 54.90° in the PXRD pattern of AgNPs@cellulose–PEVA confirmed the presence of elemental Ag [41]. In addition, the presence of these peaks in the PXRD patterns of the freshly prepared and recovered catalysts confirmed that the catalyst was stable and did not undergo structural changes during the reaction. Moreover, the catalyst was reusable and did not lose its catalytic activity.

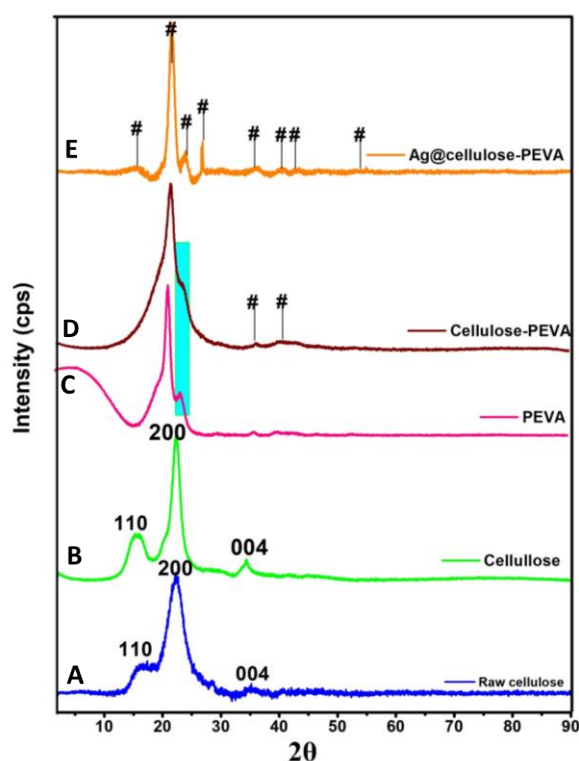


Figure 3a.5. Powder X-ray diffraction patterns of (A) raw cellulose, (B) cellulose, (C) poly(ethylene-co-vinyl acetate) (PEVA), (D) the cellulose–PEVA composite, and (E) AgNPs@ cellulose–PEVA hybrid. Here, # represents the emergence of a new plane.

3a.4.3 SEM and EDX analyses

The SEM images revealed the surface morphologies of the cellulose–PEVA composite and AgNPs@cellulose–PEVA hybrid, which varies from the particle-to-particle arrangement in a sample. The SEM image of cellulose–PEVA revealed that the composite was denser than the AgNPs@cellulose–PEVA hybrid, confirming the presence of AgNPs on the composite matrix surface (Figures 3a.6a and 3a.6c). The SEM image of the AgNPs@cellulose–PEVA hybrid revealed the presence of a crosslinked network in its structure. The mesh-like surface of the cellulose–PEVA composite facilitated the insertion of AgNPs in the crosslinked network and the formation of a heterogeneous catalytic surface for organic reactions. The elemental composition of the cellulose–PEVA composite and AgNPs@cellulose–PEVA hybrid were determined using EDX, and the results are presented in Figures 3a.6b and 3a.6d, respectively. The experimental data indicated that the cellulose–PEVA composite comprised C (76.4 %), O (13.5 %), and Pt (10.2 %), and the AgNPs@cellulose–PEVA hybrid contained C (58.2 %), O (24.5 %), Pt (16.8 %), and Ag (0.24 %). The presence of Pt in the cellulose–

PEVA composite and AgNPs@cellulose-PEVA hybrid was attributed to the Pt coating. Therefore, the EDX results confirmed the presence of Ag in the AgNPs@cellulose-PEVA hybrid.

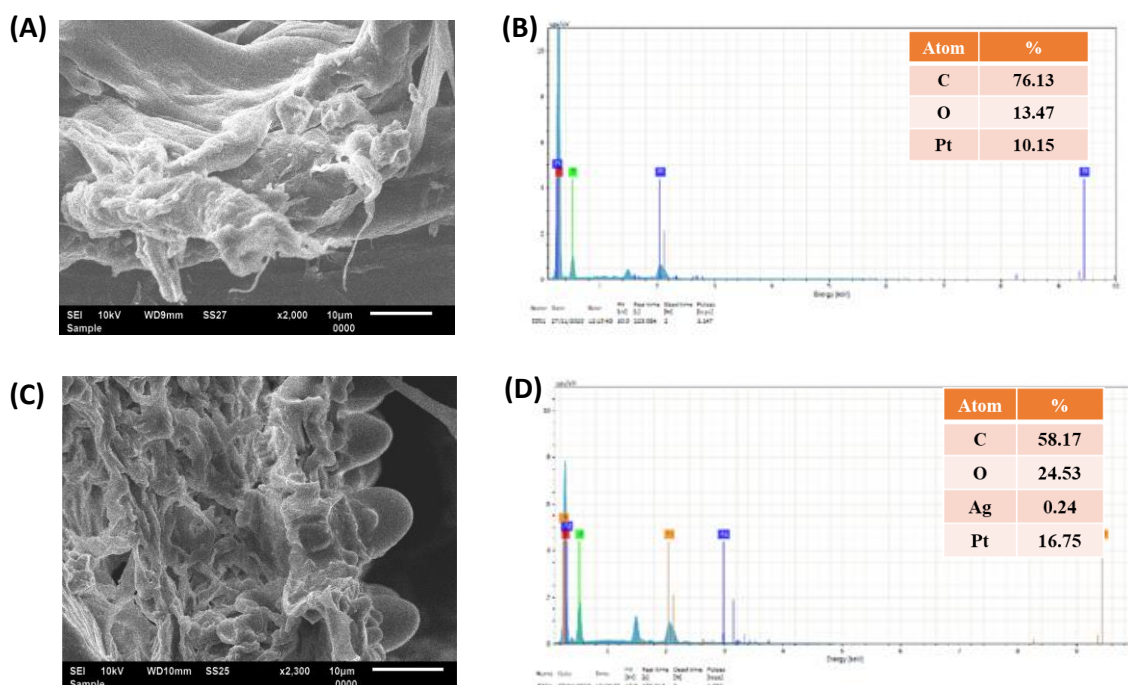


Figure 3a.6. Scanning electron microscopy images of the (A) cellulose–poly(ethylene-co-vinyl acetate) (PEVA) composite and (C) AgNPs@cellulose–PEVA hybrid. Energy-dispersive X-ray mappings of the (B) cellulose–PEVA composite and (D) AgNPs@cellulose–PEVA hybrid.

3a.4.4 RGB analysis

Digital images of the components of the hybrid catalyst were obtained using a smartphone and were used for RGB analysis using the ImageJ software (Figure 3.7). The digital images revealed the changes in color intensity. In the 8-bit digital images, the intensity of each primary color ranged between 0 and 255. Therefore, 256 values were available for the intensity of each color, where 0 represented black. The remaining 255 values indicated the maximum intensities or pure colors. The images turned dark or bright if the numerical values of the components decreased or increased, respectively. The digital images darkened in the following order: rice straw < PEVA < cellulose–PEVA < AgNPs@cellulose–PEVA (Figure 3a.7a). The RGB intensities of rice straw, PEVA, cellulose–PEVA, and AgNPs@cellulose–PEVA indicated that the values of the R-, G-, and B-components decreased in the following order: rice straw > PEVA >

cellulose–PEVA > AgNPs@cellulose–PEVA (Figure 3a.7b)

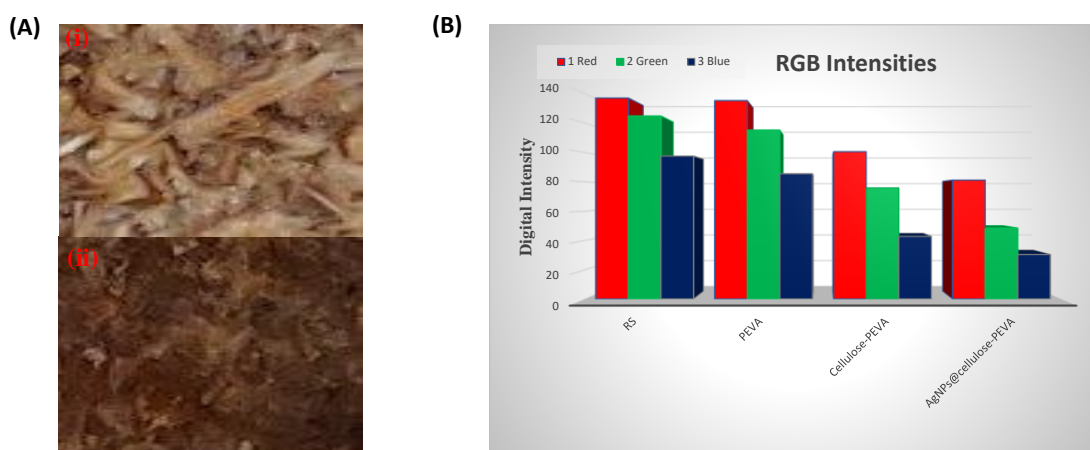


Figure 3a.7. (A) (i) the cellulose–PEVA composite and (ii) the AgNPs@cellulose–PEVA hybrid. (B) Bar graph of the RGB intensities of RS, PEVA, the cellulose–PEVA composite and the AgNPs@cellulose–PEVA hybrid.

3a.4.5 Mechanical Testing

PEVA and the cellulose–PEVA composite were subjected to tensile testing. The strain of PEVA was 68.7 % at a stress of 1.6 MPa and the maximum displacement of PEVA was 25.8 mm at a bearing force of 37.8 N (Figures 3a.8a and 3a.8b). The strain and maximum displacement of the cellulose–PEVA composite were 76 % at 2.3 MPa and 27.4 mm at a force of 53.0 N, respectively (Figure 3a.8c and 3a.8d). These results indicated that the cellulose incorporated in the PEVA matrix reinforced the composite and increased its mechanical strength. Furthermore, mechanical strength impact tests were performed in the Izod and Charpy modes. The impact energies of the AgNPs@cellulose–PEVA hybrid in the Izod and Charpy modes were 1.865 and 5.939 kJ/m, respectively.

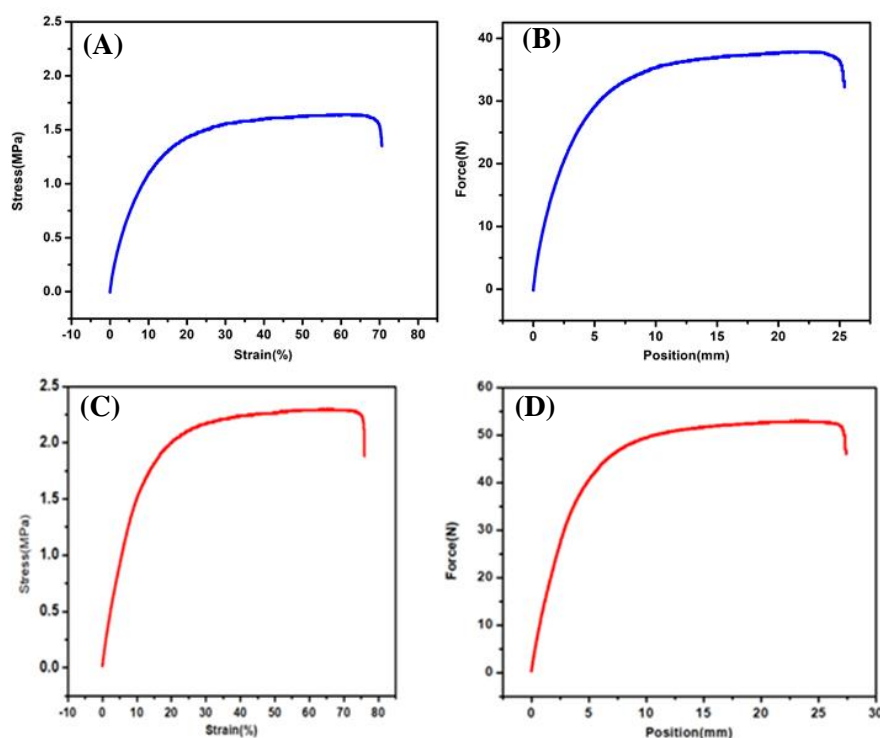
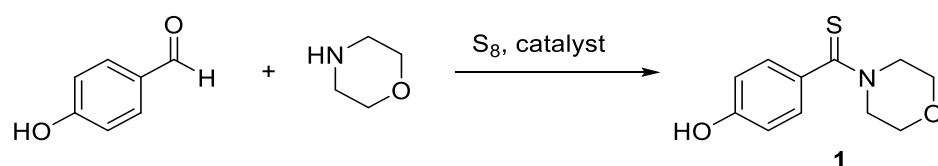


Figure 3a.8. (A) Stress–strain and (B) force–position curves of poly(ethylene-co-vinyl acetate). (C) Stress–strain and (D) force–position curves of the cellulose–poly(ethylene-co-vinyl acetate composite).

3a.4.6 Catalytic activity of the AgNPs@cellulose-PEVA nanohybrid for the Willgerodt–Kindler reaction

The catalytic activity of the AgNPs@cellulose–PEVA hybrid was investigated for the synthesis of thioamides. A one-pot multicomponent reaction using 4-hydroxy-benzaldehyde (1 mmol), morpholine (1.2 mmol), and elemental S (1.2 mmol) was selected as the model reaction (Scheme 3.2). First, the reaction was performed in DMF in the presence of 5 mg of AgNPs@cellulose–PEVA at 110 °C for 6 h, and the yield of the desired product was 71 % (Table 3a.1, entry 1). The yields of the reactions performed over cellulose or the cellulose–PEVA composite were lower (Table 3a.1, entries 2 and 3, respectively). Dimethyl sulfoxide (DMSO) has been reported to act as a promoter for the modified Willgerodt–Kindler reaction [42]. Therefore, in this study, DMSO was used as the solvent for the reaction. The yield of the reaction in DMSO was lower than that of the reaction in DMF (Table 3a.1, entry 4). In addition, when water was used as a non-toxic solvent, the reaction did not proceed (Table 3a.1, entry 5). Furthermore, the yields of the reactions performed in ethanol and tetrahydrofuran were low (Table 3a.1, entries 6 and 7, respectively). Based on these results, DMF was selected as the optimal

solvent for the Willgerodt–Kindler reaction. Next, the reaction performance was monitored by changing the reaction temperature and time. The yield increased with decreasing the reaction temperature and time (Table 3a.1, entries 8–10). Decreasing the amount of catalysts caused a decrease in yield (Table 3a.1, entry 13). The optimal reaction conditions were determined to be 5 mg of catalyst, 80 °C, and 2.5 h (Table 3a.1, entry 11).



Scheme 3a.2. Reaction of benzaldehyde, morpholine, and elemental S in the presence of the AgNPs@cellulose–PEVA hybrid as the catalyst.

Table 3a.1. Optimization of the reaction conditions for the synthesis of thioamides using the Willgerodt–Kindler reaction.

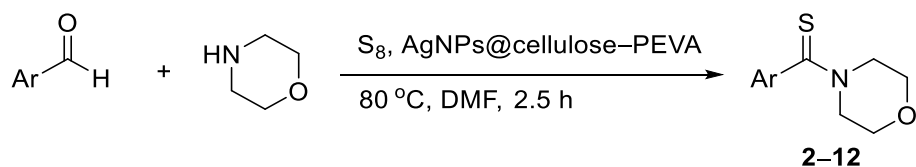
Entry	Catalyst	Solvent	Catalyst (mg)	Temp. (°C)	Time (h)	Yield ^a (%)
1	AgNPs@cellulose–PEVA	DMF	5	110	6	71
2	Cellulose	DMF	5	110	6	43
3	Cellulose–PEVA	DMF	5	110	6	45
4	AgNPs@cellulose–PEVA	DMSO	5	110	6	64
5	AgNPs@cellulose–PEVA	H ₂ O	5	110	6	-
6	AgNPs@cellulose–PEVA	EtOH	5	110	6	37
7	AgNPs@cellulose–PEVA	THF	5	110	6	35
8	AgNPs@cellulose–PEVA	DMF	5	90	6	75

9	AgNPs@cellulose–PEVA	DMF	5	80	6	79
10	AgNPs@cellulose–PEVA	DMF	5	80	4	84
11	AgNPs@cellulose–PEVA	DMF	5	80	2.5	98
12	AgNPs@cellulose–PEVA	DMF	5	80	2	87
13	AgNPs@cellulose–PEVA	DMF	4	80	2.5	85

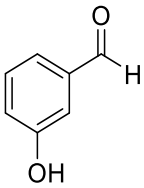
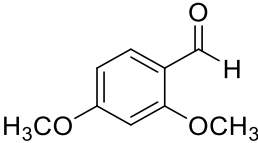
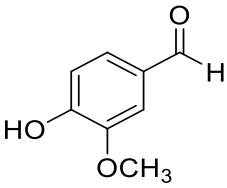
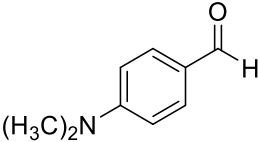
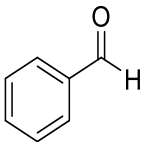
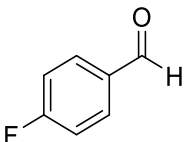
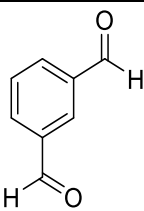
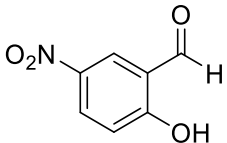
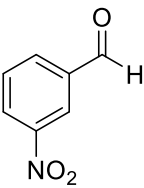
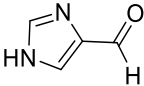
^aIsolated yield. Here, AgNPs, PEVA, DMF, DMSO, EtOH, and THF denote Ag nanoparticles, poly(ethylene-co-vinyl acetate), dimethylformamide, dimethyl sulfoxide, ethanol, and tetrahydrofuran, respectively.

Various aromatic aldehydes were used to synthesize thioamides (Figure A9-A38) using the Willgerodt–Kindler reaction under the optimal reaction conditions to examine the scope and limitations of the reaction. The results are summarized in Table 3a.2. The yields of the reactions using aromatic aldehydes with electron-withdrawing and electron-donating groups were high, indicating substrate generality. However, the product yields of the reactions using aromatic aldehydes with electron-donating groups were higher than those of the reactions using aldehydes with electron-withdrawing groups.

Table 3a.2. Synthesis of various substituted thioamides using the Willgerodt–Kindler reaction and AgNPs@cellulose–PEVA as the catalyst.

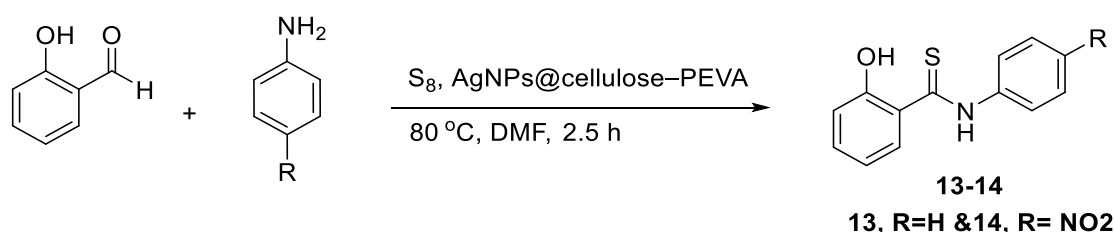


Entry	Aromatic aldehyde	Product	Yield ^a (%)
1		2	94

2		3	89
3		4	91
4		5	87
5		6	88
6		7	93
7		8	90
8		9	86
9		10	85
10		11	83
11		12	84

^aIsolated yield.

Further, to check the electronic effect of aromatic amines, thioamides were synthesized using aniline and 4-nitroaniline. As explained in scheme-3.2, amines play an important role in reaction mechanism first is to open the S₈ ring of elemental sulphur and another is to attack at electrophilic carbonyl carbon, for both attack nucleophilicity of amine is matter importantly. Further, to check the nucleophilicity of amine, aniline was used (Scheme-3.3) in which lone pair at nitrogen participate in resonance with aromatic benzene ring. Delocalization of lone pair with benzene ring diminishes the nucleophilicity of aniline, which results in a low yield (90 %) of thioamide (13). Thereafter, effect of nitro group on aniline (p-nitroaniline) was studied (Scheme-3.3). Nitro group is an electron-withdrawing group, which decreases the electron density at benzene ring via increasing the resonance or mesomeric effect. From the study, it was found that nitro group substituted aniline produced an even lower yield (86 %) of thioamide (14). Thioamide is an important functional group for the synthesis of various natural and biologically important compounds. Thioamides are an excellent class of organic compounds with diverse pharmaceutical activities such as antifungal, antioxidant, antibacterial, antithyroid, antiulcerative, etc. Herein, various thioamides were synthesized (1-14) with excellent yield.



Scheme 3a.3. Reaction of salicylaldehyde, aromatic amines, and elemental Sulphur in the presence of the AgNPs@cellulose–PEVA hybrid as the catalyst.

3a.4.7 Reusability of the AgNPs@cellulose–PEVA hybrid catalyst

The primary advantage of heterogeneous catalysts is their reusability. Regeneration and reusability are attractive features of the developed catalyst in terms of sustainability. The AgNPs@cellulose–PEVA catalyst was easily separated from the reaction mixtures via centrifugation. Subsequently, the AgNPs@cellulose–PEVA catalyst was washed with methanol and water and dried at approximately 55 °C. Thereafter, the recovered catalyst was used for the next catalytic run. The catalyst was highly stable and could be reused for at least eight runs without significant catalytic activity loss, as illustrated in

Figure 3a.9a. The catalyst recovered after five reaction cycles was subjected to SEM analysis. The surface of the recovered catalyst was not significantly different from that of the fresh catalyst, indicating the high recyclability of the AgNPs@cellulose–PEVA catalyst for the synthesis of thioamides. A blank experiment without the AgNPs@cellulose–PEVA catalyst was performed at 80 °C. The efficiencies of the reactions performed with and without a catalyst were the same over the first 60 min. However, as the reaction time was increased, the efficiency of the reaction without the AgNPs@cellulose–PEVA catalyst was low; moreover, the reaction was not complete even after 160 min, and the product yield was only 45 %. These results indicated that the AgNPs@cellulose–PEVA catalyst was critical for an efficient reaction (Figure 3a.9b).

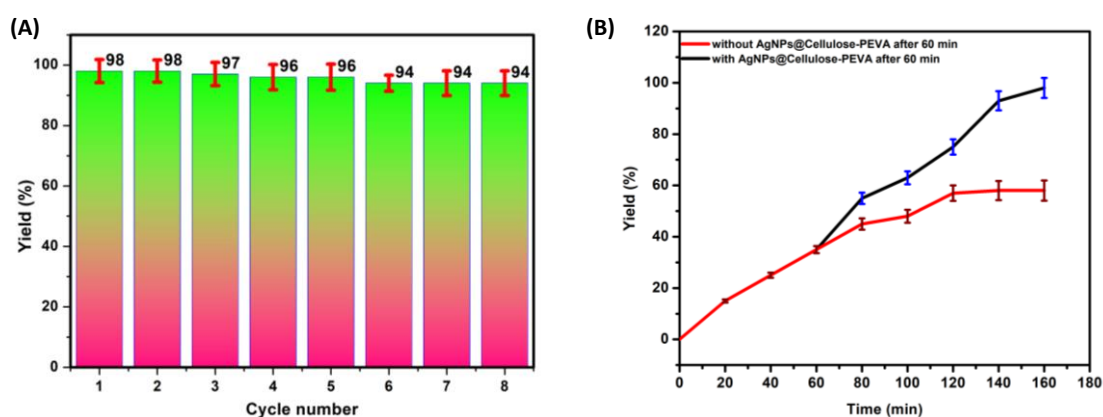
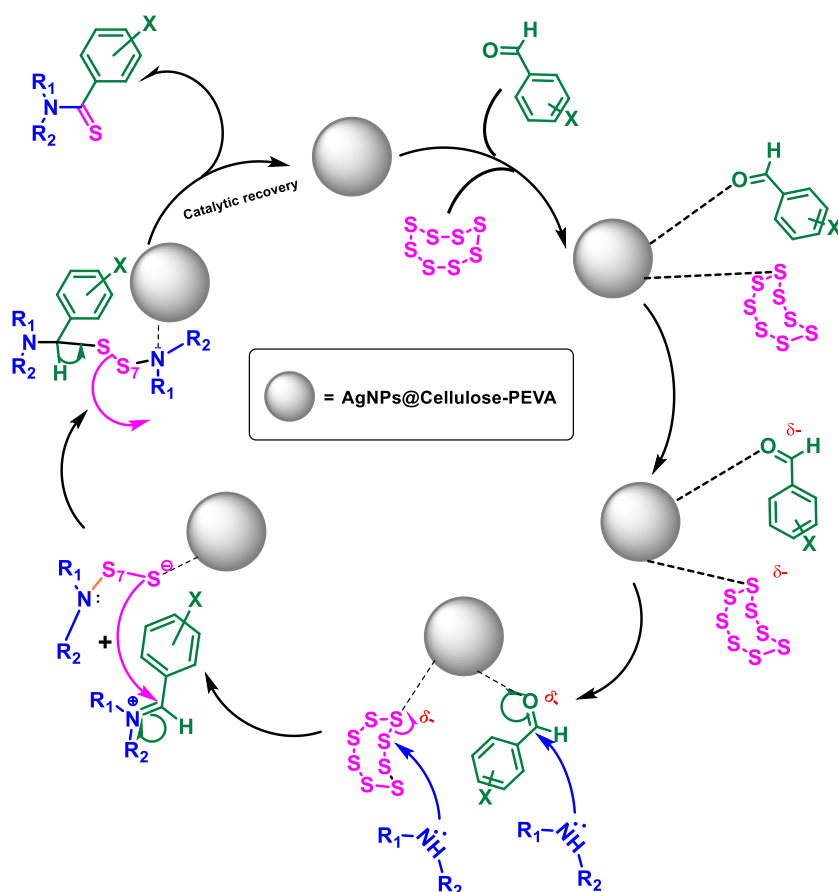


Figure 3a.9. (A) Reusability of the AgNPs@cellulose–PEVA catalyst, (B) Reaction yields with or without the AgNPs@cellulose–PEVA catalyst.

3a.4.8 Proposed mechanism

A mechanism for the synthesis of thioamides using the AgNPs@cellulose–PEVA catalyst was proposed, as illustrated in Scheme 3.4. The AgNPs anchored on the surface of the cellulose–PEVA composite via hydrogen bonding facilitated the nucleophilic attack of morpholine by increasing the electrophilicity of the carbonyl groups through non-covalent interactions [43]. The attack of morpholine on S caused the S₈ ring to open and induced the formation of polysulfide ions. During the next step, enamine was formed via water removal, and simultaneously, the polysulfide ions acted as a nucleophile, attacking enamine and forming new C–S bonds. Lastly, H was eliminated, and the polysulfide moiety formed thioamide and the catalyst.



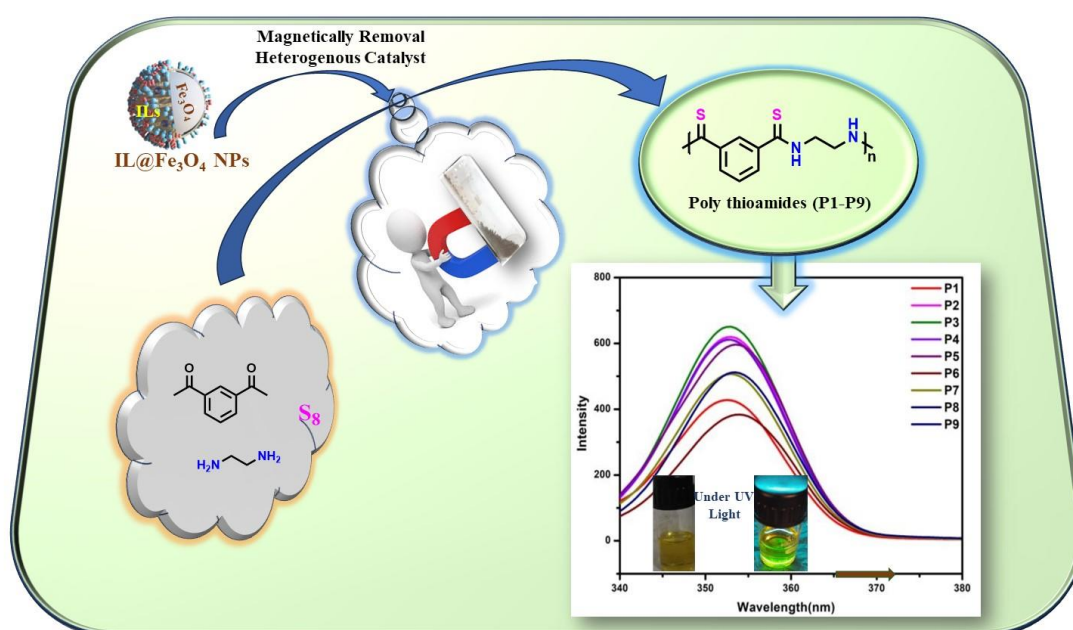
Scheme 3.4. Proposed mechanism for the synthesis of thioamides using the Willgerodt–Kindler reaction and the AgNPs@cellulose–PEVA catalyst.

3a.5 Conclusion

A solid support comprising a biomass-derived cellulose–PEVA hybrid embedded with AgNPs was prepared. The developed hybrid catalyst was used for the synthesis of thioamides using the Willgerodt–Kindler reaction. Several biologically important thioamides were prepared using various aldehydes and the fabricated hybrid catalyst. The AgNPs@cellulose–PEVA hybrid catalyst presented excellent catalytic efficacy for the Willgerodt–Kindler reaction, facilitating the selective formation of C=S bonds. The AgNPs@cellulose–PEVA catalyst exhibited high stability, excellent reusability, and sustained heterogeneity in the reaction media. We believe that the fabricated hybrid catalyst can promote the large-scale preparation of thioamides.

Chapter 3B

Ionic liquid functionalized Fe_3O_4 core-shell nanoparticles: A magnetically separable Brønsted acid catalyst for the synthesis of polythioamides



Singh, A.; Singh, N.; Kaur, N. *Appl Organomet Chem* 2022, **36**, e6909.

3b.1 Aim and Objectives

In these days' the development of multicomponent-based polymerization gaining much attraction, keeping this point in view we synthesized fluorescent conjugated and non-conjugated polythioamide in one pot using di-aldehyde, di-amines, and elemental sulfur in the presence of IL@Fe₃O₄NPs as a catalyst via willgerodt kindler reaction. Here ionic liquid coated over magnetized iron nanoparticles heterogenous catalysts were synthesized. Polymerization of multicomponent reaction proceeds smoothly in the presence of a catalyst at ambient temperature with excellent yield. As magnetic catalyst recovered easily from the reaction mixture, this method shows excessive potential for an efficient polymerization approach toward structurally diversified willgerodt kindler reaction. By the development of a new magnetic catalyst, we overawed the limitations of multicomponent polymerization such as the poor solubility of polymer, low molecular weight, stoichiometric balance, easy removal of the catalyst, and complicated workup.

3b.2 Introduction

The development of polymer with various functionalities is an efficient methodology and has great industrial applications as it has properties of Stimuli-responsive, controllability, and reversibility [1-2]. Besides this heterocyclic polymers have drawn attention due to their photophysical, mechanical, and electrical properties [3]. Polymerization usually starts with a simple reactant to obtain the desired polymer product [4]. A tandem polymerization has advantages over normal polymerization reactions, as a specific product is obtained without isolating the intermediate and minimum workup [5]. In the last few years, various reactions including Ugi [6-9], Mannich [10], Biginelli [11-16], Passerini [17-21], Kabachnik-fields Reaction [22], Hantzsch [16], etc. have been used to synthesize polymer into chemistry. Based on the reactant used, multicomponent reactions are categorized as isocyanide [$\text{—N}\equiv\text{CH}$] based multicomponent reaction (MCR), non-isocyanide-based multicomponent reaction, and metal-catalyzed MCR [25-27]. Direct use of metal in MCR is not a good approach, as its removal from the reaction mixture is very difficult and causes environmental pollution [28-30]. Avoiding the direct use of metal in MCR is an attractive alternative [31]. Multicomponent polymerization from three or more reactants with metal-free conditions attracted particular attention of scientists [32-33]. Willgerodt-kindler is a three-component reaction of aldehyde, amines, and elemental

sulfur used for tandem polymerization synthesis [34-35]. These type of thioamide-based polymers shows high luminescence and can be used for adsorption of heavy metal ions [35-36]. In the last few years, poly-thioamide has gained great attention due to its high efficiency in the removal of Mercury, Gold, and polypeptides [25]. Willgerodt kindler reaction shows semi-conductivity, high refractivity, electrochemical properties, and sulfur-containing polyamide has wide applications [34]. However, the use of long reaction time, high temperature, use of organic solvent, low yield, use of metal-based catalysts, and non-sustainability limit their wide applications [37]. Besides this, their workup and purification are also difficult [37]. To overcome these limitations, we require a catalyst that is eco-friendly, has high catalytic efficiency, recyclability, and is easy to remove. Addressing the indispensable need for a sustainable catalytic system, a new composite is synthesized with ionic liquid (ILs), because of its excellent chemical and physical properties gained much attention [38-39]. In these days fabrication of iron oxide nanoparticles received considerable attention due to less expensive production methods, environmentally friendly processes, and facile catalyst recovery [40]. Ionic liquid with a substituted group can be used as a catalyst and green solvent in various transformations [41-42]. Ionic liquid also be used in many applications such as electrochemical bio-sensing, bio-diesel preparation, thermal energy management, formation of carbonate from CO₂, etc. [43]. Because of consistency and insupportable viscosity, it's very difficult to remove and reuse ionic liquid which limits its applications. To overcome this limitation, it is necessary to modify ionic liquid, so that it can be easily reused and removed from the reaction mixture. Magnetically removable IL1-2@Fe₂O₃ catalyst satisfied the requirement of green catalyst, as it eliminates the tedious techniques such as filtration and centrifugation which are used for recovery of catalyst. Thus, magnetically recovery of catalyst avoids the catalyst loss, saves energy, and is less time-consuming [44]. The use of expensive metals such as Pt, Ag, Au, Pd, etc. is replaced by magnetically recoverable catalysts, which cause lots of negative effects on the environment [45-46].

In this respect, we restrained magnetic Fe₂O₃ nanoparticles in the core of an acidic ionic liquid, and a magnetic catalyst with a porous surface was obtained [47]. Magnetically separable nanoparticles have excellent properties and are an emerging class that can be easily separated by a simple application of a magnet with minimum catalyst loss. Among all these methods one which preserves the composition and

structure of ligands is widely accepted. Since the catalyst is on a nanoparticle scale and has a large surface area, highly effective for catalytic activity. Fe_2O_3 nanoparticles are very popular however, the bare use of these nanoparticles is highly unstable when used in both acidic and basic conditions, due to their aggregation in solution [48].

Addressing the need for a catalytic sustainable system, a magnetically removable catalyst was developed. Recently we have reported the synthesis of thioamides and polymerization of biginelli reaction, catalyzed Ionic liquid@ Fe_3O_4 NPs [49-50]. Thus, based on our previous work, herein we synthesized magnetically removal IL1-2@ Fe_3O_4 heterogeneous catalyst which was further used for the synthesis of polymer via willgerodt kindler reaction with a simple and facile method. Fe_3O_4 NPs have high affinity towards the functional groups, present in ionic liquid and we found that IL1-2@ Fe_3O_4 performs high catalytic properties for synthesis for thioamide-based polymer and recycled with minimum loss of activity. To evaluate stimulus of the morphology and catalyst structure on its properties, the nanoparticle mixture was characterized using infrared spectroscopy (IR), Dynamic light scattering (DLS) technique, Nuclear magnetic resonance (NMR), scanning electron microscopy (SEM), powder X-ray diffraction (PXRD) and energy dispersive spectroscopy (EDS).

3b.3 Experimental Section

3b.3.1 General information

All the chemicals used in this work were purchased from TCI, Avra, and Sigma-Aldrich Co and were used further without purification. Physical and chemical properties of synthesized material were investigated through various techniques including; A JEOL instrument operated at 400 MHz was used to obtain ^1H -NMR spectra and similarly, an instrument operated at 100 MHz was used to obtain ^{13}C -NMR spectra. The deuterated solvent is used as an internal reference to measure the chemical shifts. Further, molecular mass and poly-dispersive index (PDI) of synthesized polythioamides were evaluated at room temperature through GPC (Agilent 1260 Infinity II GPC/SEC MDS). Thereafter, FTIR analysis was performed using the Hyperion 2000 (Bruker Optics) FTIR system. Surface morphology of synthesized materials was examined through SEM, EDS, and elemental dot mapping using a JEOL JSM-6610-LV instrument. A UV-visible absorption spectrophotometer (Shimadzu UV-2400) was used to determine the photophysical properties of materials. The UV cuvette was made up of quartz with a path length of 1.0 cm. Further, fluorescence

behavior of material was determined using PerkinElmer LS 55 fluorescence. Thereafter, to get insight into the structure HRTEM (Hitachi H-7500, Japan) and AFM were used. PXRD measurements were performed to analyze the crystallinity and planes of materials, using a Miniflex (Rigaku) diffractometer. DLS utilizing the external probe feature of a particle size analyzer (Metrohm Microtrac Ultra Nanotrac).

3b.3.2 Synthetic procedures

Iron oxide nanoparticles synthesis: Fe_3O_4 Nanoparticles were prepared via the control precipitation method. Ferric chloride hexahydrate ($\text{FeCl}_3 \cdot 6\text{H}_2\text{O}$) and ferrous chloride tetrahydrate ($\text{FeCl}_2 \cdot 4\text{H}_2\text{O}$) in a ratio of 0.25:0.65 were dissolved in distilled water and were kept on a magnetic stirrer for 30 min at 80 °C to make a homogenous solution. 0.5M NaOH was prepared and added dropwise to the homogenous solution till pH reached around 11. Black precipitates were obtained, centrifuged the ppts, and washed with distilled water.

3b.3.3 Synthesis of ionic liquids

IL1 [Scheme 3b.1] was synthesized to dissolve 1-Hydroxy-2-napthoicacid in acetonitrile (ACN), further triethylamine was added to initiate the reaction and was refluxed for 40 min at 75 °C, a homogeneous mixture was obtained. In the obtained mixture 1,2-dibromoethane was added and refluxed for 48 hrs at the same reaction conditions. The reaction was concentrated on a rota-evaporator and white crystals were obtained. N-methylimidazole was added in the obtained white crystals; refluxed the reaction for overnight at same reaction conditions and was characterized through ^1H -NMR (figure 3b.1), ^{13}C -NMR (figure 3b.2), and Mass spectroscopy (figure 3b.3). Formed IL1 was characterized by FTIR $\nu(\text{cm}^{-1})$: 2972, 2922, 2728, 2669, 1721, 1662, 1463, 1400 1252, 1164, 1041, 764, 576 and confirmed the presence of functional group like -COOH (figure 3b.4).

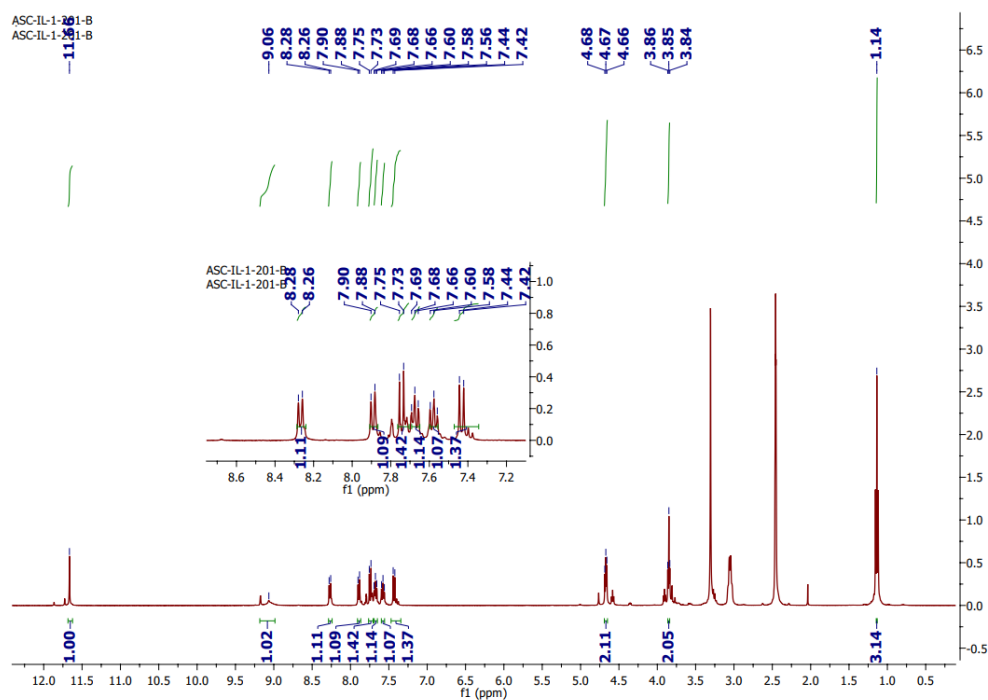


Figure 3b.1: ^1H -NMR Spectra of IL1.

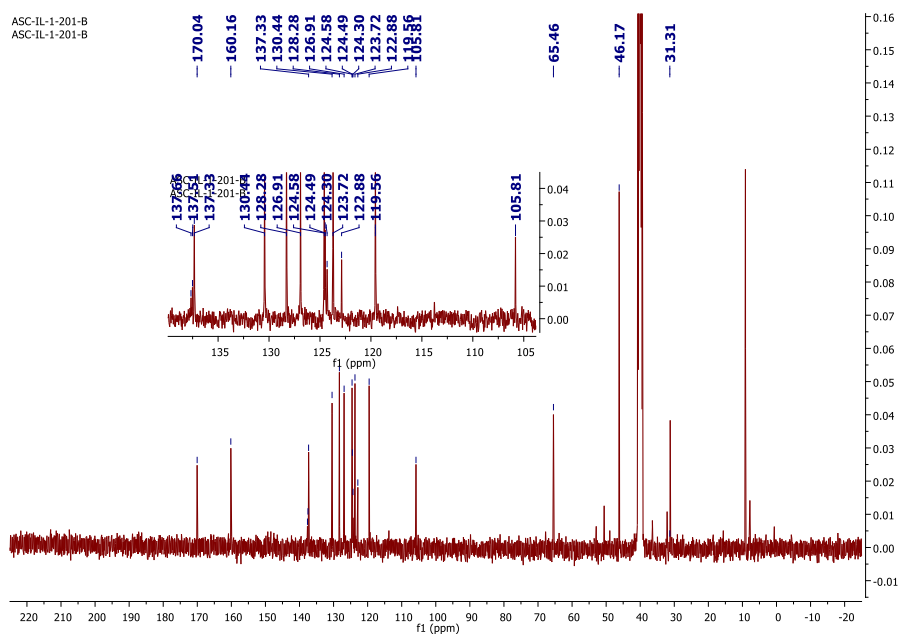


Figure 3b.2: ^{13}C -NMR Spectra of IL1.

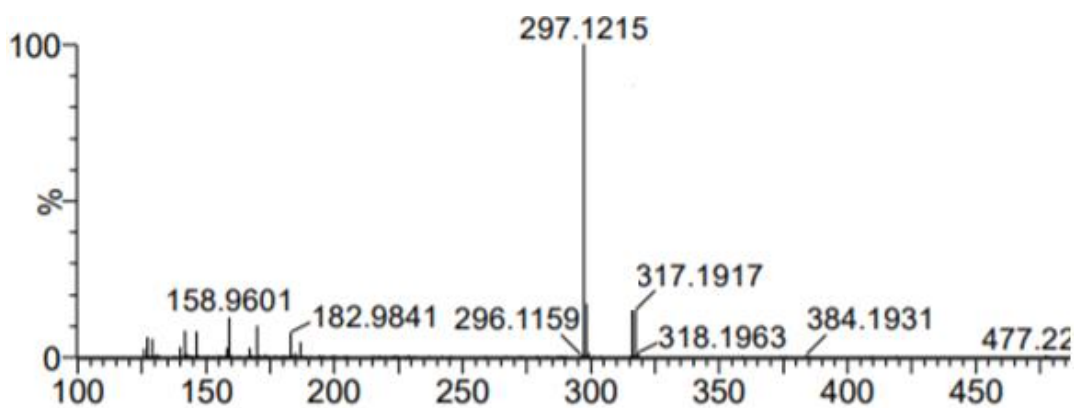


Figure 3b.3: Mass spectroscopy of IL1.

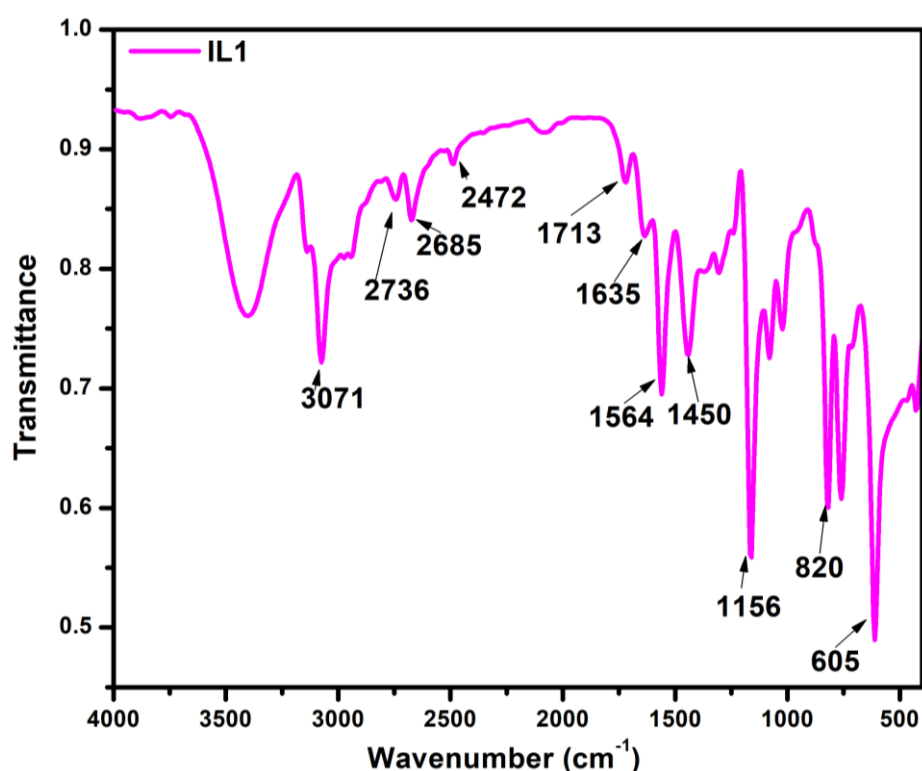


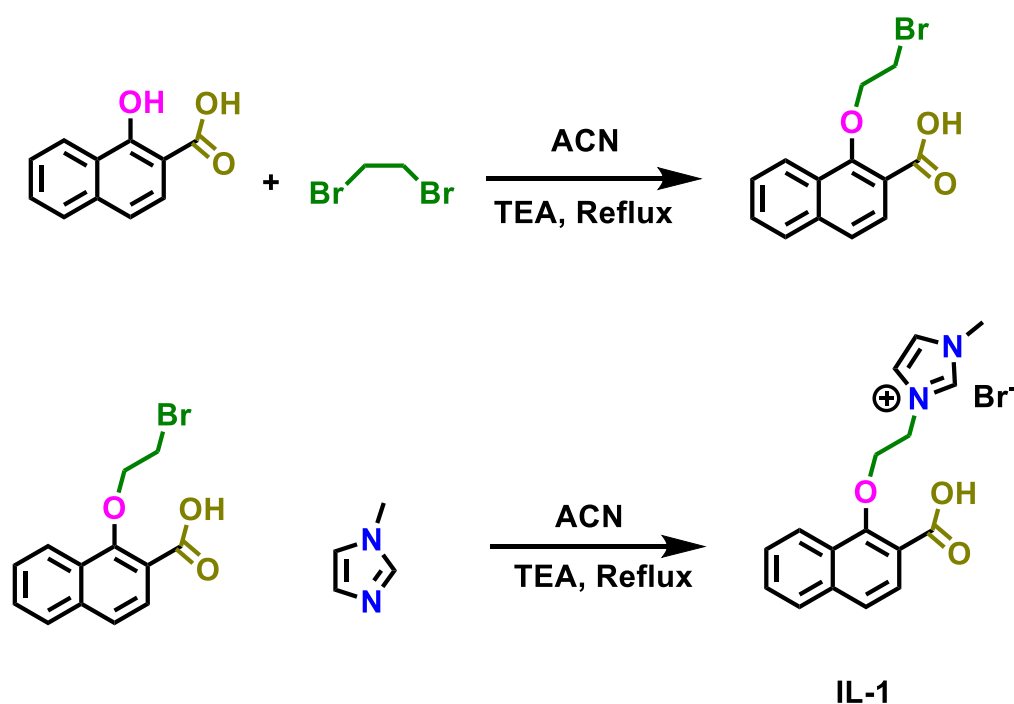
Figure 3b.4: IR spectroscopy of IL1.

Similarly, IL2 [figure 3b.5(B)] was synthesized using 3-hydroxy-4-nitrobenzoic acid following the same procedure and characterized through FTIR, Mass spectroscopy, ^1H -NMR, and ^{13}C -NMR. Further, the synthesis of a new catalyst (IL1-2@Fe₃O₄), was carried out via a controlled precipitation method (scheme 3b.2) and fully characterized using different techniques.

Characterization of IL1: ^1H NMR (400 MHz, DMSO- d_6) of IL1 δ (ppm) 11.66 (s, 1H, O-H), 8.27 (d, 1H, ArH), 7.87 (d, 1H, ArH), 7.79 (s, 1H, ArH), 7.74 (d, 2H, ArH), 7.67 (t, 1H, ArH), 7.57 (t, 1H, ArH), 7.40 (d, 2H, ArH), 4.67 (t, 3H, -CH₂), 3.85 (t, 3H,

-CH₂), 3.31 (s, 3H, -CH₃). ¹³C NMR (100 MHz, CDCl₃), δ=170.1, 160.2, 137.3, 130.4, 128.3, 126.9, 124.6, 124.5, 124.3, 123.7, 122.9, 119.6, 105.8, 65.5, 46.2, 31.1. Mass data Calculated: 297.1215, Found: 297.1215.

Characterization of IL2: ¹H NMR (400 MHz, DMSO-d₆) of IL1 δ(ppm) 11.65 (s, 1H, O-H), 8.26 (d, 1H, ArH), 7.88 (d, 1H, ArH), 7.73 (s, 1H, ArH), 7.67 (d, 1H, ArH), 7.57 (d, 1H, ArH), 7.42 (s, 1H, ArH), 4.65 (t, 3H, -CH₂), 3.84 (t, 3H, -CH₂), 3.34 (t, 3H, -CH₃). ¹³C NMR (100 MHz, CDCl₃), δ=170.0, 160.17, 137.33, 130.43, 128.27, 126.89, 124.57, 123.72, 119.55, 105.80, 65.46, 46.17, 31.18. Mass data Calculated: 292.0911, Found: 292.0911.



Scheme 3b.1: Synthesis of ionic liquid (IL1).

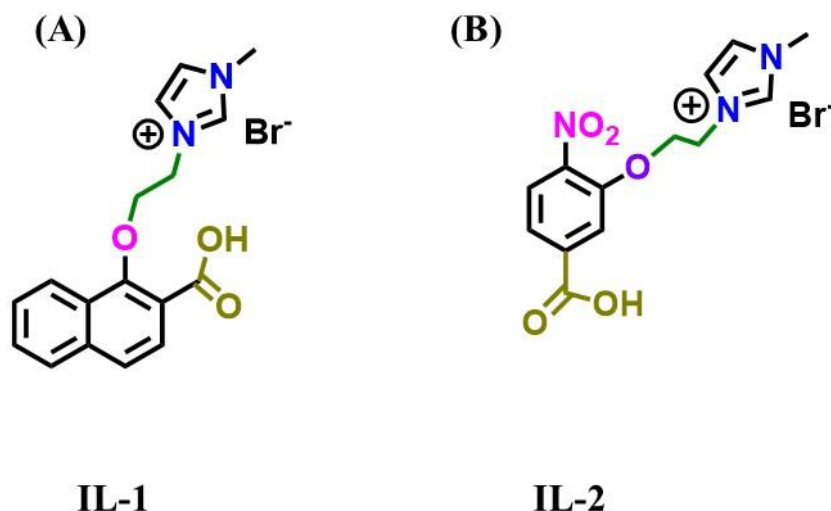
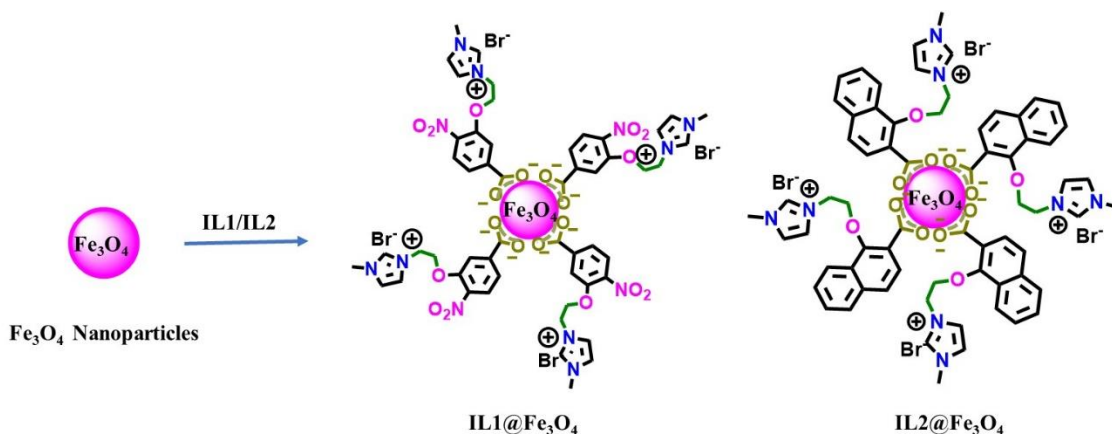


Figure 3b.5: Chemical Structure of prepared ionic liquids (A) IL1 and (B) IL2.



Scheme 3b.2: Synthesis and structural features of IL1@Fe₃O₄ and IL2@Fe₃O₄ via control precipitation method.

3b.4 Results and Discussion

3b.4.1 Crystal structure and crystallinity

PXRD pattern of Fe₂O₃ and IL1-2@Fe₃O₄ was determined to check the crystalline structure and plane of compounds (figure 3b.6). From this pattern we compare the pattern of bare Fe₂O₃ with coated Fe₂O₃ with ionic liquids (IL1-2) which elucidated the coating of ILs over single phase iron oxide nanoparticles. From obtained spectra it was found that Fe₂O₃ NPs [figure 3b.6A(i)] have a crystalline nature with diffraction peaks at 30.08, 36.06, 43.12, 57.16, 59.12, and 62.67 are indexed as (220), (311), (400), (422), (511), and (400) respectively. All these planes correspond to cubic unit cells of

magnetite and it match with inverse spinel of crystal. the diffraction peaks of IL2@Fe₃O₄ [figure 3b.6A(iii)] are broader with very high intensity than those of IL1@Fe₃O₄ [figure 3b.6A(ii)] indicating more crystallinity and fine nature of hybrid.

Further, to check the hydrodynamic size distribution and size of the catalyst, dynamic light scattering (DLS) was performed (figure 3b.6b-d). Shows bare Fe₃O₄ has an average diameter of 34.5 nm (figure 3b.6b). The average diameter for each IL1@Fe₃O₄ and IL2@Fe₃O₄ is 84.60 nm and 82.30 nm respectively which shows hydrodynamic size increases with coating of IL1-2 on bare Fe₃O₄ (figure 3b.6c-d).

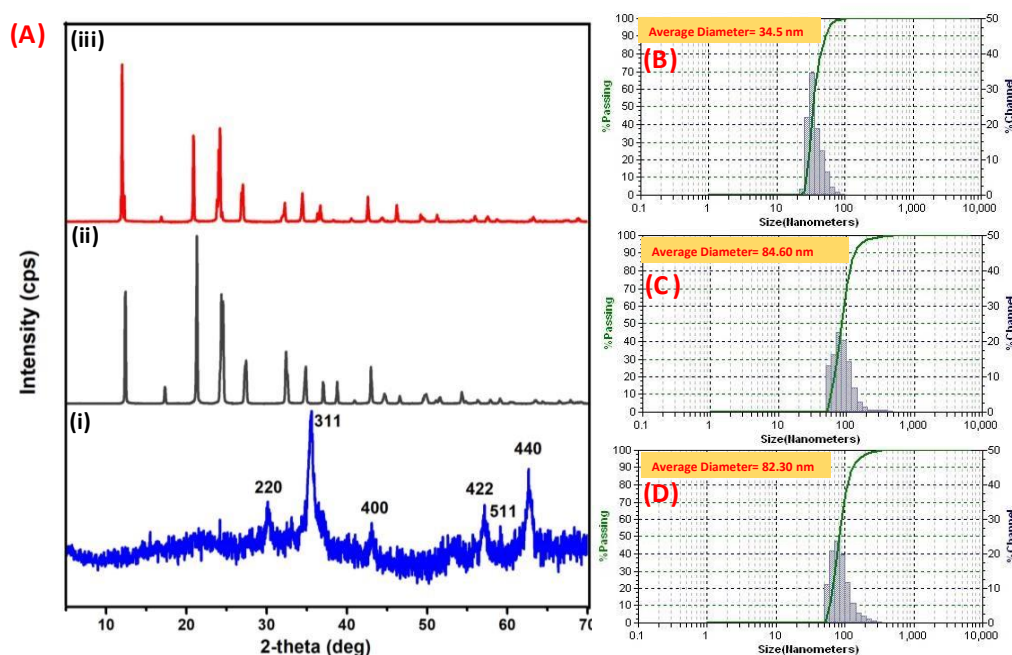


Figure 3b.6: (A) PXRD spectra of (i) Fe₂O₃, (ii) IL1@Fe₃O₄, and (iii) IL2@Fe₃O₄. Dynamic light scattering (DLS) of (B) Fe₂O₃, (C) IL1@Fe₃O₄, and (D) IL2@Fe₃O₄.

3b.4.2 Surface morphology analysis

To reveal the surface morphology of bare and coated Fe₂O₃ with ionic liquids (IL1-2) scanning electron microscopy was performed (SEM). Figure-3b.7a shows the SEM image of pure Fe₂O₃, which reveals the spherical morphology of nanoparticles. Except few most of the particles are in spherical form and also reveal that particles are agglomerated in solution form. The SEM analysis of IL1@Fe₃O₄ (figure 3b.7b) and IL2@Fe₃O₄ (figure 3b.8a) spherical morphology of catalyst. Due to π - π interaction of the aromatic benzene ring it shows scrap-like morphology. Thereafter, the surface morphology of both IL1-2@Fe₃O₄ was analyzed through Elemental dot mapping and

it came to know individual atoms i.e., Iron, Carbon, Oxygen, and Nitrogen distribution throughout surface confirming the homogeneity of the material (figure 3b.7e-h). Similarly, HRTEM of IL2@Fe₃O₄ confirmed core-shell particles of the catalyst (figure 3b.8c). The experimental data (figure 3b.7c and 3b.7d) indicated that iron-oxide nanoparticles composite comprised Fe (63.23%) and O (15.94 %) and the IL1@Fe₃O₄ hybrid contained C (9.16 %), O (11.40 %), N (2.39 %), Br (11.35 %), and Fe (45.16 %) respectively. Similarly, the EDS of IL2@Fe₃O₄ is shown in (figure 3b.8b). All these characterizations confirm the formation of IL1-2@Fe₃O₄ heterogeneous catalyst.

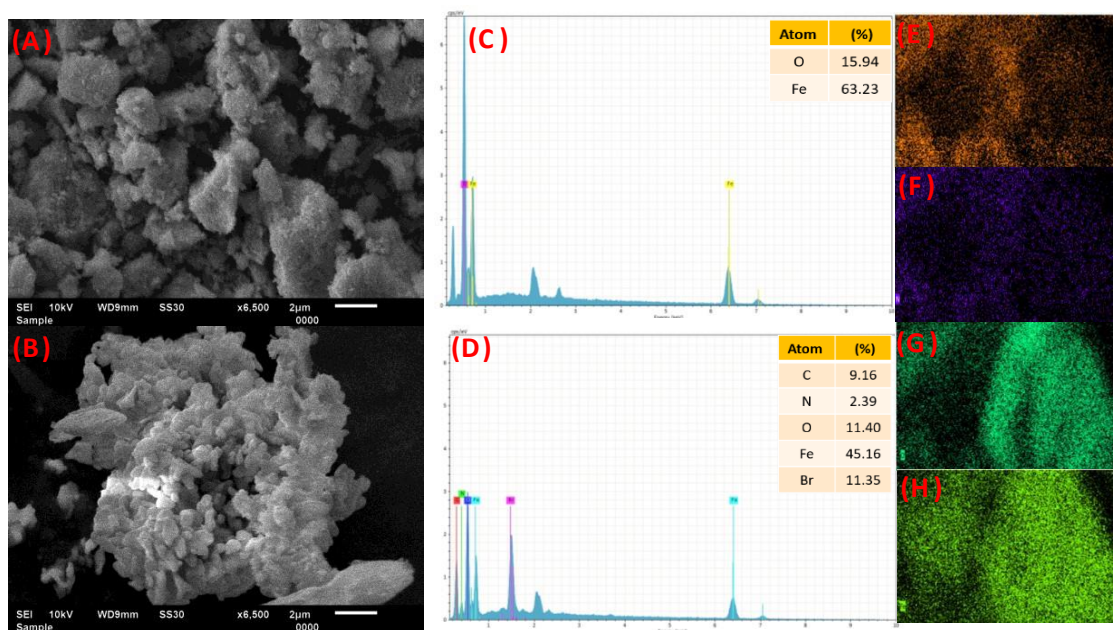


Figure 3b.7. SEM Image of (a) Fe₂O₃, (c) IL1@Fe₂O₃ and EDS spectra of (b) Fe₂O₃, (d) IL1@Fe₂O₃. Elemental dot mapping of IL1, individual mapping of (e) C (9.16%), (f) O (11.40%), (g) N (2.36%), and (h) Fe (45.16%).

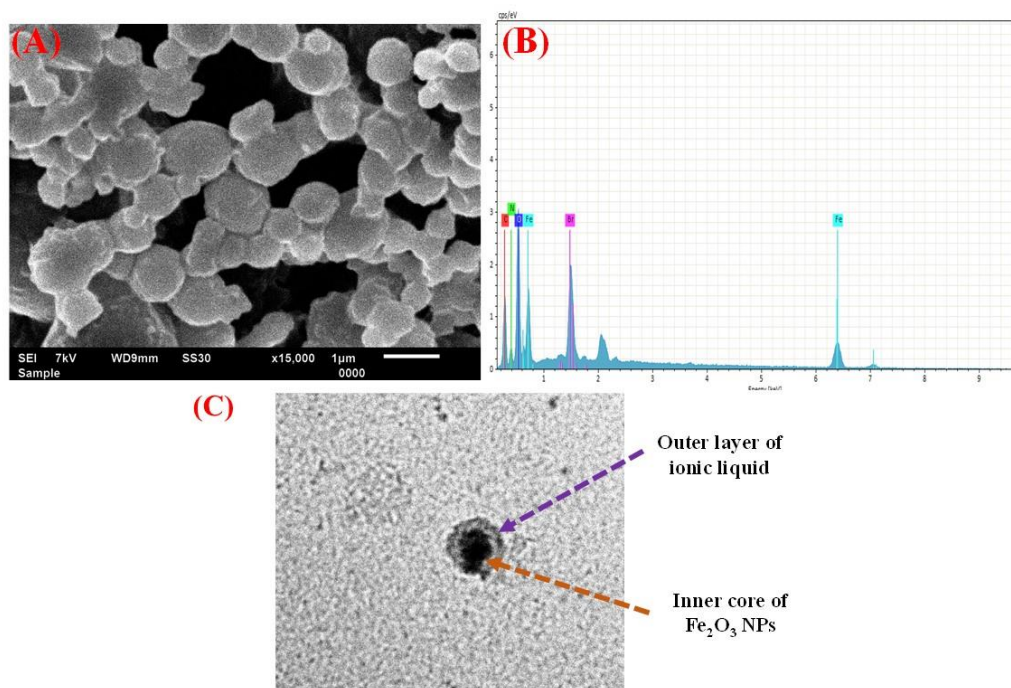


Figure 3b.8. SEM Image of (a) IL1@Fe₂O₃, EDS spectra of (b) IL2@Fe₂O₃, and (c) HRTEM Image of Core-shell IL@Fe₂O₃ nanoparticles.

3b.4.3 Atomic force microscopy (AFM)

Further, atomic force microscopy was performed to analyze the surface morphology of both IL1@Fe₂O₃ and IL2@Fe₂O₃. From the analysis, we found the porous surface of IL1@Fe₂O₃ (figure 3b.9a-b) which provides the heterogenous surface to react and trigger the formation of poly-thioamides. Figure-3b.9b shows the 3D top view of IL2@Fe₂O₃, appearance of many peaks and valleys on the surface indicates the rough surface of catalyst which is responsible for the adsorption of reactant to carry out reaction. Similarly, surface morphology of IL2@Fe₂O₃ was analyzed through AFM.

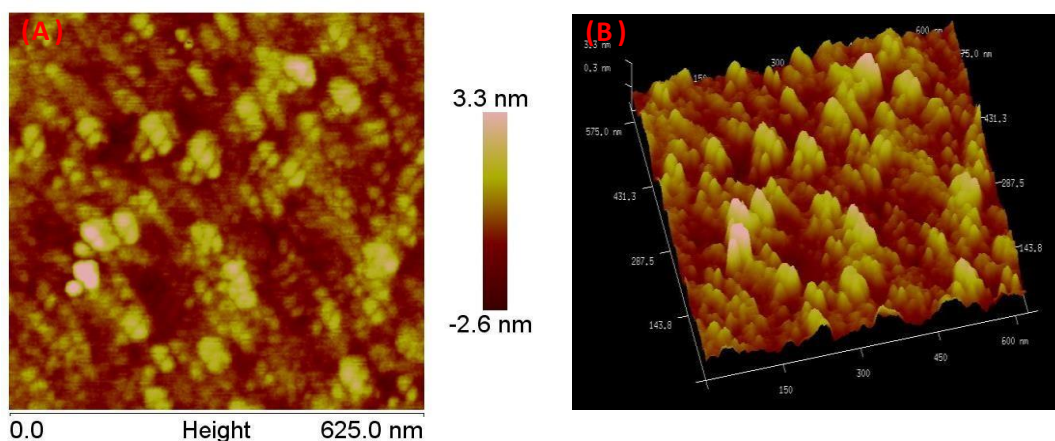


Figure 3b.9. Atomic force microscopy (AFM) images in (A) 2-dimensional and (B) 3-dimensional of IL1@Fe₂O₃.

Both ionic liquid IL1 and IL2 show multifunctional properties due to the presence of cationic, anionic, and carboxylic functionality. The COOH group can immobilize with Fe₃O₄ NPs and reaction was catalyzed by the cationic part i.e., imidazolium moiety. Fe₃O₄ NPs were synthesized using the control precipitation method. Similarly, IL1@Fe₃O₄ and IL2@Fe₃O₄ were synthesized using the same conditions. The formed nanoparticles were examined using different characterization such as PXRD, AFM, DLS, and SEM were used for the particle size distribution of NPs. Further magnetic properties of NPs were checked with a piece of magnet. Both IL1@Fe₃O₄ and IL2@Fe₃O₄ easily separated from the reaction mixture by simple an application of magnet (figure 3b.10). Magnetic character of Fe₃O₄, IL1@Fe₃O₄, and IL2@Fe₃O₄ were evaluated using a simple magnet which used during removal of heterogenous catalyst from the reaction mixture (figure 3b.10a-c)



Figure 3b.10. Magnetically separation of A) Fe₃O₄, B) IL1@Fe₃O₄, and C) IL2@Fe₃O₄.

3b.4.4 X-ray photoelectron spectroscopy (XPS)

To analyze the binding energy of all atoms X-ray photoelectron spectroscopy was performed. Figure-6 depicts the XPS spectra of IL1@Fe₃O₄, which investigated the chemical environment and atomic state of all elements present in IL1@Fe₃O₄. The full range spectra (0-1300 eV) demonstrated the existence of C1s, O1s, N1s, and Fe2p in the prepared sample (figure 3b.11a), confirming the presence of iron oxide nanoparticles in synthesized ionic liquid. The XPS spectra of Fe2p for the synthesized material (figure 3b.11c) show the two characteristic double peaks for both Fe₃O₄ phases, which were observed at 724 and 710.5 eV, corresponding to Fe2p_{1/2} and Fe2p_{3/2} respectively. Which is the good agreement of Fe2p from Fe₃O₄. Further carbon bonded to carbon, nitrogen, and oxygen via single/double bonds, were also observed in the prepared material (figure 3b.11a).

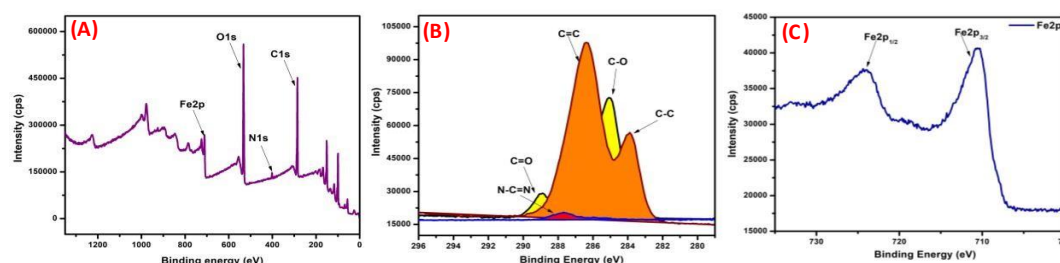


Figure 3b.11. XPS spectra of a) IL1@Fe₃O₄ core peak of C1s, N1s, O1s, and Fe2p, b) 1s core peaks of C, O, N, and c) 2p core peaks of Fe.

3b.4.5 Photophysical properties of the catalyst

To analyze the degree of reactivity of catalyst photophysical properties are the important parameter. UV-visible absorption and emission spectra of IL1@Fe₃O₄ and IL2@Fe₃O₄ were recorded by using photophysical properties and obtained results were compared with bare Fe₃O₄ NPs. Different absorption profiles of IL1@Fe₃O₄ and IL2@Fe₃O₄ were recorded at room temperature and absorption spectra were compared with bare Fe₃O₄ nanoparticles. From the spectra, two bands were found at 345 nm and 471 nm for Fe₃O₄. Similarly, absorption spectra were recorded for IL1@Fe₃O₄ with shifting of a band at 362 nm and 486 nm which confirms the presence of Fe₃O₄. The shifting of band toward a lower wavelength compared to IL1-2, a blue shift was observed which was probably due to ligand-to-metal charge transfer or Fe³⁺ field transmission. Further, absorption spectra of hybrid were compared with IL1-2, and a red shift was observed which may be due to different structural profiles, that they

gained during the fabrication of IL1-2, also confirms fabrication was done successfully.

3b.4.6 Adsorption isotherm and acidic strength of the catalyst

Brunauer Emmett Teller (BET) analysis was done to check the N_2 adsorption of all three i.e., Fe_2O_3 , IL1@ Fe_2O_3 , and IL2@ Fe_2O_3 at room temperature (Figure 3b.12). The obtained value of pore volume (PV), average pore diameter (APD), and surface area (SA) for all three are shown in table S2. From observed data, we found that SA, PV, and APD are slightly larger for IL1@ Fe_2O_3 .

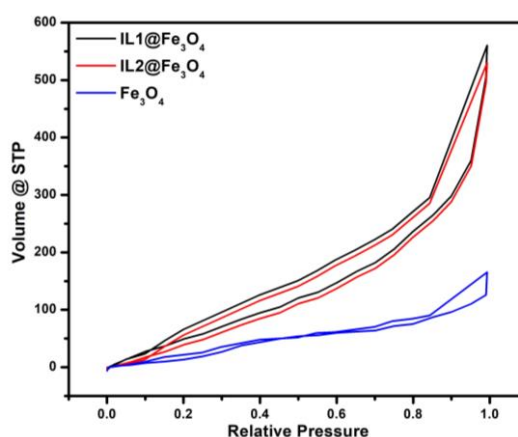


Figure 3b.12: N_2 adsorption-desorption spectra (BET) of Fe_2O_3 , IL1@ Fe_2O_3 , and IL2@ Fe_2O_3 .

A titrimetric analysis experiment was performed to check the acidic strength of Fe_2O_3 , IL1@ Fe_2O_3 , and IL2@ Fe_2O_3 . To perform this experiment 10 mg of each Fe_2O_3 , IL1@ Fe_2O_3 , and IL2@ Fe_2O_3 were dissolved separately in a 50 mL beaker containing 10 mL of 0.5N hydrochloric acid (HCl). To make a homogenous solution all three solutions were stirred continuously at room temperature for 30 min. After preparing a homogenous solution remaining portion of hydrochloric acid was estimated via back titration using 0.5N sodium hydroxide solution. From the obtained result of back titration and BET, it is found that IL1@ Fe_3O_4 NPs showed maximum basic strength (5.22) per unit area followed by IL2@ Fe_3O_4 . Besides this bare Fe_3O_4 exhibited minimum basic strength per unit area, as illustrated in table 3b.1. After investigating the physical and chemical properties of the prepared heterogeneous catalyst, the capability of synthesized compounds as solid support materials, was explored for the synthesis of poly-thioamides.

Table 3b.1: Acidic strength calculation of Fe_3O_4 , IL1@ Fe_3O_4 , and IL2@ Fe_3O_4 .

SNo.	Catalyst	Volume of 0.5 N HCl (mL)	Basic unit count (BU) (mmol/g)	Surface Area (SA) (m ² g ⁻¹)	RBA (mmol/g)	Relative basic unit (RBA/0.23)
1	Fe ₃ O ₄	0.46	0.23	22.0	0.23	1
2	IL1@Fe ₃ O ₄	0.60	0.30	88.0	1.20	5.22
3	IL2@Fe ₃ O ₄	0.30	0.15	108.0	0.74	3.22

3b.4.7 Thermal stability of the catalyst

Furthermore, thermo-gravimetric analysis (TGA) was accomplished to check the thermal stability and composition of synthesized catalysts, IL1-2@Fe₃O₄. From the analysis we observed that, initially weight losses for the Fe₃O₄, IL1@Fe₃O₄, and IL2@Fe₃O₄ started when the temperature was enlarged from 60 °C to 120 °C which may be because of loss of water from the materials. Beyond this temperature weight loss for IL1-2@Fe₃O₄ was observed, which may be due to the decomposition of Fe₃O₄ NPs coated with ILs. From the TGA analysis we found the weight loss for IL1@Fe₃O₄ was about 28 % (figure 3b.13b) and weight loss was 50 % for IL2@Fe₃O₄ (figure 3b.13a), which helps to estimate the fraction of ILs coated of Fe₃O₄ NPs, which was more for IL2@Fe₃O₄ compared to IL1@Fe₃O₄ NPs.

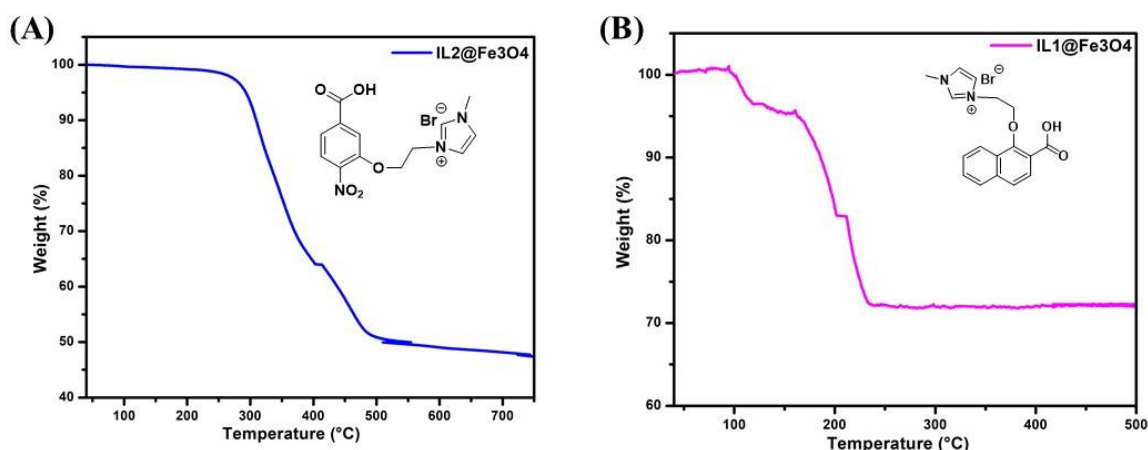
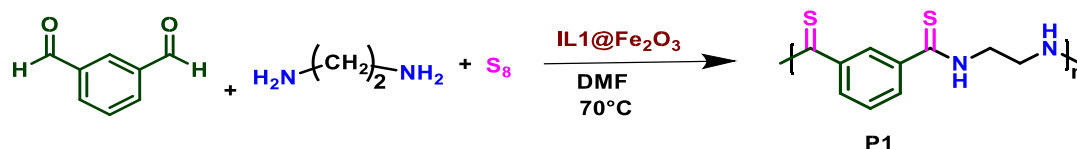


Figure 3b.13: TGA of A) IL2@Fe₃O₄, and B) IL1@Fe₃O₄.

3b.5 Experimental Section

3b.5.1 Multicomponent Tandem Polymerization via Willgerodt Kindler Reaction

The synthesis of thioamide-based polymer via willgerodt kindler reaction is a three-component reaction, based on this reaction we design an efficient polymerization method for polythioamide synthesis. This is a one-pot synthesis using dialdehyde, diamine, and elemental sulfur as reactants (Scheme-3b.3) to synthesize polymers. The accomplishment of the entire reaction was monitored by thin-layer chromatography (TLC) in a hexane and ethyl acetate solvent system. Further reaction was optimized and the role of catalyst, solvent, and stoichiometry has been studied.

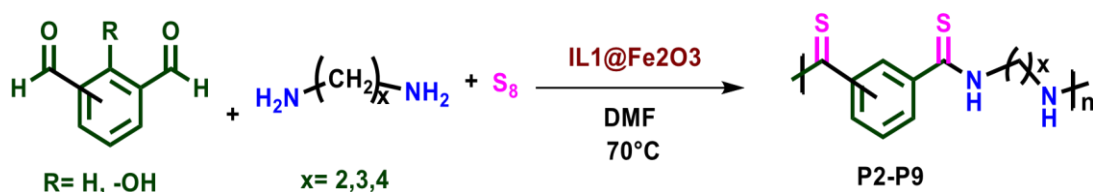


Scheme-3b.3: Synthesis of polymer (P1) using Willgerodt Kindler reaction and IL1-2@Fe₃O₄ as the catalyst.

3b.5.2 Catalytic activity of magnetite IL1-2@Fe₃O₄ nanohybrids

The most efficient catalyst IL1-2@Fe₃O₄ was selected for heterogenization to magnetically separable nano-catalyst. Here, conditions for the synthesis of polythioamide with these catalysts were optimized and originated our investigation by optimizing the reaction conditions such as solvent, type of catalyst, and amount of catalyst. The optimization reaction was carried out in different solvents such as DMSO, DMF, methanol, chloroform, and water. Catalytic amounts varied from 5 to 30 mg for optimization of the catalytic efficiency. The catalytic activity of IL12@Fe₃O₄ was investigated for the synthesis of Poly-thioamides in different reaction conditions. Initially, effect of solvent was studied, and it was found that reaction got precipitated when we used methanol and acetonitrile as a solvent which led to a low yield of poly-thioamides. Further when we try to use DMSO, water, and chloroform no polymerization reaction takes place due to the insolubility of reactants. In DMF (Table-1, entry-4) all reactant possesses excellent solubility, and reactions proceed smoothly with high yield formation of poly-thioamides. When reaction was carried out in a non-toxic solvent such as water, under same reaction conditions catalyst was not effective and reaction did not proceed (table-1 entry-5). DMSO acted promoter for polymerization of poly-thioamides via Willgerodt Kindler reaction. When DMSO was employed as a solvent for the reaction (table-1 entry-1), it was not effective for reaction

conditions. Other solvents such as methanol and chloroform afforded low yield, based on all these optimizations DMF is the best solvent for synthesis of poly-thioamides. With the optimization conditions in our hand, we prolonged the substrate scope using various dialdehyde, diamines, and elemental sulfur for the synthesis of poly-thioamides (scheme-3b.4) and synthesized thioamides (Figure 3b.14) were characterized through $^1\text{H-NMR}$, $^{13}\text{C-NMR}$, IR, and GPC.



Scheme-3b.4: Synthesis of various polymers (P2-P9) using willgerodt kindler reaction and IL1-2@Fe₃O₄ as the catalyst.

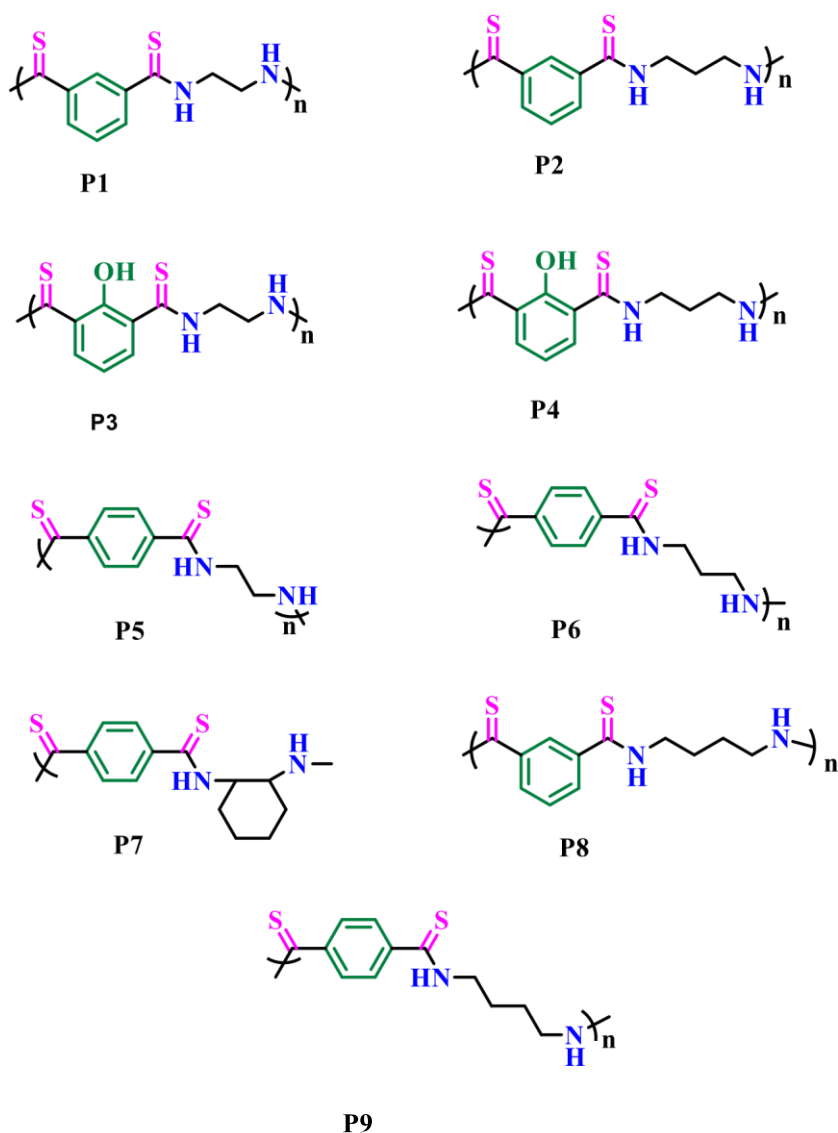


Figure 3b.14. molecular structure of synthesized poly-thioamides (P1-P9).

3b.5.3 Synthesis of polythioamides in presence of a catalyst

The polymerization reaction which was carried out via willgerodt kindler reaction taken as a model reaction, that was inspected under different catalytic conditions (Table 3b.2). To carry out polymerization reaction firstly synthesized material i.e., IL1-2 and IL1-2@Fe₃O₄ have been examined for polymerization (Scheme 3b.2). Reaction was carried out at 80 °C for 4 h in DMF and progress of reaction was scrutinized with TLC. The result of an investigation of catalyst is explained in (table 3b.3) and illustrates that both IL1 and IL2 afforded only 34 % and 37 % yield respectively. Whereas, magnetically catalyst IL1-2@Fe₃O₄ affords high polymerization yield.

Also, from the investigation, it was observed that IL2@Fe₃O₄ shows high catalytic activity with 87 % yield compared to IL1@Fe₃O₄ which produces 83 % yield. This may be due to one more functional group, which is present on IL2@Fe₃O₄. As Fe₃O₄ NPs have high affinity towards functional groups such as -COOH, -OH, and -NO₂, hence ILs act as a structure-directing agent. Mechanistically from the literature it was found that both IL1@Fe₃O₄ and IL2@Fe₃O₄ possess lewis acid character [51], which triggers the nucleophilic attack during polymerization (P1-P9). The formation of P1-P9 was confirmed via infrared spectroscopy, NMR spectroscopy, and gel permeable spectroscopy. Further catalytic activity of both IL1-2@Fe₃O₄ was examined for the synthesis of polythioamide via a one-pot multicomponent reaction by means of diamines, dialdehyde, and elemental sulfur. Starting with isophthalaldehyde, ethylenediamine, and elemental sulfur a multicomponent reaction, was selected as a model reaction for the synthesis of polymer (P1, scheme-3b.2). First, the reaction was performed in DMSO (table 3b.2, entry 1) in presence of 4 mg of IL1@Fe₃O₄ as a catalyst at same reaction conditions mentioned in scheme-3b.2.

Table 3b.2: Effect of solvent on the synthesis of poly-thioamides.

Entry	Solvent	Yield (%)
1.	DMSO	70
2.	Methanol	65
3.	Chloroform	55
4.	DMF	80
5.	Water	-

Table 3b.3: Screening of catalyst for polymerization.

Entry	Catalyst	Yield (%)
1.	IL1	65
2.	IL2	61
3.	IL1@Fe ₃ O ₄	82
4.	IL2@Fe ₃ O ₄	85

3b.5.4 Polymerization Reaction in presence of a new catalyst

Isophthalaldehyde (1 eq.), ethylenediamine (1.2 eq), elemental sulfur (2.4 eq), and 5 mol% IL1-2@Fe₃O₄ were taken in a 100 mL round bottom flask. Thereafter reaction was run for 4 h at 80 °C with incessant stirring. Accomplishment of reaction was checked with TLC in hexane and ethyl-acetate system. After accomplishment of reaction, the mixture was decanted into distilled water and precipitates were obtained. Precipitate was extracted by filtration and dried at ambient temperature. Thereafter, the precipitate was dissolved in ethyl-acetate whereas unreacted sulfur remained undissolved, filtering the sulfur and concentrating the solution, solid product was

acquired, which was characterized by FT-IR, GPC (Figure 3b.15 and Table 3b.4), and NMR spectroscopy. FT-IR peaks found at $\nu(\text{cm}^{-1})$: 3171, 3034, 2938, 1667, 1522, 1404, 1273. ^1H NMR (400 MHz, DMSO-d_6) of IL1 $\delta(\text{ppm})$ 10.44 (s, 1H, N-H), 7.80 (d, 1H, ArH), 7.73 (s, 2H, ArH), 7.66 (s, 1H, ArH), 4.04 (t, 2H, $-\text{CH}_2$), 3.62 (t, 1H, $-\text{CH}_2$), 3.10 (t, 1H, $-\text{CH}_2$). ^{13}C NMR (400 MHz, CDCl_3), $\delta=197.3$, 143.2, 127.8, 127.4, 44.8, 44.3.

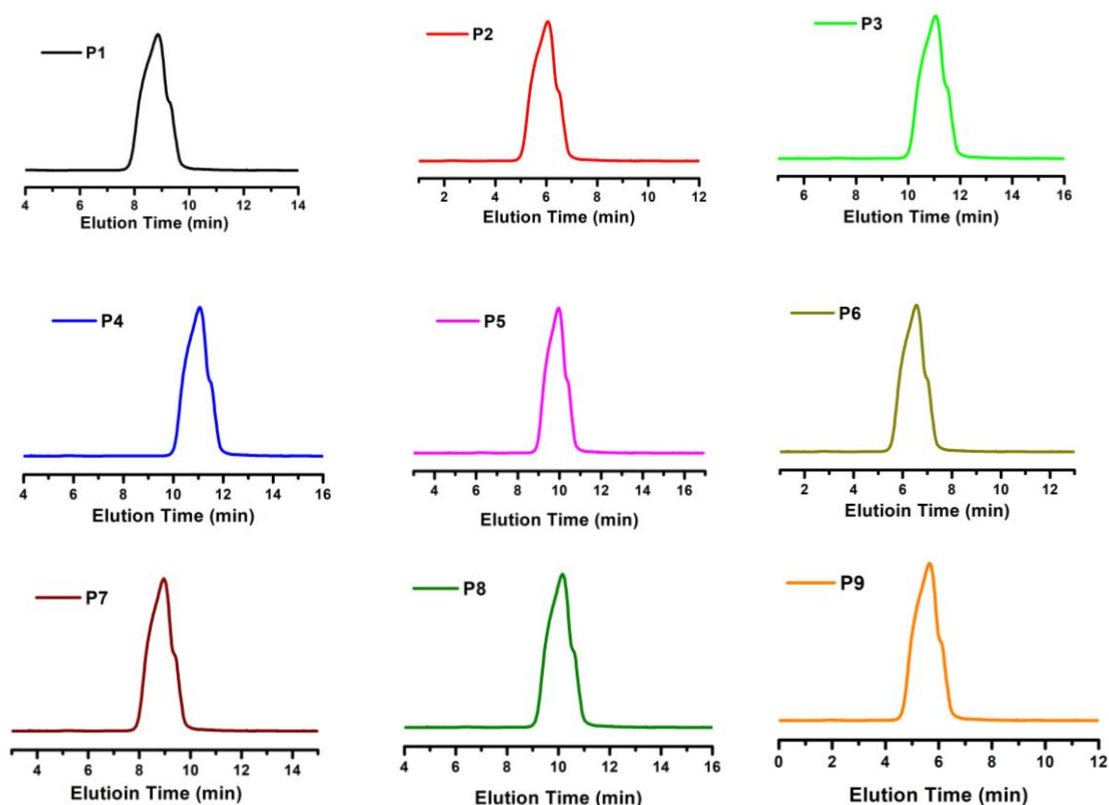


Figure 3b.15: Gel Permeation Chromatography for synthesis of polythioamides.

Table-3b.4: GPC data and solubility of all synthesized polymers (P1-P9).

SNo.	Polymer	Mn	Mw (g/mol)	PDI ^a
1.	P1	156510	111000	1.41
2.	P2	166510	121540	1.37
3.	P3	166767	116620	1.43
4.	P4	178643	128520	1.39
5.	P5	155844	133200	1.17
6.	P6	164008	145140	1.13
7.	P7	152076	104880	1.45

8.	P8	188663	146250	1.29
9.	P9	169275	152500	1.11

^aEvaluated by GPC in THF solution at room temperature.

3b.5.5 Fluorescence behavior of synthesized poly-thioamides (P1-P9)

From the fluorescence study, of synthesized poly-thioamide via Willgerodt Kindler multicomponent reaction was found that molecules show a fluorescent nature because of thioamide monomer, which has fluorescent properties. Which is responsible for the greenish-yellow (Figure 3b.16a) appearances, when a solution of polymer (P1) was put under the UV chamber. Further, fluorescent nature was confirmed via fluorescence spectroscopy (Figure 3b.16b), and found that a band at approximately 352 nm appeared for all synthesized polymers (P1-P9).

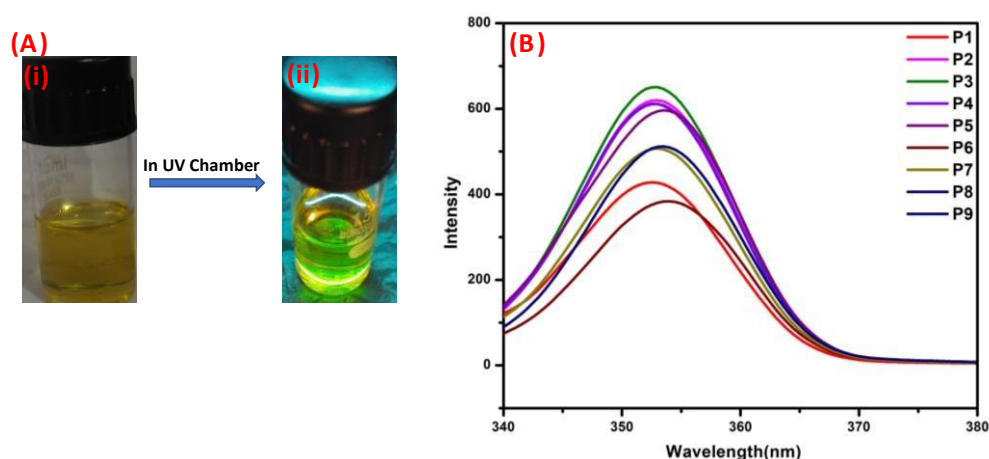


Figure 3b.16. (A) Image of polymer (P1) under UV chamber and (B) Emission profile of the synthesized poly-thioamides (P1-P9) in methanol (10 mM) excited at a wavelength of 340 nm.

3b.5.6 Reusability of Catalyst

At the end of polymerization reaction catalyst was separated with an external piece of magnet and catalyst was washed from distilled water. With 2-3 times proper washing catalyst was dried at an appropriate temperature overnight and was reused for next polymerization reaction. SEM (Figure 3b.17a) and DLS (Figure 3b.17b) experiments were performed to study the surface morphology of recovered catalyst. Undoubtedly, there is a change in the surface morphology of catalyst but it was equally efficient in producing a high yield up to tenth cycle (Figure 3b.18).

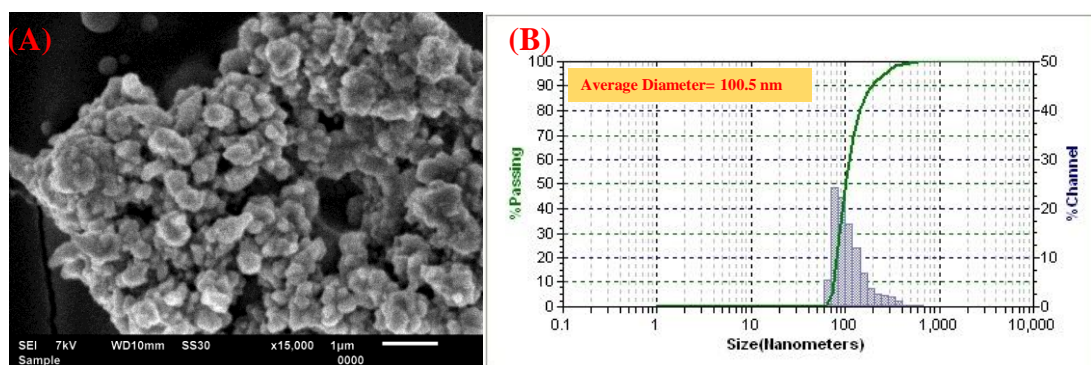


Figure 3b.17: A) SEM image of IL1@Fe₂O₃ after 7th cycle and B) DLS image of IL1@Fe₂O₃ after 7th cycle.

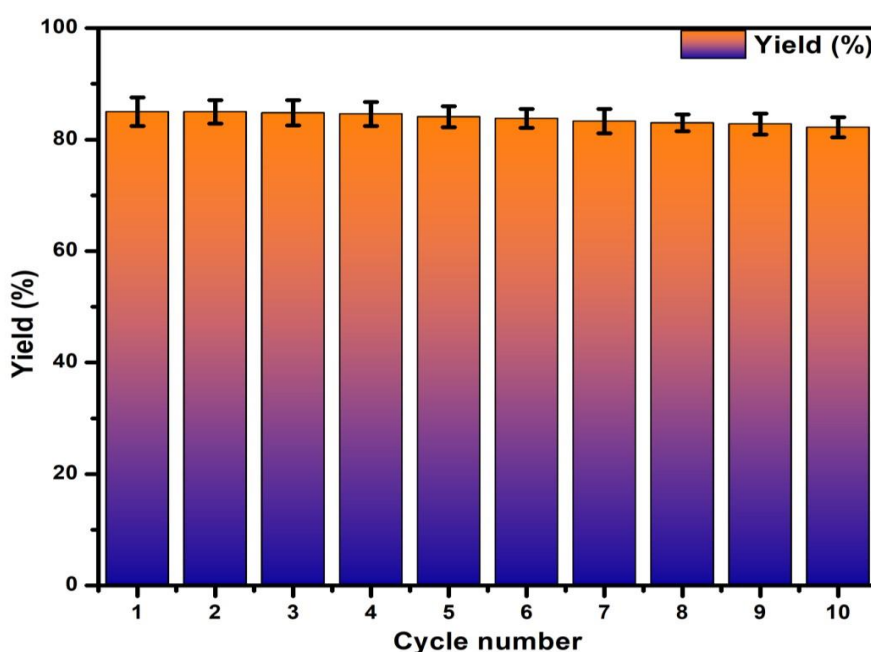


Figure 3b.18: Reusability of the IL1-2@Fe₃O₄ catalyst.

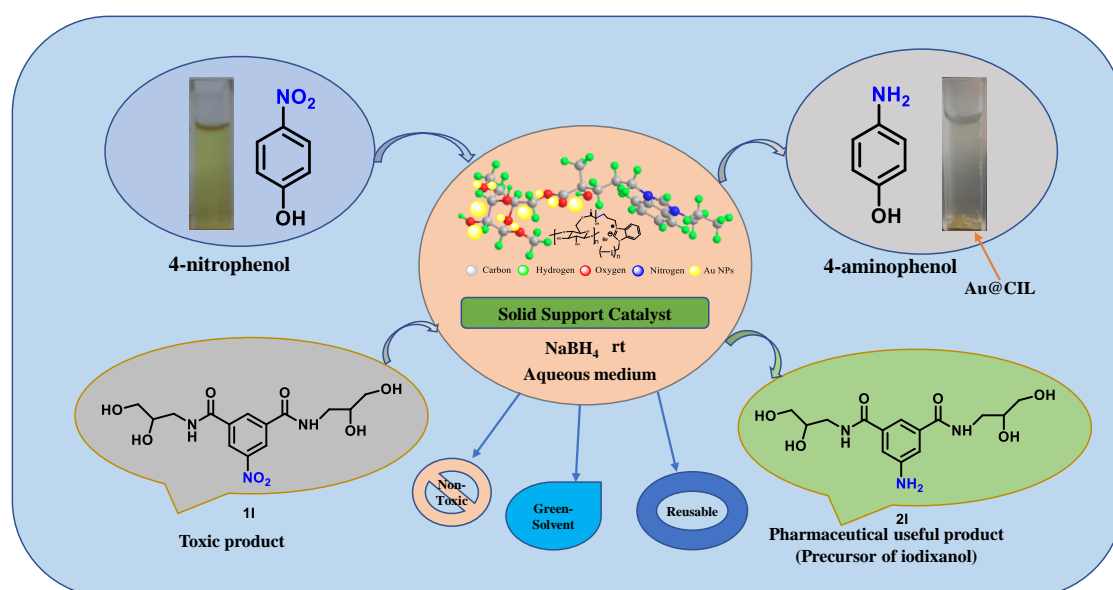
3b.6 Conclusion

A low-cost ionic liquid coated over magnetized iron oxide nanoparticles heterogeneous catalyst was synthesized. The prepared catalyst was used for the synthesis of polymers by means of the Willgerodt–Kindler reaction. Different polymers (P1-P9) were synthesized with various dialdehydes, diamines, and elemental sulfur. The IL1-2@Fe₃O₄ catalyst presented admirable catalytic effectiveness for the polymerization using Willgerodt–Kindler reaction, enabling the selective development of thioamide bonds. The IL1-2@Fe₃O₄ catalyst exhibited high stability, admirable reusability, and

sustained heterogeneity in the reaction media. We believe that the catalyst can endorse the significant synthesis of polythioamides.

Chapter 4

Biomass-derived Ionic liquid functionalized Cellulose embedded with AuNPs as Solid Support Catalyst: An efficient Catalyst for the Synthesis of Iodixanol and Iohexol



Singh, A.; Singh, N.; Kaur, N.; Jang, D. O. *Appl Organomet Chem* 2022, **36**, e6855.

4.1 Aim and Objectives

In response to the increasing need for green and cost-effective catalysts, a novel biomass-derived heterogeneous catalyst that is effective in a number of environmentally friendly applications has been synthesized. The heterogeneous catalyst (Au@CIL), composed of ionic-liquid-functionalized cellulose embedded with Au nanoparticles (NPs), was developed for the selective reduction of the nitro group. The Au NPs are formed by the reduction of Au^{3+} to Au^0 with ascorbic acid while embedded in the solid support system. In water at 30 °C, the heterogeneous catalyst Au@CIL selectively transforms aromatic nitro compounds into the corresponding amines in the presence of other functional groups, such as hydroxy, amino, aldehyde, carboxylic acid, and amide. Thereafter, the catalyst has excellent activity for the synthesis of medically important iodixanol and iohexol.

4.2 Introduction

Metal nanoparticles (NPs) have been studied as efficient catalysts owing to their wide applications in the pharmaceutical industry, production of fine chemicals, biology, CO₂ reduction, CO oxidation, selective hydrogenation, and C–C cross-coupling [1–4]. The dispersion of gold (Au) NPs remained stable for several months [5]. Au NPs with large surface areas can act as heterogeneous catalysts with high reactivity and high selectivity, and they can be recycled without any loss of catalytic activity [7]. They can also be employed in green chemistry because water can be used as a solvent [8]. Because of their high surface energy, AuNPs are endangered to association and aggregation in aqueous phase catalytic reactions [9]. Which results in a change in the shape and size of nanoparticles that may lead to deactivating the surface area and catalytic activity [10]. The main drawback is to restore AuNPs from the reaction mixture which limits their use as catalysts [11].

To overcome these limitations many efforts have been conducted to enhance the catalytic activity of AuNPs. By immobilization of nanoparticles on many materials such as acidic Ta₂O₅, solid support material enhances their stability [12–14]. Due to its renewable nature and hefty reservation on the earth, biomass is a huge energy source and has attracted great attention from scientists [15–17]. Biopolymers and natural polymers including starch, gelatin, cellulose, chitosan, and sodium alginate, all these natural polymers provide solid support in heterogeneous catalysis and show

extraordinary ability toward organic synthesis [18-19]. Cellulose is mostly found in plants, but also in some animals and bacteria [20]. Due to low cost, high oxygen content, and low greenhouse gas emission, it can be used in the pharmaceutical industry, biofuels, synthesis, etc. [21]. Because of spherical and porous beads of cellulose, its catalytic efficacy can be increased to a greater extent by the embedding of metal ion nanoparticles [20]. Moreover, application of cellulose becomes more widened in a chemically modified hydrophobic state [22]. The cross-linking properties and large cavity size of biopolymers help in the insertion of metal with strong binding energy [2]. From last year natural or synthetic polymer is the widely used substance for the stabilization of nanoparticles with a certain affinity toward metals, which are soluble in different solvents [23]. Thus, this solid-supported catalyst is easily separated from a reaction mixture, with proper washing, recovery, and reuse of the catalyst [24]. For supporting and stabilizing the nanoparticles, natural and synthetic polymers are broadly used materials [25]. Because of the unique and distinctive properties of ionic liquids such as wide solubility range, nonflammability, and their properties have been changed by simply a variation of cations and anions, which helps to increase the catalytic activity [26]. Moreover, ionic liquids (ILs) are used to enhance the mechanical and thermal stability of solid support material. CNC-IL hybrid is an admirable support material for metal nanoparticles due to excellent chemical stability, mechanical properties, high surface-to-volume ratio, size, and eco-friendliness [27]. Ionic liquid-based hybrid is recycled easily from reaction mixture and it enhances the adsorption capacity of solid-supported material, which enhances catalytic activity [28].

Many solid-supported materials were reported for stabilization of nanoparticles such as graphene-supported Fe/Ni NPs, SiO₂-supported Cu NPs, COF-supported Pd NPs, polymer-supported Pd, cellulose-supported Ag NPs, etc. [29-36]. There are several other polymers like hydrogel, have been employed as a solid support material for metal nanoparticles [37]. Firstly, metal nanoparticles embedded in material were reduced with suitable reducing agents, to get solid-supported metal nanoparticles-based heterogeneous catalysts [34]. Many catalysts were reported for the reduction of NO₂ such as Cu catalyzed, Ruthenium complexes, NaI/ PPh₃ mediated reduction, MOF, etc. [35]. which require organic solvent, high temperature, toxic reagents, more time consuming, low conversion, and low yield, to overcome all these limitations we propose an ionic liquid functionalized cellulose, embedded with Au nanoparticles heterogeneous

catalyst referred as Au@CIL [37]. Presence of ionic liquid on a solid support system helps in stabilization of Au nanoparticles and prevents agglomeration through creation of a protective environment [38]. After the complete incorporation of ionic liquid into cellulose it no longer remains a true liquid, nevertheless, it is measured as a supported ionic liquid phase [39]. Furthermore, the blocking effect of ionic liquid plays an important role in preventing hydrogen bonding among cellulose [39]. Because of this effect, all free hydroxyl groups help in the embedding of metal nanoparticles through non-covalent interaction [39]. To determine the morphology, activity, selectivity, and stability ionic liquid play an excellent role [40]. A solid-solid solvent-free synthesis route is developed with utilization of sustainable resources, for selective nitro reduction and minimizing the environmental pollution caused by solvents [40]. Prevalence of NH_2 group aliphatic/aromatic in industries, agrochemicals, pharmaceuticals, and dyes inspired us to develop eco-friendly selective strategies for their synthesis [40]. Whereas nitro derivatives are the most common toxic and pollutant dyes found in industrial wastewater [41-42].

Herein, we synthesized an Au NPs embedded solid support catalyst (Au@CIL) for the selective reduction of Nitro compounds, with a simple and facile method. Abundant hydroxyl groups present on the surface of ionic liquid functionalized cellulose help in the adsorption of Au NPs. Ionic liquid stabilized the solid support system by a combination of electrostatic protection layers. Because of the variation of size of Au NPs make them are used as heterogeneous catalysts in wide applications. We found that Au@CIL performed excellent catalytic properties for selective reduction of NO_2 group and recycling with minimum loss of catalytic activity. At last, the synthesized, Au@CIL heterogeneous catalyst was fully characterized and used for selective reduction of the nitro group.

4.3 Experimental Section

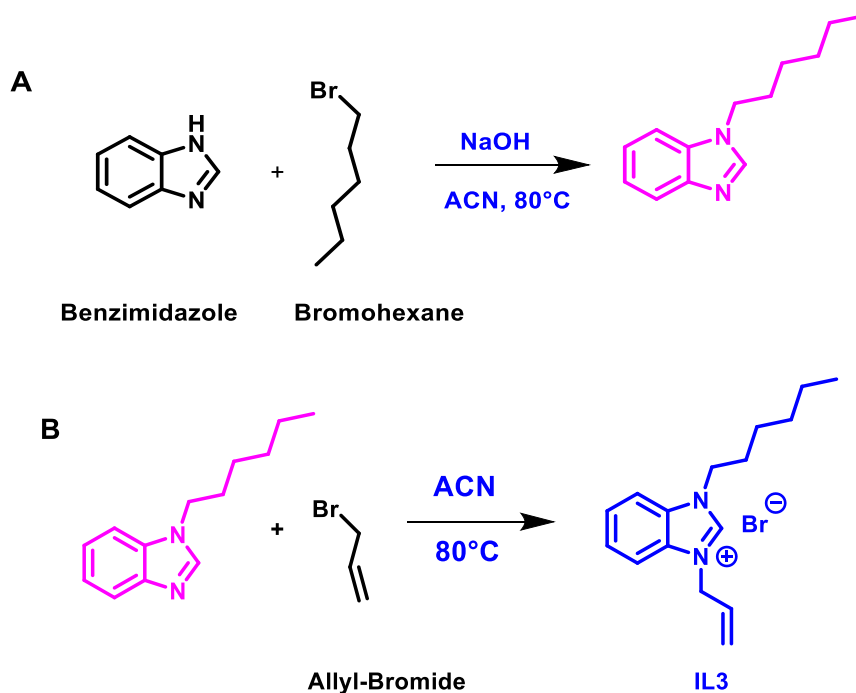
4.3.1 Materials

Benzimidazole, bromo-hexane, Allyl-bromide, and NaOH were used for the synthesis of ionic liquid purchased from Sigma-Aldrich, and the cellulose nanocrystals were isolated from rice straw via acid hydrolysis [43]. Hydrogen tetrachloroaurate (III) trihydrate is used as a source of Au purchased from Sigma-Aldrich. Ascorbic acid used for reduction of Au nanoparticles and NaBH_4 used in reaction were also purchased from

Sigma-Aldrich. Other chemicals such as 4-nitrophenol, 4-nitroaniline, 2-nitrobenzaldehyde, 2-nitrobenzoic acid, 4-nitroisophthalic acid, 3-amino-1,2-propanediol, and 4-nitroisophthalate all purchased from TCI chemicals.

4.3.2 Preparation of Benzimidazole based ionic liquid (IL3)

Firstly, ionic liquid was synthesized (Scheme 4.1) from benzimidazole using a procedure, benzimidazole (1 g) was taken in 100 mL RB and dissolved properly in acetonitrile at 80 °C. As benzimidazole dissolved completely, NaOH (0.5g) was added to a reaction mixture which was continuously stirred for 30 min. White precipitates of reaction mixture were obtained, bromo-hexane (900 μ L) was added and reaction was run overnight at the same temperature. Benzimidazole was functionalized and further reacted with allyl bromide at the same temperature overnight to give an ionic liquid (IL3). The synthesized ionic liquid was fully characterized with ^1H -NMR, ^{13}C -NMR, and HRMS (Figure 4.1-4.3).



Scheme 4.1. (A) functionalization of Benzimidazole and (B) Synthesis of IL3.

^1H NMR (400 MHz, DMSO- D_6) (ASC-1) δ 9.98 (s, 1H), 8.10 (t, $J = 4.2$ Hz, 1H), 7.98 (t, $J = 5.2$ Hz, 1H), 7.63 (d, $J = 9.2$ Hz, 2H), 6.16 – 5.99 (m, 1H), 5.37 (d, $J = 17.0$ Hz, 2H), 5.18 (d, $J = 5.7$ Hz, 2H), 4.48 (t, $J = 7.3$ Hz, 2H), 1.91 – 1.81 (m, 2H), 1.28 – 1.16 (m, 6H), 0.79 (t, $J = 6.9$ Hz, 2H). ^{13}C NMR (100 MHz, DMSO- D_6) δ 142.77, 131.64,

131.38, 127.03, 120.83, 114.36, 49.28, 47.21, 31.09, 28.96, 25.85, 22.35, 14.33. HRMS data [M+H]⁺: calculate 243.1861, found 243.1872.

Elemental Composition Report

Page 1

Single Mass Analysis

Tolerance = 300.0 PPM / DBE: min = -1.5, max = 50.0

Element prediction: Off

Number of isotope peaks used for i-FIT = 5

Monoisotopic Mass, Even Electron Ions

3 formula(e) evaluated with 1 results within limits (all results (up to 1000) for each mass)

Elements Used:

C: 16-16 H: 0-300 N: 0-2

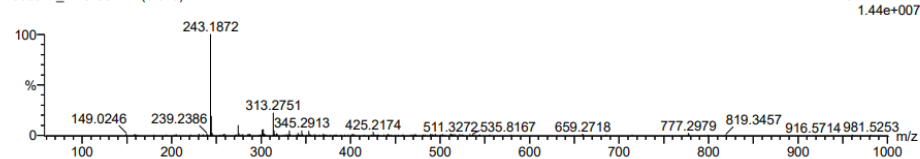
Sample Name : 300921_ASC-351

IITRPR

XEVO G2-XS QTOF

Test Name :

1: TOF MS ES+
1.44e+007



Minimum: -1.5
Maximum: 2.0 300.0 50.0

Mass	Calc. Mass	mDa	PPM	DBE	i-FIT	Norm	Conf(%)	Formula
243.1872	243.1861	1.1	4.5	6.5	2536.3	n/a	n/a	C16 H23 N2

Figure 4.1: HRMS data of ASC-1

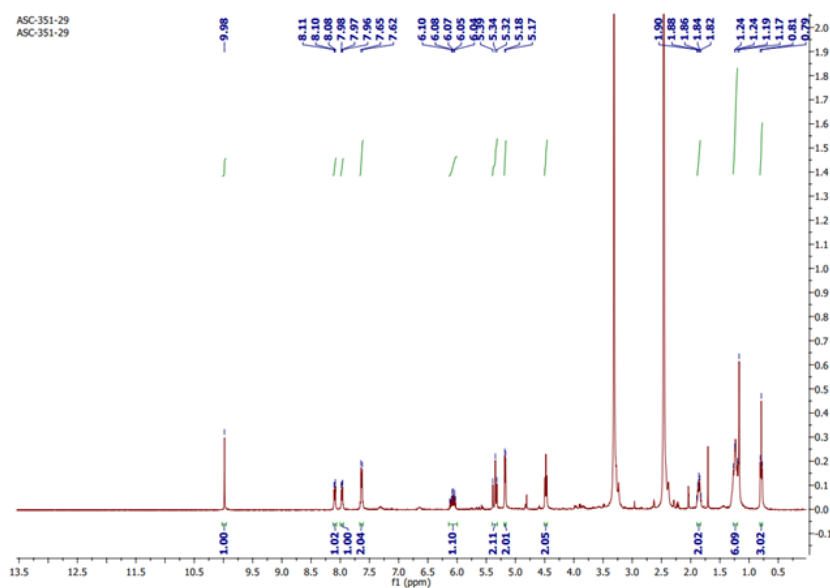


Figure 4.2: ¹H-NMR of ASC-1

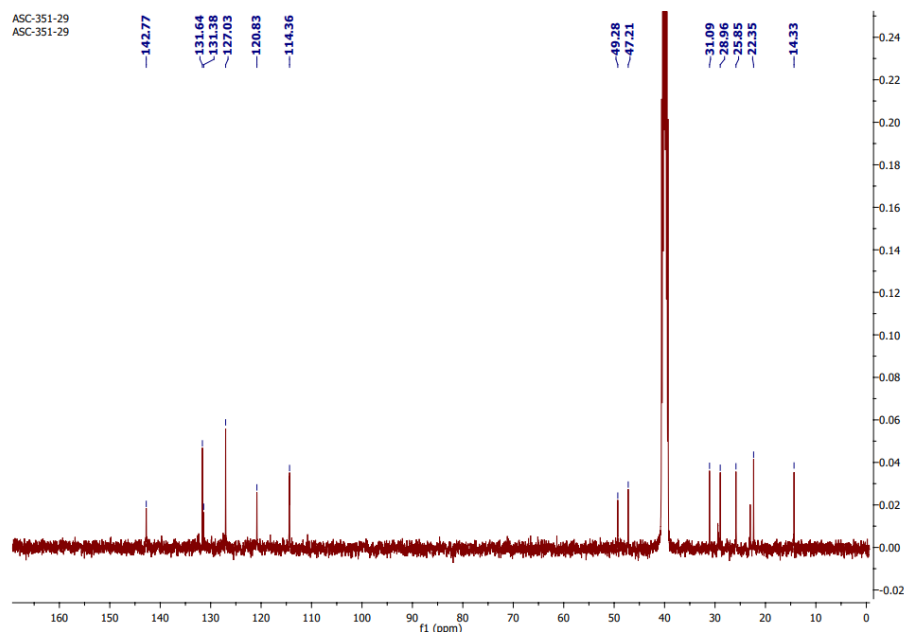


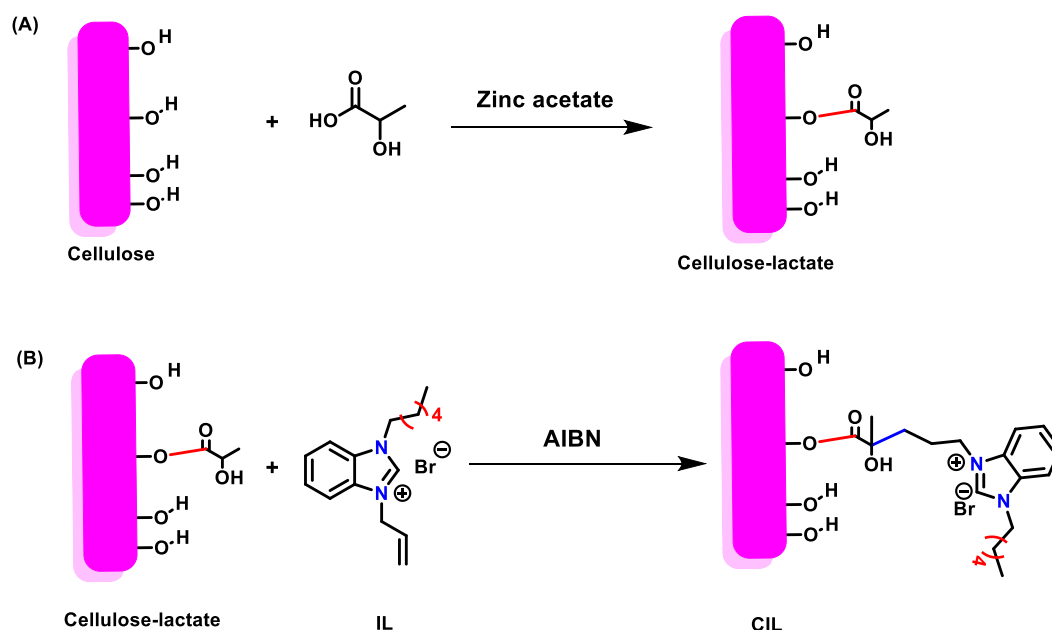
Figure 4.3: ^{13}C -NMR of ASC-1

4.3.3 Preparation of Cellulose-Ionic liquid hybrid

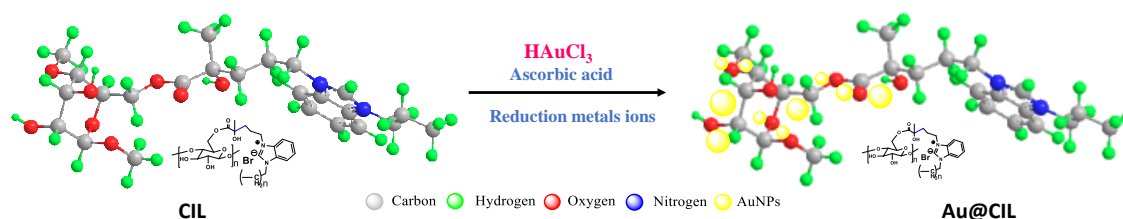
Cellulose was extracted from biomass as reported in our previous work [45], and further used as a precursor for the preparation of a hybrid in solid form. For this cellulose (1 g) was reacted with linker (lactic acid) in the presence of zinc acetate via formation of an ester bond (Scheme 4.2). Azobisisobutyronitrile (AIBN) 0.2 g was added in a mixture of lactic acid functionalized cellulose and ionic liquid (0.4 g), which generated a radical reaction between hydroxyl group of lactic acid and allyl group of ionic liquid result in formation of cellulose-ionic liquid hybrid (CIL).

4.3.4 Preparation of Au@CIL hybrid

For the preparation of Cellulose-Ionic liquid/Au nanohybrid (Scheme 4.3), in a clean beaker, CIL hybrid (1g) and HAuCl_3 (0.1g) were taken with continuous stirring for 30 min at room temperature to make a homogenous solution. 1mL ascorbic acid (50 μM) was added dropwise in a homogenous solution color changed to light pink indicating a reduction of Au^{+3} into Au^0 nanoparticles. Au@CIL hybrid was obtained which was further washed with distilled water to remove unreacted material.



Scheme 4.2. Functionalization of cellulose with (A) Lactic acid and (B) IL.



Scheme 4.3. Embedded of AuNPs on solid support material.

4.3.5 Characterization method

Zeta (ζ) potential is used to determine charge distribution on the molecule, Jeol instrument working at 400 MHz for ^1H NMR and 100 MHz for ^{13}C NMR. The chemical shift was measured in ppm with tetramethyl silane as an internal reference. High-resolution mass spectroscopy (HRMS) was performed using a Xevo G2-XS QTOF (WATERS) mass spectrometer. Powder X-ray diffraction (PXRD) measurements were performed using a Miniflex (Rigaku) diffractometer. Fourier-transform infrared (FTIR) spectra were recorded using the Hyperion 2000 (Bruker Optics) FTIR system. To study the surface morphology JEOL JSM-6610-LV was used for scanning electron microscopy (SEM), energy dispersive spectroscopy (EDS), and elemental dot mapping. A UV-visible absorption spectrophotometer (Shimadzu UV-2400) was used throughout the experiment with a cuvette made up of quartz.

4.3.6 Catalytic activity of Au@CIL hybrid for selective Nitro-Reduction

80 μL of 0.1 M NaBH_4 was taken in a 10 mL vial, with 2.8 mL of nitro derivatives (0.04 mM aqueous solution) which is going to reduce. Further, 0.04 g of Au@CIL was added as a heterogeneous catalyst. The reaction mixture was sonicated properly for 5 min at room temperature. Catalytic reduction of nitro derivatives was recorded with a UV-visible spectrophotometer and background correction was done using denoised water as a reference.

4.4 Result and Discussion

Formation of Au@CIL heterogeneous catalyst mainly involved three steps (Scheme 4.2 & 4.3), the preparation of ionic liquid, functionalization of cellulose, and formation of Au NPs on the surface of cellulose-ionic liquid, and the whole assembly was fully characterized using different techniques.

4.4.1 Characterizations

4.4.1.1 Fourier Transform Infrared-Spectroscopy (FTIR)

Data of neat cellulose was explained in figure 4.4(AI) major peaks at 3336, 1632 and 1027 cm^{-1} confirm the presence of O-H stretching, bending, and C-O-C pyranose ring skeletal stretching of cellulose. A signal at 2910 cm^{-1} attributed to asymmetric vibration of $-\text{CH}_2$. Broadening of -OH peaks explains the inter and intramolecular hydrogen bonding. Vibrational peaks at 1157, 1107, 1047, 1025, and 885 cm^{-1} are attributed to asymmetric stretching of -COC bridge, asymmetric stretching of anhydrous glucose ring, -CO stretching in a plane, -CH bending and -CH deformation of cellulose respectively. As lactic acid reacts with a hydroxyl group of cellulose ester bond formation confirms a new peak [Figure 4.4(AII)] of carbonyl at 1650 cm^{-1} . Further, when ionic liquid reacts with cellulose via lactic acid two new peaks [Figure 4.4(AIII)] start appearing one at 1646 cm^{-1} and another at 1427 cm^{-1} confirming the -NCN- group of ionic liquid. Thereafter, FTIR data were extended to examine the structural changes occurring when Au nanoparticles were embedded on the cellulose-ionic liquid surface. From the spectra, we found that the stretching vibration of -OH shifts from 3338 to 3311 cm^{-1} also bending vibration from 1646 to 1638 cm^{-1} respectively [Figure 4.4(BII)].

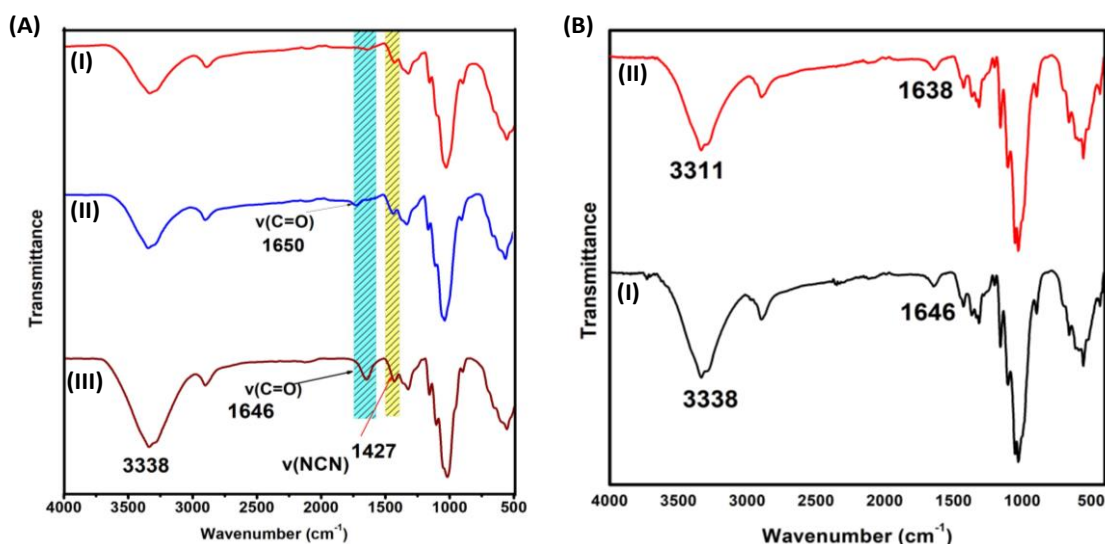


Figure: -4.4: A) FTIR Spectra of (I) Cellulose, (II) Cellulose-lactic acid, (III) Cellulose-ionic liquid, and B) (I) Cellulose-ionic liquid, (II) Au@CIL.

This shift is because, of increased hydrogen bonding between hydroxyl groups on hybrid and Au nanoparticles. Hydroxyl group and ionic liquid available on assembly are suitable reaction sites for nucleation and growth of Au nanoparticles. Electrostatic interaction/hydrogen bonding plays an excellent role in attachment between the hybrid and material present in reaction mixture [44]. Thereafter to confirm the binding of Au NPs with assembly energy of hydrogen bond was calculated for the free hydroxyl group and after binding with Au NPs using equation-4.1:

$$E_H = K^{-1} \left(\nu_0 - \frac{\nu}{\nu_0} \right) \quad \dots\dots\dots 4.1$$

ν_0 is the frequency of the free hydroxyl group (3650 cm^{-1}), and ν is the frequency of hydroxyl and frequency of hydroxyl group after binding with Au NPs. K is constant ($3.8 \times 10^{-3} \text{ kJ}^{-1}$). After calculation, it was found that E_H was 13.8 and 14.1 kJ^{-1} for cellulose and Au@CIL respectively. Both evidence of shifting of -OH frequency and increase of energy indicate interaction of -OH with Au nanoparticles.

4.4.1.2 Crystal structure and crystallinity-X-Ray diffraction

PXRD was used to determine the variation in crystal structure and planes of materials as a result of Au nanoparticles embedded in a cellulose-ionic liquid hybrid (Figure 4.5). The pattern [Figure 4.5(AI)] shows characteristic peaks at $2\theta = 16.04^\circ$ (110), 22.46° (200), and 34.38° (004) which corresponds, to the lattice planes for cellulose.

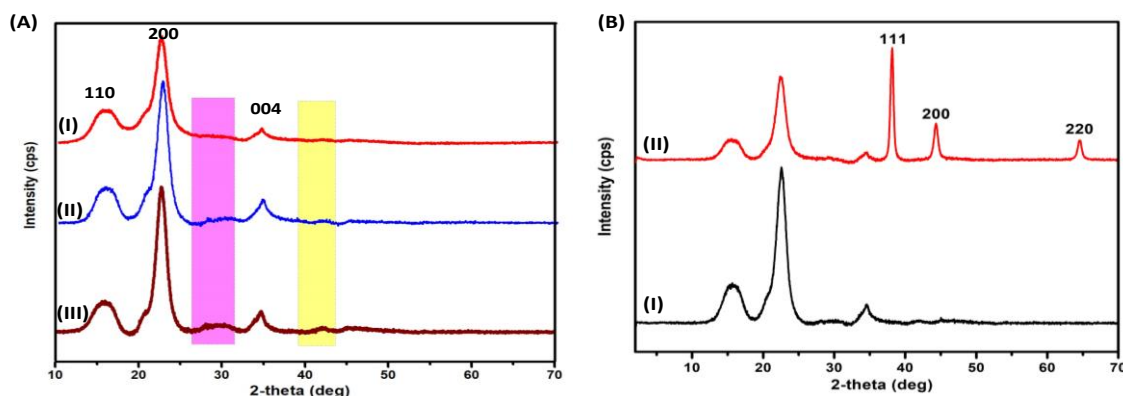


Figure: -4.5: A) PXR D Spectra of (I) Cellulose, (II) Cellulose-lactic acid, (III) Cellulose-ionic liquid, and B) (I) Cellulose-ionic liquid, (II) Au@CIL.

Further, the reaction of cellulose with lactic acid and ionic liquid appearing in two more plans figure 4.5(AI & AII) at $2\Theta = 29^\circ$ and 43° indicates the functionalization of cellulose with ionic liquid. Two significant changes were observed when Au NPs embedded in a cellulose-ionic liquid hybrid. Further, the crystalline nature of Au@CIL was also confirmed, by appearing of three additional peaks [Figure 4.5(BII)] at $2\Theta = 39^\circ$ (111), 45° (200), and 66° (220) which corresponds to the FCC crystalline structure of Au nanoparticles. All obtained peaks from XRD are in good agreement with literature and most intense peak obtained at (111) plane suggests the growth of Au NPs over cellulose-ionic liquid assembly.

4.4.1.3 Surface Morphology Analysis

Scanning Electron Microscopy (SEM) images reveal the type of surface morphology which varies from particle-to-particle arrangement in the sample. Therefore, to reveal this morphology, various samples were examined under SEM analysis. The dense structure (Figure 4.6a) of cellulose-ionic liquid is because of interlinked network assembly. Furthermore, SEM analysis (Figure 4.6b) was performed after embedding of AuNPs over cellulose/ionic liquid polymer. EDX spectra (Figure 4.6c-d) displayed that Au nanoparticles were embedded over the surface of a cellulose-ionic liquid. From these spectra, it was found that elemental composition of Au@CIL includes carbon (53.75 %), oxygen (42.21 %), nitrogen (2.10 %), and gold (1.94 %). Elemental dot mapping (Figure 4.7d-g) also confirms the uniform distribution of elements on Au@CIL. This further supports that Au nanoparticles were embedded in Cellulose-ionic liquid support. Further to check the shape of gold nanoparticles, embedded in cellulose-ionic liquid HRTEM

was performed (Figure 4.7a-c), from the figure it was found that AuNPs dispersed over the material without any aggregation (Figure 4.7a) and it was clear that AuNPs were successfully formed on the surface of material with perfect shape and size. Fivefold pentagonal symmetry can also be seen in figure 4.7c, two more symmetries, trigonal and hexagonal also appeared during formation of AuNPs (Figure 4.7b).

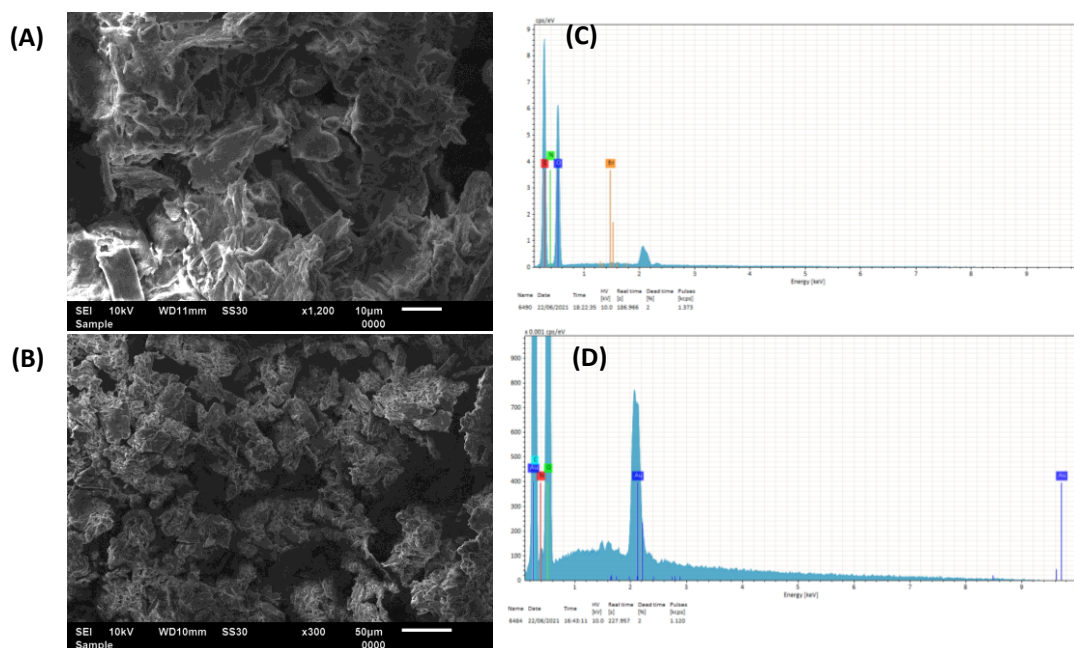


Figure 4.6: SEM images of A) Cellulose-ionic liquid and B) Au@CIL. EDX of C) Cellulose-ionic liquid and D) Au@CIL.

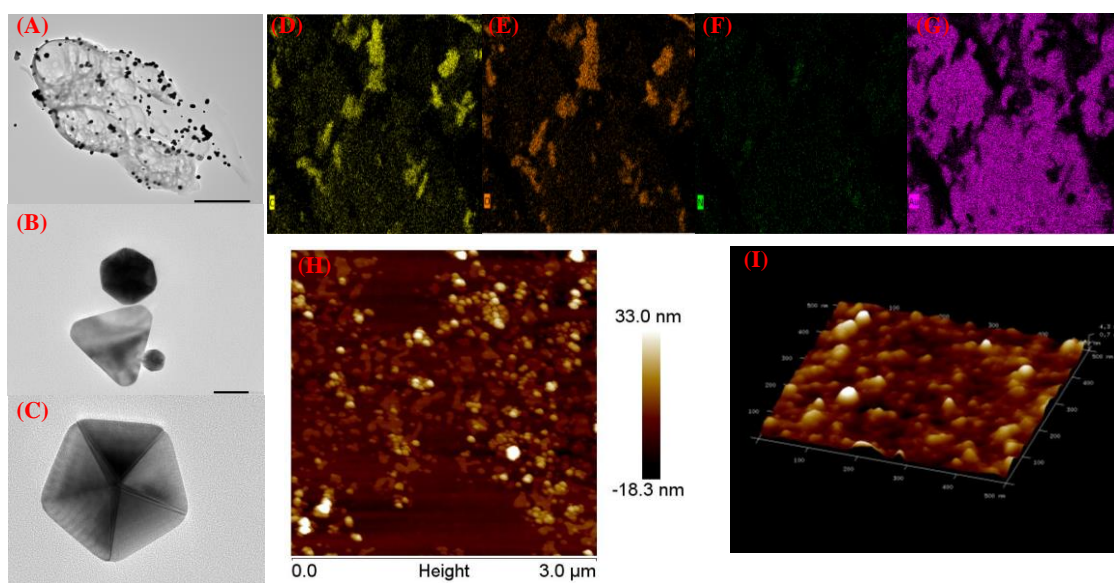


Figure 4.7: HRTEM of a) Au@CIL, b) trigonal and hexagonal shape of AuNPs embedded on CIL Surface, and c) pentagonal shape of AuNPs embedded on CIL

Surface. Elemental dot mapping of Au@CIL shows uniform distribution of all atoms

d) Carbon (yellow), e) Oxygen (orange), f) Nitrogen (green), and g) Gold (violet).

AFM images of Au@CIL in h) 2D and i) 3D.

Atomic Force Microscopy (AFM) was performed to get further insight into the surface morphology of the catalyst, which reveals 2-dimensional (Figure 4.7h) and 3-dimensional (Figure 4.7i). AFM images of height profile 3.0 μm , reveal the star-like AuNPs on a surface which is responsible for the roughness of Au@CIL and morphology confirmed the AuNPs with an average diameter of 30 nm. AuNPs embedded cellulose-ionic liquid hybrid are advantages for their application in selective nitro reduction.

4.4.1.4 Zeta potential

Thereafter, to check the dispersibility of nanoparticles Zeta potential plays an important role. As only hydroxyl group is present on the cellulose surface it shows negative zeta potential Figure 4.8a at the whole range of pH. After the functionalization of cellulose with ionic liquid zeta potential value was reversed from -39 mV to +43 mV, which indicates the successful functionalization of cellulose. Above 35 mV zeta potential value, nanoparticle suspension maintains stability. Therefore Cellulose-ionic liquid has wide dispersibility in water at a wide range of pH. Blocking effect of ionic liquid plays an important role in preventing hydrogen bonding among cellulose in the solid state. The low value of zeta potential at high acidic and basic medium also reveals that it is prone to solidify under these conditions because of charge shielding. Moreover, the effect of Au nanoparticles on the zeta potential of cellulose-ionic liquid was studied (Figure 4.8b). From spectra, it was found that zeta potential increases as Au nanoparticles are embedded on a cellulose-ionic liquid surface.

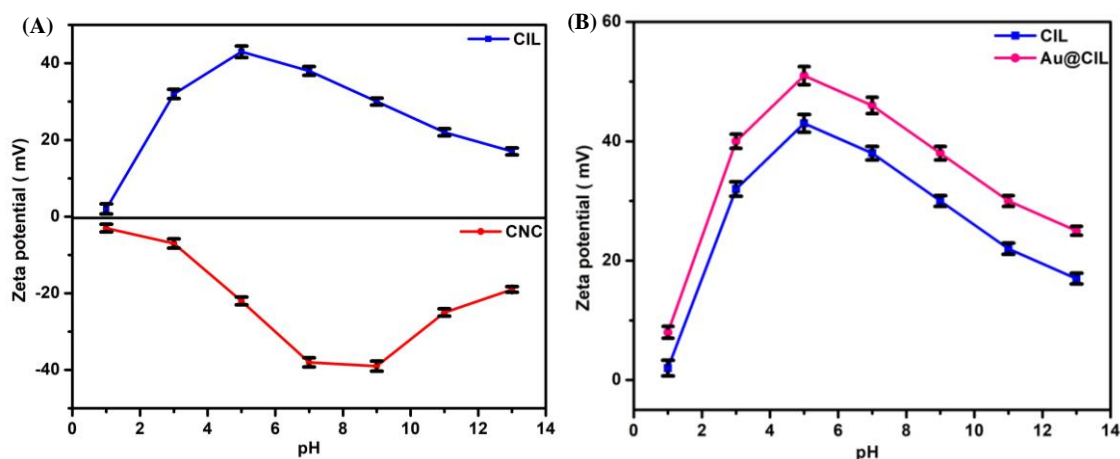
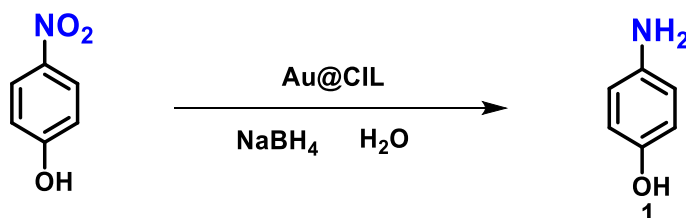


Figure 4.8: Zeta potential A) Comparison of CNC with CIL and B) Comparison of CIL with Au@CIL as a function of pH values.

A primary mechanism for the formation of Au@CIL was proposed by considering all the characterizations such as FTIR, PXRD, SEM, EDX, Elemental dot mapping, Zeta potential, HRTEM, and AFM. Ionic liquid increases high surface-to-volume ratio. Because of the blocking effect, a large number of hydroxyl groups are used for Au nanoparticle's adsorption and tight attachment to the surface. Au^{+3} reduces to Au^0 , after addition of ascorbic acid, and color changes to pink, which indicates the successful reduction. Solid phase hybrid presents the synthetic pathway that impeded the mobility of Au nanoparticles, stabilized the nanoparticles, and inhibited the particle's growth.

4.4.2 Catalytic activity of Au@CIL for selective nitro reduction

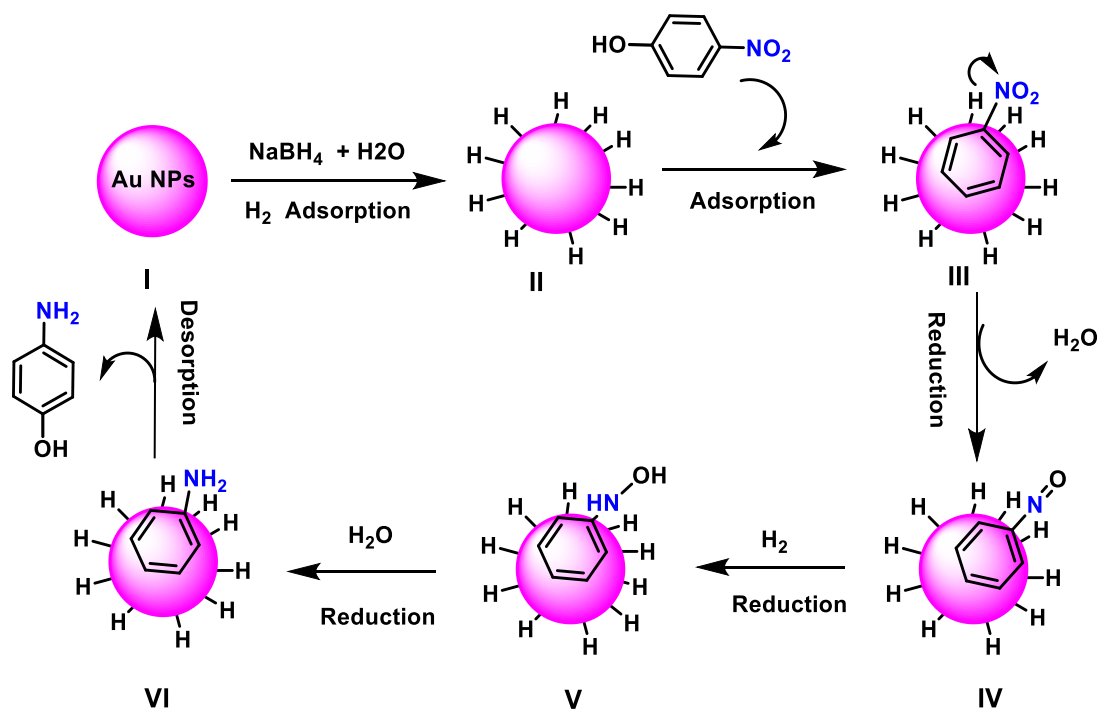
To carry out the reduction reaction 3.0 mL of 0.4 mM aqueous solution of 4-nitrophenol was taken in a glass vial and 100 μL of 0.1 M NaBH_4 was added. Further reaction mixture was sonicated for 2 min to make a homogenous solution. To this mixture, Au@CIL (0.04 g) was incorporated as a heterogeneous catalyst. From this analysis, we got greater than 99 % yield within 12 min of reaction time at room temperature (Scheme 4.4).



Scheme 4.4: Model reaction for the reduction of 4-nitrophenol in presence of Au@CIL.

4.4.3 Mechanistic insight

Taking 4-nitrophenol, a representative example, it reduces into its corresponding amino derivatives, and reaction proceeds via formation of some intermediate, such as nitroso and N-phenylhydroxylamine (Scheme 4.5). Such products lead to a reduction in nitro derivatives. To assume mechanism, time-dependent spectra of 4-nitrophenol were recorded via UV-visible spectroscopy using NaBH_4 in presence of Au@CIL catalyst. After 2 min a new band was noted at 285 nm which corresponds to 4-aminophenol.

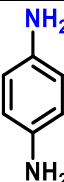
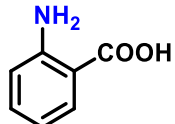
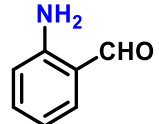
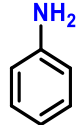
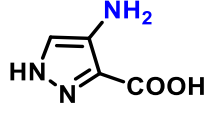
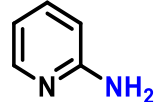



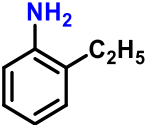
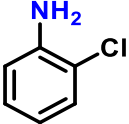

Scheme 4.5: Proposed reaction mechanism for nitro reduction taking 4-nitrophenol as an example.

After obtaining all evidence in support of the mechanism, reduction of different nitro derivatives was carried out. We have chosen the nitro aromatic derivatives because of their great interest. Selective reduction of nitro derivatives may be the building block for synthesis of large numbers of chemicals. In starting reduction of 4-nitrophenyl was carried out and time-dependent titration was recorded in UV-visible spectroscopy (Figure 4.9). Reduction of 4-nitrophenol was carried out by NaBH_4 , in the presence of Au@CIL heterogeneous catalyst. At the start of reaction absorbance band at 401 nm faded gradually. Meanwhile, a new peak starts appearing at 298 nm, indicating the formation of 4-aminophenol (Figure 4.9) and intensity of peak increasing with reaction time. Further change in color from yellow to colorless was also evidence for reduction of 4-nitrophenol and 94 % conversion was carried out within 12 min at room temperature. Same reaction was run in absence of Au NPs i.e., using NaBH_4 and cellulose, and reaction was monitored for several days. No changes in spectra were observed, significant that no reaction occurred. Similarly, various aromatic nitro derivatives were used to reduce into their corresponding amines, and results are summarized in table-4.1 (2-11). Conversion of these compounds to respective amine was achieved at room temperature with high selectivity. 4-fluoronitrobenzene and 2-chloronitrobenzene is easily reduced into their corresponding amine with high

percentage of yield (table-4.1, entry 9-10). Thereafter, when bromine is substituted on nitrobenzene yield of 4-bromoaminobenzene was decreased (table-4.1, entry-7). Electron withdrawing group (EWG) such as carboxylic acid also decreases the product yield, this is probably due to EWG withdrawing the electron density from a nitro group which destabilizes the intermediate (table-4.1, entry 2-5). Electron donating groups (EDG) such as amine, hydroxy and alkyl groups increase the product yield, this is because EDG stabilizes the intermediate via donating electron density to nitro group (table-4.1, entry 1-8).

Table-4.1 Reductions of various aromatic nitro derivatives into corresponds amines using Au@CIL as the heterogenous catalyst.

$\text{Ar}-\text{NO}_2 \xrightarrow[\text{NaBH}_4, \text{H}_2\text{O}]{\text{Au@CIL}} \text{Ar}-\text{NH}_2$ <p style="text-align: right;">2-11</p>			
Entry	Aromatic amines	Product	Yield ^a (%)
1.		2	>99
2.		3	98
3.		4	99
4.		5	>99
5.		6	92
6.		7	98

7.		8	95
8.		9	>99
9.		10	>99
10.		11	>99

^a Isolated yield

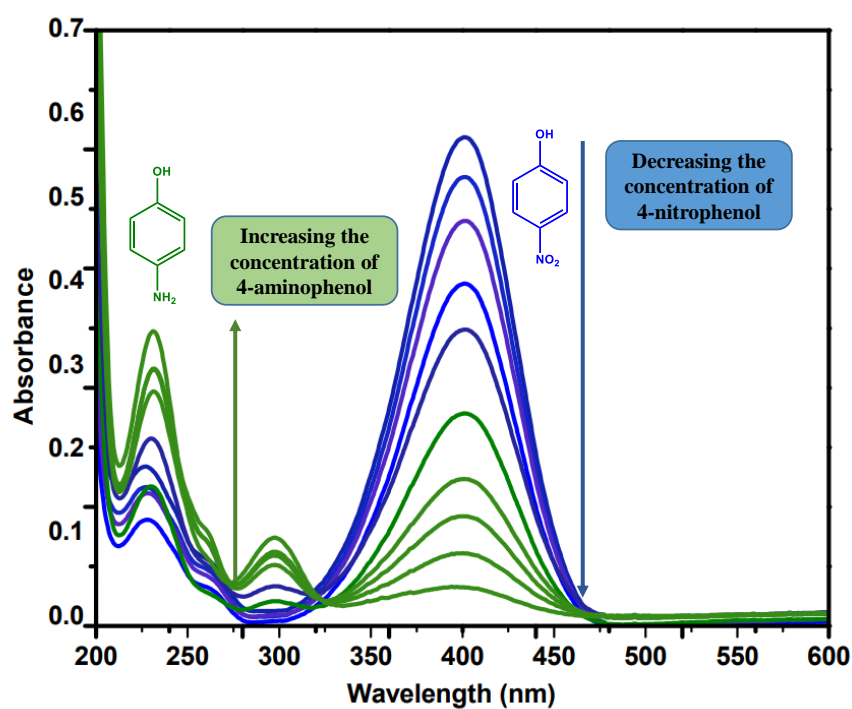


Figure 4.9: Time-dependent UV-visible spectra of 4-nitrophenol reduction by Au@CIL.

During the reduction of 2-nitrobenzaldehyde at Au@CIL catalytic surface led to formation of 2-aminobenzaldehyde illustrated by UV-visible titration shown in figure-

4.10(a). As reduction was started, the original band of 2-nitrobenzaldehyde at 235 nm shifted to new spectra having to band at 285 nm and 306 nm which correspond to 2-aminobenzaldehyde. UV-visible spectra of parent compound and reduced compound are clearly separated [Figure-4.10(a)]. Furthermore, new spectra start appearing with a band at 275 nm.

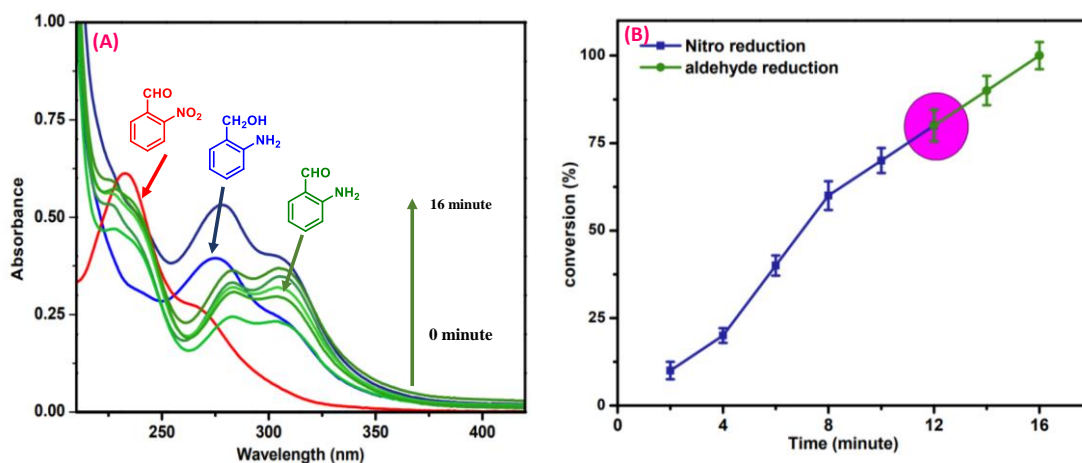


Figure 4.10: A) Time-dependent UV-visible spectra of 2-nitrobenzaldehyde reduction by Au@CIL and B) time dependent reduction of 2-nitrobenzaldehyde.

From study, it was found that corresponding band at 275 nm indicates the formation of 2-amino-benzyl alcohol. To monitor this selective reduction, again time-dependent conversion was monitored (Figure-4.10b). From figure, it was found that after complete reduction of nitro group at 12 min, reduction of aldehyde also started. Therefore, from this titration, it was concluded that reduction of nitro group in presence of aldehyde is time-dependent and reduction of aldehyde starts, as a nitro group is reduced completely. Furthermore, catalytic activity was checked in presence of an amine group and titration was recorded in UV-visible spectra where absorption band of 4-nitro-aniline at 381 nm faded gradually and intensity of band at 239 increased during conversion with a new band at 307 nm, start appearing which corresponds to formation of benzene-1,4-diamine (Figure 4.11(a)). Thereafter, catalyst was used to reduce nitro group in presence of a carboxylic group, which was monitored through absorption spectra. From spectra, it was found that a single band of 2-nitrobenzoic acid was obtained at 272 nm (Figure 4.11(b)). Further during titration, a new band starts appearing at 308 nm, this spectrum

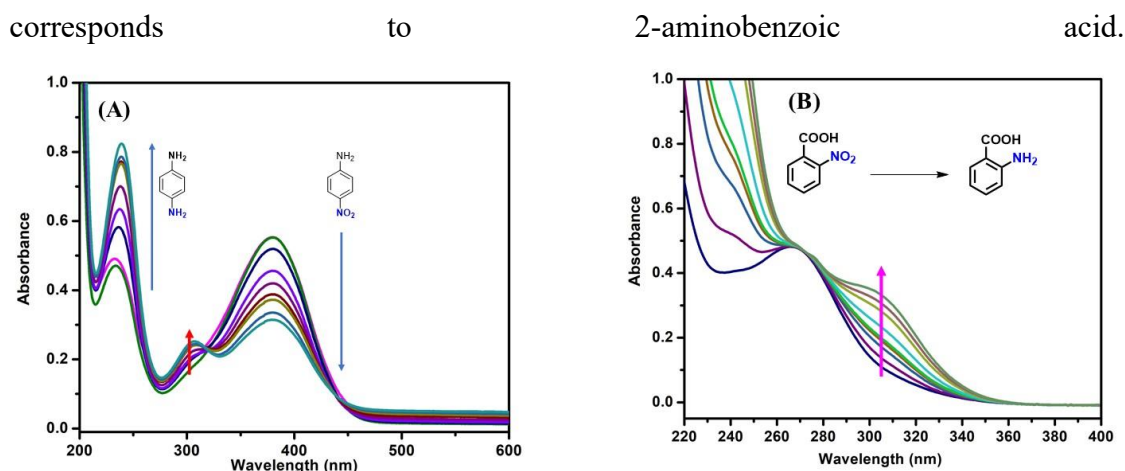
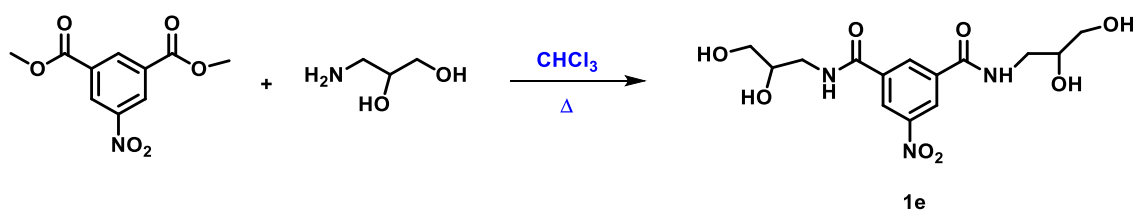


Figure 4.11: A) UV Absorption titration curve of 3-nitroaniline and B) 2-nitrobenzoic acid.

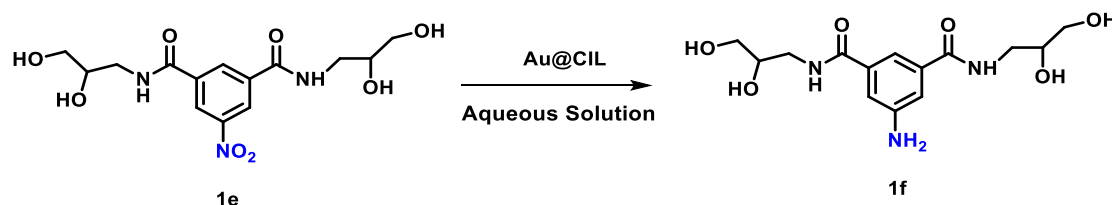
Taking all these points in view and reduction ability of Au@CIL, we synthesized (1e) a nitro-based compound (Scheme 4.6) from dimethyl-isophthalate in lieu of medical importance. For this dimethyl-isophthalate (1 mmol, 194.2 mg) and 3-amino-1,2-propanediol (1.2 mmol, 109.3 mg) were taken in a 50 mL round bottom flask. Further reaction mixture was dissolved in chloroform (anhydrous) and was refluxed for 4 hours. Synthesized derivative (1e) was characterized with D-mass (Figure A39), ^1H -NMR (Figure A40), and ^{13}C -NMR spectroscopy (Figure A41). Direct use of 1e is toxic and harmful for human beings, because of its serious side effect.



Scheme 4.6: Formation of nitro derivatives of dimethyl-isophthalate.

So, it is important to reduce this derivative into respective amino compounds, which have a lot of medicinal importance [46-48]. Keeping in view that reduction should be economically favorable, for this purpose, we use Au@CIL heterogeneous catalyst for their conversion (Scheme 4.7), and reduction of 1e was carried out using the procedure mentioned above. Further, reduced compound was characterized through D-mass (Figure A42), ^1H -NMR (Figure A43), and ^{13}C -NMR spectroscopy (Figure A44). During ^1H -NMR spectroscopy, a new peak appeared ($\delta=5.45$), which corresponded to $-\text{NH}_2$ group formation and all other aromatic protons shifted towards unfilled. After that

reduction efficiency of Au@CIL was compared with reduction efficiency of highly expensive palladium oxide (PdO) catalyst and found that Au@CIL is highly effective over PdO [49]. Catalytic activity of each catalyst was monitored through LCMS technique shown in figure-4.12.



Scheme 4.7: Reduction of nitro derivatives of dimethyl-isophthalate by Au@CIL.

In LCMS spectra a peak starts appearing at a retention time of 3.77 which corresponds to formation of 1f and its intensity increases with time. Some extra peaks were also observed in spectra which corresponds to intermediates (Scheme 4.5) formation. Figure-4.12a shows nitro reduction with PdO within a time interval of five minutes, this reduction was compared when titration was carried out with Au@CIL (Figure 4.12b). Further, to calculate the reduction ability, we have done the LCMS analysis using the well-known reducing agent i.e., PdO, and synthesized Au@CIL. From the LCMS analysis, we have observed that the time taken for reduction using PdO was 30 min whereas the synthesized Au@CIL took 5 min for the same percentage of conversion of nitro group to amino group (Figure A51).

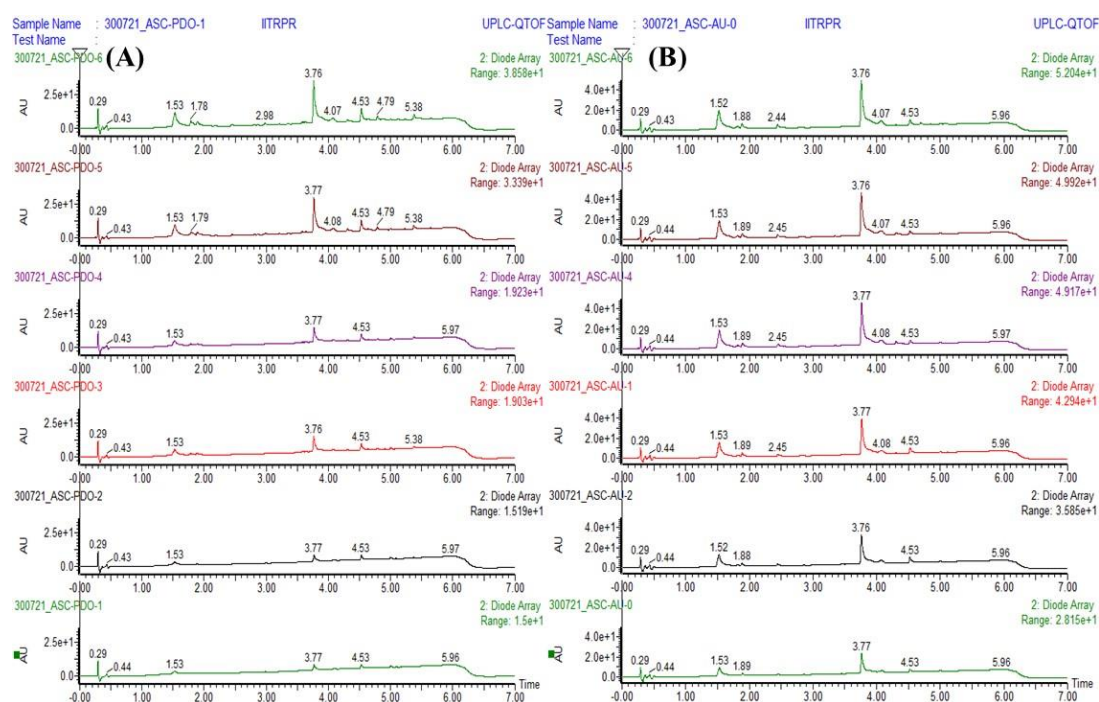
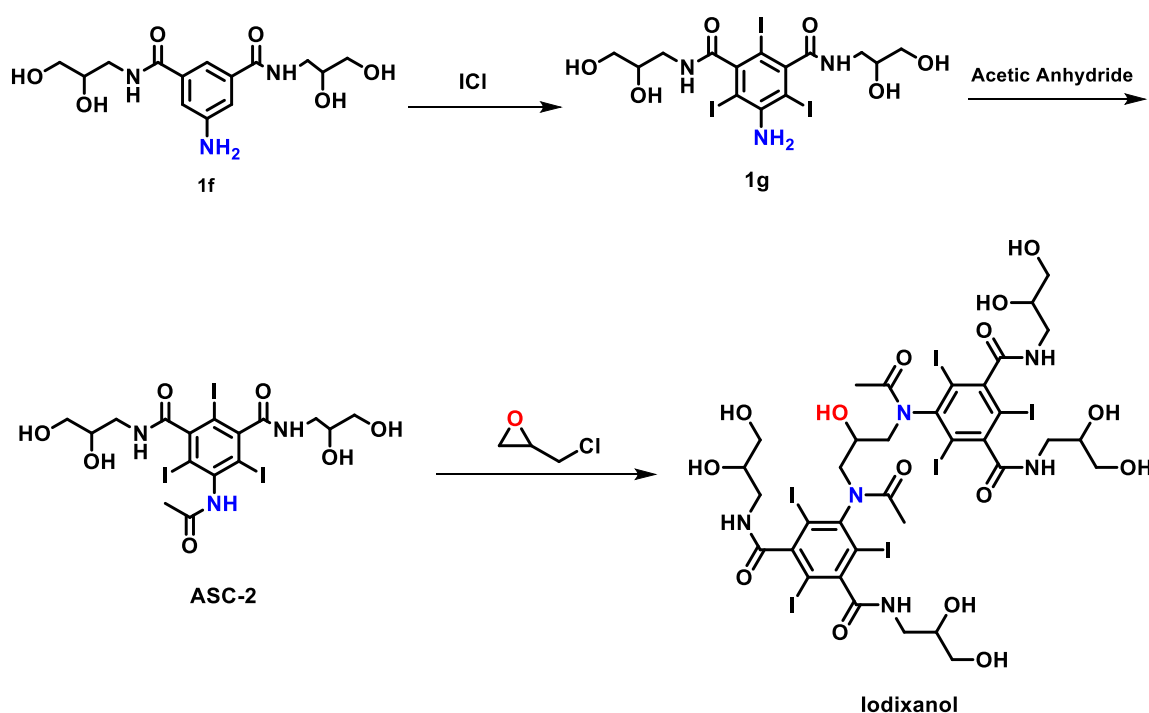


Figure 4.12: Comparative LCMS titration during reduction of 1e with a) PdO and b) Au@CIL.

4.4.4 Synthesis of iodixanol

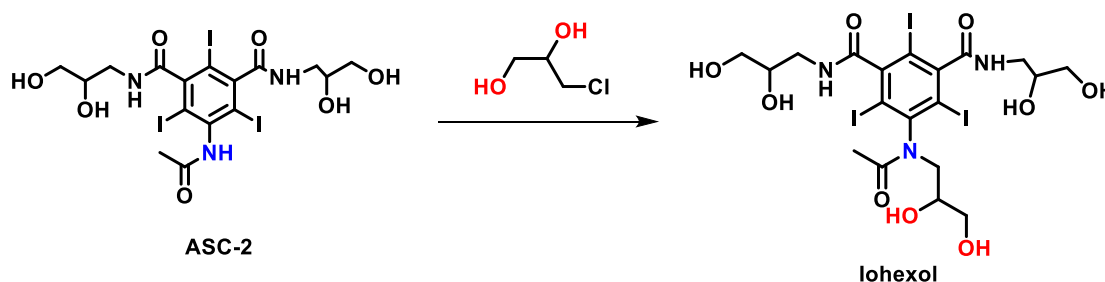
This is a multistep reaction used for the synthesis of iodixanol. compound (1f) synthesis in scheme-4.7, after reduction of compound (1e) was used for the synthesis of iodixanol (Scheme 4.8). To carry out the synthesis firstly compound (1f, 1eq) is reacted with iodine monochloride (ICl, 3.3eq) in alcoholic solvent (MeOH, 10mL). Reaction mixture was refluxed at 65 °C with continuous stirring for four hrs. After complete workup of reaction mixture, compound (1g) was extracted. Further, compound (1g, 1eq) reacts with acetic anhydride (1.2eq) in presence of sodium hydride to give compound (ASC-2). Thereafter, iodixanol drug was synthesized via dimerization of compound (ASC-2). Dimerization was carried out by taking ASC-2 (1eq), dissolved in alcoholic solvent (MeOH, 10mL). A catalytic amount of sodium hydride was added to the solution to enhance the reactivity of ASC-2 and epichlorohydrin (1.2eq) was added to reaction mixture, as a linker for dimerization of ASC-2. The reaction mixture was refluxed at 60 °C for 12 hrs with continuous stirring. After a complete workup of reaction mixture iodixanol was obtained, which was further characterized with ¹H-NMR, ¹³C-NMR, and HRMS spectroscopy. Molecular ion peak in the HRMS spectrum (Figure-A52) at m/z 1550.7211 corresponds to [M+H], confirming the formation of iodixanol.



Scheme 4.8. Synthesis of Iodixanol.

4.4.5 Synthesis of iohexol

Synthesized compound ASC-2 (Scheme 4.8) was further used for the synthesis of iohexol (Scheme 4.9). ASC-2 100mg (1.0 eq) was weighed and dissolved in 10 mL of pure methanol. The catalytic amount of sodium hydride (5 mg) was added to a solution to trigger the reaction. The reaction mixture was refluxed for 5 min over a magnetic stirrer. Thereafter, 12.6 μ l (1.2 eq) of 3-chloro-1,2-propanediol was added and refluxed for 4 hrs. After a complete workup of reaction mixture iohexol was obtained, which was further characterized with ^1H -NMR, ^{13}C -NMR, and HRMS spectroscopy (Figure A55-A57). The molecular ion peak in the HRMS spectrum (Figure A55) at m/z 821.8900 corresponds to $[\text{M}+\text{H}]$, confirming the formation of iohexol.



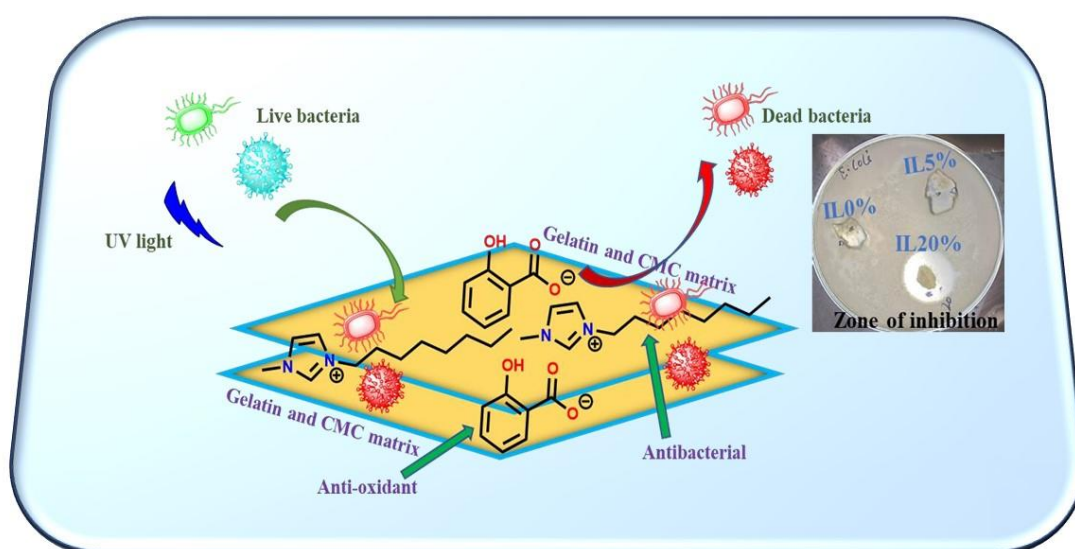
Scheme 4.9: Synthesis of Iohexol.

4.5 Conclusion

In summary, we have developed a heterogeneous catalytic system based upon gold NPs embedded in a hybrid solid support consisting of biomass-derived cellulose combined with an ionic liquid. The catalyst, Au@CIL, was successfully applied to the selective reduction of aromatic nitro compounds to aromatic amines in high yields, regardless of the presence of electron-withdrawing or electron-donating substituents. The present method was also applied to the synthesis of the medically important derivative, iodixanol and iohexol. The catalyst Au@CIL has high stability and reusability, along with sustained heterogeneity in the reaction media, and the proposed method exhibited a high Eco-scale value and a low E factor. The developed strategy thus has tremendous scope for amine synthesis on an industrial scale.

Chapter 5A

Development and characterization of gelatin/carboxymethyl cellulose based polymeric film with inclusion of ionic liquid to enhance the shelf life of food



Singh, A.; Singh J.; Singh, N.; Kaur, N. *Food Packaging and shelf life*, 2024, 42, 101251.

5a.1 Aim and Objectives

Approximately 35 % of food undergoes spoilage during transportation, storage, and harvesting leading to food wastage globally. So, it is necessary to develop and design a material through an eco-friendly approach to reduce food spoilage. Gelatin is the key biopolymer with the potential uses in numerous sectors such as food packaging since it is biodegradable and biocompatible. But for instance, food packaging material gelatin itself is not so stable and flexible. To overcome this drawback, we have constructed carboxy methyl cellulose and gelatin-based polymeric films with the inclusion of ionic liquid. Polymeric film with the addition of ionic liquid, shows tremendous antibacterial and antioxidant properties towards food packaging. The antibacterial activity of polymeric film was tested on both Gram-negative *E. coli* (*Escherichia coli*) and Gram-positive *S. aureus* (*Staphylococcus aureus*) bacteria. It was observed that the ionogel matrix shows excellent antibacterial and antioxidant properties in food packaging. Further, polymeric film with incorporation of ionic liquid was applied for food packaging applications and increases the shelf life of red apples by preventing air oxidation.

5a.2 Introduction

Microorganisms, toxic gases, dirt, fly ash, release of petroleum products, soil, and other pollutants are the foremost problems in all types of industries such as textiles, petroleum, chemical, fertilizer, and food industries which can create a hostile odor throughout their growth. Over the last decades, synthesis of bio-polymer-based materials using an eco-friendly method, with antimicrobial properties has fueled the great interest of scientists. [1-2]. Besides these properties, biopolymers can be easily extracted from bio-wastes and have a wide range of applications [3]. In hospitals, the major harm is caused because of nosocomial, which is a substantial and unnecessary loss of health resources [4]. A wide variety of microorganisms are responsible for the diseases and infections acquired in the hospital [5]. Therefore, marvelous efforts are going on to replace antimicrobial compounds with bio-degradable materials [6-7]. It is well known that antimicrobial materials derived from bio-polymers may reduce or inhibit microbial contamination from food, which is an important concern for human health [8]. Different strategies have been proposed with inclusion of antimicrobial agents to minimize the proliferation of microbes found in different food packages [9].

Every year millions of deaths occur because of increasing foodborne microbial illness [10]. In spite of all the efforts going on in this area of research and applications like bio-medical devices and materials [11]. All products are derived from biodegradable polymers, which further show excellent applications such as packing and bioactive films [12].

Traditionally, synthetic antioxidants such as butylated hydroxy toluene, propyl gallate, and butylated hydroxy anisole, have been used in food for the last decades [13]. But all these synthetic antioxidants have several health-related issues, that have aroused interest in natural antioxidants, such as gelatin, which is inexpensive, biodegradable, and easily derived from plants and has received significant attention due to its availability of antioxidant and antibacterial properties [14-15]. According to the Food and Drug Administration, gelatin is classified as generally recognized as safe (GRAS), which means that gelatin can be directly added to food to increase its life [16]. Gelatin itself does not exhibit excellent antioxidant and antibacterial properties, besides these its thermal stability is also not good [17].

In lieu, of increasing the thermal stability of polymeric matrix, carboxy methyl cellulose (CMC) was inserted between the gelatin layers [18]. Insertion of CMC also increases the strength of the polymeric matrix [19]. Therefore, we intend to make such a gelatin and CMC polymeric matrix film more adaptable with the inclusion of IL which exhibits both antibacterial and antioxidant properties [19].

The use of ionic liquids has been found to be highly beneficial for synthesis of antibacterial and antioxidant polymeric matrix, because of their excellent plasticizing and solvating properties [20]. There are a few examples reported by some researchers, who developed materials from bio-polymer and ionic liquid which exhibit the properties of both antibacterial and antioxidant [21]. A method reported from chitosan-based material doped with ionic liquid which exhibits both antibacterial and antioxidant properties was further investigated by the observation of zone inhibition against *S. aureus* [2]. Aboomeirah et al. synthesized a material from gelatin and alginate utilized for wound healing properties and further, used for bio-mimicking skin substitute [22].

In present work, we developed a polymeric matrix from biopolymers and ionic liquid which have the combined potential of both. In this regard, an ionic liquid was synthesized from 1-methyl benzimidazole and salicylate anion, where anionic moiety showed excellent antioxidant properties and cationic moiety has potential towards

antibacterial action. Furthermore, ionic liquid also works as a cross-linker between the gelatin and CMC to strengthen the polymeric matrix.

Thereafter, the synthesized films were systematically characterized to analyze the surface morphology; thermal stability; plasticizing effect of ionic liquid; crystallinity, storage and loss modulus, mechanical properties (tensile strength, modulus, and elongation at break), and optical properties using SEM, PXRD, TGA, AFM, rheology analysis, mechanical testing, and solid-state UV- visible spectrophotometer respectively. The *S. aureus* and *E. coli* bacteria were taken to check the antimicrobial activity of synthesized polymeric film. Further, antioxidant properties of the prepared matrix were calculated via the DPPH free radical scavenging method [23]. Thus, a novel ionic polymeric film was synthesized, which exhibits antioxidant, antibacterial, and UV-blocking properties and inhibits food spoilage. Thereafter, polymeric film was tested for food preservation ability on a piece of red apple.

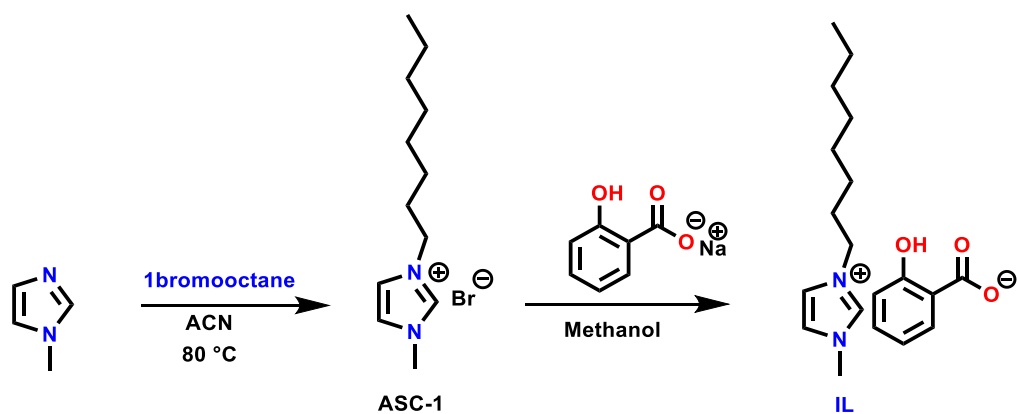
5a.3 Materials and methods

5a.3.1 Materials

1-methyl imidazole (ImH), 1bromooctane, and salicylic acid were all purchased from Sigma Aldrich (India). Acetonitrile and methanol (solvent) used for the synthesis were purchased from TCI Chemicals (Hyderabad, India). Thereafter, bio-polymers such as CMC and gelatin (GL), used for the polymeric films were also purchased from TCI Chemicals (Hyderabad, India). The microbial strains *S. aureus* (MTCC-740) and *E. coli* (MTCC-119) were supplied from the Institute of Microbial Technology, Chandigarh, India.

5a.3.2 Synthesis of ionic liquid (IL)

The Ionic liquid (IL) was designed and synthesized in such a way that offers antibacterial and antioxidant properties (Scheme 5a.1). Initially, 1-methyl imidazole (1 mmol, 82.10 mg) was functionalized using 1bromooctane (1.5 mmol, 289.68 mg) through refluxing in acetonitrile (10 mL) as shown in figure-1. Further, reaction mixture was concentrated at reduced pressure using a rota-evaporator. A light-yellow liquid product was obtained and purified with two to three washing. The synthesized compound (ASC-1) was characterized through ^1H , ^{13}C , and mass spectroscopy (Figure 5a.1-5a.3). Thereafter, bromide anion was exchanged with salicylate anion in methanol at refluxing conditions. The exchange of bromide with salicylate anion was confirmed through ^1H and ^{13}C NMR spectroscopy (Figure 5a.4-5a.5).



Scheme 5a.1. Synthesis of ASC-1 and IL.

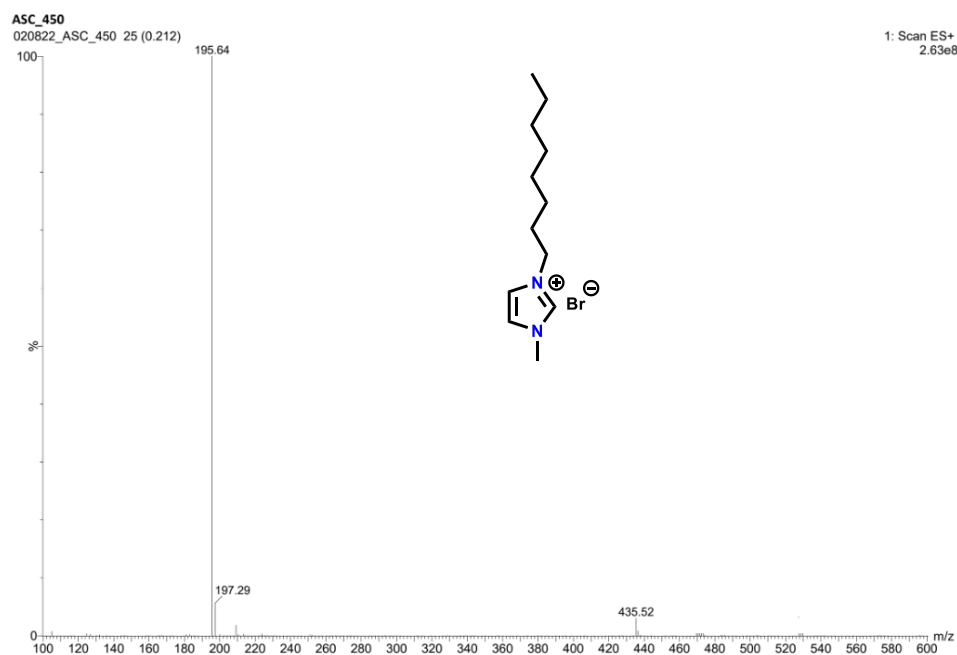


Figure 5a.1. Mass of ASC-1.

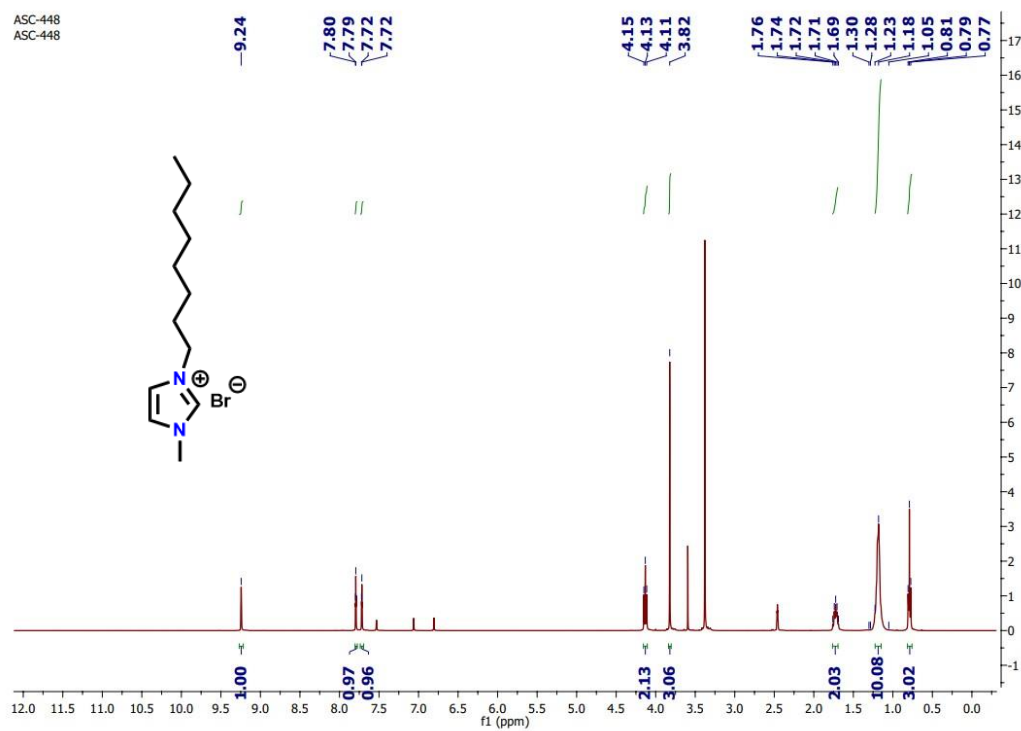


Figure 5a.2. ¹H NMR of ASC-1.

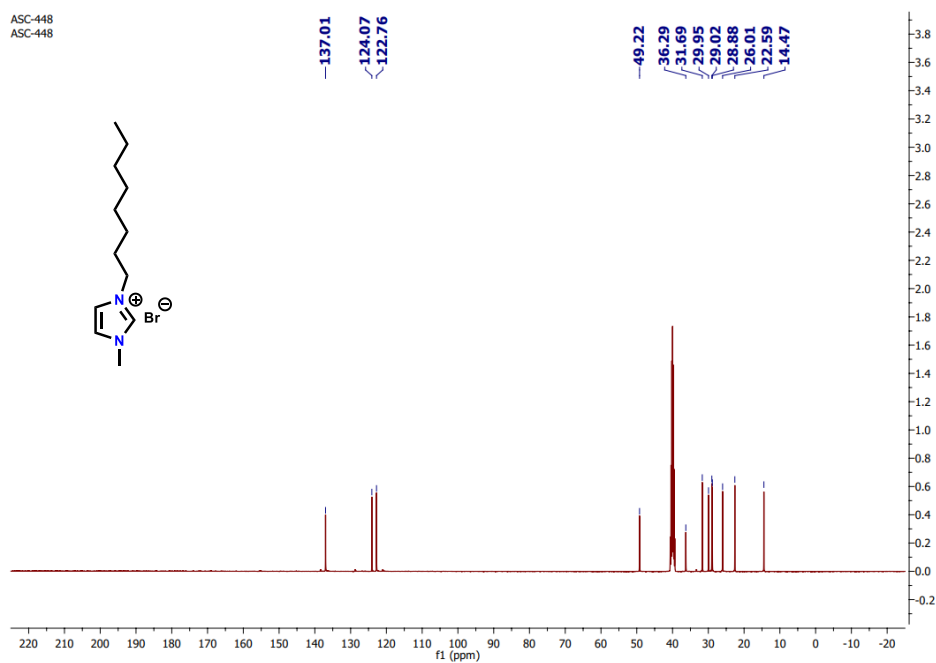


Figure 5a.3. ¹³C NMR of ASC-1.

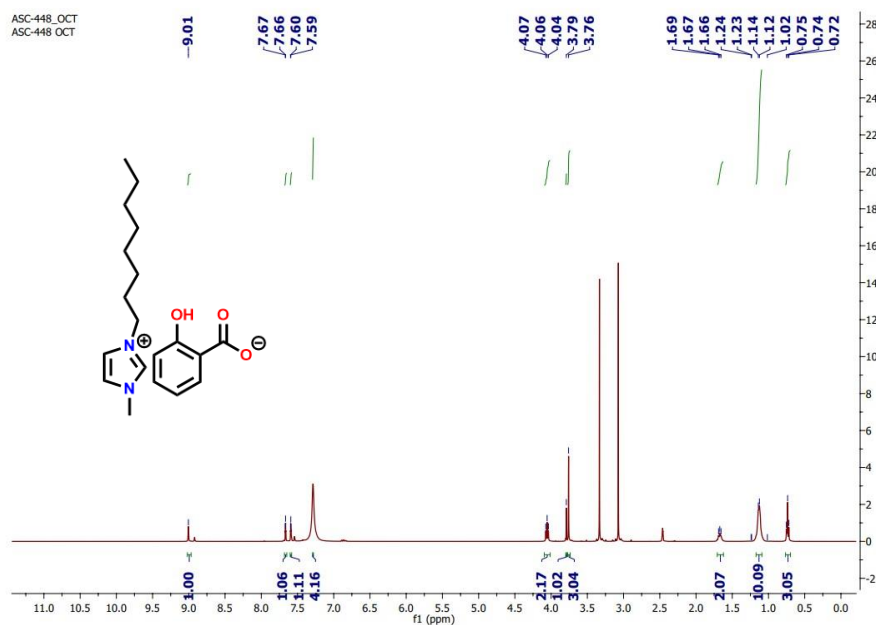


Figure 5a.4: ^1H NMR of IL.

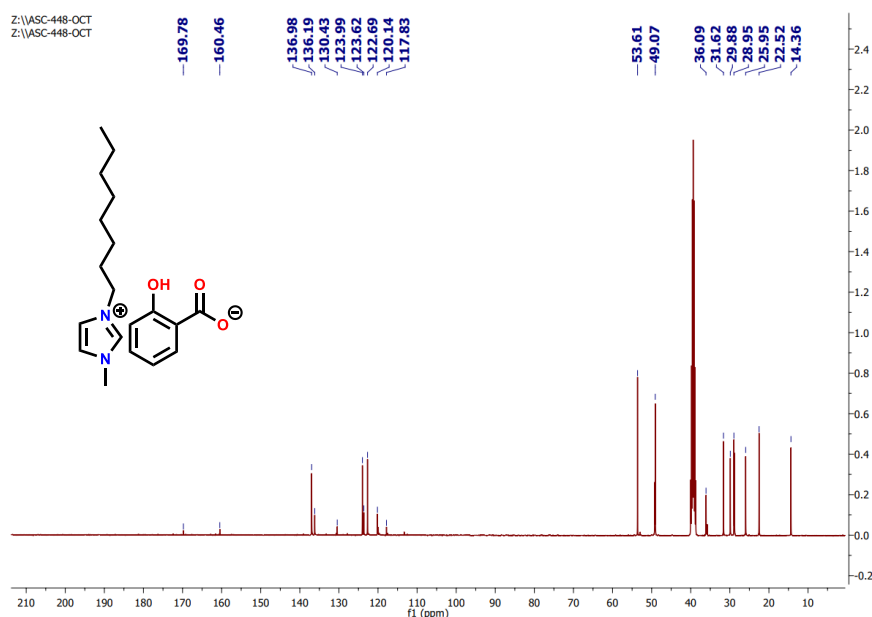


Figure 5a.5. ^{13}C NMR of IL.

Characterization of IL. ^1H -NMR (400 MHz, DMSO-d_6) δ 9.01 (s, 1H), 7.67 (d, $J = 1.6$ Hz, 1H), 7.59 (d, $J = 1.6$ Hz, 1H), 4.06 (t, $J = 7.2$ Hz, 1H), 3.79 (s, 1H), 3.76 (s, 1H), 1.78 – 1.58 (m, 2H), 1.29 – 0.95 (m, 10H), 0.74 (t, $J = 6.73$ Hz, 3H). ^{13}C -NMR (100 MHz, DMSO-d_6) 169.8, 160.5, 137.0, 136.2, 130.4, 124.0, 123.6, 122.7, 120.1, 117.8, 53.6, 49.1, 36.1, 31.6, 29.9, 29.0, 26.0, 22.5, 14.4.

5a.3.3 Film preparation

The carboxy methyl cellulose (CMC)-0.5g with a degree of substitution 0.65-0.90 and an average molecular weight of 90000 g/mol, solution was prepared in a glass beaker containing double distilled water (30 mL). Thereafter, a solution of gelatin powder (Type-A, 300 Bloom, 0.5 g) was also prepared in a separate beaker containing distilled water (Figure-5a.6). Both the solution was mixed with constant stirring at room temperature till to obtain a homogenous solution [24]. The synthesized ionic liquid was added in different compositions of 0 %, 5 %, and 20 % w/w with respect to CMC-gelatin, followed by mixing through mechanical stirring. Further, a homogenous solution of CMC-gelatin and IL polymeric matrix was poured into the clean glass petri dish and left to dry in a hot air oven at 65 °C for 150 min to get different polymeric films (Figure 5a.7). All synthesized films with different composition of IL, were characterized using various techniques.

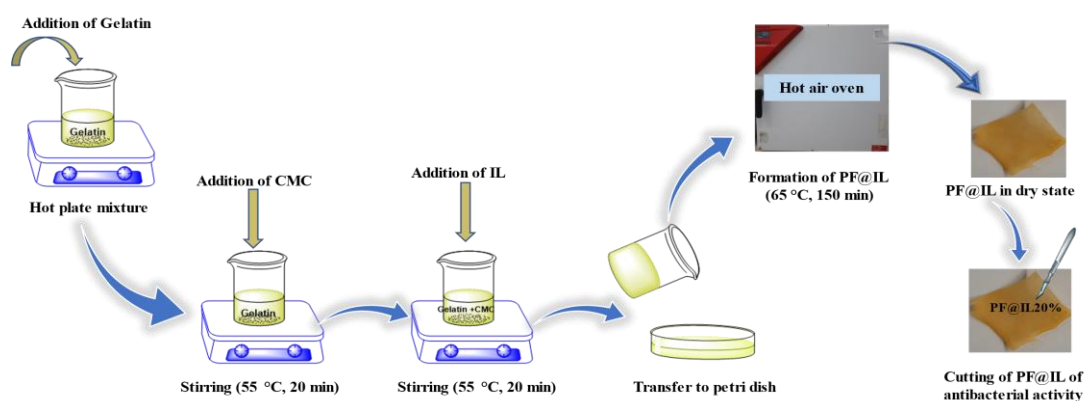


Figure 5a.6. Schematic diagram for the synthesis of antibacterial and antioxidant polymeric film.

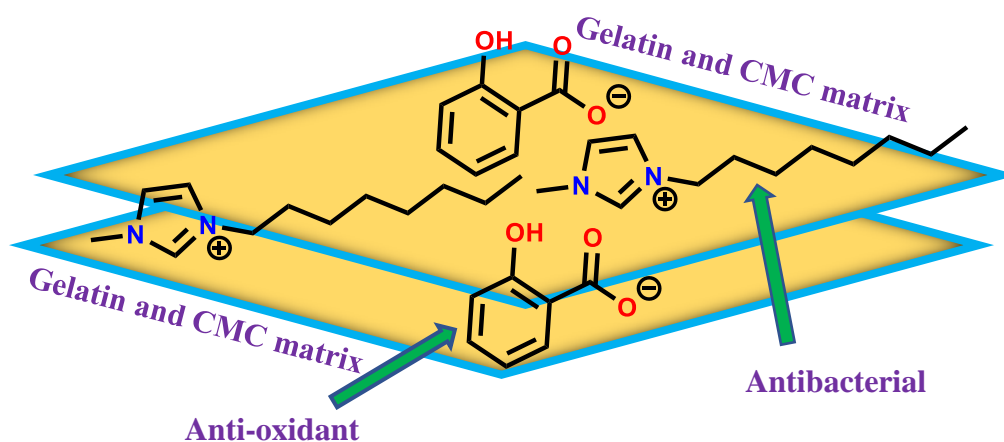


Figure 5a.7. Synthesis diagram of CMC-gelatin and ionic liquid (IL) polymeric film.

5a.3.4 Antibacterial Activity Test against *E. coli* and *S. aureus* bacterial strain

To determine the anti-microbial activity of PF@IL20% membrane, activated bacterial culture (100 μ L) of *S. aureus* and *E. coli* was spread on the surface of 50 \times 15 mm Petri dishes containing 15 mL of heat sterilized (121 $^{\circ}$ C, 15 min) luria broth. Turning the color of Nev's Ink autoclave tape from white to black indicated that the inside temperature is adequate for sterilization. Next, a piece of PF@IL20% membrane sample was placed on a solid medium with a value of 10^7 CFU/mL and incubated for 24 h and at a temperature of 37 $^{\circ}$ C. Thereafter, the zone of inhibition (ZOI) of the sample was measured with absolute digimatic calipers Digital Caliper 1112-200 INZIZE Co, Ltd, China) to an accuracy of 0.01 mm. The average value was calculated from the four different locations around each sample independently.

Furthermore, PF@IL with the inclusion of IL0 %, IL5 %, and IL20 % were screened against strain *S. aureus* and *E. coli* using the reported procedure from our lab [25]. To calculate bacterial viability (%). Firstly, luria broth was prepared in double distilled water and heat sterilized (121 $^{\circ}$ C, 15 min). Further, activated microbial cultures of *E. coli* and *S. aureus* were inoculated in falcon tubes containing 10 mL of media and incubated on a rotary shaker (37 $^{\circ}$ C). When optical density (OD) reached to 0.48, then polymeric films with the inclusion of IL0 %, IL5 %, and IL20 % were placed in the bacterial culture, and incubated for 24 h at 37 $^{\circ}$ C. The OD of bacteria was measured with the help of a UV-visible spectrophotometer at 600 nm, which helped to calculate the microbial cell growth. The cell viability was calculated as per following (Equation 5a.1):

$$\text{Bacterial viability (\%)} = \frac{OD_{600}(\text{control}) - OD_{600}(\text{test})}{OD_{600}(\text{control})} \times 100 \quad 5a.1$$

5a.3.5 Sample preparation of bacterial strain for AFM and SEM analysis

The PF@IL (1.2mm \times 1.2mm \times 22 μ m) was placed in the *E. coli* and *S. aureus* (10^7 CFU/mL) culture and was incubated (37 $^{\circ}$ C) for 24h. Thereafter, a cell pellet was formed upon centrifugation (1300 rpm and 2 min) of 1.0 mL of cells and further prepared phosphate buffer saline (PBS, 0.1 M, pH 7) was used to wash the cell pellet [19]. Afterward, cell pellet was fixed with glutaraldehyde solution (2.5% V/V), and sequentially dehydrated at room temperature with addition of ethanol at different concentrations such as 30, 40, 50, 60, 80, and 99.9 %. The morphology of PF@IL20% treated bacterial cells was then analyzed through both AFM and SEM.

5a.3.6 Characterization

Physical and chemical properties of the developed PF@IL20% were investigated through various techniques including; FTIR system (Hyperion 2000, Bruker Optics) was used to analyze the bending and stretching mode of the materials. Thereafter, planes and crystallinity of materials were measured through a Miniflex (Rigaku) diffractometer. Mass spectra of synthesized ionic liquid were analyzed through a Xevo G2-XS QTOF (WATERS) spectrometer. Thermogravimetric analysis (TGA) was performed on a TGA/DSC 1 STARE SYSTEM from Mettler Toledo with temperature increments of 5 °C min⁻¹ in air to check the thermal stability of materials. Furthermore, proton NMR spectra of ionic liquid were obtained at 400 MHz using a JEOL instrument. Similarly, ¹³C-NMR spectra were recorded while instrument was operated at 100 MHz. During the NMR analysis chemical shifts were measured using a deuterated solvent as an internal reference. Photophysical properties of polymeric material with the inclusion of ionic liquid were determined using a solid-state UV-visible absorption spectrophotometer (Shimadzu UV-2400). The uniform distribution of ionic liquid over the gelatin-CMC matrix was analyzed through a JEOL JSM-6610-LV instrument. The tensile test was carried out using an ASTM E8 Tensile Tester without an Extensometer at room temperature. Atomic force microscopy (AFM) images were acquired using a scanning probe microscopy (Digital Instrument Nanoscope III). Surface morphologies and elemental analysis of PF@IL20% polymeric film were studied through a JEOL JSM-6610-LV instrument.

5a.4 Result and discussion

Ionic liquid was prepared from 1-methyl imidazole and salicylate anion, which was further used as an antimicrobial material. Depending upon the composition of ionic liquid (IL0 % to IL20 %) ionogel matrix shows different properties, with increasing the percentage of ionic liquid ionogel matrix shows significant improvement. The surface morphology of prepared ionogel was analyzed through SEM (PF@IL20%) and from the analysis it was observed that ionic liquid distributed uniformly over the matrix. From the morphology, it can be clearly seen that a crosslinked network formed between CMC and gelatin, whereas ionic liquid works as a crosslinker. Crosslinking occurs between the polymers and ionic liquid, because of hydrogen bonding between them. Due to hydrogen bonding available between polymers and ionic liquid, plasticizing and opaque polymeric matrix film was obtained (Figure 5a.8).

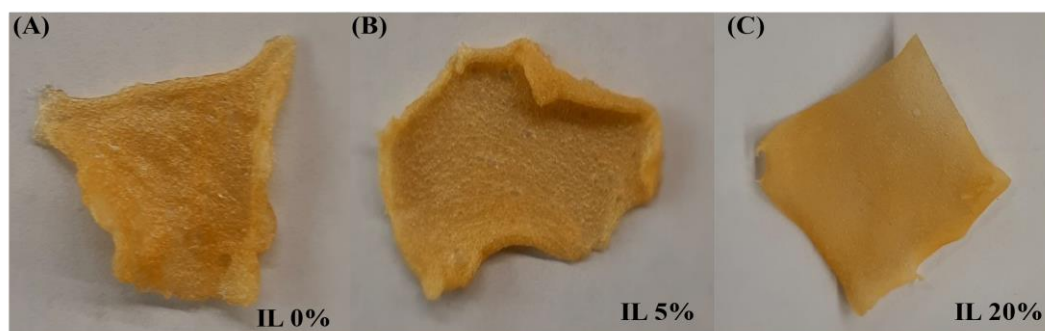


Figure 5a.8. Digital images of prepared polymeric films with different proportions of ionic liquid A) IL0 %, B) IL5 %, and C) IL20 %.

5a.4.1 FTIR & PXRD investigation

The IR spectra of all prepared polymeric matrices were evaluated and plasticizing effect of ionic liquid was achieved through hydrogen bonding available between ionic liquid and polymers. Formation of hydrogen bonding between polymers and the ionic liquid was confirmed through FTIR measurement of prepared polymeric matrix (Figure 5a.9a). The amide bond of polymeric matrix shifted to a higher wavenumber (1586 cm^{-1} to 1638 cm^{-1}) after the inclusion of ionic liquid (IL5 %) with additional two peaks appear at 2933 cm^{-1} and 2878 cm^{-1} which corresponds to $-\text{CH}_2$ stretching and bending respectively. Further, amide bond shifted to a higher wavenumber with more addition of ionic liquid (IL20 %).

PXRD was performed to check the crystallinity nature of the all-synthesized polymeric matrix with the inclusion of ionic liquid (IL) at a different concentration (IL0 % to IL20 %). From the experiment, we observed that polymeric films with IL0 % show a highly amorphous nature. Thereafter, there was a significant appearance of crystalline peaks with inclusion of ionic liquid (IL5 %), and crystallinity further increased with more inclusion of ionic liquid (IL20 %) as shown in figure-5a.9b. From all the spectra it was observed that ionic liquid generates plasticizing effect in the polymeric films via hydrogen bonding between ions and polymeric backbone (CMC and gelatin), leads to more crystalline nature of polymeric film. In addition to this Plasticizing effect is also confirmed via mechanical testing and FTIR measurement.

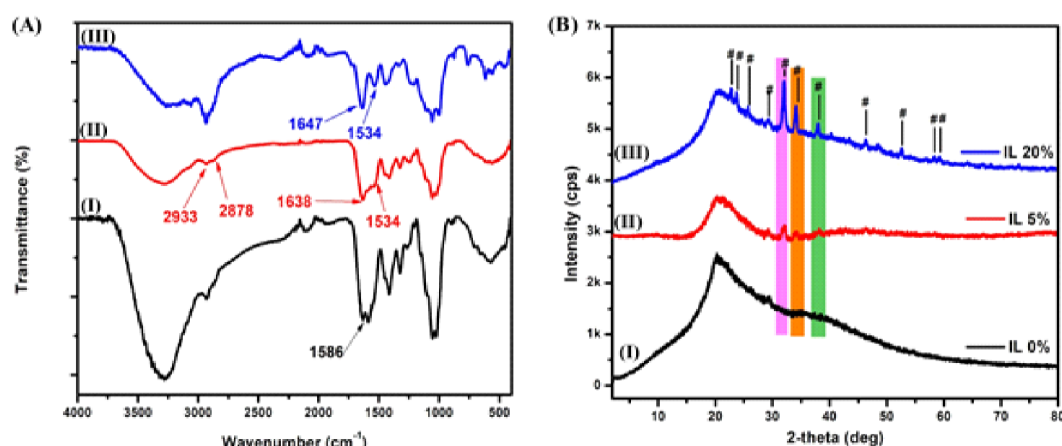


Figure 5a.9. (A) IR spectra of polymeric matrix with different composition of ionic liquid I) IL0 %, II) IL5 %, and III) IL20 %. (B) PXRD spectra of polymeric matrix with different compositions of ionic liquid I) IL0 %, II) IL5 %, and III) IL20 %.

5a.4.2 Morphological and elemental composition analysis of polymeric films

SEM analysis was executed to reveal the surface morphology of the polymeric matrix. Figure-5a.11a, indicates the mesh-like structure of a polymeric matrix with uniform distribution of ionic liquid over it. The crosslinked network formed in the polymeric matrix is probably due to the hydrogen bonding between the polymeric material and ionic liquid (Figure 5a.10). We observed the same type of morphology with the inclusion of ionic liquid, while when there is no inclusion of ionic liquid this type of morphology was absent. Furthermore, elemental composition was also confirmed through EDS analysis (Figure 5a.11b), which indicates that it contains C (43.4 %), N (8.1 %), and O (48.5 %) over the polymeric matrix. From SEM analysis, it was concluded that morphology of polymeric matrix with the inclusion of ionic liquid (PF@IL) is mesh like structure. Furthermore, smoothness of polymeric matrix was measured through AFM (Figure 5a.12) analysis and it was observed that smoothness varies from 6.01 nm to 24.3 nm.

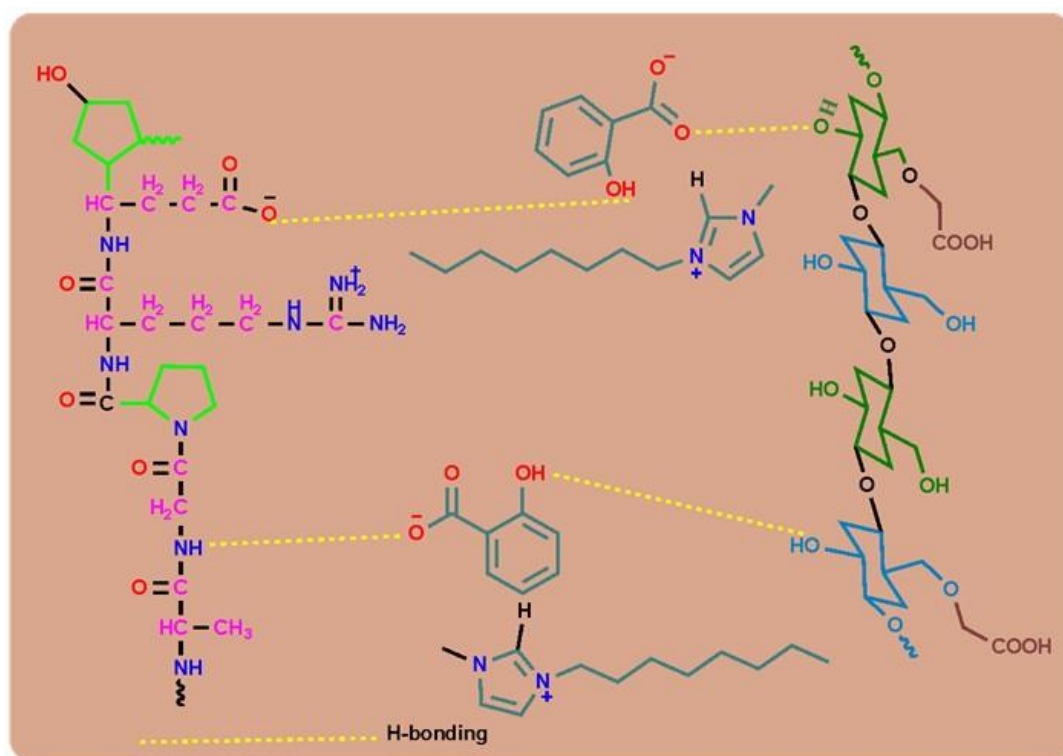


Figure 5a.10. Schematic diagram to show the crosslinking between the gelatin and CMC through hydrogen bonding of IL (crosslinker).

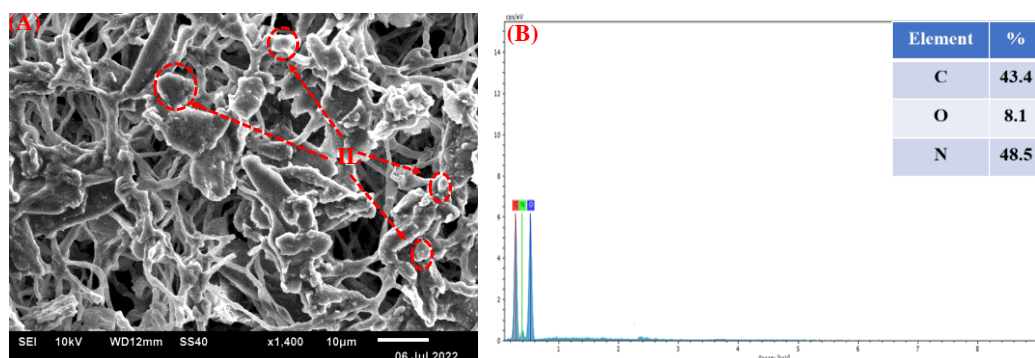


Figure 5a.11. A) SEM image and B) electron diffraction spectroscopy (EDS) graph of PF@IL20%.

5a.4.3 Mechanical properties

All the prepared films were analyzed through mechanical properties, which are shown in figure 8, using a UTM (INSTRON) instrument without an extensometer, at 27 °C and with a crosshead speed of 2 mm/min. To carry out this experiment samples were prepared with dimensions of 3.20 mm wide and 3.70 mm thick, and their calculated surface area was 11.8 mm² (ASTM standards). A prepared film without the incorporation of ionic liquid (IL0 %) exhibits minimum mechanical strength along with the results 60 MPa, 0.98 mm, and 121 MPa which corresponds to tensile strength, elongation at break, and modulus respectively. All these values start increasing when

the inclusion of ionic liquid takes place (IL5 %) with increases in all values to 67 MPa, 1.4 mm, and 288 MPa for tensile strength, elongation at break, and modulus respectively. From the obtained data it was observed that all these mechanical strength increases with the inclusion of ionic liquid. The increase in mechanical strength is probably due to an increase in the plasticizing effect of ionic liquid and the hydrogen bonding between polymeric materials and ionic liquid. Increasing the mechanical strength, we further incorporated the ionic liquid up to 20 % with respect to polymeric matrix, values increase to 83 MPa, 1.73 mm, and 400 MPa corresponding to tensile strength, elongation at break, and modulus respectively (Figure 5a.13a-5a.13c).

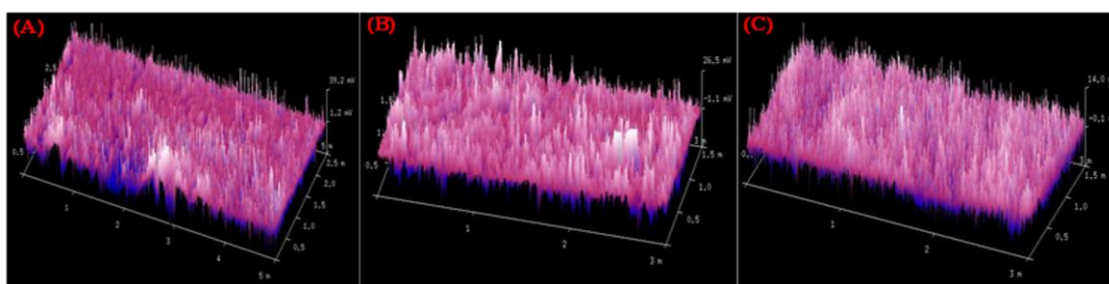


Figure 5a.12. Three-dimensional AFM images for the morphology of prepared polymeric films with inclusion of ionic liquid A) IL0 %, B) IL5 %, and C) IL20 %.

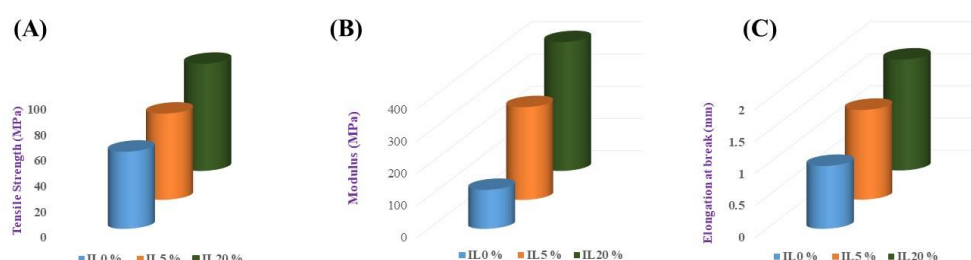


Figure 5a.13. Mechanical study of polymeric films with different percentages of ionic liquid A) tensile strength, B) modulus, and C) elongation at break.

5a.4.4 Thermal degradation analysis

For any materials with biomedical applications such as sensing of mycotoxins, food packing, drug delivery, coating, UV shielding, wound dressing, etc. material is essential to be sterilized at 150 °C. In these aspects to understand the thermal behavior of all the prepared polymeric films TGA was executed on a TGA/DSC 1 STAR[®] SYSTEM from Mettler Toledo, Switzerland, in an N₂ atmosphere (Figure 5a.14a). TGA was performed in the range of 42 °C to 813 °C with temperature increment of 10 °C/min. In a typical TGA experiment, 5 mg of sample was placed in a pan-shaped alumina tube. From the experiment, it was observed that the polymeric matrix was quite stable up to 270 °C. During thermal analysis initially, weight loss has appeared because of loss of moisture

from the polymeric matrix. Thereafter, weight loss was detected due to the formation of volatile components, and after that weight loss was observed due to the decomposition of polymeric matrix. During the decomposition of a polymeric matrix into carbon and hydrocarbon when temperature reaches above 320 °C weight loss is around 78 %. Significant thermal degradation of polymeric films occurred above 320 °C was ascribed to degradation of biopolymer. The thermal stability of polymeric films at 160 °C makes them resistant to heat during the sterilization process and because of these properties, polymeric films are suitable for food packaging applications.

5a.4.5 Rheology study

To examine the gel properties of prepared PF@IL20% films, oscillatory rheology experiments were performed using stainless-steel parallel plate geometry on an MCR 102 rheometer (Anton Paar). A dynamic sweep experiment was carried out at 37 °C, by varying the strain from 0.01 to 100 % at a constant regular frequency of 10 rad/s. Similarly, a frequency sweep experiment was carried out in a frequency range of 100 to 0.0 rad/s at constant strain (0.1 %).

A rheological experiment with PF@IL20% was executed in aqueous media (pH 7) to examine the gel properties and the obtained result is summarized in figure 9b. Same frequency conditions were used to execute all other frequency sweep experiments. It came to know from frequency sweep experiment that storage modulus (G') does not depend upon the angular frequency (rad/sec), and loss modulus (G'') was less than storage modulus (G') at all frequency values, indicates the formation of gel type material (Figure 5a.14b). From the rheology it came to know that at same angular frequency of 17.8 rad/sec, G' is 4760 Pa, whereas G'' is 599 Pa. From the obtained data it was confirmed that G'' is much lower than G' , indicating the material is in a gel state [26].

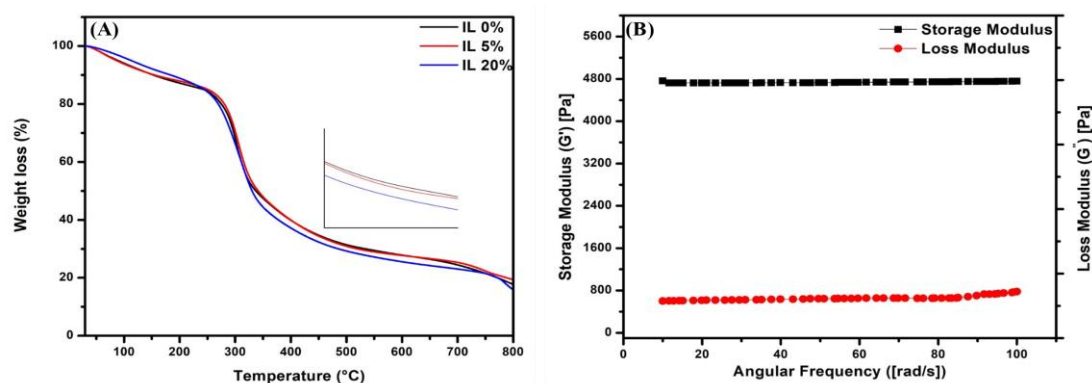


Figure 5a.14. A) Thermogravimetric analysis (TGA) of all prepared matrices and B) rheology study of PF@IL20%.

5a.4.6 Optical (light transmission) properties

It is necessary for any bioactive polymeric films (PF@IL20%) they block the passage of harmful UV light regions and only allow the visible range of light (400-800 nm) at its best. Further, to analyze the optical properties transmittance of each prepared polymeric film was calculated. From the obtained data sun protection factor values (SPF) were calculated using the equation-5a.2.

$$\text{SPF (spectrophotometric)} = \text{CF} \times \sum_{290}^{320} [\text{EE}(\lambda) \times \text{I}(\lambda) \times \text{Abs}(\lambda)] \quad 5a.2$$

Where EE and I represent the erythemal effect spectrum and intensity spectrum respectively. Abs is the absorbance of prepared polymeric films. Here correction factor (CF) has a constant value =10.

From figure-5a.15b it was clear that the prepared film with IL0 % has some opacity in the UV region (200-350 nm) and further, this opacity decreased to 0 % with more inclusion of ionic liquid (IL20 %). The prepared polymeric film PF@IL20% has very high opacity in the visible region (400-800 nm). From the obtained transmittance data of all polymeric films, we calculated the sun protection factor (SPF) values (Figure 5a.15b). From obtained transmittance and SPF data, it can be concluded that the prepared polymeric films with 20 % inclusion of ionic liquid have excellent UV Blocking capacities. UV light is the most critical factor for any eatable items, which leads to nutrient loss and degradation of food items. In lieu of avoiding the spoilage and nutrient loss of food, ideal food packing materials are necessary.

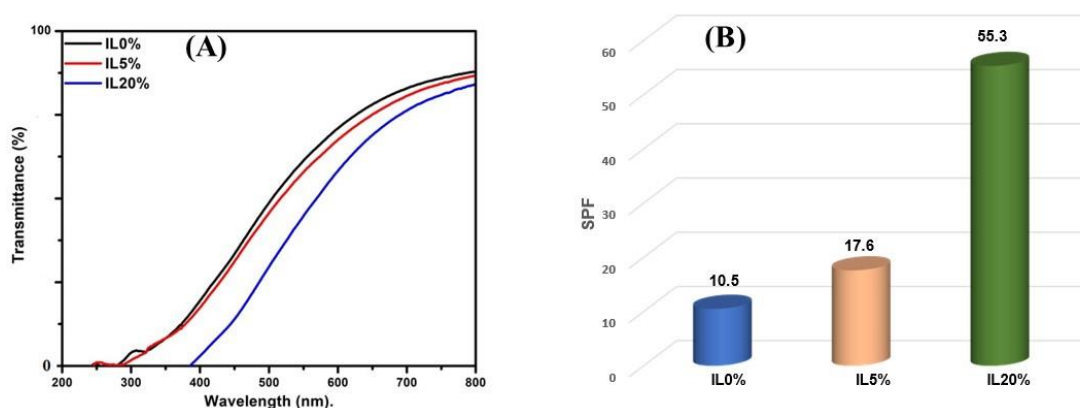


Figure 5a.15. a) Transmittance of prepared polymeric films with different compositions of ionic liquid and b) Sun protection factor of prepared polymeric films with different compositions of ionic.

5a.4.7 Antibacterial Activity

Anti-bacterial activity of polymeric films with the inclusion of IL0 %, IL5 %, and IL20 %, against both *E. coli* and *S. aureus* were assayed. The results (Figure 5a.16a & 5a.16b)

revealed the growth inhibition of *E. coli* bacterial colonies surrounding the PF@IL20%. However, the ZOI was slightly observed with no inclusion of ionic liquid (IL0 %). Thereafter, ZOI starts appearing with the inclusion of ionic liquid (IL5 %).

Furthermore, the antibacterial activity of polymeric films was examined with respect to concentration of ionic liquid and treatment time. The obtained data (Figure 5a.16c & 5a.16d) shows that the viability of *E. coli* and *S. aureus* decreases sharply within 4 h of incubation time when it is treated with the polymeric matrix IL0 %, IL5 %, and IL20 %.

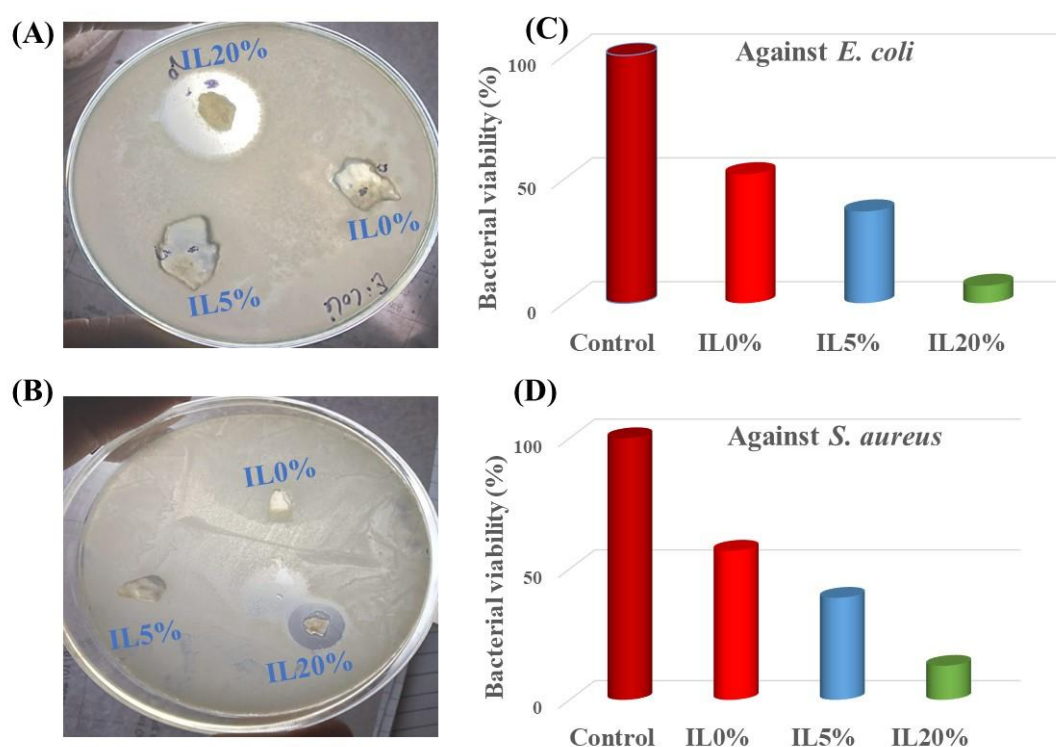


Figure 5a.16. Films against bacteria (A) *E. coli* and (B) *S. aureus* treated with polymeric films with inclusion of IL0 %, IL5 %, and IL20 %. Percentage bacterial viability of polymeric films against bacteria (C) *E. coli* and (D) *S. aureus*.

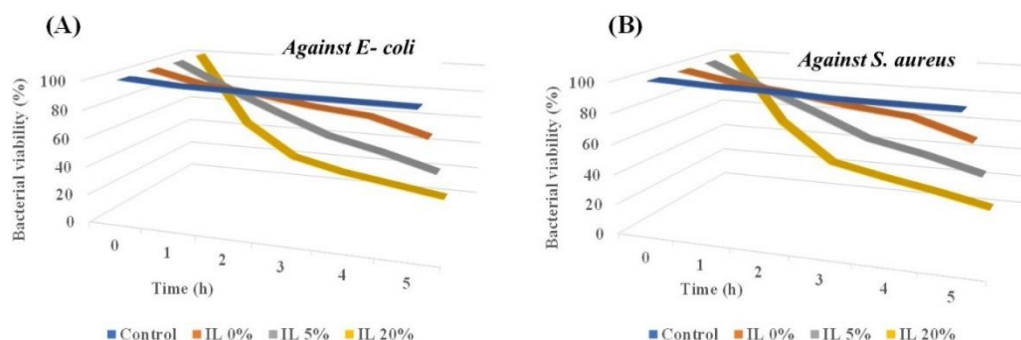


Figure 5a.17. Time course of persisting growth curve of (A) *E. coli* and (B) *S. aureus*.

However, among the investigatory composite PF@IL20% exhibits excellent antibacterial efficacy against both *E. coli* and *S. aureus*.

From the viability data (Figure 5a.17a & 5a.17b), it is clear that PF@IL20% exhibits the inhibition of up to 85-95 % growth of *E. coli* and *S. aureus*. From the obtained data it was observed that the antibacterial activity of the polymeric matrix with IL20 % is higher as compared to those of polymeric matrix with IL0 % and IL5 %. The difference obtained in antibacterial potential of polymeric films (IL0 %, IL5 %, IL20 %) may be ascribed to the effect of percentage ionic liquid inclusion along with the charge density of imidazolium cations. From The literature reports [19] and observed data it came to know that the cationic moiety (ionic liquid) present on the surface of the polymeric film, supports the electrostatic interaction with the cell wall comprising phosphate groups, while a long hydrocarbon chain inserts into the lipid membrane of bacteria. Similarly, surface interaction between the PF@IL20% and bacteria cells resulted in antimicrobial activities. Further, the obtained antibacterial result showed that the cationic part and gelatin-CMC-based polymeric matrix played a potent role in the antibacterial activity of the prepared PF@IL20% against both *E. Coli* and *S. aureus* pathogenic strains. All the tested PF@IL0%, PF@IL5%, and PF@IL20% exhibited potential antibacterial activities with minimum inhibitory concentration (MIC) values of 52 ± 2 , 37 ± 2 , and $7 \pm 2 \mu\text{g mL}^{-1}$ against *E. coli*, respectively. Similarly, the synthesized PF@IL0%, PF@IL5%, and PF@IL20% showed inhibition potential against *S. aureus* with MIC values of 57 ± 2 , 39 ± 2 , and $13 \pm 2 \mu\text{g mL}^{-1}$ respectively. From the obtained data it is clear that polymeric material with no ionic liquid exhibits slight inhibition against bacteria and inhibition starts increasing with more inclusion of ionic liquid (PF@IL20%). The difference in the MIC may be attributed to the difference in the ionic liquid composition. Thus, it can be concluded from the results in accordance with

literature reports [27], showing the concentration-dependent antibacterial activity profile of ionic liquid.

5a.4.8 Bacterial sample preparation for SEM and AFM analysis

The morphological changes observed in bacteria after being treated with PF@IL20% were analyzed through AFM and SEM. To carry out this experiment bacterial samples of both strains *S. aureus* and *E. coli* were diluted. Treated samples with PF@IL20% were incubated at 37 °C. Thereafter, incubated bacterial samples were washed with prepared phosphate buffer saline (PBS) followed by washing with 2.5 % glutaraldehyde solution for 30 min and dehydrolyzation of the sample at room temperature with different concentrations of ethanol (20, 40, 60, 70, 90 and 100 %). To elaborate the mechanism of bacteria by PF@IL20%, the SEM images were recorded using JEOL JSM-6610-LV instrument, all the obtained result reveals the surface morphological changes persuaded in *E. coli* bacterial cells after contact with PF@IL20% composite (Figure 5a.16a & 5a.16b). The smooth, intact and unchanged cell wall membrane of *E. coli* bacteria is clearly shown (Figure 5a.18a). But the PF@IL20% treated cell wall membranes were shrunk, collapsed and distorted, which is revealed from SEM analysis after 2 h (Figure 5a.18b) and 4 h (Figure 5a.18c). It can be indicated that morphology of *E. coli* bacteria was entirely changed after being treated with PF@IL20%, which result into bacterial cell death. Similarly, we performed the AFM analysis using the Buker-SPM Multimode, for *S. aureus* cell wall membrane of bacteria to recognize the bacterial cell inhibition mechanism upon interaction with PF@IL20%. The AFM images in different modes revealed the morphological and surface changes that occur in Gram-positive *S. aureus* cell wall, after being treated with PF@IL20% (Figure 5a.18d-5a.18f). This ruptured morphology indicated the bacterial cell membrane was entirely distorted, and damaged, which resulting in *S. aureus* bacterial cell death [28-29].

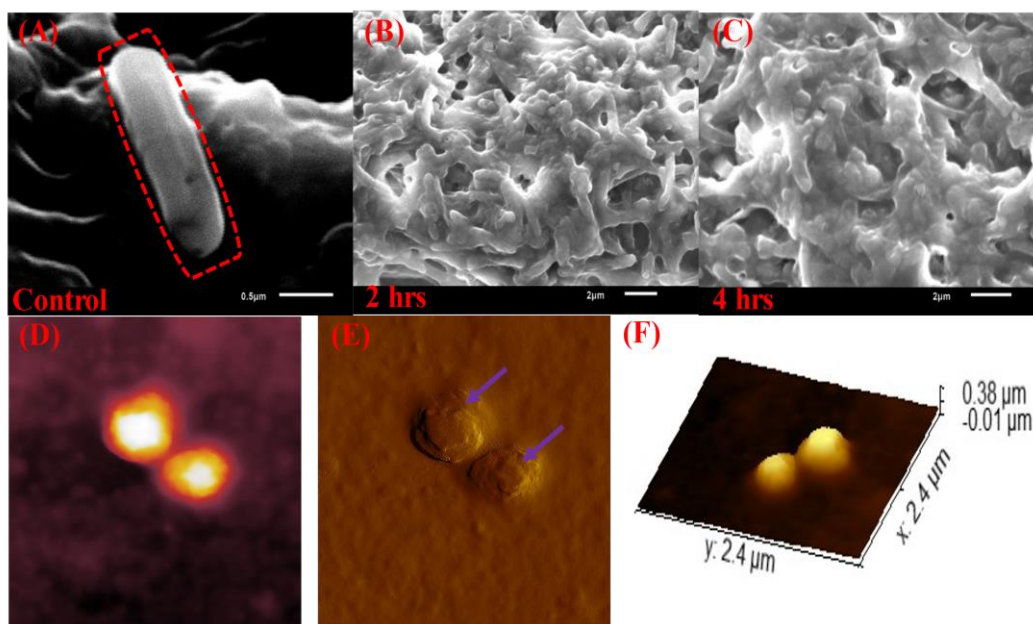


Figure 5a.18. SEM images A) untreated *E. coli* bacteria, treated *E. coli* bacteria with PF@IL20% (B) after 2 h and (C) after 4 h. (D-F) AFM images of *S. aureus* after being treated with PF@IL20% in three different modes.

5a.4.9 Antioxidant properties

5a.4.9.1 Radical scavenging method

The free radical scavenging method was used to measure the antioxidant activity of materials [30]. Where 100 mg of PF@IL20% with different percentages of ionic liquid, were taken in 5 mL of 0.1 mM of DPPH solution in ethanol. At 515 nm, absorbance was recorded after 60 min using a spectrophotometer. All the experiments were performed in triplicate and the average results were calculated. Furthermore, radical scavenging activity (RSA) was calculated using the equation below-5a.3 [31-32].

$$\text{RSA (\%)} = \frac{A_0 - A_1}{A_0} \times 100 \quad 5a.3$$

Where A_0 and A_1 are the absorbance values of control and treated samples (equation-5a.3).

The free radical scavenging activity of prepared PF@IL20% was monitored using the DPPH free radical scavenging test. From the results (Figure. 5a.19) it was observed that film without ionic liquid (IL0 %) showed no RSA, whereas the increased ionic liquid concentration, results in enhanced antioxidant properties. The obtained RSA results are the confirmatory for ionic liquid role as the bioactive material in the polymeric film.

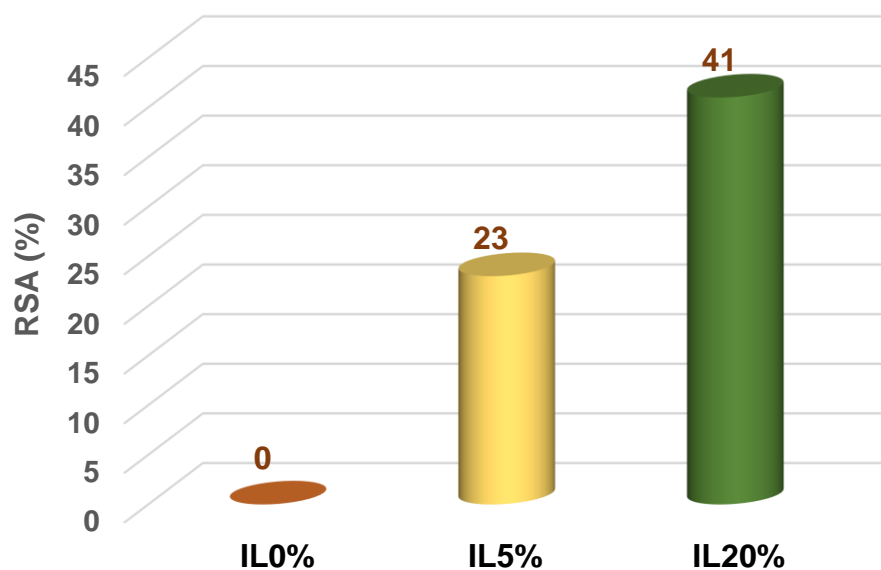


Figure 5a.19. Radical scavenging activity (RSA) of prepared polymeric films with different compositions of ionic liquid.

5a.4.9.2 Developed polymeric film for food packaging

Additionally, the prepared PF@IL20% polymeric film was tested for food preservation by visually measuring the air oxidation of the fruit (red apple). For the analysis, a piece of freshly cut red apple was wrapped inside the PF@IL20% and similarly, an unwrapped piece was in air. After 150 min. both the wrapped and control pieces were compared visually to check the air-oxidation prevention ability of PF@IL20%. The synthesized PF@IL20% was further tested to check their food preservation ability using a piece of red apples. Covering a piece of red apple with PF@IL20% dramatically decreased air-oxidation and remained as such for 7 h without spoilage (Figure-5a.20). PF@IL20% showed excellent bacterial growth inhibition with the inclusion of ionic liquid due to high MIC value of salicylate anion against bacteria. In addition to this, from all obtained results we observed that no chemical changes were observed in ionic liquid, during the preparation of polymeric films. From the food preservation test, it was clear that PF@IL20% is highly applicable for edible food packaging with excellent antibacterial, antioxidant, and UV shielding properties.

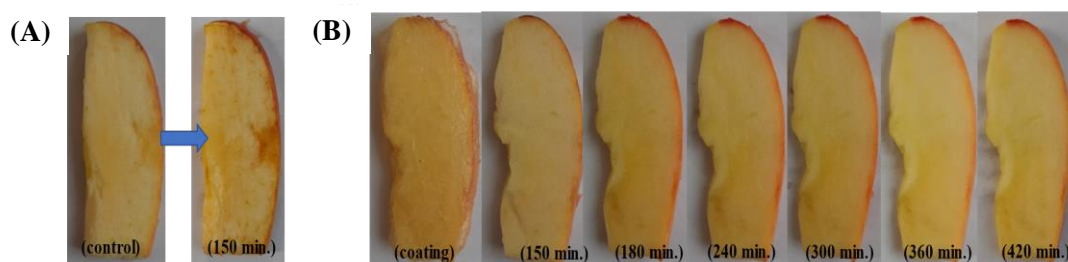
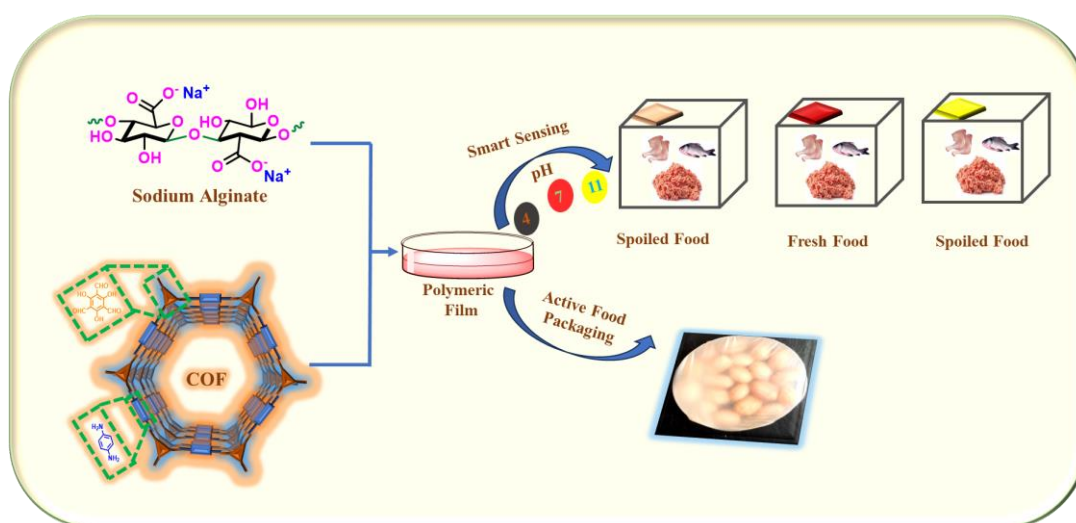


Figure 5a.20. Food preservation test for a piece of red apple using PF@IL20%, A) control piece of red apple after 150 min and B) piece of apple with a coating of PF@IL20% with different time intervals up to 7 h.

5a.5 Conclusions

An ionic liquid was synthesized from 1-methyl imidazole with a long hydrocarbon chain and their bromide anion was replaced with salicylate anion. The synthesized ionic liquid with a different composition (IL0 %, IL5 %, and IL20 %), was incorporated into the polymeric matrix of gelatin/CMC. The antibacterial effect of the prepared gelatin-CMC-based polymeric films against *S. aureus* and *E. coli* were evaluated. It is evident from the data that polymeric films containing 20 % IL (PF@IL20%) have strong antibacterial properties against pathogenic strains of *E. coli* and *S. aureus*. The change in surface morphology of bacterial cell death was analyzed via SEM and AFM. Additional PF@IL20 % exhibits excellent antioxidant properties and high SPF against UV rays. Furthermore, PF@IL20 % is utilized for the preservation of food items.

Biodegradable Sodium alginate/COF Based Polymeric Film That Monitors Food Spoilage and Extends Shelf Life



5b.1 Aim and Objective

As the human population increases very rapidly, it is necessary to develop an efficient biodegradable packaging material to increase the shelf life of food, guarantee food safety, and reduce spoilage from extreme conditions. To overcome all these problems, this work focuses on the synthesis of smart sensing strips and antimicrobial active food packaging films to monitor food spoilage and increase their shelf life. For smart sensing of food spoilage, covalent organic frameworks (COFs) were synthesized from 2,4,6-triformylphloroglucinol (TFP) and p-phenylenediamine. Thereafter, COF was incorporated into sodium alginate polymeric material to obtain sensing strips with highly colorimetric response and augmented mechanical properties. The smart sensing strips were demonstrated on packaged poultry meat. Sensing strips are highly pH-responsive and color changes according to the pH of the surroundings. Sensing responses of COF were also studied on the biogenic amines that evolved during the spoilage of meat. In addition to this antimicrobial citral was incorporated into the SA/COF film to prepare active packaging film, which reduces food spoilage from high humidity, molding, and high-temperature conditions. Active packaging film was applied to the peanuts, which increases their shelf life, reduces food wastage, and avoids mold formation.

5b.2 Introduction

In last few years, consumers are not only focused on the taste of food products but also on their traceability, safety, nutritional value, and quality [1-2]. According to a report, 55 % of children and 40 % of the global population are living in tropical climates and it is estimated that these numbers may increase to 66 % and 50 % respectively [3]. Food supply chain is continuously affected by the loss of topsoil, physical damage, temperature, bacterial action, lack of traceability, failures of warehouses, etc. [4-6]. Because of these issues, almost one-third of produced food in tropical regions is wasted or spoiled before the food reaches the consumers [7-8]. So, in lieu of these problems and increasing the demand for food day by day, it is necessary to synthesize smart, sustainable, and active food packaging material to control spoilage, increase the shelf life, and monitor the quality and freshness of food items [9]. Spoilage food is even responsible for a large number of foodborne diseases such as Cyclosporiasis, Cryptosporidiosis, Giardiasis, Norovirus, and Listeriosis [10]. Therefore, synthesis of active food packaging material with excellent functional qualities increases the attention

of polymer chemists. To mitigate the wastage and spoilage of food, biodegradable packaging plays a pivotal role by acting as a physical barrier to UV rays, moisture, oxygen, dust, temperature, and bacteria [11-12]. Incorporation of some additives such as ionic liquid (IL), covalent organic framework (COF), metal-organic framework (MOF), and metal nanoparticles in the biopolymeric films help to enhance the antioxidant and antibacterial properties of active food packaging films [13-16]. The pH of food items varied with the spoilage and decomposition of food [17-18]. A visual indicator based on polymeric films is important to monitor the freshness of food and observable color change throughout food spoilage [19-20]. To assess the quality and freshness of food with the variations of its pH values is a practical application of polymeric strips [21-22].

Thus, it is practical to assess the food's freshness by identifying any variation in its pH values. Because of easy handling, eco-friendliness, biodegradability, readily recognizable visual color fluctuation, and reusability, biopolymers-based pH sensing strips have attracted scientists in the field of freshness monitoring and food packaging [23-24]. In this field, few packaging materials and sensing strips were reported for monitoring the quality of food including fish, shrimp, chicken, pig, etc. [25-27].

Shikonin extracted from *Lithospermum erythrorhizon* plant is pH-responsive organic compound incorporated into the carrageenan and gelatin matrix and further used for monitoring the freshness of milk [27]. Synthetic dye pyranoflavylum is an excellent indicator and was grafted onto chitosan and alginate, giving smart labeling strips for monitoring the quality of food [28]. Gelatin and agar-based polymeric matrix doped with sulfur quantum dots is an antibacterial, antioxidant, and anti-UV food packaging film [29]. Petunia dye was extracted from petunia flowers, and incorporated into biopolymers for the smart sensing of sulfur dioxide in grapes [30]. Thereafter, isolated soy protein, whole arrowroot powder, and cabbage anthocyanin were used for the preparation of pH-sensitive indicator film for monitoring the spoilage of meat and shrimp [31]. Color indication depends upon the evolution of volatile nitrogen inside the packed food items [31]. Anthocyanins extracted from natural sources are used for monitoring fish and milk spoilage with incorporation into the backbone of Gellan gum and gelatin [32]. The blue flowers of *Stachytarpheta jamaicensis* are the source of anthocyanins that have a wide range of colors from pink to yellow according to the pH

of the surroundings and their total phenolic contents [33-34]. As the population of the world increases day by day and people are demanding healthy food, it is also necessary to prepare active food packaging for the protection of food from bacteria, humidity, temperature, dust, UV-rays, and oxygen to increase the shelf life of food [35-37]. Active food packaging keeps the food fresh for a long time without any freezer requirement [38]. Due to some intrinsic drawbacks in these strategies such as slow sensing rate, reusability, release of dyes, and voids left in polymeric strips [39]. To remove all these challenges, we are required to synthesize a material with both smart sensing and active packaging properties. Huge numbers of biodegradable and non-toxic polymers extracted from synthetic or natural sources such as chitosan, alginate, gelatin, cellulose, pectin, gellan gum, and carrageenan have been well-documented for active packaging [40]. Alginate is one of the most abundant polysaccharides found in brown algae [41]. Due to its abundance and biodegradability, alginate has a large number of applications in a variety of sectors including, film formation, biosensors, active food packaging, water treatment, and biosensors [42-43]. Food packaging material made from alginate alone exhibited poor mechanical strength and negligible antimicrobial activity, hence cannot fit for active food packaging [44]. Recent researchers focused on how the bacterial, antioxidant, UV-ray barrier, and mechanical properties of alginate can be increased in active food packaging.

To address all these limitations and improve the sensing efficacy of the material, herein covalent organic framework (COF) was synthesized and incorporated into the alginate polymeric chain. COFs are generally two-dimensional polymeric networks with highly porous surface areas. Alginate, which acts as a solid support, is an abundant natural polymer that has been granted Generally Recognized as Safe (GRAS) to extend the shelf life of food. COF incorporated into the alginate chain rapidly responds to analytes according to pH of the surrounding environment and has excellent capabilities to monitor the freshness of packaged poultry food. In addition to this alginate polymeric and COF film with inclusion of citral shows antimicrobial properties, which are further used as active packaging material.

5b.3 Materials and Method

5b.3.1 Materials

2,4,6-triformylphloroglucinol (TFP), 1,4-phenylenediamine, and nafion solution both were purchased from Sigma Aldrich and used as such without any further purification. The solvent required dioxane, mesitylene, tetrahydrofuran (THF), and acetone for synthesis were purchased from TCI chemicals. Thereafter, sodium alginate was used as a solid support for the synthesis of smart sensing strips and active packaging film purchased from AVRA chemicals. *S. aureus* (MTCC-740) and *E. coli* (MTCC-119) the microbial strains both were purchased from the Institute of Microbial Technology, Chandigarh, India.

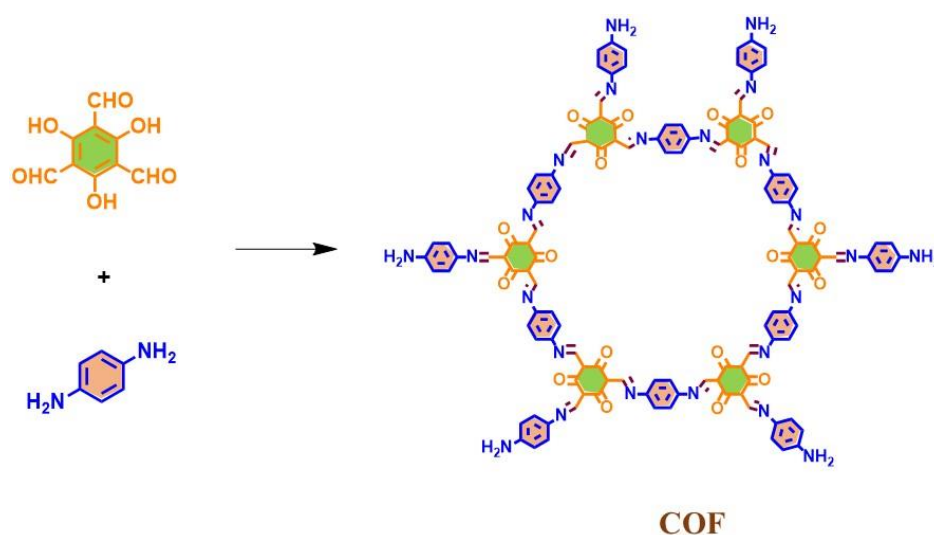
5b.3.2 Material Characterization

Physical and chemical properties of the developed PF@IL20% were investigated through various techniques including; FTIR system (Hyperion 2000, Bruker Optics) was used to analyze the bending and stretching mode of the materials. Thereafter, planes and crystallinity of materials were measured through a Miniflex (Rigaku) diffractometer. Mass spectra of synthesized ionic liquid were analyzed through a Xevo G2-XS QTOF (WATERS) spectrometer. Thermogravimetric analysis (TGA) was performed on a TGA/DSC 1 STARE SYSTEM from Mettler Toledo with temperature increments of 5 °C min⁻¹ in air to check the thermal stability of materials. Furthermore, proton NMR spectra of ionic liquid were obtained at 400 MHz using the JEOL instrument. Similarly, ¹³C-NMR spectra were recorded while the instrument was operated at 100 MHz. During the NMR analysis chemical shifts were measured using a deuterated solvent as an internal reference. Photophysical properties of polymeric material with the inclusion of ionic liquid were determined using a solid-state UV-visible absorption spectrophotometer (Shimadzu UV-2400). The uniform distribution of ionic liquid over the gelatin-CMC matrix was analyzed through a JEOL JSM-6610-LV instrument. The tensile test was carried out using a UTM (INSTRON) tensile tester without an extensometer at room temperature. Atomic Force Microscopy (AFM) images were acquired using a scanning probe microscopy (Digital Instrument Nanoscope III). Surface morphologies and elemental analysis of PF@IL20% polymeric film were studied through a JEOL JSM-6610-LV instrument. The N₂ Adsorption and desorption experiments were carried out through Quantachrome Instrument, Autosorb-IQ, USA. All the samples were degassed at 493 K for 7 h before the experiment in degassing port.

Brunauer-Emmett Teller (BET) was used to calculate relative pressure from 0.05 to 1.0 and their pore size distribution of material from the desorption branch was calculated using a Barrett-Joyner-Halenda (BJH) plot.

5b.3.3 Synthesis of COF

The COF was synthesized using 2,4,6-trihydroxybenzene-1,3,5-tricarbaldehyde and 1,4-phenylenediamine as a linker. For this 0.1 mmol of 2,4,6-trihydroxybenzene-1,3,5-tricarbaldehyde and 0.3 mmol of 1,4-phenylenediamine were taken in a 50 mL round bottom flask. Thereafter, 2 mL of each dioxane and mesitylene were added to reaction and allowed to stir for 24 hrs at 120 °C. Red color precipitates were obtained which were filtered out followed by washing with THF. At the end washing with acetone was done to obtain COF with very high purity. Finally, a red color compound (COF) was obtained (scheme-5b.1) and further characterized using various techniques.



Scheme 5b.1. Synthesis of COF.

5b.3.4 Smart polymeric strips for monitoring food spoilage

Different solutions were prepared at different pH and COF powder was dispersed in each solution at room temperature with continuous sonication until it dispersed properly. Thereafter, sodium alginate was added to each pH solution separately and a homogenous solution was prepared with continuous stirring at 60 °C for 30 min. Polymeric strips were prepared by casting the homogenous solution on a watch glass and allowed to dry in a hot air oven at 65 °C (figure 5b.1). Digital photographs of strips at pH 4, pH 7, and pH 11 were taken using a smartphone. From the obtained photographs it was observed that different colors of polymeric strips were obtained at different pH solutions.

Furthermore, a reference strip was prepared with a pH-10 buffer solution for monitoring the food spoilage. The reference strip along with a sensing strip prepared at pH-7 was used to monitor the meat (chicken) at room temperature (figure 5b.2a). Change in color of the smart strip was monitored and compared with the reference strip.



Figure 5b.1: Schematic diagram for the synthesis of SA/COF sensing strip.

5b.3.5 Antibacterial Activity Test

To determine the anti-microbial activity of SA/COF with inclusion of citral, activated bacterial culture (100 μ L) of *S. aureus* and *E. coli* was spread on the surface of 50 \times 15 mm Petri dishes containing 15 mL of heat sterilized (121°C, 15 min) luria broth. Turning the color of Nev's Ink autoclave tape from white to black indicated that inside temperature is adequate for sterilization. Next, a piece of SA/COF with inclusion of citral membrane samples was placed on a solid medium and incubated for 24 h at a temperature of 37 °C. Thereafter, the zone of inhibition (ZOI) of the sample was measured with absolute digimatic calipers (Digital Caliper 1112-200 INZIZE Co, Ltd, China)_to an accuracy of 0.01 mm. The average value was calculated from the four different locations around each sample independently.

5b.3.6 Active packaging for preservation of peanuts

Sodium alginate and COF-derived polymeric film were also evaluated as active biodegradable packaging materials for increasing the shelf life of peanuts under temperature, thermal stress, heat, and humidity. Plant-extracted compound citral exhibits antibacterial properties and was incorporated into the SA/COF film by simple dipping method till saturation adsorption. Peanuts were purchased from the local market and packaged with citral-loaded SA/COF film at room temperature (figure 5b.2b). Similarly, a batch of peanuts was kept without any packaging to compare with the packaged one. Packaging was monitored regularly and after 20 days both control and packaged peanuts were compared. From the obtained result it was clear that peanuts with smart packaging remained as such even after 20 days, whereas control peanuts

spoiled completely. Further, formation of mold on peanuts was calculated on both the packaging (figure 5b.2c).

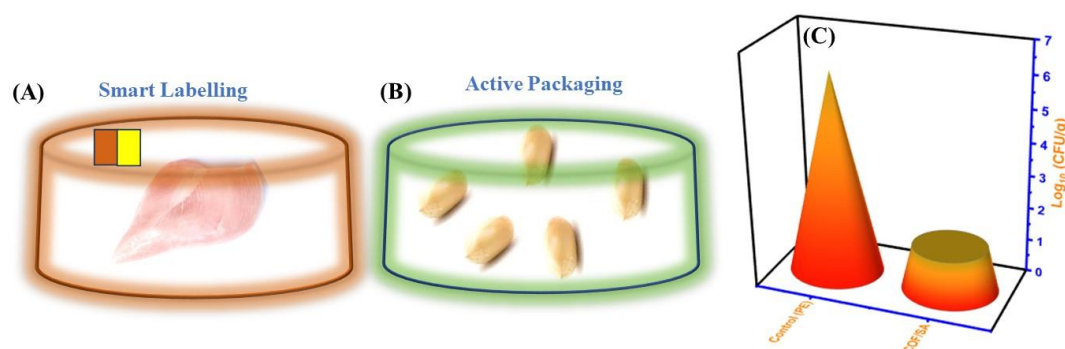


Figure-5b.2. Active packaging of a) chicken, b) peanuts using SA/COF polymeric film, and c) total mold growth on peanuts with and without active packaging.

5b.3.7 Synthesis of smart sensing strips for food monitoring

Smart labeling is an excellent technology commonly used across the world to monitor the safety and security of food. Colorimetric and smart sensing provide information about the spoilage of food visually. Colorimetric responses of strips based on the pH of food surrounding (figure 5b.3a). To carry out the synthesis of smart labeling, sodium alginate (0.5 g) was taken in a 50 mL glass beaker containing 30 mL of distilled water. The mixture was stirred continuously at 80 °C to make a homogeneous polymeric solution. Thereafter, 5 mg of COF dispersed in distilled water at pH-7 was poured into the polymeric solution and stirred continuously at the same temperature for 30 min. At pH-7 red color strips were formed, whereas when pH of solution decreased from 7 to 4 orange color strips were obtained. Concurrently, the color of sensing strips changed to yellow when pH increased from 7 to 11 (figure 5b.3c). The change in color of polymeric strips is based on the protonation and deprotonation mechanism of the schiff base group present in the COF networks (figure 5b.3b). During the vaporization of volatile amines from packaged food, pH of food surroundings turns into basic medium resulting changes in color of the sensing strip attached with food packaging. Biogenic amines include tryptamine, spermine, spermidine, cadaverine, and histamine generated during the spoilage of meat. Thus, highly sensitive pH-responsive smart sensing strips have potential to directly read the conditions of spoilage food through colorimetric response. Thereafter, biodegradability of prepared SA/COF film was explored and their weight loss was investigated after being exposed to soil. From the investigation 60 % weight

loss of SA/COF film was observed after 30 days (figure 5b.3d). The response time of SA/COF strip was calculated and compared with literature (figure 5b.3e). From the compared literature data, it is clear that designed SA/COF film have a much lower response time to pH.

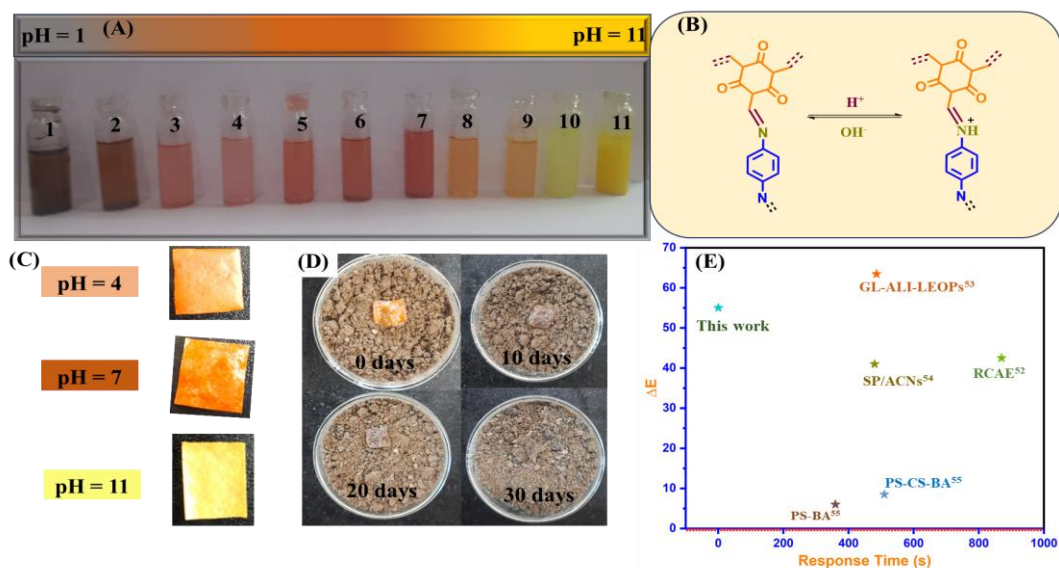


Figure 5b.3. a) Response of COF strips in different pH environments, b) equilibria of COF in acidic and basic medium, c) color of SA/COF strips prepared at pH of 4, 7 and 11, d) degradation of SA/COF film in soil at normal environmental conditions, and e) response time of SA/COF strips compared with literature.

5b.4 Result and Discussion

5b.4.1 PXRD and FTIR Spectra of COF

FTIR spectroscopy was performed to analyze the formation of bonds during synthesis of COF. Formation of an imine bond between TFP and p-phenylenediamine was confirmed with the appearance of a band at 1620 cm⁻¹. Other main characteristic peaks such as O-H stretching, C-H stretching, C-H bending, and C-O stretching were observed at 3338, 2980, 1455, and 1260 cm⁻¹ respectively. The hydroxyl group undergoes tautomerization and formation of an oxime bond also occurs. A peak at 1583 cm⁻¹ indicates the tautomerization of O-H and C=O (figure 5b.4a).

The characteristic peaks of COF appeared at 2θ values of 3.76, 5.4, 7.78, 11.32, 15.1, and 23.58 representing the 100, 110, 200, 210, 220, and 001 planes respectively (figure 5b.4b). PXRD spectra indicates that COF has FCC structure with FWHM value of 2.34.

The skeletal structure and porosity of COFs were greatly influenced by their crystalline structure, which was studied by the combination of PXRD and simulation (Material Studio software). From PXRD analysis it was observed that COF has a highly amorphous 2D structure and π - π stacking between the COF layers (figure 5b.4c).

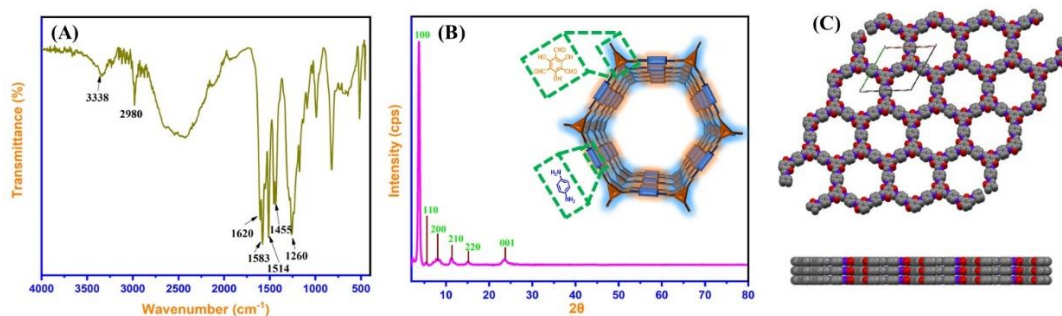


Figure 5b.4. a) FTIR, b) PXRD spectra of COF, and c) simulated structure of COF.

5b.4.2 Scanning Electron Microscopy (SEM) Observations

Surface morphology was investigated through SEM and AFM techniques, which is the essential feature of COF and SA/COF materials. JEOL JSM-6610-LV scanning electron microscope instrument with 60 sec sputtering procedure for Au coating to make conductive coating was used for surface examination. The surface topography of COF shows porous flower-like structures with pore sizes varying from 2 nm to 10 nm (figure 5b.5a). Whereas SA/COF polymeric matrices have flat and dense surfaces with COF particles embedded in the SA solid support material (figure 5b.5c). From the investigation it is clear that COF forms a continuous dense structure on the surface of SA. Elemental mapping and EDS spectra of COF and SA/COF polymeric films demonstrate the uniform distribution of elements (C, N, and, O) (figure 5b.5b and 5b.5d). In addition to these, elemental mapping also confirms the porous structure of COF (figure 5b.5e-5b.5h). Furthermore, to analyze the surface topography and to get the 2D and 3D roughness (figure 5b.6) of COF, Digital Instrument Nanoscope III AFM was used.

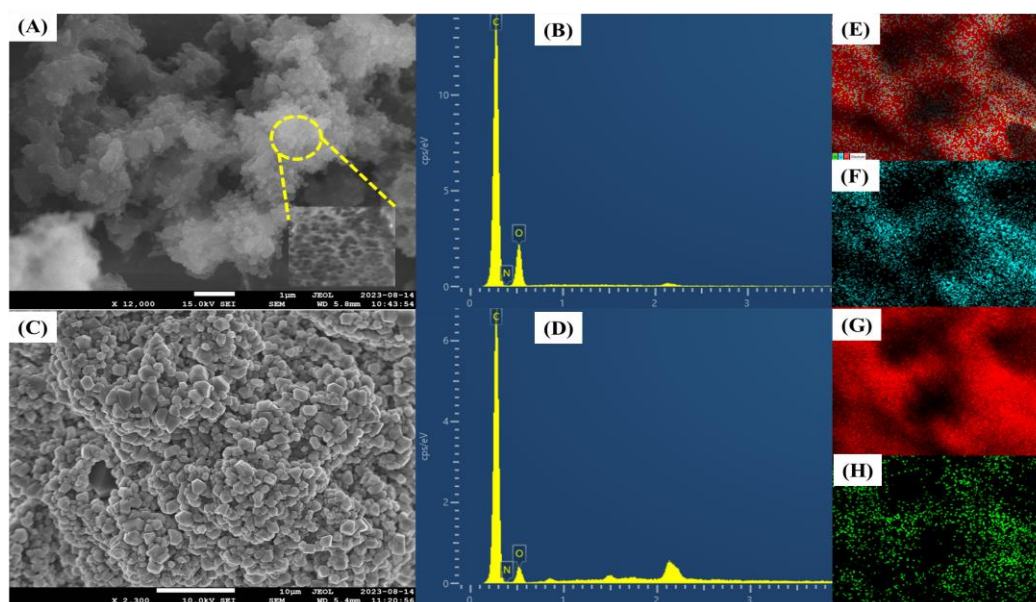


Figure 5b.5. a) FESEM and b) EDS spectra of COF3, c) FESEM and d) EDS spectra of SA/COF, (e-h) elemental mapping of COF.

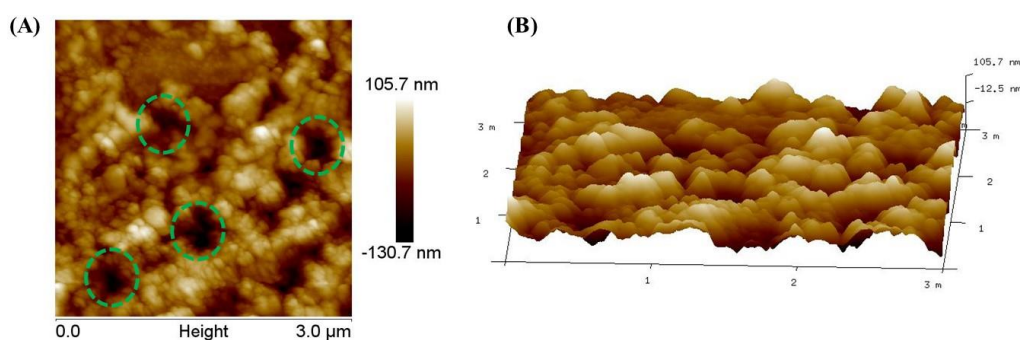


Figure 5b.6: AFM images of COF in 2-dimensional and 3-dimensional.

5b.4.3 Brunauer-Emmett teller (BET) Isotherm

For the gas sensing performance, specific surface area (SSA) plays a major role, and materials with high SSA show excellent gas sensing performance. Nitrogen (N_2) adsorption and desorption experiment was carried out on BET instrument Quantachrome Instrument, Autosorb-IQ (figure 5b.7a). Thereafter, COF sample was degassed at 493 K for 7 h, before proceeding for N_2 gas adsorption. Generally, BET is for surface area identification with the region of relative pressure. Thereafter, N_2 adsorption/desorption data help to find out the total pore volume from 0.1 to 0.9991 relative pressure (P/P_0). From the experiment it was observed that at optimum conditions, the sample has a total pore volume of $1170 \text{ cm}^3 \text{ g}^{-1}$, adsorption cross-section area 0.162 nm^2 , density 0.808 g/cm^3 and mean pore diameter 2.9569 nm (figure 5b.7b).

The large specific surface area and rich pore structure help in reducing the resistance of gas diffusion and make it a potential candidate for gas sensing.

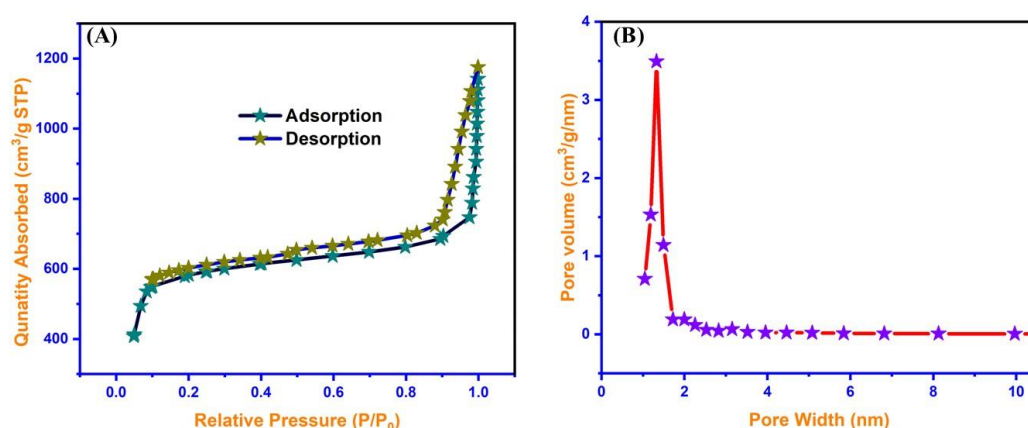


Figure 5b.7. a) N₂ adsorption and desorption curve of COF, and b) mean pore diameter spectra of COF using BJH plot.

5b.4.4 X-ray Photoelectron Spectroscopy (XPS)

XPS is a spectroscopy technique used for the characterization of valence shells or subshells of elements present over the surface of materials and to evaluate the surface bonding properties of COF. XPS survey spectra confirm the presence of characteristic peaks of C1s, N1s, and O1s at 283, 398, and 529 eV respectively (figure 5b.8a). The deconvoluted spectra of C1s indicate the presence of different carbon bonds. In C1s spectra peaks at 295.4 eV attributed to the satellite peak of π - π^* stacking of COF. Peaks at 291.2, 290.2, 284.9, and 283.0 eV correspond to C=O, C-C=N, C-C=C, and C=C respectively (figure 5b.8b). Peak at 290.2 eV is due to formation of an imine bond between amine and aldehyde. Thereafter, XPS spectra of N1s were analyzed and have a peak of N-C at 399.5 eV (figure 5b.8c). Similarly, O1s have two major peaks at 534 and 531 eV confirming the presence of O-H and O-C bonds respectively (figure 5b.8d).

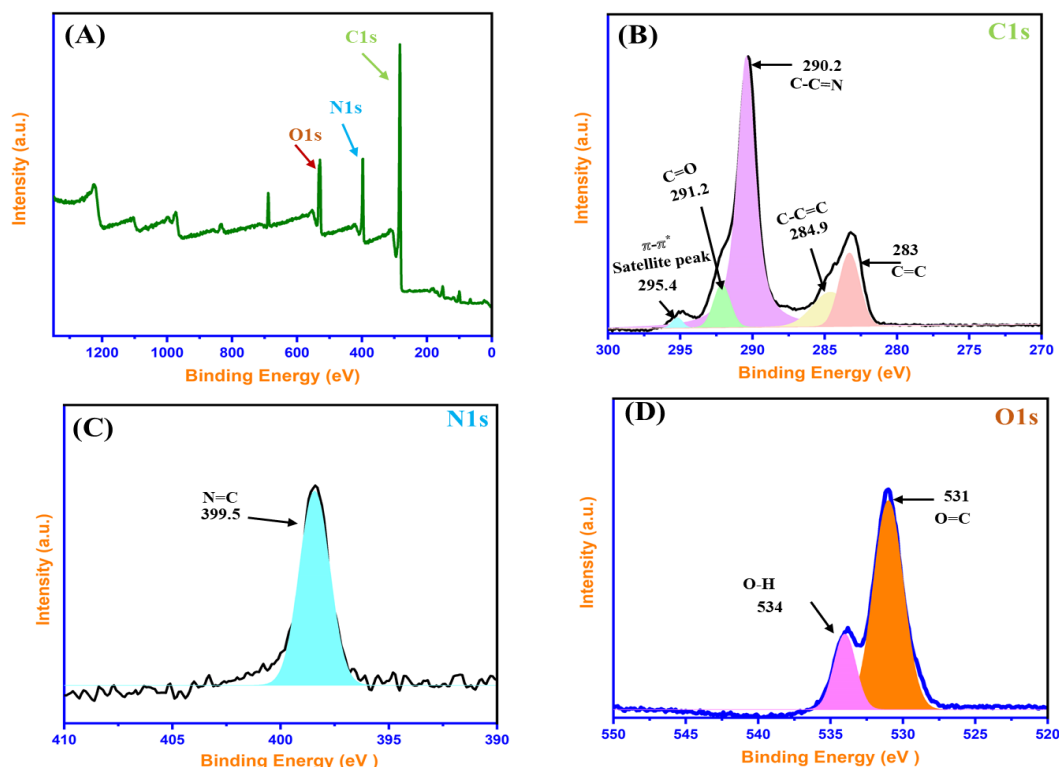


Figure 5b.8. XPS a) elemental survey, b) C1s, c) N1s, and d) O1s spectra of COF.

5b.4.5 Mechanical properties of SA and SA/COF film

SA and SA/COF were subjected to tensile testing and elongation break through Charpy and Izod mode using a UTM (INSTRON) tensile tester without an extensometer at room temperature (figure 5b.9a). Sample strips were prepared with dimensions of 3.20 mm width and 7.20 mm thickness. From the stress-strain performance, it was observed that SA/COF have young modulus and tensile strength of 1070 ± 12 MPa and 23 ± 1.5 MPa respectively, which is much higher than SA have young modulus and tensile strength of 350 ± 12 MPa and 9 ± 1.5 MPa respectively (figure 5b.9b-5b.9c). Similarly elongation at break of SA/COF (25.5 mm) is much higher than SA (9.2 mm) polymeric film (figure 5b.9d). The higher mechanical strength of SA/COF composite is due to the presence of covalent bonding and van der Waals forces. It is clear that inclusion of COF in the SA has a great impact on the mechanical strength of pure SA films. The excellent combinations of mechanical properties indicated that SA/COF polymeric films are good

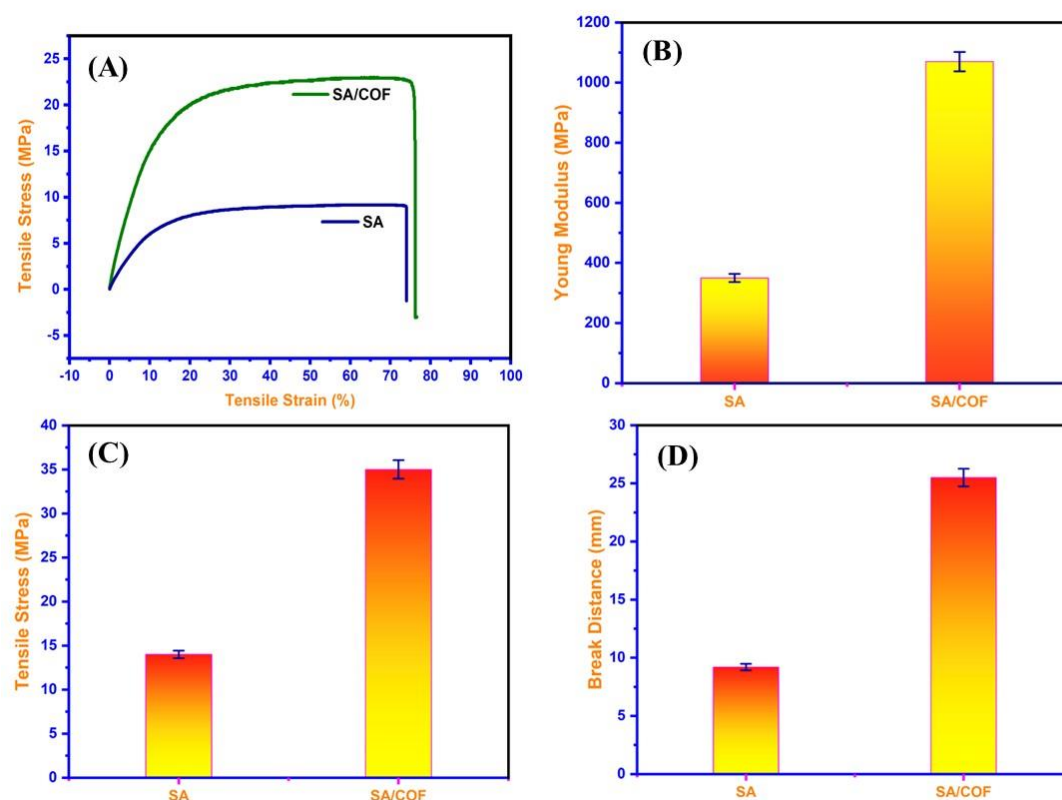


Figure 5b.9: a) Stress/strain curve, b) young modulus, c) tensile stress, and elongation at break of pure sodium alginate (SA) and SA/COF.

5b.4.6 Electrochemical performance of COF

Cyclic voltammetry (CV) is an inexpensive technique used to investigate the electrochemical activity of COF. Based on oxidation and reduction potential, electrochemical techniques provide highly selective and accurate sensing of analytes, where a glassy carbon electrode (GCE) serves as a working electrode, Pt wire acts as a reference electrode, and Ag/AgCl is used as a counter electrode. Initially, the bare glassy carbon electrode having a diameter of 3 mm was polished with 0.03 mm alumina slurry and further washed with EtOH. The COF/GCE modified working electrode was prepared by mixing 2 mg COF in 5 mL THF with nafion as a binder reagent and was first sonicated for 30 min to form a uniform suspension. Then, 5 μ L of this COF suspension was drop cast on the surface of glassy carbon electrode (GCE) and allowed to dry at room temperature. The cyclic voltammetry studies were carried out within -0.6 V to 1 V potential range at 100 mV/s scan rate in 0.1 M PBS buffer solution (pH = 7.4). Furthermore, electrochemical performance of COF was investigated towards biogenic

amines (BAs) (figure 5b.10a). In the presence of BAs, COF shows typical peaks in anodic regions as shown in figure-5b.10b. According to the cyclic voltammetry curve two peaks appeared at 0.105 eV and -0.10 eV corresponds to oxidation and reduction peaks respectively. Therefore, to check the binding authenticity, cyclic voltammetry was performed with subsequent additions of BAs from 0.0125 to 240 μM , and electrochemical behavior at every addition was recorded. Further, to explore electrokinetics behavior of BA's at modified COF/GCE electrode, cyclic voltammetry studies were performed by varying the scan rate (20–200 mV/s) using BA's 240 μM in PBS buffer solution (figure 5b.10c and 5b.11a). The slope of the linear plot of cathodic and anodic peak current versus square of scan rate illustrates that overall recognition of BA's at COF/GCE is a diffusion-controlled phenomena. Moving further, electrochemical impedance spectroscopy (EIS) of modified COF/GCE and GCE electrodes was evaluated to check charge transfer kinetics characteristics. The Nyquist plot (figure 5b.10d), exhibits the interfacial charge transfer resistance (R_{ct}) of bare GCE and modified COF/GCE electrodes are 2690 and 1830 Ω respectively. The results revealed that modified COF/GCE electrodes exhibit better electrical conductivity relative to other electrodes. Furthermore, the electrochemical properties of COF/GCE have also been evaluated using cyclic voltammetry to verify the EIS data. Thus, the electrochemical active surface area of differently modified electrodes was calculated using applying Randles-Sevcik Equation (equation 5b.1).

$$I_{pa} = (2.69 \times 10^5) A D^{1/2} n^{3/2} \nu^{1/2} C \quad (5b.1)$$

Where, I_{pa} = anodic peak current, A = electrochemical active surface area (ESA), D = diffusion coefficient of ferro ferricyanide solution ($D = 6.70 \times 10^{-6} \text{ cm}^2 \text{ s}^{-1}$), n = no. of electrons transferred ($n=1$), ν is the scan rates, and C = concentration of ferro ferricyanide solution ($C = 5 \text{ mM L}^{-1}$). The electrochemical active surface area of COF/GCE and bare GCE are 0.112 cm^2 and 0.054 cm^2 respectively (figure 5b.11b). Results have also been supported by CV profiles of COF/GCE at varying scan rates (20–220 mV s^{-1}) in mixture consisting 5 mM $[\text{Fe}(\text{CN})_6]^{3-/4-}$ solution 100 mV s^{-1} scan rate revealing enhancement of anodic and cathodic peak with shift in potential (figure 5b.10c and 5b.10d). Further, the linearity calibration plot of redox current vs square root of scan rate reveals the diffusion-controlled process (figure 5b.11e).

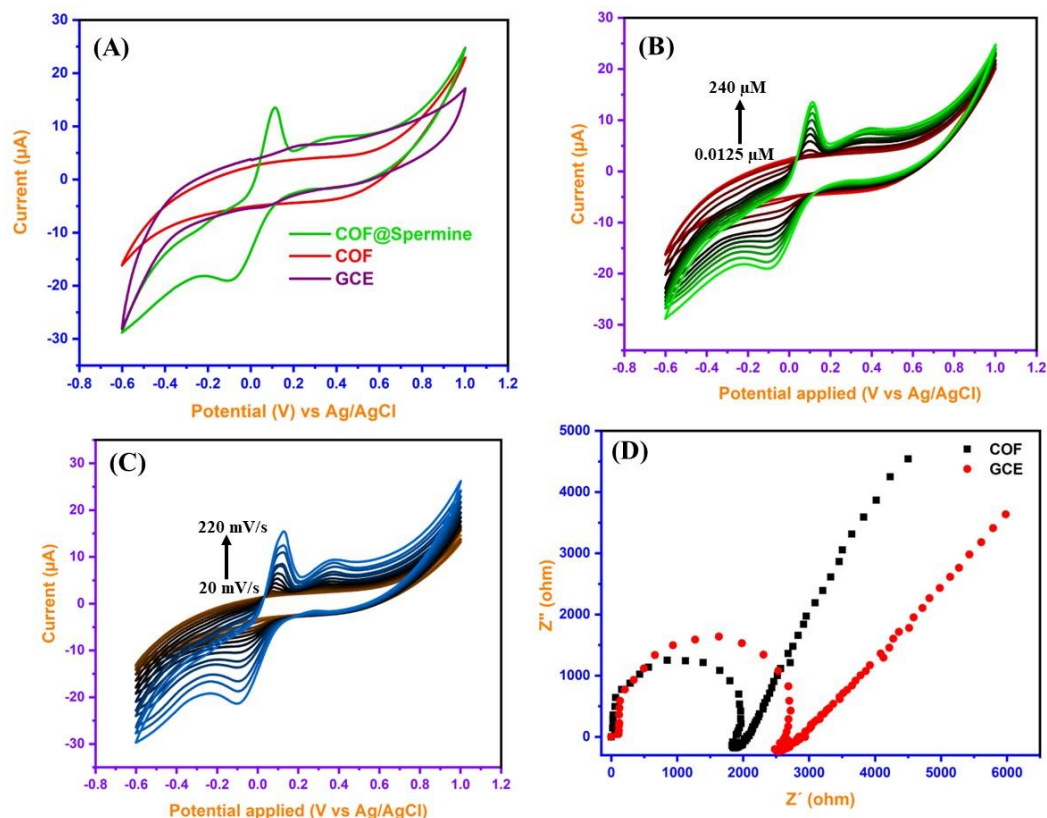


Figure 5b.10. a) Comparative cyclic voltammetry graphs of bare GCE, COF/GCE, COF@Spermine/GCE, b) Cyclic voltammetry response at COF/GCE with gradual addition of varying concentration of BA's (0.0125 to 240 μM) at a scan rate of 100 mV/s, c) CV profiles of COF/GCE at varying scan rate (20-220 mV/s) in PBS buffer (pH 7.4) consisting 240 μM of BA's, and d) EIS plot and cyclic voltammetry profiles of bare GCE, COF/GCE at frequency 50 to 3×10^6 Hz.

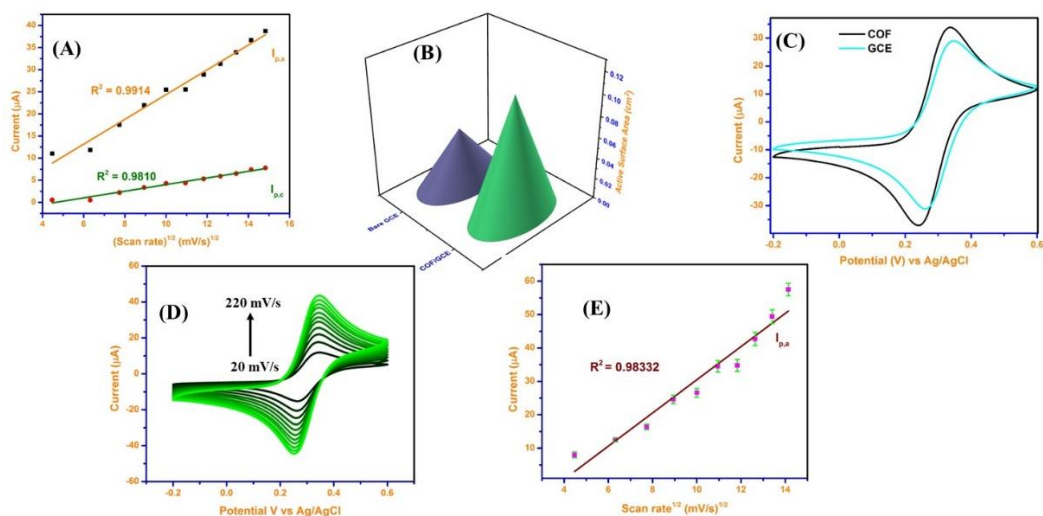


Figure 5b.11: a) Linear calibration plot showing relationship between anodic and cathodic current peak vs square root of scan rate, (b) Comparison of active surface area of differently modified electrodes, (c) Cyclic voltammetry profile of bare GCE, COF/GCE in mixture of 0.1 M KCl consisting $K_3[Fe(CN)_6]$ and $K_4[Fe(CN)_6]$, (d) Cyclic voltammetry response of COF/GCE with varying scan rates from 20 to 220 mV/s in a mixture of 0.1 M KCl consisting $K_3[Fe(CN)_6]$ and $K_4[Fe(CN)_6]$ and (e) Linear calibration plot of the anodic peak current versus square root of scan rate.

5b.4.7 Smart labeling for packaging of food items

Development of smart labeling from biodegradable and biopolymeric material and used globally for food safety and security is a tremendous technology [5, 45]. But the major problem is monitoring food spoilage to reduce food wastage across the world [46]. Static labeling used for food packaging is not able to provide information about foodborne pathogens [47]. Colorimetric sensing is an excellent technique to monitor food spoilage and odor visually [48]. Smart sensing strips are generally based on chemo-responsive compounds inserted in packaging material [49-50]. Inserted chemo-responsive compounds should be stable and non-toxic with excellent responsive properties [51]. From preliminary measurements, it is clear that COF is highly responsive to different pH environments and it was observed that the color of COF changed from red to black with decreases in pH from 7 to 1. Whereas, the color changed from red to yellow with a variation of pH from 7-11. Basically, changes in the color of COF with a variation of pH depend upon protonation and deprotonation of imine group in the framework. The change in colors of COF at different pH values was quantified using color difference (ΔE). It appears that ΔE is above 10 at a pH range of 1-4 and 9-11, which is the ideal value distinguished easily by the naked eye. The high value of ΔE indicates that this COF has potential to be used as a colorimetric chemosensor. The red shift was observed during the protonation of imine bond in an acidic medium (pH 4), while blue shift was obtained during deprotonation of imine bond in a basic medium (pH 11). The prepared SA/COF sensing strips were applied for the sensing of poultry meat and it shows the fastest response time of 0.35 s, which is more sensitive to previous reported methods. Thus, SA/COF film is highly sensitive towards amine and underpinned their potential to monitor the conditions of spoilage food. With spoilage of meat, volatile gasses are released, resulting in changes in the pH of meat continuously. During the monitoring of meat, a reference strip was prepared in a buffer solution of pH-10 and was also

introduced at room temperature as a positive control. ΔE of sensing strip and reference strip were recorded at different intervals of time.

5b.4.8 COF/SA for food packaging

Continuing our previous work gelatin gelatin-based polymeric film for increasing the shelf life of fruit, herein packaging material was derived from sodium alginate and COF with incorporation of citral as an antibacterial agent that could enhance the shelf life of legumes. Herein, SA/COF citral polymeric film was designed and further applied for packaging of protein-rich legumes type food. This type of active packaging helps to reduce the spoilage of food from high humidity, bacteria, high temperature, and storage in tropical areas. During the growth of fungi over the food, results in spoilage of food which is toxic for living beings. In lieu of designing an antimicrobial active packaging material, plant volatiles citral which causes the cell death and exhibits excellent antimicrobial activity, were incorporated over the large ($1170 \text{ cm}^3\text{g}^{-1}$) and mesoporous surface area of COF. Initially, a preliminary antibacterial test of SA/COF citral films with inclusion of citral was carried out against both gram-negative and gram-positive bacteria. Here, zones of inhibition assay were performed against both *Escherichia coli* (*E. coli*) as gram-negative and *Staphylococcus aureus* (*S. aureus*) as gram-positive bacteria for the preliminary test (figure 5b.12a-5b.12b). From the results it was observed that polymeric film with inclusion of COF and citral exhibit remarkable inhibition, whereas no zone of inhibitions was observed in pure SA sample. The bacterial action of SA/COF citral polymeric film against *E. coli* bacterial strain was studied through the FESEM technique (figure 5b.12c-5b.12d).

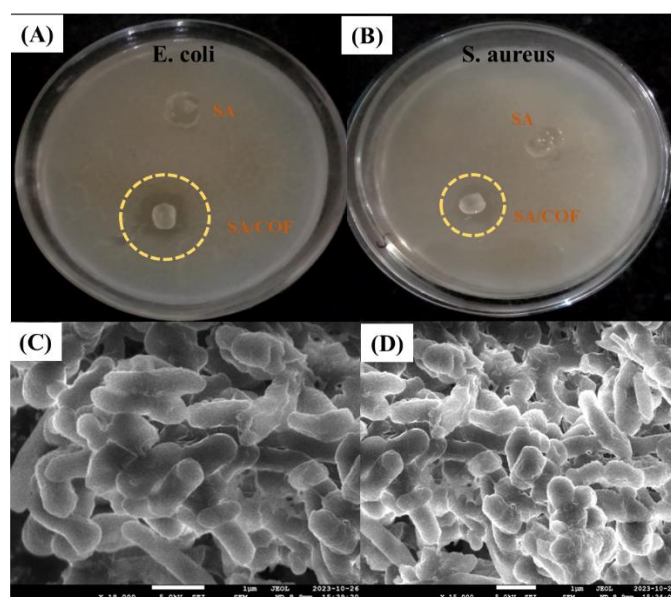


Figure 5b.12. ZOI of pure sodium alginate (SA) and SA/COF/citral in, a) *E. coli* and b) *S. aureus*, FESEM of *E. coli* c) Live and d) dead.

Furthermore, active packaging was applied to increase the shelf life of peanuts, and commercial cling film was used as control (figure 5b.13). Continuing monitoring for 20 days it was observed that mold growth occurred rapidly on peanuts packaging with cling film, whereas no mold was observed on peanuts with active SA/COF/citral polymeric film packaging. Thereafter, total growth of molding on the sample was calculated by culturing in agar solution and was expressed as \log_{10} CFU/g. It is clear from the result that peanuts with active SA/COF/citral packaging have a lesser CFU (1.35 CFU/g) value whereas packaging with commercial cling packaging has a higher CFU value (6.13 CFU/g). Thus, our designed SA/COF/citral active packing material has potential to prevent the spoilage of peanuts in tropical environments.



Figure 5b.13. Photographs of raw peanuts packaged with active SA/COF/citral film and cling film.

5b.5 Conclusion

In Summary, COF was synthesized and a biodegradable SA/COF polymeric film was prepared which has potential to monitor food spoilage in different pH environments that can address the challenges related to food packaging. SA/COF smart strips change their color with evolution of biogenic amines from meat samples and reporting the spoilage of meat samples. Spoilage of meat can be monitored through naked eye. In addition to this COF also exhibits excellent electrochemical response towards biogenic amines. High porosity and large surface area of COF help for inclusion of citral in it, which have antimicrobial properties. SA/COF film embedded with citral applied for increases the shelf life of raw peanuts via preventing mold formation in typical conditions of temperature and humidity. Thus, a biodegradable polymeric film was derived from SA and COF, which provide a promising platform for food safety and security from specific climates.

References (Chapter 1)

1. Wang, Y.; Cheng, Y.; Yin, C.; Zhang, J.; Zhang, X.; Zhang, J. Seashell-Inspired Switchable Waterborne Coatings with Complete Biodegradability, Intrinsic Flame-Retardance, and High Transparency. *ACS Nano* **2023**, *17* (13), 12433–12444.
2. Zheng, A.; Qin, Y.; Xia, Q.; Zhang, X.; Chen, Y. Double-Network Protein Hydrogels as Flexible Pressure Sensors for Contactless Delivery. *ACS Appl Polym Mater* **2023**, *5* (4), 2312–2322.
3. Li, P.; Zhou, T.; Bai, L.; Chen, H.; Wang, W.; Yang, H.; Yang, L.; Wei, D. Highly Sensitive and Stable Flexible Sensors Based on Antifreezing and Self-Healing Double-Network Composite Hydrogels for Human Motion Monitoring. *ACS Appl Polym Mater* **2023**, *5* (9), 7621–7630.
4. Renou, S.; Grand, M.; Daux, V.; Tcherkez, G.; Akoka, S.; Remaud, G. NMR-Based Method for Intramolecular ¹³C Distribution at Natural Abundance Adapted to Small Amounts of Glucose. *Anal Chem* **2023**, *95* (28), 10540–10549.
5. Yang, Z.; Sarkar, A. K.; Amdursky, N. Glycoproteins as a Platform for Making Proton-Conductive Free-Standing Biopolymers. *Biomacromolecules* **2023**, *24* (3), 1111–1120.
6. Yu, Z.; Xu, S.; Wang, P.; Liu, D.; Lu, H. Phosphorus Removal and Storage Polymer Synthesis by Tetrasphaera-Related Bacteria with Different Carbon Sources. *ACS ES and T Water* **2023**, *3* (5), 1374–1384.
7. Wehrmaker, A. M.; Zenker, H. E.; De Groot, W.; Sanders, M.; Van Der Goot, A. J.; Janssen, A. E. M.; Keppler, J.; Bosch, G. Amino Acid Modifications during the Production (Shearing, Sterilization) of Plant-Based Meat Analogues: An Explorative Study Using Pet Food Production as an Example. *ACS Food Science and Technology* **2022**, *2* (11), 1753–1765.
8. Zhao, L.; Hu, J.; Gao, L.; Wang, J.; Ma, X.; Liu, Y.; Ao, Y.; Yan, F.; Liu, L. Improvement of Interfacial Properties and Bioactivity of CF/PEEK Composites by Rapid Biomineralization of Hydroxyapatite. *ACS Biomater Sci Eng* **2023**, *9* (7), 4117–4125.
9. Li, C.; He, J.; Ren, H.; Zhang, X.; Du, E.; Li, X. Preparation of a Chicken ScFv to Analyze Gentamicin Residue in Animal Derived Food Products. *Anal Chem* **2016**, *88* (7), 4092–4098.

10. De Vries, S.; Pustjens, A. M.; Kabel, M. A.; Salazar-Villanea, S.; Hendriks, W. H.; Gerrits, W. J. J. Processing Technologies and Cell Wall Degrading Enzymes to Improve Nutritional Value of Dried Distillers Grain with Solubles for Animal Feed: An in Vitro Digestion Study. *J Agric Food Chem* **2013**, *61* (37), 8821–8828.
11. Fujii, T.; Matsuda, Y.; Seki, T.; Shikida, N.; Iwai, Y.; Ooba, Y.; Takahashi, K.; Isokawa, M.; Kawaguchi, S.; Hatada, N.; Watanabe, T.; Takasugi, R.; Nakayama, A.; Shimbo, K.; Mendelsohn, B. A.; Okuzumi, T.; Yamada, K. AJICAP Second Generation: Improved Chemical Site-Specific Conjugation Technology for Antibody-Drug Conjugate Production. *Bioconjug Chem* **2023**.
12. Mruthunjayappa, M. H.; Sharma, V. T.; Dharmalingam, K.; Sanna Kotrappanavar, N.; Mondal, D. Engineering a Biopolymer-Based Ultrafast Permeable Aerogel Membrane Decorated with Task-Specific Fe-Al Nanocomposites for Robust Water Purification. *ACS Appl Bio Mater* **2020**, *3* (8), 5233–5243.
13. Ramos, N. C.; Manyé Ibáñez, M.; Mittal, R.; Janik, M. J.; Holewinski, A. Combining Renewable Electricity and Renewable Carbon: Understanding Reaction Mechanisms of Biomass-Derived Furanic Compounds for Design of Catalytic Nanomaterials. *Acc Chem Res* **2023**, *56*, 19, 2631–2641.
14. Li, J.; Lu, J.; Sang, H.; Zhang, Y.; Qi, B.; Luo, J.; Wan, Y.; Zhuang, Y. Acid-Resistant Polyimide Ultrafiltration Membranes for Direct Separation of Lignin from Deep Eutectic Solvents. *ACS Appl Polym Mater* **2023**, *5* (7), 5641–5649.
15. Pawlas, J.; Choi, J. H.; von Barga, C.; Maibom-Thomsen, S.; Rasmussen, J. H.; Ludemann-Hombourger, O. Elevating 1-Tert-Butyl-3-Ethylcarbodiimide (TBEC) as a Reagent for Sustainable Peptide Synthesis: Quality Assessment and Minimizing Racemization, Precipitation, and Radical-Induced Side Reactions by TBEC/Oxyma Couplings in an Environmentally Sensible Solvent. *Org Process Res Dev* **2023**, *27* (7), 1348–1364.
16. Hickey, R. J. Controlling Polymer Material Structure during Reaction-Induced Phase Transitions. *Acc Mater Res*, **2023**, *4*, 9, 798–808.
17. Liu, Y.; Yu, B.; Chen, X.; Li, D.; Zhou, C.; Guo, Z. R.; Xu, W.; Yang, S.; Zhang, J. One-Droplet Synthesis of Polysaccharide/Metal-Organic Framework Aerogels for Gas Adsorption. *ACS Appl Polym Mater* **2023**, *5* (6), 4327–4332.

18. Li, L.; Jing, J.; Yang, S.; Fang, S.; Liu, W.; Wang, C.; Li, R.; Liu, T.; Zheng, L.; Yang, C. Bletilla Striata Polysaccharide Nanoparticles Improved the Therapeutic Efficacy of Omeprazole on the Rat Gastric Ulcer Induced by Ethanol. *Mol Pharm* **2023**, *20* (4), 1996–2008.
19. Thompson, M. S.; Johnson, S. A.; Gonsales, S. A.; Brown, G. M.; Kristufek, S. L.; Byers, J. A. Adding Polypeptides to the Toolbox for Redox-Switchable Polymerization and Copolymerization Catalysis. *Macromolecules* **2023**, *56* (8), 3024–3035.
20. Yasuda, A.; Inagawa, A.; Uehara, N. Charge-Selective Aggregation Behavior of Thermoresponsive Polyelectrolytes Having Low Charge Density in Aqueous Solutions of Organic Counterions. *Langmuir* **2023**, *39* (5), 1730–1739.
21. Chen, K.; Zhang, S.; Li, A.; Tang, X.; Li, L.; Guo, L. Bioinspired Interfacial Chelating-like Reinforcement Strategy toward Mechanically Enhanced Lamellar Materials. *ACS Nano* **2018**, *12* (5), 4269–4279.
22. Black, I. M.; Ndukwe, I. E.; Vlach, J.; Backe, J.; Urbanowicz, B. R.; Heiss, C.; Azadi, P. Acetylation in Ionic Liquids Dramatically Increases Yield in the Glycosyl Composition and Linkage Analysis of Insoluble and Acidic Polysaccharides. *Anal Chem* **2023**, *95*(34), 12851–12858.
23. Si, L.; Shi, Z. K.; Hou, J. Y.; Miao, C. X.; Hou, Q.; Xu, Z.; Ai, S. Lignin-Derived Carbon Dot/Cellulose Nanofiber Films for Real-Time Food Freshness Monitoring. *ACS Appl Nano Mater* **2022**, *5* (11), 16620–16632.
24. Zhai, X.; Wu, Z.; Sun, Q.; Sun, J.; Tursun, R.; Zhang, M.; Duan, H.; Zhang, D. Fe₂O₃ Nanorod/Bacterial Cellulose Carbon Nanofiber Composites for Enhanced Acetone Sensing. *ACS Appl Nano Mater* **2023**, *6* (13), 12168–12176.
25. Gaurav, K.; Mehta, N. K.; Majumdar, R. K.; Priyadarshini, M. B.; Pal, P.; Xavier, K. A. M.; Sharma, S. Carboxy Methyl Cellulose, Xanthan Gum, and Carrageenan Coatings Reduced Fat Uptake, Protein Oxidation, and Improved Functionality in Deep-Fried Fish Strips: An Application of the Multiobjective Optimization (MOO) Approach. *ACS Omega* **2023**, *8* (36), 32855–32866.
26. Mushi, N. E.; Nishino, T.; Berglund, L. A.; Zhou, Q. Strong and Tough Chitin Film from α -Chitin Nanofibers Prepared by High Pressure Homogenization and Chitosan Addition. *ACS Sustain Chem Eng* **2019**, *7* (1), 1692–1697.

27. Liu, Y.; Yang, Y.; Tuersun, Y.; Du, W.; Xu, Y.; Zhao, X.; Zhu, G.; Ma, J.; Lin, N. Covalent Immobilization of Natural Biomolecules on Chitin Nanocrystals. *Biomacromolecules* **2023**, *24* (2), 1042–1051.
28. Schröder, P.; Cord-Landwehr, S.; Schönhoff, M.; Cramer, C. Composition and Charge Compensation in Chitosan/Gum Arabic Complex Coacervates in Dependence on PH and Salt Concentration. *Biomacromolecules* **2023**, *24* (3), 1194–1208.
29. Isobe, N.; Kaku, Y.; Okada, S.; Kawada, S.; Tanaka, K.; Fujiwara, Y.; Nakajima, R.; Bissessur, D.; Chen, C. Identification of Chitin Allomorphs in Poorly Crystalline Samples Based on the Complexation with Ethylenediamine. *Biomacromolecules* **2022**, *23* (10), 4220–4229.
30. Park, H.; Oh, J.; Park, Y.; Kim, S.; Kim, J. Environmentally Sustainable Particulate Filter Fabricated via Induced Phase Separation of Bioderived Fungal Chitin and Poly(Lactic Acid). *ACS Appl Polym Mater* **2023**, *5*, 1, 452–462.
31. Das, D.; Bhattacharjee, S.; Bhaladhare, S. Preparation of Cellulose Hydrogels and Hydrogel Nanocomposites Reinforced by Crystalline Cellulose Nanofibers (CNFs) as a Water Reservoir for Agriculture Use. *ACS Appl Polym Mater* **2023**, *5* (4), 2895–2904.
32. Huang, Q. M.; Yang, H.; Wang, S.; Liu, X.; Tan, C.; Luo, A.; Xu, S.; Zhang, G.; Ye, H. Laser-Induced Graphene Formation on Chitosan Derivatives toward Ecofriendly Electronics. *ACS Appl Nano Mater* **2023**, *6* (12), 10453–10465.
33. Chen, Z. C.; Liu, H. J.; Chang, Y. C.; Chen, B. J.; Chang, S. J. Ag-Nanoparticle-Coupled UV-Responsive Gelatin Nanofiber Photodetectors. *ACS Appl Nano Mater* **2023**, *6* (11), 9298–9305.
34. Jiang, Y.; Li, G.; Liu, J.; Li, M.; Li, Q.; Tang, K. Gelatin/Oxidized Konjac Glucomannan Composite Hydrogels with High Resistance to Large Deformation for Tissue Engineering Applications. *ACS Appl Bio Mater* **2021**, *4* (2), 1536–1543.
35. Cao, Y.; Wang, L.; Zhang, K.; Fang, Y.; Nishinari, K.; Phillips, G. O. Mapping the Complex Phase Behaviors of Aqueous Mixtures of κ -Carrageenan and Type B Gelatin. *Journal of Physical Chemistry B* **2015**, *119* (30), 9982–9992.
36. Bayline, J. L.; Tucci, H. M.; Miller, D. W.; Roderick, K. D.; Brletic, P. A. Chemistry of Candy: A Sweet Approach to Teaching Nonscience Majors. *J Chem Educ* **2018**, *95* (8), 1307–1315.

37. Li, L. L.; Xu, J. H.; Qi, G. Bin; Zhao, X.; Yu, F.; Wang, H. Core-Shell Supramolecular Gelatin Nanoparticles for Adaptive and “on-Demand” Antibiotic Delivery. *ACS Nano* **2014**, 8 (5), 4975–4983.
38. Varadarajan, A.; Kearney, L. T.; Keum, J. K.; Naskar, A. K.; Kundu, S. Effects of Salt on Phase Behavior and Rheological Properties of Alginate-Chitosan Polyelectrolyte Complexes. *Biomacromolecules* **2023**, 24 (6), 2730–2740.
39. Cholewinski, A.; Yang, F. K.; Zhao, B. Underwater Contact Behavior of Alginate and Catechol-Conjugated Alginate Hydrogel Beads. *Langmuir* **2017**, 33 (34), 8353–8361.
40. (40) Wu, Y.; Hong, L.; Hu, X.; Li, Y.; Yang, C. Efficient Antimicrobial Effect of Alginate-Catechol/Fe²⁺-Coating on Hydroxyapatite toward Oral Care Application. *ACS Appl Bio Mater* **2022**, 5 (5), 2152–2162.
41. Gattás-Asfura, K. M.; Valdes, M.; Celik, E.; Stabler, C. L. Covalent Layer-by-Layer Assembly of Hyperbranched Polymers on Alginate Microcapsules to Impart Stability and Permeability. *J Mater Chem B* **2014**, 2 (46), 8208–8219.
42. Jin, T.; Liu, T.; Jiang, S.; Kurdyla, D.; Klein, B. A.; Michaelis, V. K.; Lam, E.; Li, J.; Moores, A. Chitosan Nanocrystals Synthesis: Via Aging and Application towards Alginate Hydrogels for Sustainable Drug Release. *Green Chemistry* **2021**, 23 (17), 6527–6537.
43. Patil, S.; Singh, N. Silk Fibroin-Alginate Based Beads for Human Mesenchymal Stem Cell Differentiation in 3D. *Biomater Sci* **2019**, 7 (11), 4687–4697.
44. Hakimifar, A.; Morsali, A. Urea-Based Metal-Organic Frameworks as High and Fast Adsorbent for Hg²⁺ and Pb²⁺ Removal from Water. *Inorg Chem* **2019**, 58 (1), 180–187.
45. Singh, K.; Mehta, S. K. Luminescent ZnO Quantum Dots as an Efficient Sensor for Free Chlorine Detection in Water. *Analyst* **2016**, 141 (8), 2487–2492.
46. Barik, B.; Nayak, P. S.; Achary, L. S. K.; Kumar, A.; Dash, P. Synthesis of Alumina-Based Cross-Linked Chitosan-HPMC Biocomposite Film: An Efficient and User-Friendly Adsorbent for Multipurpose Water Purification. *New Journal of Chemistry* **2019**, 44 (2), 322–337.
47. Thirukumaran, P.; Parveen, A. S.; Ramkumar, V.; Santhamoorthy, M.; Kim, S. C. A Sustainable Strategy for the Remediation of Oil/Water Separation Using Polybenzoxazine/Stearic Acid Functionalized Porous Carbon. *New Journal of Chemistry* **2021**, 45 (37), 17566–17575.

48. Zhang, Q.; Fu, Z.; Yu, H.; Chen, S. Nanoplatin of a SnO₂ Thin-Film on MXene-Based Sponge for Stable and Efficient Solar Energy Conversion. *J Mater Chem A Mater* **2020**, 8 (16), 8065–8074.
49. Guo, Y.; Zhou, X.; Zhao, F.; Bae, J.; Rosenberger, B.; Yu, G. Synergistic Energy Nanoconfinement and Water Activation in Hydrogels for Efficient Solar Water Desalination. *ACS Nano* **2019**, 13 (7), 7913–7919.
50. El Hamoui, O.; Gaudin, K.; Battu, S.; Barthélémy, P.; Lespes, G.; Alies, B. Self-Assembly of Nucleoside-Derived Low-Molecular-Weight Gelators: A Thermodynamics and Kinetics Study on Different Length Scales. *Langmuir* **2021**, 37 (1), 297–310.
51. Gokhale, D.; Chen, I.; Doyle, P. S. Micelle-Laden Hydrogel Microparticles for the Removal of Hydrophobic Micropollutants from Water. *ACS Appl Polym Mater* **2022**, 4 (1), 746–754.
52. Zhao, J.; Lu, Z.; He, X.; Zhang, X.; Li, Q.; Xia, T.; Zhang, W.; Lu, C. Fabrication and Characterization of Highly Porous Fe(OH)₃@Cellulose Hybrid Fibers for Effective Removal of Congo Red from Contaminated Water. *ACS Sustain Chem Eng* **2017**, 5 (9), 7723–7732.
53. Sharma, A. K.; Priya; Kaith, B. S.; Singh, A.; Isha; Vipula; Chandel, K. Enzymatic Construction of Quinine Derivative of Dextrin/PVA Based Hybrid Gel Film for the Simultaneous Detection and Removal of Copper and Lead Ions in Real Water Samples. *Chemical Engineering Journal* **2020**, 382, 122891.
54. Singh, N.; Riyajuddin, S.; Ghosh, K.; Mehta, S. K.; Dan, A. Chitosan-Graphene Oxide Hydrogels with Embedded Magnetic Iron Oxide Nanoparticles for Dye Removal. *ACS Appl Nano Mater* **2019**, 2 (11), 7379–7392.
55. Zhang, E.; Li, W.; Gao, Y.; Lei, C.; Huang, H.; Yang, J.; Zhang, H.; Li, D. High-Capacity Reusable Chitosan Absorbent with a Hydrogel-Coated/Aerogel-Core Structure and Superhydrophilicity under Oil for Water Removal from Oil. *ACS Appl Bio Mater* **2020**, 3 (9), 5872–5879.
56. Qian, D.; Bai, L.; Wang, Y. S.; Song, F.; Wang, X. L.; Wang, Y. Z. A Bifunctional Alginate-Based Composite Hydrogel with Synergistic Pollutant Adsorption and Photocatalytic Degradation Performance. *Ind Eng Chem Res* **2019**, 58 (29), 13133–13144.

57. Kim, S.; Landfester, K.; Ferguson, C. T. J. Hairy Conjugated Microporous Polymer Nanoparticles Facilitate Heterogeneous Photoredox Catalysis with Solvent-Specific Dispersibility. *ACS Nano* **2022**, *16* (10), 17041–17048.
58. Saini, S.; Mayank; Kaur, N.; Singh, N. A Cytochrome C-Urea Functionalized Dipeptide Conjugate: An Efficient HBD Framework to Synthesize 4: H -Pyrans via One-Pot Multicomponent Reaction. *Green Chemistry* **2020**, *22* (3), 956–968.
59. Wei, D. W.; Wei, H.; Gauthier, A. C.; Song, J.; Jin, Y.; Xiao, H. Superhydrophobic Modification of Cellulose and Cotton Textiles: Methodologies and Applications. *Journal of Bioresources and Bioproducts*. KeAi Communications Co. **2020**, *5*, 1–15.
60. Guo, L.; Dou, R.; Wu, Y.; Zhang, R.; Wang, L.; Wang, Y.; Gong, Z.; Chen, J.; Wu, X. From Lignin Waste to Efficient Catalyst: Illuminating the Impact of Lignin Structure on Catalytic Activity of Cycloaddition Reaction. *ACS Sustain Chem Eng* **2019**, *7* (19), 16585–16594.
61. Sun, J.; Wang, J.; Cheng, W.; Zhang, J.; Li, X.; Zhang, S.; She, Y. Chitosan Functionalized Ionic Liquid as a Recyclable Biopolymer-Supported Catalyst for Cycloaddition of CO₂. *Green Chemistry* **2012**, *14* (3), 654–660.
62. Guan, Q.; Yang, C.; Wang, S.; He, L.; Kong, Z.; Chai, X.; Xin, H.; Ning, P. Reactive Metal-Biopolymer Interactions for Semihydrogenation of Acetylene. *ACS Catal* **2019**, *9* (12), 11146–11152.
63. Pettignano, A.; Daunay, A.; Moreau, C.; Cathala, B.; Charlot, A.; Fleury, E. Sustainable Modification of Carboxymethyl Cellulose by Passerini Three-Component Reaction and Subsequent Adsorption onto Cellulosic Substrates. *ACS Sustain Chem Eng* **2019**, *7* (17), 14685–14696.
64. Tang, C.; Chai, Y.; Wang, C.; Wang, Z.; Min, J.; Wang, Y.; Qi, W.; Su, R.; He, Z. Pickering Emulsions Stabilized by Lignin/Chitosan Nanoparticles for Biphasic Enzyme Catalysis. *Langmuir* **2022**, *38* (42), 12849–12858.
65. Ghasemi, K.; Darroudi, M.; Rahimi, M.; Rouh, H.; Gupta, A. R.; Cheng, C.; Amini, A. Magnetic AgNPs/Fe₃O₄@chitosan/PVA Nanocatalyst for Fast One-Pot Green Synthesis of Propargylamine and Triazole Derivatives. *New Journal of Chemistry* **2021**, *45* (35), 16119–16130.
66. Safaiee, M.; Ebrahimghasri, B.; Zolfigol, M. A.; Baghery, S.; Khoshnood, A.; Alonso, D. A. Synthesis and Application of Chitosan Supported Vanadium Oxo in the Synthesis of 1,4-Dihydropyridines and 2,4,6-Triarylpyridines: Via

- Anomeric Based Oxidation. *New Journal of Chemistry* **2018**, 42 (15), 12539–12548.
67. Tian, B.; Liu, J.; Yang, W.; Wan, J. B. Biopolymer Food Packaging Films Incorporated with Essential Oils. *Journal of Agricultural and Food Chemistry*. American Chemical Society, **2023**, 71(3), 1325–1347.
68. Budiarto, I. J.; Rini, N. D. W.; Tsalsabila, A.; Birowosuto, M. D.; Wibowo, A. Chitosan-Based Smart Biomaterials for Biomedical Applications: Progress and Perspectives. *ACS Biomaterials Science and Engineering*. American Chemical Society, **2023**, 9(6), 3084–3115.
69. Hasanzadeh, A.; Shojaei, S.; Gholipour, B.; Vahedi, P.; Rostamnia, S. Biosynthesis of MCC/IL/Ag-AgCl NPs by Cellulose-Based Nanocomposite for Medical Antibiofilm Applications. *Ind Eng Chem Res* **2023**, 62 (11), 4729–4737.
70. Verma, C.; Kardam, S. K.; Chhajed, M.; Nandi, U.; Maji, P. K. Organic Acid-Doped Cellulose Nanocrystals in Biocomposite Laminates as Chiral Nematic Photonic Films: Implications for Intelligent Packaging. *ACS Appl Nano Mater* **2023**, 6, 4, 2791–2804.
71. Alli, Y. A.; Ejeromedoghene, O.; Oladipo, A.; Adewuyi, S.; Amolegbe, S. A.; Anuar, H.; Thomas, S. Compressed Hydrogen-Induced Synthesis of Quaternary Trimethyl Chitosan-Silver Nanoparticles with Dual Antibacterial and Antifungal Activities. *ACS Appl Bio Mater* **2022**, 5 (11), 5240–5254.
72. Liu, J.; Dong, Y.; Ma, Z.; Rao, Z.; Zheng, X.; Tang, K. Soluble Soybean Polysaccharide/Carrageenan Antibacterial Nanocomposite Films Containing Green Synthesized Silver Nanoparticles. *ACS Appl Polym Mater* **2022**, 4 (8), 5608–5618.
73. Shen, K. H.; Yeh, Y. Y.; Chiu, T. H.; Wang, R.; Yeh, Y. C. Dual Dynamic Covalently Crosslinked Alginate Hydrogels with Tunable Properties and Multiple Stimuli-Responsiveness. *ACS Biomater Sci Eng* **2022**, 8 (10), 4249–4261.
74. Zare, M.; Namratha, K.; Ilyas, S.; Hezam, A.; Mathur, S.; Byrappa, K. Smart Fortified PHBV-CS Biopolymer with ZnO-Ag Nanocomposites for Enhanced Shelf Life of Food Packaging. *ACS Appl Mater Interfaces* **2019**, 11 (51), 48309–48320.

75. Pukanen, A.; Kallio, H. P.; Schaich, K. M.; Suomela, J. P.; Yang, B. Red/Green Currant and Sea Buckthorn Berry Press Residues as Potential Sources of Antioxidants for Food Use. *J Agric Food Chem* **2018**, *66* (13), 3426–3434.
76. Saha, R.; Tayalia, P. Clove Oil-Incorporated Antibacterial Gelatin-Chitosan Cryogels for Tissue Engineering: An in Vitro Study. *ACS Biomater Sci Eng* **2022**, *8* (8), 3557–3567.
77. Leite, L. S. F.; Pham, C.; Bilatto, S.; Azeredo, H. M. C.; Cranston, E. D.; Moreira, F. K.; Mattoso, L. H. C.; Bras, J. Effect of Tannic Acid and Cellulose Nanocrystals on Antioxidant and Antimicrobial Properties of Gelatin Films. *ACS Sustain Chem Eng* **2021**, *9*, 8539–8549.
78. Martinez-Mayorga, K.; Peppard, T. L.; López-Vallejo, F.; Yongye, A. B.; Medina-Franco, J. L. Systematic Mining of Generally Recognized as Safe (GRAS) Flavor Chemicals for Bioactive Compounds. *J Agric Food Chem* **2013**, *61* (31), 7507–7514.
79. Kwon, S. J.; Kim, T.; Jung, B. M.; Lee, S. B.; Choi, U. H. Multifunctional Epoxy-Based Solid Polymer Electrolytes for Solid-State Supercapacitors. *ACS Appl Mater Interfaces* **2018**, *10* (41), 35108–35117.
80. Wu, J.; Shu, Q.; Niu, Y.; Jiao, Y.; Chen, Q. Preparation, Characterization, and Antibacterial Effects of Chitosan Nanoparticles Embedded with Essential Oils Synthesized in an Ionic Liquid Containing System. *J Agric Food Chem* **2018**, *66* (27), 7006–7014.
81. Aboomeirah, A. A.; Sarhan, W. A.; Khalil, E. A.; Abdellatif, A.; Abo Dena, A. S.; El-Sherbiny, I. M. Wet Electrospun Nanofibers-Fortified Gelatin/Alginate-Based Nanocomposite as a Single-Dose Biomimicking Skin Substitute. *ACS Appl Bio Mater* **2022**, *5* (8), 3678–3694.
82. Li, S.; Zhang, Y.; Ma, X.; Qiu, S.; Chen, J.; Lu, G.; Jia, Z.; Zhu, J.; Yang, Q.; Chen, J.; Wei, Y. Antimicrobial Lignin-Based Polyurethane/Ag Composite Foams for Improving Wound Healing. *Biomacromolecules* **2022**, *23* (4), 1622–1632.
83. Roy, S.; Rhim, J. W. Preparation of Gelatin/Carrageenan-Based Color-Indicator Film Integrated with Shikonin and Propolis for Smart Food Packaging Applications. *ACS Appl Bio Mater* **2021**, *4* (1), 770–779.
84. Yu, Z.; Boyarkina, V.; Liao, Z.; Lin, M.; Zeng, W.; Lu, X. Boosting Food System Sustainability through Intelligent Packaging: Application of

- Biodegradable Freshness Indicators. *ACS Food Science and Technology* **2023**, *3* (1), 199–212.
85. Han, Y.; Wang, S.; Cao, Y.; Singh, G. P.; Loh, S. I.; Cheerlavancha, R.; Ang, M. C. Y.; Khong, D. T.; Chua, P. W. L.; Ho, P.; Strano, M. S.; Marelli, B. Design of Biodegradable, Climate-Specific Packaging Materials That Sense Food Spoilage and Extend Shelf Life. *ACS Nano* **2023**, *17* (9), 8333–8344.
 86. Yuan, L.; Gao, M.; Xiang, H.; Zhou, Z.; Yu, D.; Yan, R. A Biomass-Based Colorimetric Sulfur Dioxide Gas Sensor for Smart Packaging. *ACS Nano* **2023**, *17* (7), 6849–6856.
 87. Koshy, R. R.; Reghunadhan, A.; Mary, S. K.; Thomas, K.; Ajish, K. R.; Thomas, S.; Pothan, L. A. Intelligent PH-Sensitive Films from Whole Arrowroot Powder and Soy Protein Isolate Incorporating Red Cabbage Anthocyanin: Monitoring Freshness of Shrimps and Ammonia in Fish Farming Ponds. *New Journal of Chemistry* **2022**, *46*, 9036–9047.
 88. Yuan, L.; Gao, M.; Xiang, H.; Zhou, Z.; Yu, D.; Yan, R. A Biomass-Based Colorimetric Sulfur Dioxide Gas Sensor for Smart Packaging. *ACS Nano* **2023**, *17* (7), 6849–6856.
 89. Zhai, X.; Li, Z.; Zhang, J.; Shi, J.; Zou, X.; Huang, X.; Zhang, D.; Sun, Y.; Yang, Z.; Holmes, M.; Gong, Y.; Povey, M. Natural Biomaterial-Based Edible and PH-Sensitive Films Combined with Electrochemical Writing for Intelligent Food Packaging. *J Agric Food Chem* **2018**, *66* (48), 12836–12846.

References (Chapter-2)

1. Singh, S.; Shauloff, N.; Jelinek, R. Solar-Enabled Water Remediation via Recyclable Carbon Dot/Hydrogel Composites. *ACS Sustainable Chemistry and Engineering* **2019**, *7* (15), 13186–13194.
2. Gokhale, D.; Chen, I.; Doyle, P. S. Micelle-Laden Hydrogel Microparticles for the Removal of Hydrophobic Micropollutants from Water. *ACS Applied Polymer Materials* **2022**, *4* (1), 746–754.
3. Shen, L.; Jin, Z.; Xu, W.; Jiang, X.; Shen, Y. X.; Wang, Y.; Lu, Y. Enhanced Treatment of Anionic and Cationic Dyes in Wastewater through Live Bacteria

- Encapsulation Using Graphene Hydrogel. *Industrial and Engineering Chemistry Research* **2019**, 58 (19), 7817–7824.
4. Guo, Y.; Zhou, X.; Zhao, F.; Bae, J.; Rosenberger, B.; Yu, G. Synergistic Energy Nanoconfinement and Water Activation in Hydrogels for Efficient Solar Water Desalination. *ACS Nano* **2019**, 13 (7), 7913–7919.
 5. Wang, D.; Xue, Z. Z.; Zhang, D.; Pan, J.; Wan, X. Y.; Shao, N.; Guan, Q. W.; Wang, G. M. The Iodoargentate Framework as a High-Performance "Sweeper" for Specific Dye Pollutant. *Crystal Growth and Design* **2018**, 18 (11), 6421–6425.
 6. Wu, M. Z.; Shi, J. Y.; Chen, P. Y.; Tian, L.; Chen, J. Two 3D Cobalt(II) Metal-Organic Frameworks with Micropores for Selective Dye Adsorption. *Inorganic Chemistry* **2019**, 58 (5), 3130–3136.
 7. Zhang, Y. di; Wang, Q. Q.; Guo, Z. H.; Zhang, P. F.; Wang, Y.; Yang, G. P.; Wang, Y. Y. Highly Enhanced Congo Red Sorption of New Functionalized Porous Eu(III)-Organic Framework by the Insertion of Sulfonate Groups. *Crystal Growth and Design* **2022**, 22 (3), 1743–1752.
 8. Ghiffary, M. R.; Prabowo, C. P. S.; Sharma, K.; Yan, Y.; Lee, S. Y.; Kim, H. U. High-Level Production of the Natural Blue Pigment Indigoidine from Metabolically Engineered *Corynebacterium Glutamicum* for Sustainable Fabric Dyes. *ACS Sustainable Chemistry and Engineering* **2021**, 9 (19), 6613–6622.
 9. Sharma, A. K.; Priya; Kaith, B. S.; Singh, A.; Isha; Vipula; Chandel, K. Enzymatic Construction of Quinine Derivative of Dextrin/PVA Based Gel Film for the Simultaneous Detection and Removal of Copper and Lead Ions in Real Water Samples. *Chemical Engineering Journal* **2020**, 382, 122891.
 10. Gholami Derami, H.; Gupta, P.; Gupta, R.; Rathi, P.; Morrissey, J. J.; Singamaneni, S. Palladium Nanoparticle-Decorated Mesoporous Polydopamine/Bacterial Nanocellulose as a Catalytically Active Universal Dye Removal Ultrafiltration Membrane. *ACS Applied Nano Materials* **2020**, 3 (6), 5437–5448.

11. Veerakumar, P.; Jeyapragasam, T.; Surabhi, S.; Salamalai, K.; Maiyalagan, T.; Lin, K. C. Functionalized Mesoporous Carbon Nanostructures for Efficient Removal of Eriochrome Black-T from Aqueous Solution. *Journal of Chemical and Engineering Data* **2019**, *64* (4), 1305–1321.
12. Sharma, A. K.; Priya; Kaith, B. S.; Isha; Singh, A.; Chandel, K.; Vipula. Riboflavin Functionalized Dextrin-Sodium Alginate Based Fluorescent Sensor: Detoxification of Cu²⁺ and Ni²⁺ Ions. *ACS Applied Polymer Materials* **2019**, *1* (11), 3084–3094.
13. Li, C.; Cao, S.; Lutzki, J.; Yang, J.; Konegger, T.; Kleitz, F.; Thomas, A. A Covalent Organic Framework/Graphene Dual-Region Hydrogel for Enhanced Solar-Driven Water Generation. *Journal of the American Chemical Society* **2022**, *144* (7), 3083–3090.
14. Priya; Sharma, A. K.; Kaith, B. S.; Vipula; Chandel, K.; Singh, A.; Isha. Chemically Modified Chitosan-sodium Alginate as Chemo-Sensor Adsorbent for the Detection of Picric Acid and Removal of Biebrich Scarlet. *International Journal of Biological Macromolecules* **2020**, *147*, 582–594.
15. Xu, T.; Zhang, J.; Guo, H.; Zhao, W.; Li, Q.; Zhu, Y.; Yang, J.; Bai, J.; Zhang, L. Antifouling Fibrous Membrane Enables High Efficiency and High-Flux Microfiltration for Water Treatment. *ACS Applied Materials and Interfaces* **2021**, *13* (41), 49254–49265.
16. Steinacher, M.; Cont, A.; Du, H.; Persat, A.; Amstad, E. Monodisperse Selectively Permeable Hydrogel Capsules Made from Single Emulsion Drops. *ACS Applied Materials and Interfaces* **2021**, *13* (13), 15601–15609.
17. Li, D.; Li, Q.; Bai, N.; Dong, H.; Mao, D. One-Step Synthesis of Cationic Hydrogel for Efficient Dye Adsorption and Its Second Use for Emulsified Oil Separation. *ACS Sustainable Chemistry and Engineering* **2017**, *5* (6), 5598–5607.
18. Qian, D.; Bai, L.; Wang, Y. S.; Song, F.; Wang, X. L.; Wang, Y. Z. A Bifunctional Alginate-Based Composite Hydrogel with Synergistic Pollutant

- Adsorption and Photocatalytic Degradation Performance. *Industrial and Engineering Chemistry Research* **2019**, 58 (29), 13133–13144.
19. Yang, C.; Shi, X.; Qi, L.; Zhu, X.; Tong, J.; Deng, H.; Du, Y. Electrical Writing Induced Covalent Cross-Linking on Hydrogel for Multidimensional Structural Information Storage. *ACS Applied Materials and Interfaces* **2021**, 13 (30), 36538–36547.
20. Mondal, B.; Bairagi, D.; Nandi, N.; Hansda, B.; Das, K. S.; Edwards-Gayle, C. J. C.; Castelletto, V.; Hamley, I. W.; Banerjee, A. Peptide-Based Gel in Environmental Remediation: Removal of Toxic Organic Dyes and Hazardous Pb^{2+} and Cd^{2+} ions from Wastewater and Oil Spill Recovery. *Langmuir* **2020**, 36 (43), 12942–12953.
21. Du, J.; Yang, X.; Xiong, H.; Dong, Z.; Wang, Z.; Chen, Z.; Zhao, L. Ultrahigh Adsorption Capacity of Acrylic Acid-Grafted Xanthan Gum Hydrogels for Rhodamine B from Aqueous Solution. *Journal of Chemical and Engineering Data* **2021**, 66 (3), 1264–1272.
22. Singh, N.; Riyajuddin, S.; Ghosh, K.; Mehta, S. K.; Dan, A. Chitosan-Graphene Oxide Hydrogels with Embedded Magnetic Iron Oxide Nanoparticles for Dye Removal. *ACS Applied Nano Materials* **2019**, 2 (11), 7379–7392.
23. Wu, Y.; Wang, Q.; Wu, T.; Liu, W.; Nan, H.; Xu, S.; Shen, Y. Detection and Imaging of Hydrogen Sulfide in Lysosomes of Living Cells with Activatable Fluorescent Quantum Dots. *ACS Applied Materials and Interfaces* **2018**, 10 (50), 43472–43481.
24. Suganya, S.; Zo, H. J.; Park, J. S.; Velmathi, S. Simultaneous Sensing of Aqueous Anions and Toxic Metal Ions by Simple Dithiosemicarbazones and Bioimaging of Living Cells. *Industrial and Engineering Chemistry Research* **2014**, 53 (23), 9561–9569.
25. Ye, T.; Durkin, D. P.; Hu, M.; Wang, X.; Banek, N. A.; Wagner, M. J.; Shuai, D. Enhancement of Nitrite Reduction Kinetics on Electrospun Pd-Carbon

- Nanomaterial Catalysts for Water Purification. *ACS Applied Materials and Interfaces* **2016**, 8 (28), 17739–17744.
26. Tiso, M.; Tejero, J.; Kenney, C.; Frizzell, S.; Gladwin, M. T. Nitrite Reductase Activity of Nonsymbiotic Hemoglobins from *Arabidopsis Thaliana*. *Biochemistry* **2012**, 51 (26), 5285–5292.
27. Özdestan, Ö.; Üren, A. Development of a Cost-Effective Method for Nitrate and Nitrite Determination in Leafy Plants and Nitrate and Nitrite Contents of Some Green Leafy Vegetables Grown in the Aegean Region of Turkey. *Journal of Agricultural and Food Chemistry* **2010**, 58 (9), 5235–5240.
28. Yi, W.; Li, Z.; Dong, W.; Han, C.; Guo, Y.; Liu, M.; Dong, C. Three-Dimensional Flower-like Nickel Oxide/Graphene Nanostructures for Electrochemical Detection of Environmental Nitrite. *ACS Applied Nano Materials* **2022**, 5 (1), 216–226.
29. Buldt, A.; Karst, U. Determination of Nitrite in Waters by Microplate Fluorescence Spectroscopy and HPLC with Fluorescence Detection. *Analytical Chemistry* **1999**, 71 (15), 3003–3007.
30. Fu, Y.; Jin, B.; Zhang, Q.; Zhan, X.; Chen, F. PH-Induced Switchable Superwettability of Efficient Antibacterial Fabrics for Durable Selective Oil/Water Separation. *ACS Applied Materials and Interfaces* **2017**, 9 (35), 30161–30170.
31. Wang, F.; Lei, S.; Ou, J.; Li, C.; Li, W. Novel All-Natural Material for Oil/Water Separation. *Industrial and Engineering Chemistry Research* **2019**, 58 (5), 1924–1931.
32. Li, T.; Liu, Y.; Wang, Y.; Wang, Y.; Ma, P.; Zhang, S.; Chen, M.; Dong, W. Superhydrophobic Composite Cotton Generated from Raspberry-like Nanoparticles and Their Applications in Oil/Water Separation. *Industrial and Engineering Chemistry Research* **2020**, 59 (37), 16305–16311.
33. Singh, A.; Singh, N.; Kaur, N.; Jang, D. O. Gold Nanoparticles Supported on Ionic-Liquid-Functionalized Cellulose (Au@CIL): A Heterogeneous Catalyst

- for the Selective Reduction of Aromatic Nitro Compounds. *Appl Organomet Chem* **2022**, 36 (10), 1–11.
34. Vo, T. S.; Hossain, M. M.; Lim, T. G.; Suk, J. W.; Choi, S.; Kim, K. Graphene Oxide-Chitosan Network on a Dialysis Cellulose Membrane for Efficient Removal of Organic Dyes. *ACS Applied Bio Materials* **2022**, 5 (6), 2795–2811.
35. Magnani, C.; Fazilati, M.; Kádár, R.; Idström, A.; Evenäs, L.; Raquez, J. M.; Io Re, G. Green Topochemical Esterification Effects on the Supramolecular Structure of Chitin Nanocrystals: Implications for Highly Stable Pickering Emulsions. *ACS Applied Nano Materials* **2022**, 5 (4), 4731–4743.
36. Lord, M. D.; Neve, G.; Keating, M.; Budhathoki-Uprety, J. Polycarbodiimide for Textile Dye Removal from Contaminated Water. *ACS Applied Polymer Materials* **2022**, 4 (8), 6192–6201.
37. Al-Salihi, S.; Fidalgo, M. M.; Xing, Y. Fast Removal of Tetracycline from Aqueous Solution by Aluminosilicate Zeolite Nanoparticles with High Adsorption Capacity. *ACS ES and T Water* **2023**, 3, 838–847.
38. Joshi, R.; Patra, S.; Srivastava, M.; Singh, B. P.; Chakraborty, A.; Shelar, S. B.; Chakravarty, R.; Chakraborty, S.; Ningthoujam, R. S. Mesoporous NaGdF₄/Ho-Yb@m-SiO₂ Up conversion Nanophosphors as a Potent Theranostic Probe. *ACS Applied Nano Materials* **2022**, 5, 12962–12971.
39. Wang, M.; Zhu, H.; Liu, B.; Hu, P.; Pan, J.; Niu, X. Bifunctional Mn-Doped N-Rich Carbon Dots with Tunable Photoluminescence and Oxidase-Mimetic Activity Enabling Bimodal Ratiometric Colorimetric/Fluorometric Detection of Nitrite. *ACS Applied Material Interfaces* **2022**, 14, 39, 44762–44771.
40. Zhang, W.; Shi, S.; Zhu, W.; Yang, C.; Li, S.; Liu, X.; Hu, N.; Huang, L.; Wang, R.; Suo, Y.; Li, Z.; Wang, J. In-Situ Fixation of All-Inorganic Mo-Fe-S Clusters for the Highly Selective Removal of Lead(II). *ACS Applied Material Interfaces* **2017**, 9 (38), 32720–32726.

References (Chapter-3a)

1. Wang, X.; Ji, M.; Lim, S.; Jang, H. Y. Thiol as a Synthon for Preparing Thiocarbonyl: Aerobic Oxidation of Thiols for the Synthesis of Thioamides. *J. Org. Chem.* **2014**, *79* (15), 7256–7260.
2. Dilworth, J. R.; Pascu, S. I.; Waghorn, P. A.; Vullo, D.; Bayly, S. R.; Christlieb, M.; Sun, X.; Supuran, C. T. Synthesis of Sulfonamide Conjugates of Cu(II), Ga(III), In(III), Re(V) and Zn(II) Complexes: Carbonic Anhydrase Inhibition Studies and Cellular Imaging Investigations. *Dalton Trans.* **2015**, *44* (11), 4859–4873.
3. Fang, Y.; Gu, Z. Y.; Wang, S. Y.; Yang, J. M.; Ji, S. J. Co-Catalyzed Synthesis of N-Sulfonylcarboxamides from Carboxylic Acids and Sulfonyl Azides. *J. Org. Chem.* **2018**, *83* (16), 9364–9369.
4. Chen, X.; Mietlicki-Baase, E. G.; Barrett, T. M.; McGrath, L. E.; Koch-Laskowski, K.; Ferrie, J. J.; Hayes, M. R.; Petersson, E. J. Thioamide Substitution Selectively Modulates Proteolysis and Receptor Activity of Therapeutic Peptide Hormones. *J. Am. Chem. Soc.* **2017**, *139* (46), 16688–16695.
5. Batjargal, S.; Wang, Y. J.; Goldberg, J. M.; Wissner, R. F.; Petersson, E. J. Native Chemical Ligation of Thioamide-Containing Peptides: Development and Application to the Synthesis of Labeled α -Synuclein for Misfolding Studies. *J. Am. Chem. Soc.* **2012**, *134* (22), 9172–9182.
6. Maini, R.; Kimura, H.; Takatsuji, R.; Katoh, T.; Goto, Y.; Suga, H. Ribosomal Formation of Thioamide Bonds in Polypeptide Synthesis. *J. Am. Chem. Soc.* **2019**, *141* (51), 20004–20008.
7. Mahanta, N.; Szantai-Kis, D. M.; Petersson, E. J.; Mitchell, D. A. Biosynthesis and Chemical Applications of Thioamides. *ACS Chem. Biol.* **2019**, *14*, 142–163.
8. Bach, A.; Eildal, J. N. N.; Stühr-Hansen, N.; Deeskamp, R.; Gottschalk, M.; Pedersen, S. W.; Kristensen, A. S.; Strømgaard, K. Cell-Permeable and Plasma-

- Stable Peptidomimetic Inhibitors of the Postsynaptic Density-95/N-Methyl-D-Aspartate Receptor Interaction. *J. Med. Chem.* **2011**, *54* (5), 1333–1346.
9. Vanjari, R.; Guntreddi, T.; Kumar, S.; Singh, K. N. Sulphur Promoted C(sp³)-C(sp²) Cross Dehydrogenative Cyclisation of Acetophenone Hydrazones with Aldehydes: Efficient Synthesis of 3,4,5-Trisubstituted 1H-Pyrazoles. *ChemComm* **2015**, *51* (2), 366–369.
10. Zhang, P.; Chen, W.; Liu, M.; Wu, H. Base-Controlled Three Component Reactions of Amines, Elemental Sulfur, and Styrenes: Synthesis of Thioamides under Metal-Free Conditions. *J. Org. Chem.* **2018**, *83* (23), 14269–14276.
11. Guntreddi, T.; Vanjari, R.; Singh, K. N. Decarboxylative Thioamidation of Arylacetic and Cinnamic Acids: A New Approach to Thioamides. *Org. Lett.* **2014**, *16*, 3624–3627.
12. Nguyen, T. B.; Tran, M. Q.; Ermolenko, L.; Al-Mourabit, A. Three-Component Reaction between Alkynes, Elemental Sulfur, and Aliphatic Amines: A General, Straightforward, and Atom Economical Approach to Thioamides. *Org. Lett.* **2014**, *16* (1), 310–313.
13. Feng, X.; Song, Y.; Lin, W. Dimensional Reduction of Lewis Acidic Metal–Organic Frameworks for Multicomponent Reactions. *J. Am. Chem. Soc.* **2021**, *143*, 8184–8192.
14. Sedighian, H.; Mamaghani, M. B.; Notash, B.; Bazgir, A. Iodide-Catalyzed Selenium-Assisted Sequential Multicomponent Synthesis of a Luminescence Benzo-Oxazino-Isoindole Framework. *J. Org. Chem.* **2021**, *86* (3), 2244–2253.
15. Qi, X.-K.; Guo, L.; Yao, L.-J.; Gao, H.; Yang, C.; Xia, W. Multicomponent Synthesis of α -Branched Tertiary and Secondary Amines by Photocatalytic Hydrogen Atom Transfer Strategy. *Org. Lett.* **2021**, *23*, 4473–4477.
16. Bian, Y.; Qu, X.; Chen, Y.; Li, J.; Liu, L. K₂S₂O₈-Promoted Aryl Thioamides Synthesis from Aryl Aldehydes Using Thiourea as the Sulfur Source. *Molecules* **2018**, *23*, 2225.

17. Saito, M.; Murakami, S.; Nanjo, T.; Kobayashi, Y.; Takemoto, Y. Mild and Chemoselective Thioacylation of Amines Enabled by the Nucleophilic Activation of Elemental Sulfur. *J. Am. Chem. Soc.* **2020**, *142* (18), 8130–8135. DOI:10.1021/jacs.0c03256
18. Zhang, P.; Chen, W.; Liu, M.; Wu, H. Base-Controlled Three Component Reactions of Amines, Elemental Sulfur, and Styrenes: Synthesis of Thioamides under Metal-Free Conditions. *J. Org. Chem.* **2018**, *83* (23), 14269–14276.
19. Kul'ganek, V. V.; Yanovskaya, L. A. Willgerodt-Kindler Reaction with Aromatic Aldehydes. *Bulletin Of the Academy of Sciences of the USSR Division of Chemical Science* **1979**, *28*, 2402–2403.
20. Okamoto, K.; Yamamoto, T.; Kanbara, T. Efficient Synthesis of Thiobenzanilides by Willgerodt-Kindler Reaction with Base Catalysts. *Synlett* **2007**, *17*, 2687–2690.
21. Xu, H.; Deng, H.; Li, Z.; Xiang, H.; Zhou, X. Synthesis of Thioamides by Catalyst-Free Three-Component Reactions in Water. *Eur. J. Org. Chem.* **2013**, 7054–7057.
22. Tayade, Y. A.; Jangale, A. D.; Dalal, D. S. Simple and Highly Efficient Synthesis of Thioamide Derivatives Using β -Cyclodextrin as Supramolecular Catalyst in Water. *ChemistrySelect* **2018**, *3*, 8895–8900.
23. Aghapoor, K.; Mohsenzadeh, F.; Khanalizadeh, G.; Darabi, H. R. The Willgerodt-Kindler Reaction in Water: High Chemoselectivity of Benzaldehydes over Acetophenones. *Monatsh. Chem. Mon.* **2007**, *138*, 61–65.
24. Mitra, B.; Pariyar, G. C.; Ghosh, P. Glycerol: A Benign Solvent-Assisted Metal-Free One-Pot Multi-Component Synthesis of 4*H*-Thiopyran and Thioamides from Easily Accessible Precursors. *ChemistrySelect* **2019**, *4*, 5476–5483.
25. Chen, Z.; Wang, X.; Cao, R.; Idrees, K. B.; Liu, X.; Wasson, M. C.; Farha, O. K. Water-Based Synthesis of a Stable Iron-Based Metal-Organic Framework for Capturing Toxic Gases. *ACS Mater. Lett.* **2020**, *2* (9), 1129–1134.

26. Ahmed, S. A.; Hasan, M. N.; Bagchi, D.; Altass, H. M.; Morad, M.; Jassas, R. S.; Hameed, A. M.; Patwari, J.; Alessa, H.; Alharbi, A.; Pal, S. K. Combating Essential Metal Toxicity: Key Information from Optical Spectroscopy. *ACS Omega* **2020**, 5 (25), 15666–15672.
27. Huang, Z.; Zhao, M.; Wang, C.; Wang, S.; Dai, L.; Zhang, L. Preparation of a Novel Zn(II)-Imidazole Framework as an Efficient and Regenerative Adsorbent for Pb, Hg, and As Ion Removal from Water. *ACS Appl. Mater. Interfaces* **2020**, 12 (37), 41294–41302.
28. Wang, L.; Zhang, H. J.; Liu, X.; Liu, Y.; Zhu, X.; Liu, X.; You, X. A Physically Cross-Linked Sodium Alginate–Gelatin Hydrogel with High Mechanical Strength. *ACS Appl. Polym. Mater.* **2021**, 3, 3197–3205.
29. Choi, J.; Hasturk, O.; Mu, X.; Sahoo, J. K.; Kaplan, D. L. Silk Hydrogels with Controllable Formation of Dityrosine, 3,4-Dihydroxyphenylalanine, and 3,4-Dihydroxyphenylalanine-Fe³⁺ Complexes through Chitosan Particle-Assisted Fenton Reactions. *Biomacromolecules* **2021**, 22 (2), 773–787.
30. Liu, Q.; Lu, Y.; Aguedo, M.; Jacquet, N.; Ouyang, C.; He, W.; Yan, C.; Bai, W.; Guo, R.; Goffin, D.; Song, J.; Richel, A. Isolation of High-Purity Cellulose Nanofibers from Wheat Straw through the Combined Environmentally Friendly Methods of Steam Explosion, Microwave-Assisted Hydrolysis, and Microfluidization. *ACS Sustain. Chem. Eng.* **2017**, 5 (7), 6183–6191.
31. Gorur, Y. C.; Reid, M. S.; Montanari, C.; Larsson, P. T.; Larsson, P. A.; Wågberg, L. Advanced Characterization of Self-Fibrillating Cellulose Fibers and Their Use in Tunable Filters. *ACS Appl. Mater. Interfaces* **2021**, 13 (27), 32467–32478.
32. Sobhanadhas, L. S.; Kesavan, L.; Lastusaari, M.; Fardim, P. Layered Double Hydroxide-Cellulose Hybrid Beads: A Novel Catalyst for Topochemical Grafting of Pulp Fibers. *ACS Omega* **2019**, 4 (1), 320–330.
33. Shen, F.; Smith, R. L.; Li, L.; Yan, L.; Qi, X. Eco-Friendly Method for Efficient Conversion of Cellulose into Levulinic Acid in Pure Water with Cellulase-Mimetic Solid Acid Catalyst. *ACS Sustain. Chem. Eng.* **2017**, 5 (3), 2421–2427.

34. Jiang, Y.; Wang, Z.; Liu, X.; Yang, Q.; Huang, Q.; Wang, L.; Dai, Y.; Qin, C.; Wang, S. Highly Transparent, UV-Shielding, and Water-Resistant Lignocellulose Nanopaper from Agro-Industrial Waste for Green Optoelectronics. *2020*, 8 (47), 17508–17519.
35. Liu, W.; Du, H.; Liu, H.; Xie, H.; Xu, T.; Zhao, X.; Liu, Y.; Zhang, X.; Si, C. Highly Efficient and Sustainable Preparation of Carboxylic and Thermostable Cellulose Nanocrystals via FeCl₃-Catalyzed Innocuous Citric Acid Hydrolysis. *ACS Sustain. Chem. Eng.* **2020**, 8, 16691–16700.
36. Hu, B.; Zhang, B.; Xie, W.; Jiang, X.; Liu, J.; Lu, Q. Recent Progress in Quantum Chemistry Modeling on the Pyrolysis Mechanisms of Lignocellulosic Biomass. *Energy Fuels* **2020**, 34 (9), 10384–10440.
37. Shrotri, A.; Kobayashi, H.; Fukuoka, A. Cellulose Depolymerization over Heterogeneous Catalysts. *Accounts of Chemical Research* **2018**, 51 (3), 761–768.
38. Wang, G.; Xiang, J.; Lin, J.; Xiang, L.; Chen, S.; Yan, B.; Fan, H.; Zhang, S.; Shi, X. Sustainable Advanced Fenton-like Catalysts Based on Mussel-Inspired Magnetic Cellulose Nanocomposites to Effectively Remove Organic Dyes and Antibiotics. *ACS Appl. Mater. Interfaces* **2020**, 12, 51952–51959.
39. Li, D. D.; Zhang, J. W.; Cai, C. Pd Nanoparticles Supported on Cellulose as a Catalyst for Vanillin Conversion in Aqueous Media. *J. Org. Chem.* **2018**, 83 (14), 7534–7538.
40. Can, M.; Demirci, S.; Sunol, A. K.; Philippidis, G.; Sahiner, N. Natural Celluloses as Catalysts in Dehydrogenation of NaBH₄ in Methanol for H₂ Production. *ACS Omega* **2020**, 5 (25), 15519–15528.
41. Eisa, W. H.; Abdelgawad, A. M.; Rojas, O. J. Solid-State Synthesis of Metal Nanoparticles Supported on Cellulose Nanocrystals and Their Catalytic Activity. *ACS Sustain. Chem. Eng.* **2018**, 6 (3), 3974–3983.
42. Nguyen, T. T. T.; Nguyen, L. A.; Quoc Anh Ngo, Q. A.; Marina Koleski, M.; Nguyen, T. B. The catalytic role of elemental sulfur in the DMSO-promoted

- oxidative coupling of methylhetarenes with amines: Synthesis of thioamides and bis-aza-heterocycles. *Org. Chem. Front.* **2021**, 8, 1593–1598.
43. Maleki, A.; Movahed, H.; Paydar, P. Design and development of a novel cellulose/ γ -Fe₂O₃/Ag nanocomposite: A potential green catalyst and antibacterial agent. *RSC Adv.* **2016**, 6, 13657–13665.
44. Kanai, N.; Nishimura, K.; Umetani, S.; Saito, Y.; Saito, H.; Oyama, T.; Kawamura, I. Upcycling of Waste Hop Stems into Cellulose Nanofibers: Isolation and Structural Characterization. *ACS Agric. Sci. Technol.* **2021**, 1 (4), 347–354.
45. Khatri, C. K.; Mali, A. S.; Chaturbhuj, G. U. Sulfated Polyborate Catalyzed Kindler Reaction: A Rapid, Efficient, and Green Protocol. *Monatsh. Chem.* **2017**, 148 (8), 1463–1468.
46. Agnimonhan, H. F.; Ahoussi, L. A.; Glinma, B.; Kohoudé, J. M.; Gbaguidi, F. A.; Kpoviessi, S. D. S.; Poupaert, J.; Accrombessi, G. C. Willgerodt-Kindler Reaction's Microwave-Enhanced Synthesis of Thiobenzamides Derivatives in Heterogeneous Acid Catalysis with Montmorillonite K-10. *Org. Chem. Curr. Res.* **2017**, 06 (02), 2–6.
47. Ray, S.; Bhaumik, A.; Dutta, A.; Butcher, R. J.; Mukhopadhyay, C. A New Application of Rhodanine as a Green Sulfur Transferring Agent for a Clean Functional Group Interconversion of Amide to Thioamide Using Reusable MCM-41 Mesoporous Silica. *Tetrahedron Lett.* **2013**, 54 (17), 2164–2170.
48. Wei, J.; Li, Y.; Jiang, X. Aqueous Compatible Protocol to Both Alkyl and Aryl Thioamide Synthesis. *Org. Lett.* **2016**, 18 (2), 340–343.
49. Wang, X.; Ji, M.; Lim, S.; Jang, H. Y. Thiol as a Synthon for Preparing Thiocarbonyl: Aerobic Oxidation of Thiols for the Synthesis of Thioamides. *J. Org. Chem.* **2014**, 79 (15), 7256–7260.
50. Tayade, Y. A.; Jangale, A. D.; Dalal, D. S. Simple and Highly Efficient Synthesis of Thioamide Derivatives Using β -Cyclodextrin as Supramolecular Catalyst in Water. *ChemistrySelect* **2018**, 3 (31), 8895–8900.

References (Chapter -3b)

1. Kataoka, S.; Tsuruoka, A.; Aoki, D.; Otsuka, H. Fast and Reversible Cross-Linking Reactions of Thermoresponsive Polymers Based on Dynamic Dialkylaminodisulfide Exchange. *ACS Appl Polym Mater* **2021**, 3 (2), 888–895.
2. Shida, N.; Ninomiya, K.; Takigawa, N.; Imato, K.; Ooyama, Y.; Tomita, I.; Inagi, S. Diversification of Conjugated Polymers via Postpolymerization Nucleophilic Aromatic Substitution Reactions with Sulfur-, Oxygen-, and Nitrogen-Based Nucleophiles. *Macromolecules* **2021**, 54 (2), 725–735.
3. He, B.; Zhang, J.; Zhang, H.; Liu, Z.; Zou, H.; Hu, R.; Qin, A.; Kwok, R. T. K.; Lam, J. W. Y.; Tang, B. Z. Catalyst-Free Multicomponent Tandem Polymerizations of Alkyne and Amines toward Nontraditional Intrinsic Luminescent Poly(Aminomaleimide)s. *Macromolecules* **2020**, 53 (10), 3756–3764.
4. Deng, H.; Hu, R.; Zhao, E.; Chan, C. Y. K.; Lam, J. W. Y.; Tang, B. Z. One-Pot Three-Component Tandem Polymerization toward Functional Poly(Arylene Thiophenylene) with Aggregation-Enhanced Emission Characteristics. *Macromolecules* **2014**, 47 (15), 4920–4929.
5. Robert, C.; Thomas, C. M. Tandem Catalysis: A New Approach to Polymers. *Chem. Soc. Rev.*, **2013**, 42, 9392–9402.
6. Cai, Z.; Ren, Y.; Li, X.; Shi, J.; Tong, B.; Dong, Y. Functional Isocyanide-Based Polymers. *Acc Chem Res* **2020**, 53 (12), 2879–2891.
7. Malecha, J. J.; Biller, J. R.; Lama, B.; Gin, D. L. System for Living ROMP of a Paramagnetic FeCl₄--Based Ionic Liquid Monomer: Direct Synthesis of Magnetically Responsive Block Copolymers. *ACS Macro Lett* **2020**, 9 (1), 140–145.
8. Li, Z.; Ren, X.; Sun, P.; Ding, H.; Li, S.; Zhao, Y.; Zhang, K. Protecting-Group-Free Iterative Exponential Growth Method for Synthesizing Sequence-Defined Polymers. *ACS Macro Lett* **2021**, 10 (2), 223–230.
9. Stiernet, P.; Lecomte, P.; De Winter, J.; Debuigne, A. Ugi Three-Component Polymerization Toward Poly(α -Amino Amide)s. *ACS Macro Lett* **2019**, 8 (4), 427–434.

10. Sinha, J.; Soars, S.; Bowman, C. N. Enamine Organocatalysts for the Thiol-Michael Addition Reaction and Cross-Linking Polymerizations. *Macromolecules* **2021**, *54* (4), 1693–1701.
11. Li, Y.; Tan, T.; Zhao, Y.; Wei, Y.; Wang, D.; Chen, R.; Tao, L. Anticancer Polymers via the Biginelli Reaction. *ACS Macro Lett* **2020**, *9* (9), 1249–1254.
12. Xue, H.; Zhao, Y.; Wu, H.; Wang, Z.; Yang, B.; Wei, Y.; Wang, Z.; Tao, L. Multicomponent Combinatorial Polymerization via the Biginelli Reaction. *J Am Chem Soc* **2016**, *138* (28), 8690–8693.
13. Mao, T.; Yang, L.; Liu, G.; Wei, Y.; Gou, Y.; Wang, J.; Tao, L. Ferrocene-Containing Polymer via the Biginelli Reaction for in Vivo Treatment of Oxidative Stress Damage. *ACS Macro Lett* **2019**, *8* (6), 639–645.
14. Wu, H.; Fu, C.; Zhao, Y.; Yang, B.; Wei, Y.; Wang, Z.; Tao, L. Multicomponent Copolycondensates via the Simultaneous Hantzsch and Biginelli Reactions. *ACS Macro Lett* **2015**, *4* (11), 1189–1193.
15. Kubicki, D. J.; Prochowicz, D.; Hofstetter, A.; Zakeeruddin, S. M.; Grätzel, M.; Emsley, L. Phase Segregation in Potassium-Doped Lead Halide Perovskites from 39K Solid-State NMR at 21.1 T. *J Am Chem Soc* **2018**, *140* (23), 7232–7238.
16. Liu, G.; Shegiwal, A.; Zeng, Y.; Wei, Y.; Boyer, C.; Haddleton, D.; Tao, L. Polymers for Fluorescence Imaging of Formaldehyde in Living Systems via the Hantzsch Reaction. *ACS Macro Lett* **2018**, *7* (11), 1346–1352.
17. Pearce, A. K.; Travanut, A.; Couturaud, B.; Taresco, V.; Howdle, S. M.; Alexander, M. R.; Alexander, C. Versatile Routes to Functional RAFT Chain Transfer Agents through the Passerini Multicomponent Reaction. *ACS Macro Lett* **2017**, *6* (7), 781–785.
18. Wu, Y. H.; Zhang, J.; Du, F. S.; Li, Z. C. Dual Sequence Control of Uniform Macromolecules through Consecutive Single Addition by Selective Passerini Reaction. *ACS Macro Lett* **2017**, *6* (12), 1398–1403.
19. Zhao, M.; Liu, N.; Zhao, R. H.; Zhang, P. F.; Li, S. N.; Yue, Y.; Deng, K. L. Facile Synthesis and Properties of Multifunctionalized Polyesters by Passerini Reaction as Thermosensitive, Biocompatible, and Triggerable Drug Release Carriers. *ACS Appl Bio Mater* **2019**, *2* (4), 1714–1723.
20. Deng, X. X.; Li, L.; Li, Z. L.; Lv, A.; Du, F. S.; Li, Z. C. Sequence Regulated Poly(Ester-Amide)s Based on Passerini Reaction. *ACS Macro Lett* **2012**, *1* (11), 1300–1303.

21. Esen, E.; Meier, M. A. R. Sustainable Functionalization of 2,3-Dialdehyde Cellulose via the Passerini Three-Component Reaction. *ACS Sustain Chem Eng* **2020**, 8 (41), 15755–15760.
22. Kakuchi, R.; Theato, P. Efficient Multicomponent Postpolymerization Modification Based on Kabachnik-Fields Reaction. *ACS Macro Lett* **2014**, 3 (4), 329–332.
23. Tang, T.; Fei, X. D.; Ge, Z. Y.; Chen, Z.; Zhu, Y. M.; Ji, S. J. Palladium-Catalyzed Carbonylative Sonogashira Coupling of Aryl Bromides via Tert -Butyl Isocyanide Insertion. *Journal of Organic Chemistry* **2013**, 78 (7), 3170–3175.
24. Mahanta, N.; Szantai-Kis, D. M.; Petersson, E. J.; Mitchell, D. A. Biosynthesis and Chemical Applications of Thioamides. *ACS Chem Biol* **2019**.
25. Dudziński, K.; Pakulska, A. M.; Kwiatkowski, P. An Efficient Organocatalytic Method for Highly Enantioselective Michael Addition of Malonates to Enones Catalyzed by Readily Accessible Primary Amine-Thiourea. *Org Lett* **2012**, 14 (16), 4222–4225.
26. Erver, F.; Hilt, G. Double-and Triple-Cobalt Catalysis in Multicomponent Reactions. *Org Lett* **2012**, 14 (7), 1884–1887.
27. Neelamegan, H.; Yang, D. K.; Lee, G. J.; Anandan, S.; Sorrentino, A.; Wu, J. J. Synthesis of Magnetite-Based Polymers as Mercury and Anion Sensors Using Single Electron Transfer-Living Radical Polymerization. *ACS Omega* **2020**, 5 (13), 7201–7210.
28. Wheeler, P.; Phillips, J. H.; Pederson, R. L. Scalable Methods for the Removal of Ruthenium Impurities from Metathesis Reaction Mixtures. *Org Process Res Dev* **2016**, 20 (7), 1182–1190.
29. Zhu, L.; Ren, X.; Du, J.; Wu, J. H.; Tan, J. P.; Che, J.; Pan, J.; Wang, T. A Transition-Metal-Free Multicomponent Reaction towards Constructing Chiral 2: H -1,4-Benzoxazine Scaffolds. *Green Chemistry* **2020**, 22 (21), 7506–7512.
30. Zhang, C.; Su, J.; Zhu, H.; Xiong, J.; Liu, X.; Li, D.; Chen, Y.; Li, Y. The Removal of Heavy Metal Ions from Aqueous Solutions by Amine Functionalized Cellulose Pretreated with Microwave-H₂O₂. *RSC Adv* **2017**, 7 (54), 34182–34191.
31. Zhang, J.; Zang, Q.; Yang, F.; Zhang, H.; Sun, J. Z.; Tang, B. Z. Sulfur Conversion to Multifunctional Poly(O-Thiocarbamate)s through Multicomponent Polymerizations of Sulfur, Diols, and Diisocyanides. *J Am Chem Soc* **2021**, 143 (10), 3944–3950.

32. Li, X.; Lv, C.; Jia, X.; Cheng, M.; Wang, K.; Hu, Z. Nanoparticle Based on Poly(Ionic Liquid) as an Efficient Solid Immobilization Catalyst for Aldol Reaction and Multicomponent Reaction in Water. *ACS Appl Mater Interfaces* **2017**, *9* (1), 827–835.
33. Sun, Z.; Huang, H.; Li, L.; Liu, L.; Chen, Y. Polythioamides of High Refractive Index by Direct Polymerization of Aliphatic Primary Diamines in the Presence of Elemental Sulfur. *Macromolecules* **2017**, *50* (21), 8505–8511.
34. Bayram, K.; Kiskan, B.; Yagci, Y. Synthesis of Thioamide Containing Polybenzoxazines by the Willgerodt-Kindler Reaction. *Polym Chem* **2021**, *12* (4), 534–544.
35. Li, W.; Wu, X.; Zhao, Z.; Qin, A.; Hu, R.; Tang, B. Z. Catalyst-Free, Atom-Economic, Multicomponent Polymerizations of Aromatic Diynes, Elemental Sulfur, and Aliphatic Diamines toward Luminescent Polythioamides. *Macromolecules* **2015**, *48* (21), 7747–7754.
36. Cao, W.; Dai, F.; Hu, R.; Tang, B. Z. Economic Sulfur Conversion to Functional Polythioamides through Catalyst-Free Multicomponent Polymerizations of Sulfur, Acids, and Amines. *J Am Chem Soc* **2020**, *142* (2), 978–986.
37. Baumruck, A. C.; Yang, J.; Thomas, G. F.; Beyer, L. I.; Tietze, D.; Tietze, A. A. Native Chemical Ligation of Highly Hydrophobic Peptides in Ionic Liquid-Containing Media. *Journal of Organic Chemistry* **2021**, *86* (2), 1659–1666.
38. Haron, G. A. S.; Mahmood, H.; Noh, M. H.; Alam, M. Z.; Moniruzzaman, M. Ionic Liquids as a Sustainable Platform for Nanocellulose Processing from Bioresources: Overview and Current Status. *ACS Sustain Chem Eng* **2021**, *9* (3), 1008–1034.
39. Huang, T.; Xu, Z.; Yan, P.; Liu, X.; Fan, H.; Zhang, Z. C. Direct Partial Oxidation of Methane Catalyzed by an in Situ Generated Active Au(III) Complex at Low Temperature in Ionic Liquids. *Organometallics* **2021**, *40* (3), 370–382.
40. Zhao, Q.; Liu, L. One-Step Conversion of Crab Shells to Levulinic Acid Catalyzed by Ionic Liquids: Self-Healing of Chitin Fraction. *ACS Sustain Chem Eng* **2021**, *9* (4), 1762–1771.
41. Li, X.; Zangiabadi, M.; Zhao, Y. Molecularly Imprinted Synthetic Glucosidase for the Hydrolysis of Cellulose in Aqueous and Nonaqueous Solutions. *J Am Chem Soc* **2021**, *143* (13), 5172–5181.

42. Valverde, D.; Porcar, R.; Lozano, P.; García-Verdugo, E.; Luis, S. V. Multifunctional Polymers Based on Ionic Liquid and Rose Bengal Fragments for the Conversion of CO₂ to Carbonates. *ACS Sustain Chem Eng* **2021**, 9 (5), 2309–2318.
43. Yao, P.; Li, S.; Lambert, A.; Cheng, Q.; Yang, Z.; Zhu, X. Amino Acid-Based Imidazole Ionic Liquid: A Novel Soft Matrix for Electrochemical Biosensing Applications. *ACS Sustain Chem Eng* **2021**, 9 (11), 4157–4166.
44. Yu, J.; Wang, Y.; Sun, L.; Xu, Z.; Du, Y.; Sun, H.; Li, W.; Luo, S.; Ma, C.; Liu, S. Catalysis Preparation of Biodiesel from Waste Schisandra Chinensis Seed Oil with the Ionic Liquid Immobilized in a Magnetic Catalyst: Fe₃O₄@SiO₂@[C₄mim]HSO₄. *ACS Omega* **2021**, 6 (11), 7896–7909.
45. Hou, Y.; Liu, L.; Qiu, S.; Zhou, X.; Gui, Z.; Hu, Y. DOPO-Modified Two-Dimensional Co-Based Metal-Organic Framework: Preparation and Application for Enhancing Fire Safety of Poly(Lactic Acid). *ACS Appl Mater Interfaces* **2018**, 10 (9), 8274–8286.
46. Li, X.; Shen, J.; Wang, B.; Feng, X.; Mao, Z.; Sui, X. Acetone/Water Cosolvent Approach to Lignin Nanoparticles with Controllable Size and Their Applications for Pickering Emulsions. *ACS Sustain Chem Eng* **2021**, 9 (15), 5470–5480.
47. You, J.; Liu, L.; Huang, W.; Manners, I.; Dou, H. Redox-Active Micelle-Based Reaction Platforms for in Situ Preparation of Noble Metal Nanocomposites with Photothermal Conversion Capability. *ACS Appl Mater Interfaces* **2021**, 13 (11), 13648–13657.
48. Kaur, M.; Mayank; Bains, D.; Singh, G.; Kaur, N.; Singh, N. The Solvent-Free One-Pot Multicomponent Tandem Polymerization of 3,4-Dihydropyrimidin-2(1H)-Ones (DHPMs) Catalyzed by Ionic-Liquid@Fe₃O₄NPs: The Development of Polyamide Gels. *Polym Chem* **2021**, 12 (8), 1165–1175.
49. Singh, A.; Saini, S.; Singh, N.; Kaur, N.; Jang, D. O. Cellulose-Reinforced Poly(Ethylene-Co-Vinyl Acetate)-Supported Ag Nanoparticles with Excellent Catalytic Properties: Synthesis of Thioamides Using the Willgerodt-Kindler Reaction. *RSC Adv* **2022**, 12 (11), 6659–6667.
50. Xu, W.; Ollevier, T.; Kleitz, F. Iron-Modified Mesoporous Silica as an Efficient Solid Lewis Acid Catalyst for the Mukaiyama Aldol Reaction. *ACS Catal* **2018**, 8 (3), 1932–1944.

References (Chapter-4)

- (1) Wan, M.; Zhao, H.; Peng, L.; Zhao, Y.; Sun, L. Facile One-Step Deposition of Ag Nanoparticles on SiO₂ Electrospun Nanofiber Surfaces for Label-Free SERS Detection and Antibacterial Dressing. *ACS Applied Bio Materials* **2021**, 4, 6549–6557.
- (2) Huang, Y.; Zou, R.; Lin, Y.; Lu, C. Electronic Metal – Support Interactions for Electrochemiluminescence Signal Amplification. *ACS Catalysis* **2021**, 11, 11291–11297.
- (3) Yang, Y.; Zhang, J.; Liu, J.; Wu, D.; Xiong, B.; Yang, Y.; Hua, Z. Nickel Nanoparticles Encapsulated in SSZ-13 Cage for Highly Efficient CO₂ Hydrogenation. *ACS Catalysis* **2021**, 11, 13240–13248.
- (4) Figueras, M.; Gutiérrez, R. A.; Viñes, F.; Ramírez, P. J.; Rodríguez, J. A.; Illas, F. Supported Molybdenum Carbide Nanoparticles as an Excellent Catalyst for CO₂ Hydrogenation. *ACS Catalysis* **2021**, 11, 9679–9687.
- (5) Qin, P.; Yan, J.; Zhang, W.; Pan, T.; Zhang, X.; Huang, W.; Zhang, W.; Fu, Y.; Shen, Y.; Huo, F. Prediction Descriptor for Catalytic Activity of Platinum Nanoparticles / Metal – Organic Framework Composites. *ACS Catalysis* **2021**, 11, 11872–11881.
- (6) Kopelent, R.; Tereshchenko, A.; Guda, A.; Smolentsev, G.; Artiglia, L.; Sushkevich, V. L.; Bugaev, A.; Sadykov, I. I.; Baidya, T.; Bodnarchuk, M.; van Bokhoven, J. A.; Nachtegaal, M.; Safonova, O. v. Enhanced Reducibility of the Ceria–Tin Oxide Solid Solution Modifies the CO Oxidation Mechanism at the Platinum–Oxide Interface. *ACS Catalysis* **2021**, 11, 9435–9449.
- (7) Hung, W. H.; Aykol, M.; Valley, D.; Hou, W.; Cronin, S. B. Plasmon Resonant Enhancement of Carbon Monoxide Catalysis. *Nano Letters* **2010**, 10 (4), 1314–1318.
- (8) Liu, Y.; Gao, T. N.; Chen, X.; Li, K.; Ma, Y.; Xiong, H.; Qiao, Z. A. Mesoporous Metal Oxide Encapsulated Gold Nanocatalysts: Enhanced Activity for Catalyst Application to Solvent-Free Aerobic Oxidation of Hydrocarbons. *Inorganic Chemistry* **2018**, 57 (20), 12953–12960.
- (9) Bentría, E. T.; Akande, S. O.; Becquart, C. S.; Mousseau, N.; Bouhali, O.; El-Mellouhi, F. Capturing the Iron Carburation Mechanisms from the Surface to Bulk. *Journal of Physical Chemistry C* **2020**, 124 (52), 28569–28579.

- (10) Li, Z.; Ruiz, V. G.; Kanduč, M.; Dzubiella, J. Highly Heterogeneous Polarization and Solvation of Gold Nanoparticles in Aqueous Electrolytes. *ACS Nano* **2021**, *15* (8), 13155–13165.
- (11) Ba Fakih, F.; Shanti, A.; Stefanini, C.; Lee, S. Optimization of Gold Nanoparticles for Efficient Delivery of Catalase to Macrophages for Alleviating Inflammation. *ACS Applied Nano Materials* **2020**, *3* (9), 9510–9519.
- (12) Diao, W.; Wang, G.; Wang, L.; Zhang, L.; Ding, S.; Takarada, T.; Maeda, M.; Liang, X. Opposite Effects of Flexible Single-Stranded DNA Regions and Rigid Loops in DNAzyme on Colloidal Nanoparticle Stability for “Turn-On” Plasmonic Detection of Lead Ions. *ACS Applied Bio Materials* **2020**, *3* (10), 7003–7010.
- (13) Smiljanić, M.; Petek, U.; Bele, M.; Ruiz-Zepeda, F.; Šala, M.; Jovanović, P.; Gabersček, M.; Hodnik, N. Electrochemical Stability and Degradation Mechanisms of Commercial Carbon-Supported Gold Nanoparticles in Acidic Media. *Journal of Physical Chemistry C* **2021**, *125* (1), 635–647.
- (14) Sashuk, V.; Sobczak, G.; Misztalewska-Turkiewicz, I. Photoswitching, Colloidal Stability, and Reversible Self-Assembly of Gold Nanoparticles Covered with Thiolated Donor-Acceptor Stenhouse Adducts. *Journal of Physical Chemistry C* **2021**, *125* (9), 5306–5314.
- (15) Hulnik, M. I.; Kuharenko, O. v.; Vasilenko, I. v.; Timashev, P.; Kostjuk, S. v. Quasiliving Cationic Polymerization of Anethole: Accessing High-Performance Plastic from the Biomass-Derived Monomer. *ACS Sustainable Chemistry and Engineering* **2021**, *9* (19), 6841–6854.
- (16) Kim, H.; Cha, I.; Yoon, Y.; Cha, B. J.; Yang, J.; Kim, Y. D.; Song, C. Facile Mechanochemical Synthesis of Malleable Biomass-Derived Network Polyurethanes and Their Shape-Memory Applications. *ACS Sustainable Chemistry and Engineering* **2021**, *9* (20), 6952–6961.
- (17) Kalusulingam, R.; Gajula, S.; Koilraj, P.; Shanthana Lakshmi, D.; Tayade, R. J.; Srinivasan, K. Biomass-Derived Humin-like Furanic Polymers as an Effective UV-Shielding Agent for Optically Transparent Thin-Film Composites. *ACS Applied Polymer Materials* **2021**, *3* (4), 1932–1942.
- (18) Heedy, S.; Marshall, M. E.; Pineda, J. J.; Pearlman, E.; Yee, A. F. Synergistic Antimicrobial Activity of a Nanopillar Surface on a Chitosan Hydrogel. *ACS Applied Bio Materials* **2020**, *3*, 8040–8048.

- (19) Luna-Murillo, B.; Pala, M.; Paioni, A. L.; Baldus, M.; Ronsse, F.; Prins, W.; Bruijninx, P. C. A.; Weckhuysen, B. M. Catalytic Fast Pyrolysis of Biomass: Catalyst Characterization Reveals the Feed-Dependent Deactivation of a Technical ZSM-5-Based Catalyst. *ACS Sustainable Chemistry and Engineering* **2021**, 9 (1), 291–304.
- (20) Dewan, A.; Sarmah, M.; Bharali, P.; Thakur, A. J.; Boruah, P. K.; Das, M. R.; Bora, U. Pd Nanoparticles-Loaded Honeycomb-Structured Bio-Nanocellulose as a Heterogeneous Catalyst for Heteroaryl Cross-Coupling Reaction. *ACS Sustainable Chemistry and Engineering* **2021**, 9 (2), 954–966.
- (21) Fernandes, T. A.; Costa, I. F. M.; Jorge, P.; Sousa, A. C.; André, V.; Cerca, N.; Kirillov, A. M. Silver(I) Coordination Polymers Immobilized into Biopolymer Films for Antimicrobial Applications. *ACS Applied Materials and Interfaces* **2021**, 13 (11), 12836–12844.
- (22) il Kim, M.; Park, C. Y.; Seo, J. M.; Kang, K. S.; Park, K. S.; Kang, J.; Hong, K. S.; Choi, Y.; Lee, S. Y.; Park, J. P.; Park, H. G.; Park, T. J. In Situ Biosynthesis of a Metal Nanoparticle Encapsulated in Alginate Gel for Imageable Drug-Delivery System. *ACS Applied Materials and Interfaces* **2021**, 13 (31), 36697–36708.
- (23) Hosokawa, S.; Oshino, Y.; Tanabe, T.; Koga, H.; Beppu, K.; Asakura, H.; Teramura, K.; Motohashi, T.; Okumura, M.; Tanaka, T. Strong Metal-Support Interaction in Pd/Ca₂AlMnO₅+ δ : Catalytic NO Reduction over Mn-Doped CaO Shell. *ACS Catalysis* **2021**, 11, 7996–8003.
- (24) Zeng, L.; Cao, Y.; Li, Z.; Dai, Y.; Wang, Y.; An, B.; Zhang, J.; Li, H.; Zhou, Y.; Lin, W.; Wang, C. Multiple Cuprous Centers Supported on a Titanium-Based Metal–Organic Framework Catalyze CO₂ Hydrogenation to Ethylene. *ACS Catalysis* **2021**, 11696–11705.
- (25) Lanaridi, O.; Sahoo, A. R.; Limbeck, A.; Naghdi, S.; Eder, D.; Eitenberger, E.; Csendes, Z.; Schnürch, M.; Bica-Schröder, K. Toward the Recovery of Platinum Group Metals from a Spent Automotive Catalyst with Supported Ionic Liquid Phases. *ACS Sustainable Chemistry and Engineering* **2021**, 9 (1), 375–386.
- (26) He, H.; Ouyang, J. Enhancements in the Mechanical Stretchability and Thermoelectric Properties of PEDOT:PSS for Flexible Electronics Applications. *Accounts of Materials Research* **2020**, 1 (2), 146–157.

- (27) Babucci, M.; Akçay, A.; Balci, V.; Uzun, A. Thermal Stability Limits of Imidazolium Ionic Liquids Immobilized on Metal-Oxides. *Langmuir* **2015**, *31* (33), 9163–9176.
- (28) Miller, R. J.; Smith, V. M.; Love, S. A.; Byron, S. M.; la Cruz, D. S. de; Miller, K. M. Synthesis and Evaluation of Cellulose-Based, 1,2,3-Triazolium-Functionalized Polymerized Ionic Liquids: Thermal Transitions, Ionic Conductivities, and Morphological Properties. *ACS Applied Polymer Materials* **2021**, *3* (2), 1097–1106.
- (29) Lalsare, A. D.; Khan, T. S.; Leonard, B.; Vukmanovich, R.; Tavazohi, P.; Li, L.; Hu, J. Graphene-Supported Fe/Ni, β -Mo₂C Nanoparticles: Experimental and DFT Integrated Approach to Catalyst Development for Synergistic Hydrogen Production through Lignin-Rich Biomass Reforming and Reduced Shale Gas Flaring. *ACS Catalysis* **2021**, *11* (1), 364–382.
- (30) Zhang, Y.; Zhang, M.; Han, Z.; Huang, S.; Yuan, D.; Su, W. Atmosphere-Pressure Methane Oxidation to Methyl Trifluoroacetate Enabled by a Porous Organic Polymer-Supported Single-Site Palladium Catalyst. *ACS Catalysis* **2021**, *11* (3), 1008–1013.
- (31) Totarella, G.; Beerthuis, R.; Masoud, N.; Louis, C.; Delannoy, L.; de Jongh, P. E. Supported Cu Nanoparticles as Selective and Stable Catalysts for the Gas Phase Hydrogenation of 1,3-Butadiene in Alkene-Rich Feeds. *Journal of Physical Chemistry C* **2021**, *125* (1), 366–375.
- (32) Qu, Z.; Chen, X.; Zhong, S.; Deng, G. J.; Huang, H. NaI/PPh₃-Mediated Photochemical Reduction and Amination of Nitroarenes. *Organic Letters* **2021**, *23* (14), 5349–5353.
- (33) Baldwin, A. F.; Caporello, M. A.; Chen, G.; Goetz, A. E.; Hu, W.; Jin, C.; Knopf, K. M.; Li, Z.; Lu, C. v.; Monfette, S.; Puchlopek-Dermenci, A. L. A.; Shi, F. Kilogram-Scale Preparation of an Aminopyrazole Building Block via Copper-Catalyzed Aryl Amidation. *Organic Process Research and Development* **2021**, *25* (4), 1065–1073.
- (34) Liu, G. F.; Qiao, X. X.; Cai, Y. L.; Xu, J. Y.; Yan, Y.; Karadeniz, B.; Lü, J.; Cao, R. Aluminum Metal-Organic Framework-Silver Nanoparticle Composites for Catalytic Reduction of Nitrophenols. *ACS Applied Nano Materials* **2020**, *3* (11), 11426–11433.

- (35) Pachisia, S.; Kishan, R.; Yadav, S.; Gupta, R. Half-Sandwich Ruthenium Complexes of Amide-Phosphine Based Ligands: H-Bonding Cavity Assisted Binding and Reduction of Nitro-Substrates. *Inorganic Chemistry* **2021**, *60* (3), 2009–2022.
- (36) Li, S.; Zhao, W.; Zhang, N.; Luo, Y.; Tang, Y.; Du, G.; Wang, C.; Zhang, X.; Li, L. A Tough Flexible Cellulose Nanofiber Air Cathode for Oxygen Reduction Reaction with Silver Nanoparticles and Carbon Nanotubes in Rechargeable Zinc-Air Batteries. *Energy and Fuels* **2021**, *35* (10), 9017–9028.
- (37) Wang, L.; Wang, F.; Xu, B.; Zhou, M.; Yu, Y.; Wang, P.; Wang, Q. Efficient Regulation of the Behaviors of Silk Fibroin Hydrogel via Enzyme-Catalyzed Coupling of Hyaluronic Acid. *Langmuir* **2021**, *37* (1), 478–489.
- (38) Bordet, A.; Moos, G.; Welsh, C.; Licence, P.; Luska, K. L.; Leitner, W. Molecular Control of the Catalytic Properties of Rhodium Nanoparticles in Supported Ionic Liquid Phase (SILP) Systems. *ACS Catalysis* **2020**, *10* (23), 13904–13912.
- (39) Karimi, B.; Mansouri, F.; Vali, H. Minimizing the Size of Palladium Nanoparticles Immobilized within the Channels of Ionic Liquid-Derived Magnetically Separable Heteroatom-Doped Mesoporous Carbon for Aerobic Oxidation of Alcohols. *ACS Applied Nano Materials* **2020**, *3* (11), 10612–10627.
- (40) Zhao, L.; Hu, C.; Cong, X.; Deng, G.; Liu, L. L.; Luo, M.; Zeng, X. Cyclic (Alkyl)(Amino)Carbene Ligand-Promoted Nitro Deoxygenative Hydroboration with Chromium Catalysis: Scope, Mechanism, and Applications. *Journal of the American Chemical Society* **2021**, *143* (3), 1618–1629.
- (41) Li, H. P.; Dou, Z.; Chen, S. Q.; Hu, M.; Li, S.; Sun, H. M.; Jiang, Y.; Zhai, Q. G. Design of a Multifunctional Indium-Organic Framework: Fluorescent Sensing of Nitro Compounds, Physical Adsorption, and Photocatalytic Degradation of Organic Dyes. *Inorganic Chemistry* **2019**, *58* (16), 11220–11230.
- (42) Das, D.; Biradha, K. Luminescent Coordination Polymers of Naphthalene Based Diamide with Rigid and Flexible Dicarboxylates: Sensing of Nitro Explosives, Fe(III) Ion, and Dyes. *Crystal Growth and Design* **2018**, *18* (6), 3683–3692.
- (43) Kanai, N.; Nishimura, K.; Umetani, S.; Saito, Y.; Saito, H.; Oyama, T.; Kawamura, I. Upcycling of Waste Hop Stems into Cellulose Nanofibers: Isolation and Structural Characterization. *ACS Agricultural Science & Technology* **2021**, *1* (4), 347–354.

- (44) Li, D. D.; Zhang, J. W.; Cai, C. Pd Nanoparticles Supported on Cellulose as a Catalyst for Vanillin Conversion in Aqueous Media. *Journal of Organic Chemistry* **2018**, 83 (14), 7534–7538.
- (45) Singh, A.; Saini, S.; Singh, N.; Kaur, N. Catalytic Properties: Synthesis of Thioamides Using the Willgerodt – Kindler Reaction. **2022**, 12, 6659–6667.
- (46) Byun, S.; Song, Y.; Kim, B. M. Heterogenized Bimetallic Pd-Pt-Fe₃O₄ Nanoflakes as Extremely Robust, Magnetically Recyclable Catalysts for Chemoselective Nitroarene Reduction. *ACS Applied Materials and Interfaces* **2016**, 8 (23), 14637–14647.
- (47) Wang, L.; Huang, S.; Zhu, T.; Ge, X.; Pei, C.; Hong, G.; Han, L. Metabolomic Study on Iohexol-Induced Nephrotoxicity in Rats Based on NMR and LC-MS Analyses. *Chemical Research in Toxicology* **2022**, 35 (2), 244–253.
- (48) Yang, Z.; Shao, D.; Zhou, G. Solubility in Different Solvents, Correlation, and Solvent Effect in the Solvent Crystallization Process of Iohexol. *Journal of Chemical and Engineering Data* **2019**, 64 (4), 1515–1523.
- (49) Pan, X.; Xu, Y. J. Efficient Thermal- and Photocatalyst of Pd Nanoparticles on TiO₂ Achieved by an Oxygen Vacancies Promoted Synthesis Strategy. *ACS Applied Materials and Interfaces* **2014**, 6 (3), 1879–1886.

References (Chapter-5a)

1. Wang, K.; Wang, J.; Li, L.; Xu, L.; Feng, N.; Wang, Y.; Fei, X.; Tian, J.; Li, Y. Novel Nonreleasing Antibacterial Hydrogel Dressing by a One-Pot Method. *ACS Bio mater Sci Eng*, **2020**, 6 (2), 1259–1268.
2. Wu, J.; Shu, Q.; Niu, Y.; Jiao, Y.; Chen, Q. Preparation, Characterization, and Antibacterial Effects of Chitosan Nanoparticles Embedded with Essential Oils Synthesized in an Ionic Liquid Containing System. *J Agric Food Chem*, **2018**, 66 (27), 7006–7014.
3. Go, G.; Yoo, A.; Song, H. W.; Min, H. K.; Zheng, S.; Nguyen, K. T.; Kim, S.; Kang, B.; Hong, A.; Kim, C. S.; Park, J. O.; Choi, E. Multifunctional Biodegradable Microrobot with Programmable Morphology for Biomedical Applications. *ACS Nano*, **2021**, 15 (1), 1059–1076.
4. Roy, S.; Ezati, P.; Rhim, J. W. Fabrication of Antioxidant and Antimicrobial

- Pullulan/Gelatin Films Integrated with Grape Seed Extract and Sulfur Nanoparticles. *ACS Appl Bio Mater*, **2022**, 5, 2316–2323.
5. Santos, M. R. E.; Mendonça, P. v.; Branco, R.; Sousa, R.; Dias, C.; Serra, A. C.; Fernandes, J. R.; Magalhães, F. D.; Morais, P. v.; Coelho, J. F. J. Light-Activated Antimicrobial Surfaces Using Industrial Varnish Formulations to Mitigate the Incidence of Nosocomial Infections. *ACS Appl Mater Interfaces*, **2021**, 13 (6), 7567–7579.
 6. Mei, L.; Ren, Y.; Gu, Y.; Li, X.; Wang, C.; Du, Y.; Fan, R.; Gao, X.; Chen, H.; Tong, A.; Zhou, L.; Guo, G. Strengthened and Thermally Resistant Poly(Lactic Acid)-Based Composite Nanofibers Prepared via Easy Stereocomplexation with Antibacterial Effects. *ACS Appl Mater Interfaces*, **2022**, 10 (49), 42992–43002.
 7. Morena, A. G.; Stefanov, I.; Ivanova, K.; Pérez-Rafael, S.; Sánchez-Soto, M.; Tzanov, T. Antibacterial Polyurethane Foams with Incorporated Lignin-Capped Silver Nanoparticles for Chronic Wound Treatment. *Ind Eng Chem Res*, **2022**, 59 (10), 4504–4514.
 8. Li, S.; Zhang, Y.; Ma, X.; Qiu, S.; Chen, J.; Lu, G.; Jia, Z.; Zhu, J.; Yang, Q.; Chen, J.; Wei, Y. Antimicrobial Lignin-Based Polyurethane/Ag Composite Foams for Improving Wound Healing. *Biomacromolecules*, **2022**, 23 (4), 1622–1632.
 9. Lohmann, S. C.; Tripathy, A.; Milionis, A.; Keller, A.; Poulikakos, D. Effect of Flexibility and Size of Nanofabricated Topographies on the Mechanobactericidal Efficacy of Polymeric Surfaces. *ACS Appl Bio Mater*, **2022**, 5 (4), 1564–1575.
 10. Yuan, H.; Zhao, H.; Peng, K.; Qi, R.; Bai, H.; Zhang, P.; Huang, Y.; Lv, F.; Liu, L.; Bao, J.; Wang, S. Conjugated Polymer-Quantum Dot Hybrid Materials for Pathogen Discrimination and Disinfection. *ACS Appl Mater Interfaces*, **2022**, 12 (19), 21263–21269.
 11. Rogerio, C. B.; Carvalho Abrantes, D.; de Oliveira, J. L.; Ribeiro De Araújo, D.; Germano Da Costa, T.; de Lima, R.; Fernandes Fraceto, L. Cellulose Hydrogels Containing Geraniol and Icaridin Encapsulated in Zein Nanoparticles for Arbovirus Control. *ACS Appl Bio Mater*, **2022**, 5 (3), 1273–1283.
 12. Hassan, I.; Gani, A. Alginate-Based PH-Sensitive Hydrogels Encoated with Chitosan as a Bioactive Cargo Carrier with Caffeic Acid as a Model Biomolecule. *ACS Food Science and Technology*, **2022**, 2 (4), 667–672.

13. Pukanen, A.; Kallio, H. P.; Schaich, K. M.; Suomela, J. P.; Yang, B. Red/Green Currant and Sea Buckthorn Berry Press Residues as Potential Sources of Antioxidants for Food Use. *J Agric Food Chem*, **2018**, *66* (13), 3426–3434.
14. Leite, L. S. F.; Pham, C.; Bilatto, S.; Azeredo, H. M. C.; Cranston, E. D.; Moreira, F. K.; Mattoso, L. H. C.; Bras, J. Effect of Tannic Acid and Cellulose Nanocrystals on Antioxidant and Antimicrobial Properties of Gelatin Films. *ACS Sustain Chem Eng*, **2021**, *9*, 8539–8549.
15. Saha, R.; Tayalia, P. Clove Oil-Incorporated Antibacterial Gelatin-Chitosan Cryogels for Tissue Engineering: An in Vitro Study. *ACS Bio mater Sci Eng*, **2022**, *8* (8), 3557–3567.
16. Xue, J.; Zhong, Q. Blending Lecithin and Gelatin Improves the Formation of Thymol Nanodispersions. *J Agric Food Chem*, **2014**, *62* (13), 2956–2962.
17. Tang, Y.; Zhou, Y.; Lan, X.; Huang, D.; Luo, T.; Ji, J.; Mafang, Z.; Miao, X.; Wang, H.; Wang, W. Electrospun Gelatin Nanofibers Encapsulated with Peppermint and Chamomile Essential Oils as Potential Edible Packaging. *J Agric Food Chem*, **2019**, *67* (8), 2227–2234.
18. Chen, N.; Yao, S.; Li, M.; Wang, Q.; Sun, X.; Feng, X.; Chen, Y. Nonporous versus Mesoporous Bioinspired Polydopamine Nanoparticles for Skin Drug Delivery. *Biomacromolecules*, **2023**, *24* (4), 1648–1661.
19. Bains, D.; Singh, G.; Singh, N. Sustainable Synthesis of Ionic Liquid-Functionalized Zinc Oxide Nanosheets (IL@ZnO): Evaluation of Antibacterial Potential Activity for Biomedical Applications. *ACS Appl Bio Mater*, **2022**, *5* (3), 1239–1251.
20. Kwon, S. J.; Kim, T.; Jung, B. M.; Lee, S. B.; Choi, U. H. Multifunctional Epoxy-Based Solid Polymer Electrolytes for Solid-State Supercapacitors. *ACS Appl Mater Interfaces*, **2018**, *10* (41), 35108–35117.
21. Zhan, X.; Zhang, J.; Liu, M.; Lu, J.; Zhang, Q.; Chen, F. Advanced Polymer Electrolyte with Enhanced Electrochemical Performance for Lithium-Ion Batteries: Effect of Nitrile-Functionalized Ionic Liquid. *ACS Appl Energy Mater*, **2019**, *2* (3), 1685–1694.
22. Aboomeirah, A. A.; Sarhan, W. A.; Khalil, E. A.; Abdellatif, A.; Abo Dena, A. S.; El-Sherbiny, I. M. Wet Electrospun Nanofibers-Fortified Gelatin/Alginate-Based Nanocomposite as a Single-Dose Biomimicking Skin Substitute. *ACS Appl Bio*

- Mater*, **2022**, 5 (8), 3678–3694.
23. Li, Y.; Wu, K.; Liu, Z.; He, X.; Sun, J.; Zeng, M.; Lee, S. H.; Wang, T. T. Y.; Gao, B.; Xie, Z.; Wei, C. I.; Yu, L. L. Effect of Thermal Treatments on Soluble-Free, Soluble-Conjugated, and Insoluble-Bound Phenolic Components and Free Radical Scavenging Properties of Tomato Seeds. *ACS Food Science and Technology*, **2022**, 2, 1631–1638.
 24. Danyliv, O.; Strach, M.; Nechyporchuk, O.; Nypelö, T.; Martinelli, A. Self-Standing, Robust Membranes Made of Cellulose Nanocrystals (CNCs) and a Protic Ionic Liquid: Toward Sustainable Electrolytes for Fuel Cells. *ACS Appl Energy Mater*, **2021**, 4 (7), 6474–6485.
 25. Bains, D.; Singh, G.; Kaur, N.; Singh, N. Development of an Ionic Liquid@Metal-Based Nanocomposite-Loaded Hierarchical Hydrophobic Surface to the Aluminum Substrate for Antibacterial Properties. *ACS Appl Bio Mater*, **2020**, 3 (8), 4962–4973.
 26. Singh, A.; Singh, N.; Kaur, N.; Jang, D. O. Chitosan-Poly(Vinyl Alcohol)-Ionic Liquid-Grafted Hydrogel for Treating Wastewater. *New Journal of Chemistry*, **2023**, 47 (23), 11196–11209.
 27. Zhang, M.; Ouyang, J.; Fu, L.; Xu, C.; Ge, Y.; Sun, S.; Li, X.; Lai, S.; Ke, H.; Yuan, B.; Yang, K.; Yu, H.; Gao, L.; Wang, Y. Hydrophobicity Determines the Bacterial Killing Rate of α -Helical Antimicrobial Peptides and Influences the Bacterial Resistance Development. *J Med Chem*, **2022**, 65 (21), 14701–14720.
 28. Cheng, B.; Cui, H.; Zhang, N.; Feng, H.; Chu, D.; Cui, B.; Li, Z.; Zhang, J.; Cao, S.; Li, J. (2022). Antibiotic-Free Self-Assembled Polypeptide Nanomicelles for Bacterial Keratitis. *ACS Appl Polym Mater*, **2022**, 4 (10), 7250–7257.
 29. Zhang, H.; He, J.; Peng, T.; Qu, J. Ultra-Stretchable, Antifatigue, Adhesive, and Self-Healing Hydrogels Based on the Amino Acid Derivative and Ionic Liquid for Flexible Strain Sensors. *ACS Appl Polym Mater*, **2022**, 4 (10), 7575–7586.
 30. Zhao, W.; Yu, Y.; Zhang, Z.; He, D.; Zhang, H. Bioinspired Nanospheres as Anti-Inflammation and Antisenescence Interfacial Biolubricant for Treating Temporomandibular Joint Osteoarthritis. *ACS Appl Mater Interfaces*, **2022**, 14 (31), 35409–35422.
 31. Kour, P.; Dar, A. A. Interfacially Modified Hybrid Nanoemulsion-Based Alginate Capsules: A Novel Food Grade System with Enhanced Oxidative Stability of

- Linoleic Acid with a Potential Antioxidant Property. *ACS Food Science and Technology*, **2023**, 3 (5), 838–849.
32. Chen, N.; Yao, S.; Li, M.; Wang, Q.; Sun, X.; Feng, X.; Chen, Y. Nonporous versus Mesoporous Bioinspired Polydopamine Nanoparticles for Skin Drug Delivery. *Biomacromolecules*, **2023**, 24 (4), 1648–1661.

References (Chapter-5b)

1. Facure, M. H. M.; Andre, R. S.; Mercante, L. A.; Correa, D. S. Colorimetric Detection of Antioxidants in Food Samples Using MnO₂/Graphene Quantum Dot Composites with Oxidase-like Activity. *ACS Appl Nano Mater* **2022**, 5 (10), 15211–15219.
2. Pratibha; Kapoor, A.; Rajput, J. K.; Kumar, A. Dualistic Fluorescence as Well as Portable Smartphone-Assisted RGB-Relied Sensing Assay for the Ultra-Sensitive Determination of Pendimethalin in Food and Water Samples by AIEE Active Organic Probes. *Anal Chem* **2022**, 94 (50), 17685–17691.
3. Liu, X.; Wang, S.; Wu, P.; Feng, K.; Hubacek, K.; Li, X.; Sun, L. Impacts of Urban Expansion on Terrestrial Carbon Storage in China. *Environ Sci Technol* **2019**, 53 (12), 6834–6844.
4. Mekonnen, M. L.; Mola, A. M.; Abda, E. M. Rapid Colorimetric Detection of Thiabendazole Based on Its Inhibition Effect on the Peroxidase Mimetic Activity of Ag-MoS₂ Nanozyme. *ACS Agricultural Science and Technology* **2023**, 3 (1), 82–89.
5. Pounds, K.; Bao, H.; Luo, Y.; De, J.; Schneider, K.; Correll, M.; Tong, Z. Real-Time and Rapid Food Quality Monitoring Using Smart Sensory Films with Image Analysis and Machine Learning. *ACS Food Science and Technology* **2022**, 2 (7), 1123–1134.
6. Yan, M.; Wang, B.; Wang, M. Facilely Processable Dual-Color Ratiometric Fluorescent Sensors for Highly Sensitive Detection of Food Spoilage. *ACS Food Science and Technology* **2023**, 3, 6, 1090–1097.
7. Ye, H.; Koo, S.; Beitong Zhu; Ke, Y.; Sheng, R.; Duan, T.; Zeng, L.; Kim, J. S. Real-Time Fluorescence Screening Platform for Meat Freshness. *Anal Chem* **2022**, 94 (44), 15423–15432.

8. Na, X.; Zou, B.; Zheng, X.; Du, M.; Zhu, B.; Wu, C. Synergistic Antimicrobial Hybrid Bio-Surface Formed by Self-Assembled BSA Nanoarchitectures with Chitosan Oligosaccharide. *Biomacromolecules* **2023**, 24, 9, 4093–4102.
9. Basavaraja, D.; Dey, D.; Varsha, T. L.; Thodi F. Salfeena, C.; Panda, M. K.; Somappa, S. B. Rapid Visual Detection of Amines by Pyrylium Salts for Food Spoilage Taggant. *ACS Appl Bio Mater* **2020**, 3 (2), 772–778.
10. Yang, X.; Lu, X.; Wang, J.; Zhang, Z.; Du, X.; Zhang, J.; Wang, J. Near-Infrared Fluorescent Probe with a Large Stokes Shift for Detection of Hydrogen Sulfide in Food Spoilage, Living Cells, and Zebrafish. *J Agric Food Chem* **2022**, 70 (9), 3047–3055.
11. Pracella, M.; Mura, C.; Galli, G. Polyhydroxyalkanoate Nanocomposites with Cellulose Nanocrystals as Biodegradable Coating and Packaging Materials. *ACS Appl Nano Mater* **2021**, 4 (1), 260–270.
12. LakshmiBalasubramaniam, S.; Patel, A. S.; Tajvidi, M.; Skonberg, D. Biodegradable Cellulose Nanofibril Films with Active Functionality for Food Packaging Applications. *ACS Food Science & Technology* **2023**, 3 (8), 1323–1333.
13. Enderle, A. G.; Franco-Castillo, I.; Atrián-Blasco, E.; Martín-Rapún, R.; Lizarraga, L.; Culzoni, M. J.; Bollini, M.; De La Fuente, J. M.; Silva, F.; Streb, C.; Mitchell, S. G. Hybrid Antimicrobial Films Containing a Polyoxometalate-Ionic Liquid. *ACS Appl Polym Mater* **2022**, 4 (6), 4144–4153.
14. Wang, X.; Sun, B.; Ye, Z.; Zhang, W.; Xu, W.; Gao, S.; Zhou, N.; Wu, F.; Shen, J. Enzyme-Responsive COF-Based Thiol-Targeting Nanoinhibitor for Curing Bacterial Infections. *ACS Appl Mater Interfaces* **2022**, 14, 34, 38483–38496.
15. Schwenk, G. R.; Glass, A. M.; Ji, H. F.; Ehrlich, G. D.; Navas-Martin, S.; Król, J. E.; Hall, D. C. Surfactant-Impregnated MOF-Coated Fabric for Antimicrobial Applications. *ACS Appl Bio Mater* **2023**, 6 (1), 238–245.
16. Patel, S. R.; Chaki, S. H.; Giri, R. Kr.; Khimani, A. J.; Vaidya, Y. H.; Thakor, P.; Thakkar, A. B.; Deshpande, M. P. Pristine, Ni- and Zn-Doped CuSe Nanoparticles: An Antimicrobial, Antioxidant, and Cytotoxicity Study. *ACS Appl Bio Mater* **2023**, 6 (6), 2211–2225.
17. He, D.; Chen, X.; Yang, S.; Yang, Y.; Wang, Y.; Zhang, R.; Wang, K.; Qian, J.; Long, L. A Sensitive Colorimetric and Near-Infrared Fluorescent Probe for Tracing Slight PH Variation in Food Samples. *ACS Food Science and Technology* **2023**, 3 (5), 891–897.

18. Liu, B.; Gurr, P. A.; Qiao, G. G. Irreversible Spoilage Sensors for Protein-Based Food. *ACS Sens* **2020**, 5 (9), 2903–2908.
19. Cheng, X.; Zhao, Q.; Kang, J.; Zhao, X.; He, X.; Li, J. Cellulose Nanofiber/Polyvinyl Alcohol-Based PH-Responsive Films Containing Anthocyanin and Carbon Dots. *ACS Appl Polym Mater* **2023**, 5, 8, 6307–6317.
20. Lin, T.; Wu, Y.; Li, Z.; Song, Z.; Guo, L.; Fu, F. Visual Monitoring of Food Spoilage Based on Hydrolysis-Induced Silver Metallization of Au Nanorods. *Anal Chem* **2016**, 88 (22), 11022–11027.
21. Si, L.; Shi, Z. K.; Hou, J. Y.; Miao, C. X.; Hou, Q.; Xu, Z.; Ai, S. Lignin-Derived Carbon Dot/Cellulose Nanofiber Films for Real-Time Food Freshness Monitoring. *ACS Appl Nano Mater* **2022**, 5 (11), 16620–16632.
22. Pan, X.; Chen, G.; Xu, T.; Kong, L.; Li, X.; Li, D.; Mu, C.; Xu, Z.; Ge, L. Gelatin-Based Active Edible Film with PH-Sensing for Maintaining and Monitoring Fish Freshness. *ACS Food Science and Technology* **2023**, 3 (8), 1366–1375.
23. Ebert, S.; Kaplan, S.; Gibis, M.; Terjung, N.; Weiss, J. Establishing the Mixing and Solubilization Behavior of Pork Meat and Potato Proteins at Acidic to Neutral PH. *ACS Food Science & Technology* **2021**, 1 (3), 410–417.
24. Zare, M.; Namratha, K.; Ilyas, S.; Hezam, A.; Mathur, S.; Byrappa, K. Smart Fortified PHBV-CS Biopolymer with ZnO-Ag Nanocomposites for Enhanced Shelf Life of Food Packaging. *ACS Appl Mater Interfaces* **2019**, 11 (51), 48309–48320.
25. Khan, A.; Ezati, P.; Rhim, J. W. Chitosan/Starch-Based Active Packaging Film with N, P-Doped Carbon Dots for Meat Packaging. *ACS Appl Bio Mater* **2023**, 6 (3), 1294–1305.
26. Sharma, R.; Jung, S. H.; Lee, H. II. Thin Polymeric Films for Real-Time Colorimetric Detection of Hydrazine Vapor with Parts-per-Million Sensitivity. *ACS Appl Polym Mater* **2021**, 3 (12), 6632–6641.
27. Roy, S.; Rhim, J. W. Preparation of Gelatin/Carrageenan-Based Color-Indicator Film Integrated with Shikonin and Propolis for Smart Food Packaging Applications. *ACS Appl Bio Mater* **2021**, 4 (1), 770–779.
28. Pires, A. S.; Gomes, V.; Neves, D.; Mateus, N.; De Freitas, V.; Cruz, L. Colorimetric PH-Responsive Biomaterials Based on Pyranoflavylum-Biopolymer Hybrid Conjugates. *ACS Appl Polym Mater* **2022**, 4 (7), 4961–4971.

29. Priyadarshi, R.; Riahi, Z.; Rhim, J. W.; Han, S.; Lee, S. G. Sulfur Quantum Dots as Fillers in Gelatin/Agar-Based Functional Food Packaging Films. *ACS Appl Nano Mater* **2021**, *4* (12), 14292–14302.
30. Yuan, L.; Gao, M.; Xiang, H.; Zhou, Z.; Yu, D.; Yan, R. A Biomass-Based Colorimetric Sulfur Dioxide Gas Sensor for Smart Packaging. *ACS Nano* **2023**, *17* (7), 6849–6856.
31. Koshy, R. R.; Reghunadhan, A.; Mary, S. K.; Thomas, K.; Ajish, K. R.; Thomas, S.; Pothan, L. A. Intelligent PH-Sensitive Films from Whole Arrowroot Powder and Soy Protein Isolate Incorporating Red Cabbage Anthocyanin: Monitoring Freshness of Shrimps and Ammonia in Fish Farming Ponds. *New Journal of Chemistry* **2022**, *46*, 9036–9047.
32. Zhai, X.; Li, Z.; Zhang, J.; Shi, J.; Zou, X.; Huang, X.; Zhang, D.; Sun, Y.; Yang, Z.; Holmes, M.; Gong, Y.; Povey, M. Natural Biomaterial-Based Edible and PH-Sensitive Films Combined with Electrochemical Writing for Intelligent Food Packaging. *J Agric Food Chem* **2018**, *66* (48), 12836–12846.
33. Zoratti, L.; Jaakola, L.; Häggman, H.; Giongo, L. Anthocyanin Profile in Berries of Wild and Cultivated Vaccinium Spp. along Altitudinal Gradients in the Alps. *J Agric Food Chem* **2015**, *63* (39), 8641–8650.
34. Bresciani, L.; Angelino, D.; Vivas, E. I.; Kerby, R. L.; García-Viguera, C.; Del Rio, D.; Rey, F. E.; Mena, P. Differential Catabolism of an Anthocyanin-Rich Elderberry Extract by Three Gut Microbiota Bacterial Species. *J Agric Food Chem* **2020**, *68* (7), 1837–1843.
35. Aytac, Z.; Xu, J.; Raman Pillai, S. K.; Eitzer, B. D.; Xu, T.; Vaze, N.; Ng, K. W.; White, J. C.; Chan-Park, M. B.; Luo, Y.; Demokritou, P. Enzyme- And Relative Humidity-Responsive Antimicrobial Fibers for Active Food Packaging. *ACS Appl Mater Interfaces* **2021**, *13* (42), 50298–50308.
36. Roy, S.; Ezati, P.; Rhim, J. W. Gelatin/Carrageenan-Based Functional Films with Carbon Dots from Enoki Mushroom for Active Food Packaging Applications. *ACS Appl Polym Mater* **2021**, *3* (12), 6437–6445.
37. Tran, T. N.; Mai, B. T.; Setti, C.; Athanassiou, A. Transparent Bioplastic Derived from CO₂-Based Polymer Functionalized with Oregano Waste Extract toward Active Food Packaging. *ACS Appl Mater Interfaces* **2020**, *12* (41), 46667–46677.

38. Kim, W.; Han, T.; Gwon, Y.; Park, S.; Kim, H.; Kim, J. Biodegradable and Flexible Nanoporous Films for Design and Fabrication of Active Food Packaging Systems. *Nano Lett* **2022**, *22* (8), 3480–3487.
39. Kang, Y.; Jang, J.; Kim, S.; Lim, J.; Lee, Y.; Kim, I. S. PIP/TMC Interfacial Polymerization with Electrospray: Novel Loose Nanofiltration Membrane for Dye Wastewater Treatment. *ACS Appl Mater Interfaces* **2020**, *12* (32), 36148–36158.
40. Abbaspourrad, A.; Carroll, N. J.; Kim, S. H.; Weitz, D. A. Polymer Microcapsules with Programmable Active Release. *J Am Chem Soc* **2013**, *135* (20), 7744–7750.
41. Urzedo, A. L.; Gonçalves, M. C.; Nascimento, M. H. M.; Lombello, C. B.; Nakazato, G.; Seabra, A. B. Cytotoxicity and Antibacterial Activity of Alginate Hydrogel Containing Nitric Oxide Donor and Silver Nanoparticles for Topical Applications. *ACS Biomater Sci Eng* **2020**, *6* (4), 2117–2134.
42. Orr, A.; Wilson, P.; Stotesbury, T. DNA-Crosslinked Alginate Hydrogels: Characterization, Microparticle Development, and Applications in Forensic Science. *ACS Appl Polym Mater* **2022**, *5*(1), 583–592.
43. Cholewinski, A.; Yang, F. K.; Zhao, B. Underwater Contact Behavior of Alginate and Catechol-Conjugated Alginate Hydrogel Beads. *Langmuir* **2017**, *33* (34), 8353–8361.
44. Li, C.; Liu, J.; Li, W.; Liu, Z.; Yang, X.; Liang, B.; Huang, Z.; Qiu, X.; Li, X.; Huang, K.; Zhang, X. Biobased Intelligent Food-Packaging Materials with Sustained-Release Antibacterial and Real-Time Monitoring Ability. *ACS Appl Mater Interfaces* **2023**, *15* (31), 37966–37975.
45. Cvek, M.; Paul, U. C.; Zia, J.; Mancini, G.; Sedlarik, V.; Athanassiou, A. Biodegradable Films of PLA/PPC and Curcumin as Packaging Materials and Smart Indicators of Food Spoilage. *ACS Appl Mater Interfaces* **2022**, *14* (12), 14654–14667.
46. Magnaghi, L. R.; Alberti, G.; Milanese, C.; Quadrelli, P.; Biesuz, R. Naked-Eye Food Freshness Detection: Innovative Polymeric Optode for High-Protein Food Spoilage Monitoring. *ACS Food Science and Technology* **2021**, *1* (2), 165–175.
47. Pineau, N. J.; Magro, L.; van den Broek, J.; Anderhub, P.; Güntner, A. T.; Pratsinis, S. E. Spirit Distillation: Monitoring Methanol Formation with a Hand-Held Device. *ACS Food Science and Technology* **2021**, *1* (5), 839–844.

48. Huang, Z. J.; Li, H.; Luo, J. Y.; Li, S.; Liu, F. Few-Shot Learning-Based, Long-Term Stable, Sensitive Chemosensor for On-Site Colorimetric Detection of Cr(VI). *Anal Chem* **2023**, 95 (14), 6156–6162.
49. Liu, M.; Zhu, H.; Wang, K.; Zhang, X.; Li, X.; Yu, M.; Zhu, B.; Sheng, W.; Liu, C. A Novel Fluorescent Chemodosimeter for Discriminative Detection of Cu²⁺ in Environmental, Food, and Biological Samples. *ACS Food Science and Technology* **2023**, 3 (1), 134–140.
50. Babazadeh-Mamaqani, M.; Mohammadi-Jorjafki, M.; Alipour-Fakhri, S.; Mardani, H.; Roghani-Mamaqani, H. Thermal-Induced Chromism and Fluorescence Emission of Rhodamine B-Containing Polymers with Different Polarities: Tracking Temperature and Development of Thermochromic Labels. *Macromolecules* **2023**, 56, 5843–5853.
51. Skorjanc, T.; Shetty, D.; Valant, M. Covalent Organic Polymers and Frameworks for Fluorescence-Based Sensors. *ACS Sens* **2021**, 6 (4), 1461–1481.
52. Wang, J.; Sun, X.; Zhang, H.; Dong, M.; Li, L.; Zhangsun, H.; Wang, L. Dual-Functional Intelligent Gelatin Based Packaging Film for Maintaining and Monitoring the Shrimp Freshness. *Food Hydrocoll* **2022**, 124, 107258.
53. Bao, Y.; Cui, H.; Tian, J.; Ding, Y.; Tian, Q.; Zhang, W.; Wang, M.; Zang, Z.; Sun, X.; Li, D.; Si, X.; Li, B. Novel PH Sensitivity and Colorimetry-Enhanced Anthocyanin Indicator Films by Chondroitin Sulfate Co-Pigmentation for Shrimp Freshness Monitoring. *Food Control* **2022**, 131, 108441.
54. Liu, L.; Wu, W.; Zheng, L.; Yu, J.; Sun, P.; Shao, P. Intelligent Packaging Films Incorporated with Anthocyanins-Loaded Ovalbumin-Carboxymethyl Cellulose Nanocomplexes for Food Freshness Monitoring. *Food Chem* **2022**, 387, 132908.
55. Boonsiriwit, A.; Lee, M.; Kim, M.; Inthamat, P.; Siripatrawan, U.; Lee, Y. S. Hydroxypropyl Methylcellulose/Microcrystalline Cellulose Biocomposite Film Incorporated with Butterfly Pea Anthocyanin as a Sustainable PH-Responsive Indicator for Intelligent Food-Packaging Applications. *Food Biosci* **2021**, 44, 101392.

